Seismic Response of Slab-Column Edge Connections Reinforced with Fibre-Reinforced Polymer (FRP) Composite Bars

by

Mohammed Galal Osman Mohammed ElGendy

A Thesis submitted to the Faculty of Graduate Studies of

The University of Manitoba

in partial fulfilment of the requirements of the degree of

DOCTOR OF PHILOSOPHY

Department of Civil Engineering

University of Manitoba

Winnipeg, MB, Canada

ABSTRACT

When reinforced concrete (RC) flat plate systems are used as gravity force resisting systems in regions of high seismic activity, they are required to accommodate the seismically induced drifts without jeopardizing their gravity load capacity. The elastic nature of fibre-reinforced polymer (FRP) reinforcement raises concerns about the seismic response of FRP-RC flat plate systems. The present study provides the first attempt to tackle this area.

A pioneer research program was conducted to investigate the feasibility of using FRP reinforcement in slab-column edge connections subjected to simulated seismic loads. The program consisted of three phases: experimental, analytical, and numerical. The experimental phase involved the construction and testing of seven full-scale glass FRP (GFRP)-RC edge connections under simultaneous gravity and reversed-cyclic lateral loads. The test parameters were the flexural reinforcement type (steel and GFRP) and ratio (0.7 and 1.4%), the gravity shear ratio (0.4, 0.5, and 0.6), and the GFRP shear reinforcement type (shear studs and corrugated bars).

In the analytical phase, models predicting the punching capacity of FRP-RC connections from literature were reviewed. Besides the connections tested in the experimental phase, a database comprising 68 interior and 19 edge specimens subjected to gravity loads was compiled and used to assess the models. A universal model capable of predicting the capacity of interior and edge connections subjected to gravity or cyclic loads was proposed.

The numerical phase incorporated the construction and validation of a finite element model (FEM) simulating the seismic behaviour of FRP-RC edge connections. This FEM was used to conduct a parametric study investigating the influence of gravity shear ratio, column size, slab thickness, and flexural reinforcement type and ratio on the seismic response of edge connections.

The results showed that GFRP reinforcement can be used in edge connections subjected to simulated seismic loads. The large elastic deformations of GFRP bars compensated for the absence of yielding. Furthermore, GFRP-RC edge connections without shear reinforcement were able to undergo 1.50% drift ratio if the gravity shear ratio does not exceed 0.5. Moreover, the use of well-anchored GFRP shear reinforcement resulted in a substantial increase in the drift capacity of the connections.

ACKNOWLEDGEMENTS

All praise is due to Allah, who endowed me with strength and guidance to complete this thesis. Without his bounty, grace and mercy, this work would have never been accomplished. I wish to express my deepest gratitude to my supervisor, Dr. Ehab El-Salakawy, Professor of Structural Engineering in the Department of Civil Engineering at the University of Manitoba, who convincingly guided and encouraged me every step of the way. His persistent help, advice and, most importantly, belief in me made me the researcher I am.

I would like to express my appreciation to my examining committee members, Dr. Emile Shehata, Senior Vice President at Tetra Tech Canada Inc., for his faith in me, and Dr. Nan Wu, Associate Professor in the Department of Mechanical Engineering at the University of Manitoba, for his time and support. Also, I am deeply thankful to all my colleagues for their assistance during all work stages. The financial support provided by the Natural Sciences and Engineering Research Council of Canada (NSERC) and the Manitoba Graduate Scholarship (MGS) is acknowledged. The GFRP shear reinforcement provided by Pultrall Inc. is appreciated. The assistance received from the staff of the W. R. McQuade Structures Laboratory at the University of Manitoba is acknowledged.

There is no possible way I could ever express how grateful I am to my parents. Their dedication, sacrifices, and prayers paved the way for me to become the person I am. A special thank you goes to my siblings for their love, wishes, and prayers. My love goes to my wife, Yasmine. Thank you from the bottom of my heart for your love, devotion, kindness, understanding, and generous sacrifices. Thank you for being you! Finally, I would like to send my love to my daughter, Hadia. You have been, and always will be, my guide. You are the line in the sand when I go too far.

Mohammed Galal ElGendy, August 2020

To my late sister, Ghada,

May Allah bless your soul.

To my late daughter, Laila,

You are forever in my heart.

To Mom and Dad,

I hope this achievement gets me "another" step closer to making you proud of me.

To my wife, Yasmine, and my daughter, Hadia,

You light the sky up above me.

TABLE OF CONTENTS

LIST OF TABLES

LIST OF FIGURES

LIST OF NOTATIONS

A_{Fv} = area of FRP shear reinforcement (mm^2);

A_s = area of single shear stud or vertical stem of corrugate bars, stirrups and spirals (mm^2);

a = maximum aggregate size (mm);

b_x = critical section dimension in the x direction (mm);

b_y = critical section dimension in the y direction (mm);

b_o = perimeter of critical section for shear (mm);

$b_{o,0.5d}$ = perimeter of critical section for shear located at 0.5d from column face (mm);

b_1 = width of critical section in the direction of unbalanced moment (mm);

b_2 = width of critical section perpendicular to b_1 (mm);

C = column width (mm);

C_1 = column width perpendicular to free edge (mm);

C_2 = column width parallel to free edge (mm);

c_{ts} = tension stiffening factor;

d = average depth of slab (mm);

d_b = stirrup diameter (mm);

E_c = modulus of elasticity of concrete (MPa);

E_F = modulus of elasticity of FRP reinforcement (MPa);

E_{Fv} = modulus of elasticity of FRP shear reinforcement (MPa);

E_S = modulus of elasticity of steel reinforcement (MPa);

e = distance from centroid of critical section to the point where shear stress is being calculated (mm);

e_x = load eccentricity in the x direction (mm);

e_y = load eccentricity in the y direction (mm);

f_c' = specified compressive strength of concrete (MPa);

f_{Fv} = allowable stress in FRP stirrups (MPa);

f_{fbend} = ultimate strength of bent portion of FRP stirrups (MPa);

f_{pcd} = factor to account for concrete strength (MPa);

f_t = concrete tensile strength (MPa);

f_{uv} = ultimate strength of straight portion of FRP stirrups (MPa);

G_F = fracture energy (MN/m);

h = slab thickness (mm);

I_{cr} = cracked moment of inertia per unit width of the slab (mm^4);

I_g = gross moment of inertia per unit width of the slab (mm^4);

J_c = property of the critical shear section analogous to polar moment of inertia (mm^4);

k = ratio of neutral axis depth of cracked section to depth of reinforcement, or initial stiffness (kN/m);

k_{EXP} = experimental initial stiffness (kN/m);

k_{FEM} = initial stiffness estimated by FEM (kN/m);

L_1 = slab dimension perpendicular to unbalanced moment (mm);

L_2 = slab dimension parallel to unbalanced moment (mm);

M_{cr} = cracking moment per unit width of the slab (kN.m/m);

M_f = factored unbalanced moment transferred between slab and column (kN/m);

M_n = ultimate moment per unit width of the slab (kN.m/m);

M_p = equivalent plastic moment capacity for FRP-RC slabs (kN/m);

M_{unb} = unbalanced moment transferred between slab and column (kN/m);

M/V = moment-to-shear ratio (m);

N = factor to account for effect of slab restraining;

n = number of vertical stems of shear reinforcement in a peripheral row around column;

n_F = ratio between modulus of elasticity for FRP to modulus of elasticity for concrete;

P_g = gravity lateral load (kN);

$P_{g\text{-}EXP}$ = experimental gravity lateral load (kN);

$P_{g\text{-}FEM}$ = gravity lateral load estimated by FEM (kN);

P_p = peak lateral load (kN);

$P_{p\text{-}EXP}$ = experimental peak lateral load (kN);

$P_{p\text{-}FEM}$ = peak lateral load estimated by FEM (kN);

$P_{u,CSA}$ = lateral load capacity predicted by CSA S806-12 (CSA 2017) (kN);

$P_{u,E\text{-}E}$ = lateral load capacity predicted by El-Gendy and El-Salakawy (2020c) (kN);

r_b = stirrup bend radius (mm);

$r_{c,lim}$ = reduction of compressive strength factor;

S_F = crack shear stiffness factor;

s = spacing of FRP shear reinforcement measured perpendicular to critical section (mm);

u = perimeter of loaded area (mm);

V_c = punching shear capacity provided by concrete (kN);

V_{exp} = experimental capacity of test connection (kN);

V_f = total factored shear force transferred between slab and column (kN);

V_g = gravity shear force transferred between the slab and the column (kN);

v_{CSA} = punching strength predicted by CSA S806-12 (CSA 2017) (MPa);

v_c = shear stress resistance provided by concrete (MPa);

$v_{c,inner}$ = shear stress resistance provided by concrete at inner critical section (MPa);

$v_{c,outer}$ = shear stress resistance provided by concrete at outer critical section (MPa);

$v_{E\text{-}E}$ = punching strength predicted by El-Gendy and El-Salakawy (2020c) (MPa);

v_{exp} = experimental shear stress resistance (MPa);

$v_{exp,\ 0.5d}$ = experimental shear stress resistance at critical section located at a distance of 0.5d (MPa);

$v_{exp,\ 1.5d}$ = experimental shear stress resistance at critical section located at a distance of 1.5d (MPa);

v_{FEM} = punching strength estimated by FEM (MPa);

v_f = factored shear stress on critical section (MPa);

v_n = nominal shear stress resistance (MPa);

v_{pred} = predicted shear stress resistance (MPa);

v_r = punching shear resistance (MPa);

v_s = shear stress resistance provided by shear reinforcement (MPa);

v_{sF} = shear stress resistance provided by FRP shear reinforcement (MPa);

w_d = critical compressive displacement (mm);

α = load eccentricity factor;

α_s = dimensionless coefficient to account for location of slab-column connections;

β_c = ratio of long side to short side of column;

β_d = size effect factor;

β_p = reinforcement axial stiffness factor;

β_r = factor to account for column perimeter-to-slab depth ratio;

γ_b = factor of safety generally taken as 1.3;

γ_v = fraction of unbalanced moment transferred by eccentricity of shear;

δ = inter-story drift ratio (%);

δ_p = peak drift ratio (%);

$\delta_{p\text{-}FEM}$ = peak drift ratio estimated by FEM (%);

δ_u = ultimate drift ratio (%);

$\delta_{u\text{-}EXP}$ = experimental ultimate drift ratio (%);

$\delta_{u\text{-}FEM}$ = ultimate drift ratio estimated by FEM (%);

ε_{Fv} = allowable strain in FRP shear reinforcement;

λ = factor to account for concrete density;

μ = Poisson's ratio of concrete;

ρ_F = longitudinal FRP reinforcement ratio (%);

ϕ = strength reduction factor;

ϕ_c = resistance factor for concrete; and

ϕ_F = resistance factor for FRP shear reinforcement.

CHAPTER 1. INTRODUCTION

1.1. Background

Embedded steel reinforcement in reinforced concrete (RC) structures is initially protected against corrosion by a microscopically thin passive layer, which is formed in the highly alkaline condition of the concrete pore solution (Neville 1995). In cold regions, RC structures are subjected to aggressive conditions, such as wet/dry cycles, freeze/thaw cycles and diffusion of de-icing salts through the concrete. These conditions promote cracking and reduce alkalinity of concrete, which leaves steel reinforcement vulnerable to electrochemical corrosion.

Corrosion of steel reinforcement is a major durability issue that results in the deterioration of RC structures. This, in turn, increases the number of repair cycles required for a structure to achieve its service life and, consequently, increases the maintenance cost over the service life of the structure. Different solutions have been proposed to the corrosion problem, such as increasing the concrete cover, improving the quality of concrete, and the use of different types of steel reinforcement, e.g., epoxy-coated steel, galvanized steel and stainless steel. Nevertheless, besides being cost-ineffective, these solutions have managed only to delay the corrosion process and to mitigate its effects; none of them was able to prevent it entirely.

In the last two decades, the use of fibre-reinforced polymer (FRP) composites as an alternative to the conventional steel reinforcement has proved to be an effective solution to the corrosion problem. In addition to their non-corrodible nature, FRP composites have several other advantages over conventional steel, such as high longitudinal tensile strength, no magnetic conductivity, lightweight, low electrical and thermal conductivity (for certain types of fibres), and versatility of fabrication. On the other hand, unlike steel reinforcement, FRP composites exhibit linear-elastic

behaviour up to failure, i.e., they do not undergo any ductile phase in terms of a yielding plateau prior to the brittle rupture. Moreover, FRP reinforcing bars have a relatively low elastic stiffness and compressive strength compared to steel bars. Furthermore, they have low transverse strength and stiffness, which reduces the shear strength of FRP-RC elements (ACI 2015). Due to these differences, the current design codes and standards dealing with steel-RC structures cannot be directly applied to FRP-RC structures. Instead, extensive experimental investigations must be carried out to investigate the behaviour of concrete elements reinforced with FRP composites, verify the applicability of these codes and standards on FRP-RC structures, and modify them when necessary. Accordingly, many research studies have been conducted in the last few decades to investigate the behaviour of FRP-RC members subjected to gravity loads, which resulted in the publication of design standards and guidelines for such members (JSCE 1997; CSA 2017, 2019a; ACI 2015). However, relatively few research studies have been conducted to investigate the seismic behaviour of such members.

1.2. Problem Definition

Reinforced concrete flat slabs represent a simple structural system that consists of a slab supported directly on columns without protruding beams. This system is widely favoured by designers due to its numerous advantages, such as: 1) simplicity of formwork and the associated speed of construction; 2) the relatively low storey height, which reduces the total building height, thus reduces lateral loads and allows for an increased number of floors in regions where height restrictions apply; and 3) the absence of beams, which provides flexibility for partition locations and results in greater clear storey heights. The economy of this system is further enhanced by utilizing its simplest form, namely the flat plate system, which has no variations in the slab thickness around the column, i.e., no drop panels or column capitals, as shown in Figure 1.1.

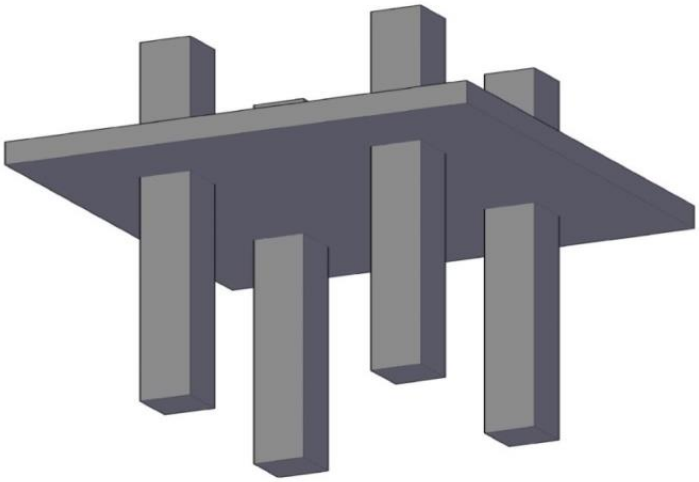

Figure 1.1: Typical flat plate system

Flat plate systems are susceptible to punching shear failure, which involves the penetration of the column, along with a surrounding part of the slab, through the remainder of the slab. This type of failure is extremely dangerous due to its brittle nature, which does not provide sufficient warning to the occupants of the building before failure. Furthermore, the failure of one connection in the system may lead to the loss of the integrity of the structure and, consequently, a progressive collapse of the whole structure when the adjacent connections fail to support the additional loads imposed on them (Swamy and Ali 1982). Punching shear failure occurs due to the concentration of shear stresses in the slab near slab-column connections. These shear stresses are caused by not only shear forces but also unbalanced moments transferred between slab and columns at slab-column connections. In a typical slab-column connection, the unbalanced moments occur due to loading conditions, different lengths of adjacent spans, discontinuity of slabs at exterior connections and, more significantly, by lateral loads such as wind or seismic loads.

Compared to beam-column joints, slab-column connections are relatively flexible under seismic loads, which may cause extensive structural and non-structural damage as excessive lateral drifts

occur. In addition, the transfer of shear forces and unbalanced moments would further promote the brittle punching shear failure leading to, in the worst case, a progressive collapse of the entire structure. The Canadian standard CSA A23.3-19 (CSA 2019b) and the American code ACI 318-19 (ACI 2019a) for steel-RC buildings allow the use of flat plate systems as a part of the seismic force resisting system (SFRS) in regions of low to moderate seismic risk, i.e., regions assigned to seismic design category (SDC) A, B and C. However, in regions of high seismic risk, i.e., regions assigned to SDC D, E and F, flat plate systems can only be used as gravity force resisting systems (GFRS), where special moment frames or shear walls are provided as the main SFRS.

Nevertheless, in regions of high seismic risk, the presence of special moment frames or shear walls does not completely eliminate the seismic forces applied to the GFRS. Additional unbalanced moments will be transferred between the slab and column, which increases the shear stresses in the slab. In addition, in general, the elements of an RC structure in a seismic zone are required to have enough ductility to be capable of deforming into the inelastic range. According to ACI 352.1R-11 (ACI 2011), this requirement extends to elements that are not considered a part of the SFRS. Consequently, even when used as a GFRS in regions of high seismic risk, flat plate systems must be designed and detailed for deformation compatibility with the main SFRS. This is required to ensure flat plate systems can maintain their gravity load capacity with a minimum level of ductility that is able to accommodate the seismically induced lateral displacements. These lateral displacements, besides inducing significant unbalanced moments, could result in large inelastic rotations in the connections, which may decrease their punching shear capacity.

The seismic response of steel-RC slab-column connections has been extensively investigated. Pan and Moehle (1989) reported that, although the available ductility of a slab-column connection

without shear reinforcement is considerably low, the relatively high flexibility of the connection may protect it from large ductility demands. It was concluded that increasing the gravity shear ratio (which is the ratio of the gravity shear transferred between the slab and the column at failure to the theoretical punching shear strength provided by concrete) decreases both the drift capacity and lateral displacement ductility of slab-column connections (Pan and Moehle 1989; Robertson and Durrani 1991, 1992; Megally and Ghali 1994, 2000a; Robertson and Johnson 2006; Cheng and Giduquio 2014; Giduquio et al. 2019). It was also concluded that properly anchored shear reinforcement could significantly increase the ductility, energy absorption and capacity of the connections (Carpenter et al. 1973; Hawkins et al. 1975; Islam and Park 1976; Megally and Ghali 1994, 2000a, 2000b, 2000c; Li et al. 2007; Matzke et al. 2015).

Flat plate systems are extensively used in parking garage structures to take advantage of the absence of beams, which allows for more clearance for vehicles. In North America, due to the harsh environmental conditions, RC parking garages are extremely vulnerable to the corrosion of steel reinforcement. As mentioned earlier, the use of FRP reinforcement instead of conventional steel reinforcement overcomes this problem. However, FRP-RC members experience wider and deeper cracks than their steel-RC counterparts due to the relatively low modulus of elasticity of FRP reinforcement. Wider cracks reduce the aggregate interlock contribution to the shear strength, while deeper cracks reduce the un-cracked concrete contribution. Furthermore, the dowel action of the longitudinal FRP reinforcement is considerably lower than that of steel reinforcement due to the low transverse shear strength of FRP reinforcement. Accordingly, the shear capacity of FRP-RC members is expected to be considerably lower than that of their steel-RC counterparts with the same flexural reinforcement ratio. On the other hand, due to the elastic nature of FRP reinforcement, FRP-RC structures do not behave in a ductile manner and, consequently, FRP

reinforcement does not seem to be suitable to reinforce structures in seismic zones. Nevertheless, due to the combination of high tensile strength and low modulus of elasticity of FRP reinforcement, FRP-RC structures exhibit large elastic deformations prior to failure. The Canadian standard for bridges CSA S6-19 (CSA 2019a) recognizes this deformable behaviour of FRP-RC structures using the deformability factor, which is an analogues factor to the ductility index for steel-RC structures. The deformability factor can be considered as an indication of the ability of a structure to dissipate the energy induced by the seismic loads; the higher the deformability factor, the more seismic-energy dissipated by the structure.

Research conducted on glass FRP (GFRP)-RC beam-column joints showed that GFRP reinforcement can be used as longitudinal and transverse reinforcement in beam-column joints subjected to seismic loads (Hasaballa et al. 2011; Ghomi and El-Salakawy 2019). It was reported that, although the GFRP-RC joints dissipated less energy than their steel-RC counterparts, they experienced considerably less residual damage due to the elastic behaviour of the FRP reinforcement; thus, requiring minimum amount of repair after surviving the seismic event. Furthermore, research conducted on FRP-RC short columns indicated the feasibility of using FRP longitudinal and transverse reinforcement in columns subjected to seismic loads (Sharbatdar and Saatcioglu 2009; Ali and El-Salakawy 2015; Tavassoli et al. 2015; Naqvi and El-Salakawy 2017; AlAjarmeh et al. 2019). To date, however, no research has been conducted on FRP-RC slab-column connections subjected to cyclic lateral loads. Accordingly, it is necessary to investigate the seismic response of FRP-RC slab-column connections to verify the feasibility of using FRP longitudinal and transverse reinforcement in the shear-critical slab-column connections.

1.3. Scope of Work

As shown in Figure 1.2, there are three types of slab-column connections according to their location in a flat plate system: interior, edge and corner connections. Exterior connections (edge and corner) are more critical to punching shear failure due to several reasons, such as: (1) the relatively higher unbalanced moments transferred at exterior connections compared to those at interior ones; (2) the less confinement of the critical perimeter due to the disruption of the slab; and (3) the probable lack of slab reinforcement anchorage due to small column cross-sections and the disruption of the slab. Therefore, the scope of this research study is to investigate the seismic response of full-scale isolated FRP-RC slab-column edge connections. The experimental test connections are assumed to be isolated from a prototype flat plate multi-story building. Each connection represents an edge column monolithically connected to a portion of the flat plate that is bounded by the contra-flexure lines. Except for a steel-RC control specimen, all slabs are reinforced with GFRP longitudinal bars with or without GFRP shear reinforcement. The isolated connections are tested under uniaxial reversed-cyclic lateral load applied to the column with a constant level of gravity load applied to the slab.

1.4. Objectives

The main objectives of this study are to:

- Investigate the feasibility of using GFRP longitudinal and transverse reinforcement in slab-column edge connections subjected to seismic loads; and
- Provide design and detailing recommendations to predict the capacity and the structural performance of FRP-RC slab-column connections subjected to seismic loads.

In order to achieve these objectives, the effects of the following parameters on the seismic response of GFRP-RC slab-column edge connections are studied:

- Flexural reinforcement type (steel and GFRP) and ratio (0.7 and 1.4%);
- Gravity shear ratio (0.4, 0.5, and 0.6); and
- Type of shear reinforcement (GFRP shear studs and corrugated bars).

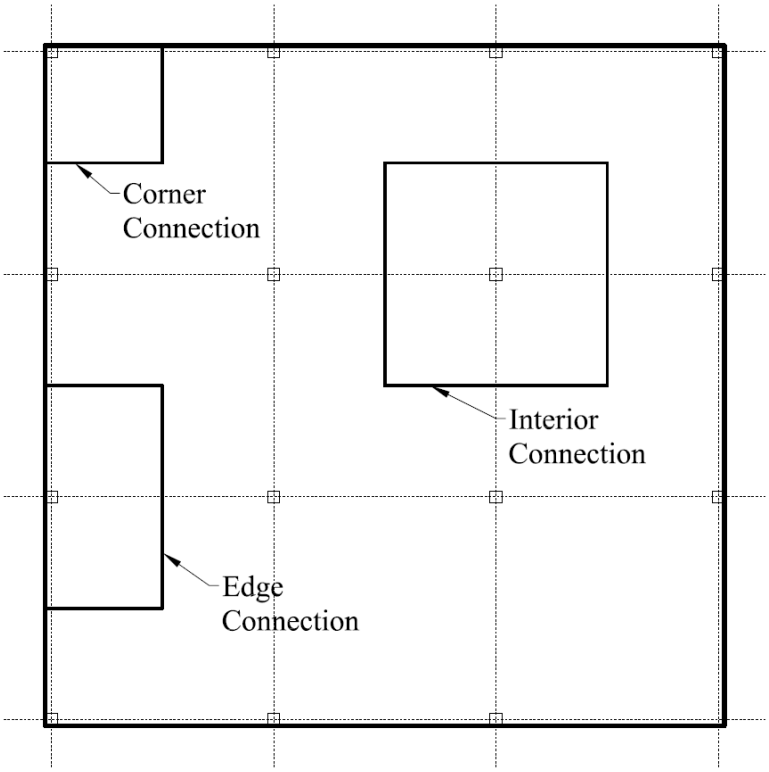

Figure 1.2: Different locations of slab-column connections

1.5. Work Methodology

The research program consists of three phases: experimental, analytical, and numerical. The research starts with the experimental phase, which involves the construction and testing of seven full-scale isolated GFRP-RC slab-column edge connections under gravity and uniaxial reversed-cyclic lateral load up to failure. Each connection represents an edge slab-column connection

isolated from a prototype flat plate multi-story building consisting of five bays of 5,500 mm-long in each direction. The isolated connections are bounded by the free edge of the slab and the lines of contra-flexure. The isolated edge connection has slab dimensions of 3,300 × 3,100 × 200 mm with 3,070-mm long square edge column. The slabs of the connections are reinforced in flexure with deformed steel bars in one connection (control specimen) and sand-coated GFRP bars with differing reinforcement ratios in six connections. Two GFRP-RC slabs were reinforced with GFRP shear reinforcement; one with shear studs and the other with corrugated bars.

In the analytical phase, different models predicting the punching shear capacity of FRP-RC connections incorporated in the current standards and guidelines or proposed in the literature are reviewed. In addition to the edge connections tested in the experimental phase under simulated seismic loads, a database comprising 68 interior and 19 edge specimens subjected to gravity loads from the literature is compiled and used to assess the different models. Based on the assessment, a universal model capable of accurately predicting the capacity of interior and edge connections, subjected to gravity or cyclic loads, is proposed.

The numerical phase comprises two stages. In the first stage, a finite element model (FEM) is constructed to simulate the seismic behaviour of the isolated FRP-RC slab-column edge connections using a commercial software package, ATENA-3D (Červenka et al. 2018). The efficiency and accuracy of the FEM is validated against the experimental results obtained from the experimental phase. In the second stage, the validated FEM is used to conduct an extensive parametric study investigating the influence of key parameters known to affect the seismic response of slab-column connections including gravity shear ratio, column size, slab thickness, and flexural reinforcement type and ratio.

1.6. Thesis Organization

The thesis consists of nine chapters as described below:

- Chapter 1 presents a brief background of the research topic, identifies the problem definition and scope of work, states the main objectives of the work, and provides a general description of the followed methodology.
- Chapter 2 provides an essential theoretical background regarding the properties of FRP reinforcement, different shear transferring mechanisms in flat slabs, the rule of shear reinforcement in slabs and the effect of cyclic loading on punching shear behaviour of slabs. In addition, it reviews previous research on steel-RC and FRP-RC slab-column connections subjected to simulated seismic load and gravity load, respectively.
- Chapter 3 explains the details of the experimental program in terms of the properties of the used materials, the characteristics of the isolated test specimens, configuration of the test setup, and the steps of the test procedure.

The following five chapters (Chapters 4 to 8) are presented in journal article format, where four articles were published and one was under review at the time of thesis submission.

- Chapter 4 (Article 1, published) investigates the feasibility of replacing steel with GFRP reinforcement and the effect of flexural reinforcement ratio on the seismic response of the connections.

  El-Gendy, M., and El-Salakawy, E. 2019. “Effect of flexural reinforcement type and ratio on the punching behavior of RC slab-column edge connections subjected to

reversed-cyclic lateral loads." *Eng. Struct.*, 200, 109703, https://doi.org/10.1016/j.engstruct.2019.109703.

- Chapter 5 (Article 2, published) investigates the effect of one of the main parameters known to affect the seismic response of slab-column connection, which is the gravity shear ratio. The hysteretic responses of different specimens are discussed to provide evidence that FRP-RC specimens can withstand similar or higher drift ratios than those exhibited by steel-RC counterparts.

  El-Gendy, M., and El-Salakawy, E. 2020. "Gravity load effect on seismic response of glass fiber-reinforced polymer-reinforced concrete slab-column edge connections." *ACI Struct. J.*, 117 (5), https://doi.org/10.14359/51724665.

- Chapter 6 (Article 3, published) addresses the contribution of different GFRP reinforcement types on the seismic response of slab-column connections. The efficiency of two different GFRP shear reinforcement types on enhancing the deformability and drift capacity of such connections is discussed in detail.

  El-Gendy, M., and El-Salakawy, E. 2020. "GFRP shear reinforcement for slab-column edge connections subjected to reversed cyclic lateral load." *J. Compos. Constr.*, 24 (2): 04020003, https://doi.org/10.1061/(ASCE)CC.1943-5614.0001000.

- Chapter 7 (Article 4, published) assesses the available empirical models incorporated in different design codes and guidelines and proposed by several researchers. A comprehensive database is established using specimens subjected to gravity and cyclic lateral loads. The database is then used to evaluate the design models. Based on this

assessment, a universal model capable of accurately predicting the capacity of interior and edge connections, subjected to gravity or cyclic loads, is proposed.

El-Gendy, M., and El-Salakawy, E. 2020. "Assessment of punching shear design models for FRP-RC slab-column connections." *J. Compos. Constr.*, 24 (5): 04020047, https://doi.org/10.1061/(ASCE)CC.1943-5614.0001054.

- Chapter 8 (Article 5, under review) illustrates the steps followed to construct and validate a FEM simulating the behaviour of the specimens tested in the previous chapters. The FEM is then used to conduct an extensive parametric study investigating the influence of different key parameters.

  El-Gendy, M., and El-Salakawy, E. forthcoming. "Finite element analysis of FRP-reinforced concrete slab-column edge connections subjected to reversed-cyclic lateral loads." *J. Compos. Constr.*, under review.

- Chapter 9 provides a summary of the major findings of the experimental and analytical work as well as recommendations for future research.

CHAPTER 2. LITERATURE REVIEW

2.1. Background

The reinforced concrete flat plate system is considered one of the most efficient and common floor systems. The absence of protruded beams results in easier formwork, greater clear storey heights, lower total building height and flexibility for partition locations. This structural system, however, is susceptible to punching shear failure, where the column along with a surrounding part of the slab suddenly penetrates through the remainder of the slab. In a typical slab-column connection, not only are concentric loads transferred from the slab to the column, but also are unbalanced bending moments. This could be attributed to loading conditions, different span length of adjacent bays, the discontinuity of the slab at exterior connections and, more significantly, due to lateral forces such as wind or seismic forces. While a portion of these unbalanced moments is resisted by flexure, the remaining portion is resisted by punching shear.

During an earthquake, lateral loads may cause significant shear forces and unbalanced moments to transfer from slabs to columns, especially at exterior slab-column connections where considerable unbalanced moments already exist due to the unsymmetrical slab geometry. Moreover, whether the flat plate system is a part of the SFRS or not, it will be subjected to significant ground motions and is required to undergo considerable drifts in the inelastic range. Consequently, the possibility of a brittle punching shear failure is magnified due to the insufficient strength and ductility of slab-column connections. Therefore, when subjected to earthquake excitation, slab-column connections should possess sufficient ductility in order to be able to deform into the inelastic range without jeopardizing their gravity load capacity. The punching shear capacity and deformability can be increased and, thus, the brittle punching shear failure can be avoided by providing shear reinforcement in the slab.

Sozen (1980) recommended a minimum interstory drift ratio (DR) of 1.5% that an RC flat plate system without shear reinforcement can withstand without failure (DR is defined as the ratio of the relative lateral displacement of two successive floors to the height of the floor (ACI 2010)). This requirement shall be satisfied in all situations, whether the system is a part of the SFRS or not.

The significance of cyclic lateral loading on the behaviour of slab-column connections was recognized in the early 1970s. Carpenter et al. (1973) reported that a considerable amount of ductility is provided to interior connections subjected to cyclic lateral loading when shear reinforcement in the form of stirrups are present. In addition, Hawkins et al. (1974) showed that interior connections subjected to cyclic lateral loads had 20% lower shear strength than their counterparts subjected to monotonic loads. Since then, the seismic response of steel-RC slab-column connections subjected to cyclic lateral loading has been extensively investigated (Hawkins et al. 1975; Islam and Park 1976; Ghali et al. 1976; Pan and Moehle 1989, 1992; Robertson and Durrani 1991, 1992; Wey and Durrani 1992; Megally and Ghali 1994, 2000a, 2000b, 2000c; Durrani et al. 1995; Hwang and Moehle 2000; Robertson et al. 2002; Stark et al. 2005; Robertson and Johnson 2006; Broms 2007; Anggadjaja and Teng 2008; Cheng et al. 2010; Cheng and Giduquio 2014; Matzke et al. 2015; Drakatos et al. 2016; Giduquio et al. 2019).

The punching shear behaviour of FRP-RC slabs subjected to concentric shear forces through a steel plate or a column stub has been studied starting late 1990s (Banthia et al. 1995; Matthys and Taerwe 2000; El-Ghandour et al. 2003; Ospina et al. 2003; Dulude et al. 2013; Hassan et al. 2013a, 2013b, 2015, 2017). However, the behaviour of FRP-RC slab-column connections subjected to shear force and unbalanced moment transfer has only attracted attention recently due to the

sophisticated test setup and complex connection behaviour (El-Gendy and El-Salakawy 2016, 2018a; Gouda and El-Salakawy 2016a, 2016b; Mostafa and El-Salakawy 2018; Hussein and El-Salakawy 2018; Salama et al. 2019). It was demonstrated that the presence of well-anchored FRP shear reinforcement significantly increases the punching shear capacity and deformability of the connections (El-Gendy and El-Salakawy 2016; Hussein and El-Salakawy 2018; Salama et al. 2019). Moreover, increasing the ratio of the unbalanced moment to the gravity shear applied to the connections resulted in significant reductions in the punching capacity and deformability of the connections (El-Gendy and El-Salakawy 2016; Gouda and El-Salakawy 2016b).

This chapter includes a summary of the main properties of FRP bars, a discussion on the shear transferring mechanisms in slabs, a review of different experimental setups used in the literature to investigate the seismic response of slab-column connections, and a review of the previous research pertaining to slab-column connections and other FRP-RC members subjected to lateral loads.

2.2. Properties of FRP Composite Bars

As mentioned earlier, the material characteristics of FRP reinforcement are essentially different from those of steel. The main differences are summarized in ACI 440.1R-15 (ACI 2015) as follows:

- FRP is linear elastic up to failure whereas steel yields;
- FRP is anisotropic whereas steel is isotropic;
- FRP has lower modulus of elasticity; thus, design for serviceability often controls;
- FRP bars have a low creep-rupture threshold than steel;

- FRP bars have different coefficients of thermal expansion in longitudinal and radial directions;
- FRP has less endurance time in fire than that of steel; and
- Degradation of FRP bars, if present, is benign to the surrounding concrete unlike steel that expands and causes failure of the member.

The following sections provide detailed information regarding the main material characteristics of FRP reinforcement.

2.2.1. Physical properties

Two important physical properties of FRP bars are described in ACI 440.1R-15 (ACI 2015): density and coefficient of thermal expansion. The density of FRP bars is considerably lower than that of steel ones (in the range of one-sixth to one-fourth that of steel bars). Therefore, transportation and labor costs are considerably reduced due to the corresponding lighter weight of the FRP bars.

Unlike steel bars that have the same coefficient of thermal expansion in all directions, FRP bars have different coefficients in the longitudinal and transverse directions depending on the type of the constituents (fibres and resin) and the fibre-volume fraction. In general, the properties of the fibres control the longitudinal coefficient, while the transverse coefficient is dependent on the properties of the resin.

2.2.2. Mechanical properties and behaviour

2.2.2.1. Tensile behaviour

Unlike steel reinforcement, FRP bars are brittle in nature and they do not undergo a yielding plateau prior to rupture when they are loaded in tension. Instead, they exhibit a linear elastic stress-strain relationship up to failure as shown in Figure 2.1. In addition, as listed in Table 2.1, FRP bars have considerably higher ultimate tensile strength and lower stiffness than those of steel bars. Many parameters affect the tensile strength and modulus of FRP bars, such as the type of fibres and resin, the fibre-volume fraction, the diameter of the bar, and the quality control of the manufacturing process. Consequently, having two bars with the same diameter, made of the same constituent materials and with the same fibre-volume fraction does not mean that they have the same tensile properties. Therefore, the tensile properties of FRP composite bars should be obtained by conducting tensile tests or directly from the manufacturer for each batch. On the other hand, most FRP bars cannot be bent after being manufactured since they are made of thermosetting resin, which cannot be reshaped after curing. Instead, FRP bent bars can be prefabricated with bends. In this case, a strength reduction of 40 to 50% in the bend portion compared with the strength of a straight bar is expected due to stress concentrations.

2.2.2.2. Compressive behaviour

The compressive strength and modulus of FRP bars are generally less than the tensile ones of the same product. The current design standards and guidelines in North America (CSA 2017; ACI 2015) consider FRP bars in compression zones to have zero compressive strength. The failure of FRP bars under axial compression may be triggered by transverse tensile failure, internal buckling of the fibres, and/or shear failure depending on the type of constituents and the fibre-volume fraction.

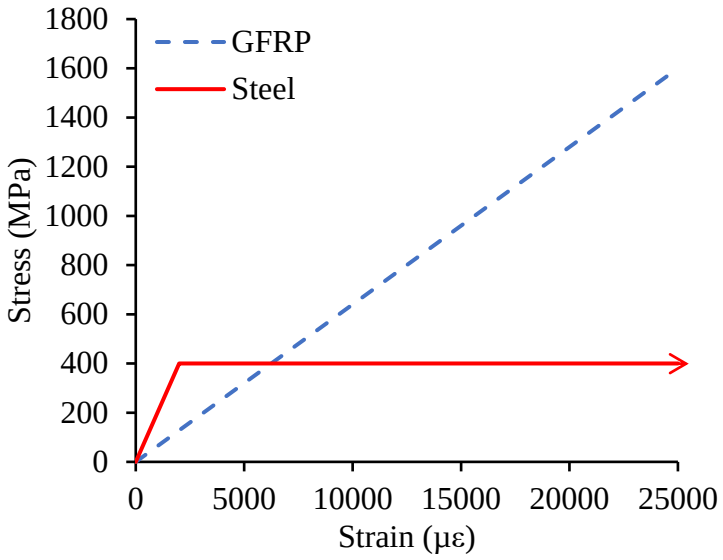

Figure 2.1: Stress-strain relationship for steel and FRP bars

Table 2.1: Typical tensile properties of reinforcing bars (ACI 2015)

Reinforcement type	Steel	GFRP	CFRP	AFRP
Ultimate tensile strength (MPa)	276-517 [a]	483-1,690	600-3,690	1,720-2,540
Tensile modulus (GPa)	200	35-51	120-580	41-125
Ultimate tensile strain (με)	1,400-2,500a	12,000-31,000	5,000-17,000	19,000-44,000

[a] At yielding

2.2.2.3. Shear behaviour

In general, FRP bars are weak in interlaminar shear because the resin is usually unreinforced in the transverse direction of the bar and, consequently, interlaminar shear strength depends on the weak resin. Placing fibres in the transverse direction across the axial fibres would increase the shear resistance.

2.2.2.4. Bond behaviour

Bond stresses between FRP bars and concrete are transferred by the adhesion between the bar and the surrounding concrete (chemical bond), the frictional resistance due to roughness of the FRP bar's surface, the bearing of the bar deformations against concrete (mechanical bond/interlock), and the hydrostatic pressure exerted on the bars due to the shrinkage of concrete and/or the expansion of the bar when subjected to high temperatures. When an embedded FRP bar is subjected to tensile stresses, chemical bond is the dominant mechanism until the initial pullout/slip of the bar; thereafter, frictional bond and mechanical interlock become the governing mechanisms depending on the surface texture (Benmokrane et al. 1996; Cosenza et al. 1997).

The bond strength of FRP bars in concrete depends on several parameters such as bar diameter, concrete cover, surface condition (e.g., sand-coated, ribbed, helically wrapped, or braided), embedment length, mechanical properties of the bar, and environmental conditions (Hao et al. 2009; Masmoudi et al. 2011). Alves et al. (2011) reported that No. 16 sand-coated GFRP bars showed 30–50% higher bond strength than No. 19 bars. Hossain et al. (2014) observed an increase of approximately 20% in bond strength for No. 19.1 GFRP bars when concrete cover was increased from 40 to 60 mm.

2.2.3. Durability of FRP composites

Durability of FRP composites and FRP-RC structural members is defined as their ability to resist several harmful environmental and physical effects, such as cracking, oxidation, chemical degradation, delamination, wear, fatigue, or a combination thereof for a specified period of time, under specified load and environmental conditions. The main durability issues affecting internal

FRP reinforcement are alkaline environments, alternate wet-and-dry cycles, freezing-and-thawing cycles, and temperature and humidity variations.

Among the three common fibre types, glass fibres are the most susceptible to degradation due to moisture and alkalinity, while aramid fibres show a tendency to creep and absorb moisture, and carbon fibres are relatively inert to the environment. However, the resin in the FRP bars surrounds the fibres and protects them from the environment. Subsequently, constituents are used based on both performance and durability requirements; different fibre-resin combinations result in differing degrees of resistance to environmental conditions.

2.3. Shear Transferring Mechanisms in Flat Plate Systems

In general, flat plate systems may exhibit two different types of shear failure depending on the type of loading and the geometry of the slab-column connections. These two types are one-way shear (beam action) and two-way shear (punching shear).

2.3.1. One-way shear (beam action)

In the one-way shear mechanism, the slab behaves as a wide rectangular beam, where the failure occurs at an inclined crack extending across the entire width of the slab. This behaviour can be divided into two stages: the pre-cracking stage and the post-cracking stage.

2.3.1.1. Pre-cracking stage

When a simply supported rectangular beam is subjected to a concentrated load at mid-span as shown in Figure 2.2a, the shear stress distribution on an un-cracked section, v, is calculated from Equation 2.1. In this equation, V is the shear force acting at the cross section, Q is the first moment of area about the centroidal axis of the part of the cross section farther from the centroidal axis

than the point where the stresses are being calculated, *I* is the moment of inertia of the cross section, and *b* is the width of the cross section.

$$v = \frac{VQ}{Ib} \qquad \text{Equation 2.1}$$

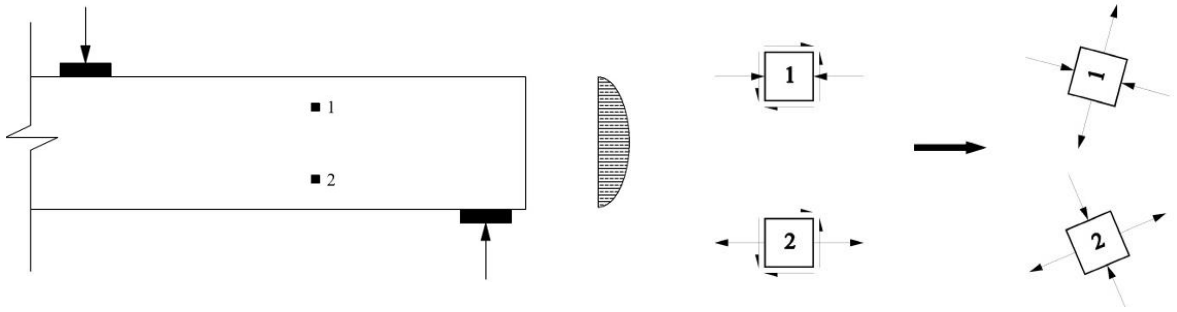

a) Shear stress distribution b) Stresses on elements in the shear span

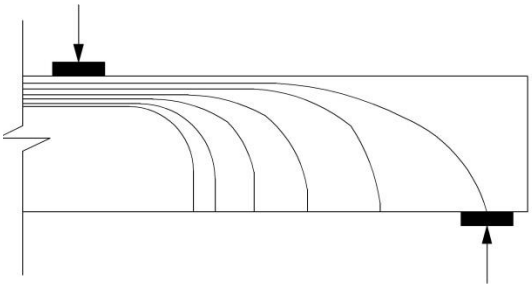

c) Compressive stress trajectories in a beam/one-way slab

Figure 2.2: Stresses in an uncracked beam/one-way slab

The orientation of the principal stresses acting on two different elements in the beam is shown in Figure 2.2b. Following the surfaces on which principal tension stresses act in adjacent elements gives the cracking pattern (compressive stress trajectories) shown in Figure 2.2c. The cracks are steeper at the bottom of the beam, where there are no shear stresses and the principal tension stress equals the tensile flexural stress acting parallel to the longitudinal axis of the beam. The diagonal shear stresses are maximum and the flexural stresses are zero at the longitudinal axis of the beam

and, thus, 45^{o} inclined cracks appear in the mid-height of the beam. At the top of the beam, shear stresses are zero and the flexural stresses are compressive stresses, which cause flatter cracks near the top of the beam (Wight and MacGregor 2011).

2.3.1.2. Post-cracking stage

After the beam is cracked (Figure 2.3), the shear stress distribution is shown in Figure 2.3c and the shear stresses can be calculated from Equation 2.2, where *jd* is the flexural lever arm (distance between tension and compression components of the bending moment applied at the section). This stress distribution assumes that about 30% of the shear stress is transferred through the uncracked portion of the cross section while the remaining is transferred through the crack mainly by means of aggregate interlock and dowel action.

$$v = \frac{V}{b \times jd} \qquad \text{Equation 2.2}$$

Shear failure occurs when inclined shear cracks take place. In most cases, vertical flexural cracks start first at the bottom of the beam and extend to form flexure-shear cracks. However, in certain cases when the shear span-to-depth ratio is small, shear stresses in the web are considerably higher than the flexural stresses at the bottom of the beam; thus, a diagonal shear crack (web-shear crack) occurs prior to the occurrence of flexural cracks.

2.3.1.3. Shear strength provided by concrete

As shown in Figure 2.4, the shear strength in beams without shear reinforcement is provided by five components: 1) shear resistance of the compression zone (uncracked concrete), V_c, 2) aggregate interlock along the two surfaces of the crack, V_a, 3) dowel action of the flexural reinforcement crossing the shear crack, V_d, 4) arch action in deep members with shear span-to-

depth ratio less than 2.5, and 5) residual tensile stresses in the shear crack resulting from the small remaining connections between the two faces of the crack (ASCE-ACI Committee 426 1974). These five components together are referred to as the shear strength provided by concrete (implying the absence of shear reinforcement).

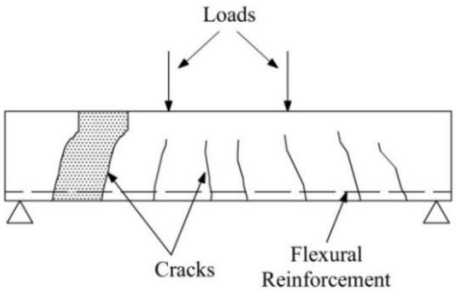

a) A cracked simply-supported beam/one-way slab

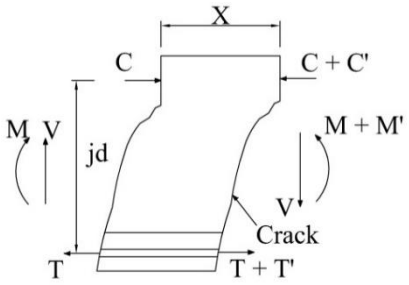

b) The portion between two cracks

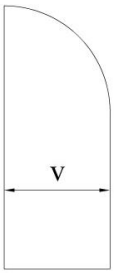

c) Shear stress distribution

Figure 2.3: Shear stresses in a cracked beam/one-way slab

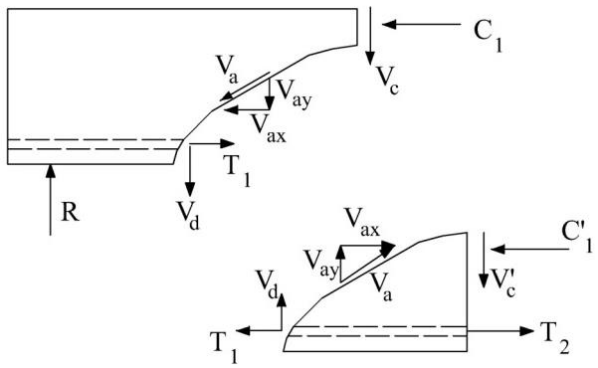

Figure 2.4: Equilibrium of forces in a cracked beam/one-way slab

The shear strength provided by concrete is affected by the following parameters: 1) tensile strength of concrete, which determines the cracking load; 2) compressive strength of concrete, which determines the uncracked concrete contribution; 3) flexural reinforcement ratio, which affects the post-cracking stiffness of the cross section and the shear resistance provided by the dowel action; 4) shear span-to-depth ratio, which controls the arch action; 5) beam size, which affects the width of cracks; 6) presence of axial forces, which delays the initiation of cracks and reduce crack widths in case of compressive forces or speed up the initiation of cracks and increase the crack widths in case of tensile forces; and 7) size of the coarse aggregate, which controls the roughness of the crack interface.

2.3.1.4. Shear strength provided by shear reinforcement

When the shear capacity of a member is less than its flexural capacity, shear reinforcement is to be used in order to increase the shear capacity of the member and ensure it will reach its flexural capacity before shear failure occurs. When a shear-reinforced beam is loaded, the strains in the vertical stems of the shear reinforcement are very low until inclined cracks start to develop. This means that shear reinforcement does not prevent inclined cracks from developing; instead, it controls their propagation and widening. As in the case of members without shear reinforcement, the entire shear is resisted by the un-cracked section prior to cracking. After flexural cracking up to inclined cracking, the shear is resisted by the shear strength provided by concrete. Once inclined cracks start to propagate, the shear stress is transferred to the stirrups, which control the widening of the inclined cracks leading to an increase in the aggregate-interlock component of the shear strength provided by concrete.

2.3.2. Two-way shear (punching shear)

The two-way shear mechanism is localized at slab-column connections in flat slab systems. It results in punching shear failure, where the column along with a pyramid-shaped part of the slab punches through the remainder of the slab as a result of the high shear stresses in the slab at the column vicinity. These high shear stresses are caused by the inevitable combination of shear forces and bending moments transferred between the slab and the column at slab-column connections.

The behaviour of slab-column connections is very complex due to their multidimensional geometry, which precludes the development of simple analysis procedures that realistically assess the actual stresses condition. Thus, most of the available analyses in North America limit the maximum shear strength of a slab to a value determined empirically from experimental tests. This value is highly dependent on the assumed location of the critical perimeter, since the critical perimeter increases with increasing its distance from the column face.

2.3.2.1. Mechanism of punching shear failure

Similar to the case of one-way shear, once inclined cracks form in the absence of shear reinforcement, shear stresses are resisted by the five components of the shear strength provided by concrete (Section 2.3.1.3). However, the ultimate shear strength of a slab is generally higher than a beam. This difference is attributed to the following five factors: (1) distribution of moments; (2) lack of symmetry; (3) inadequacy of a simple static analysis; (4) in-plane forces generated by restraints provided by the supports; and (5) interaction of flexural and shear effects (ASCE-ACI Committee 426 1974).

Distribution of moments

Two different bending moments are generated in the slab at a slab-column connection: radial moments and tangential moments. When a slab-column connection is subjected to a vertical shear force, the first crack to form is a tangential flexural crack at the location of maximum radial moment (at the column face). Radial cracks then extend from the column faces due to tangential moment. Additional tangential cracks at some distance from the column face will not form until the applied load increases significantly, since the radial moment decreases rapidly with increasing the distance from the column face. However, inclined cracks must propagate in the tangential direction (perpendicular to radial cracks). Since flexural tangential cracks are not located where they can initiate inclined cracks, inclined cracks tend to originate at mid-depth of the slabs and, accordingly, their characteristics are similar to web-shear cracks rather than flexural-shear cracks in the case of beams. Accordingly, the stiffness of the slab in the tangential direction helps to control the opening of inclined cracks; such an action is not present in beams.

Lack of symmetry

Orthogonal reinforcement mats are often used in slabs. The use of orthogonal reinforcement mats, rather than circular-radial reinforcement mats, creates a complex pattern of in-plane forces in the slab (Lenschow and Sozen 1967). Figure 2.5 shows a part of a slab with a reinforcing mat at 45^{o} to the direction of the moment, M_1. The components of the reinforcement forces, T, in the y direction are balanced by compression forces in the concrete at the level of the reinforcement (since the moment in the y direction, M_2, is zero). Accordingly, in-plane forces develop in the slab at the reinforcement level wherever flexural cracks are not parallel to the reinforcement. Such in-plane forces increase the loads for any cracking that develops after the initial cracks.

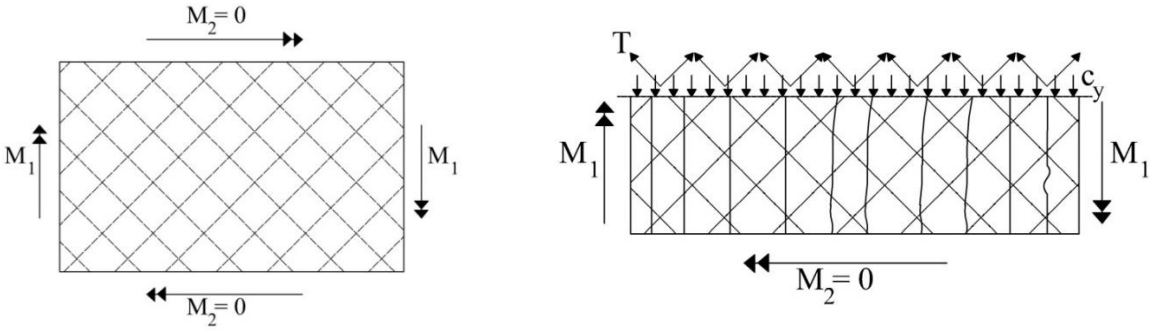

a) Moment and reinforcement orientation b) Internal forces at reinforcement level

Figure 2.5: In-plane forces in slabs – reproduced from ASCE-ACI Committee 426 (1974)

Inadequacy of a simple static analysis

Figure 2.6 shows the equilibrium of internal forces at inclined cracks in a slab and a beam. For the beam (Figure 2.6a), the tensile force, *T*, in the reinforcement crossing the inclined crack must equal the compressive force, *C*, acting above the inclined crack in order to satisfy equilibrium requirements. On the other hand, equilibrium requirements for the slab (Figure 2.6b) do not require the compressive force, C_1, acting below the inclined crack to equal the tensile force, T_1, developed in the reinforcement crossing the crack. Instead, it requires that the summation of the compressive forces developed along the entire width of the slab, C_1+C_2, equals the summation of the tensile forces developed in the reinforcement along the entire width of the slab, T_1+T_2. While maintaining equilibrium requirements, the force C_1 can be redistributed and the ratio between C_1 and C_2 may decrease with decreasing the depth of the uncracked concrete in the inclined crack location. However, there is no comparable mechanism for reducing the shear forces at that location. Concentrating the reinforcement through the failure perimeter may be thought to increase the compressive force, C_1, by increasing the uncracked concrete depth; however, the tensile force, T_1, in that reinforcement can be balanced by the compressive force outside the failure perimeter, C_2.

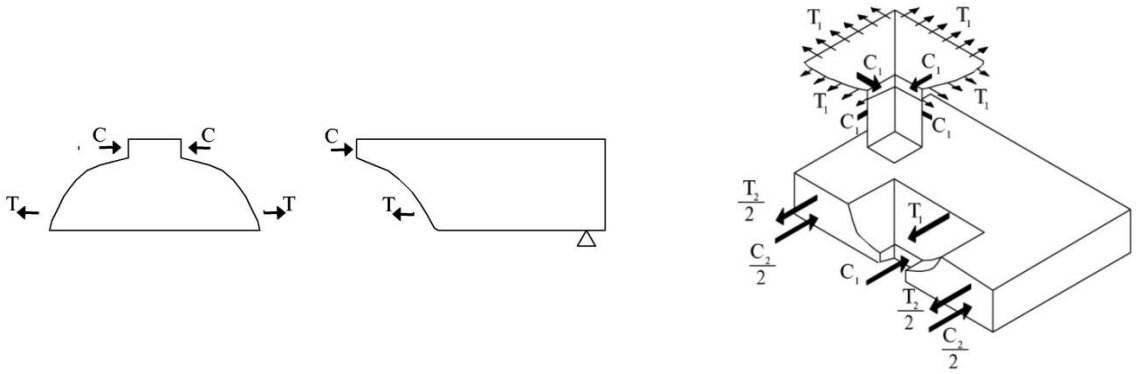

a) Beam or one-way slab b) Two-way slab

Figure 2.6: Forces at inclined cracks – reproduced from ASCE-ACI Committee 426 (1974)

In-plane forces generated by restraints provided by the supports

In-plane outward displacements tend to occur in the cracked region of the slab at the column vicinity. However, these displacements are restrained by the stiffness of the slab surrounding the failure region and, subsequently, in-plane compression forces are developed in the slab. These forces increase the flexural and shear capacities of slab-column connections. They, on the other hand, restrict the rotations of the cross sections and, subsequently, increase the brittleness of the punching failure.

Interaction of flexural and shear effects

The critical sections for moment and shear in a slab-column connection coincide at the column vicinity. Accordingly, moment-shear interaction is expected, which makes it very difficult in most cases to classify the failure as either flexural or punching failure. Generally, the failure modes change from flexural failure to punching failure with increasing the slab reinforcement ratio.

2.3.2.2. Slab-column connections transferring shear force and unbalanced moment

In most cases, slab-column connections are not only subjected to shear forces, but also to unbalanced bending moments. While the transfer of unbalanced moments at exterior connections (edge and corner connections) is inevitable due to the discontinuity of the slab, they are also transferred at interior connections. This could happen due to unequal span lengths, uneven loading conditions, or a combination thereof. Moreover, the value of the unbalanced moment transferred at a connection is dramatically increased if the connection is subjected to lateral loads (wind or seismic loads). This transfer of unbalanced moments causes the shear stress distribution at the column vicinity to become non-uniform and reduces the vertical load capacity of the connections. Moreover, the punched cone becomes confined to the region at the heavily loaded side of the slab, i.e., where the directions of the shear stresses resulting from the shear force and unbalanced moment coincide, while the region at the opposite side show little or no distress as shown in Figure 2.7.

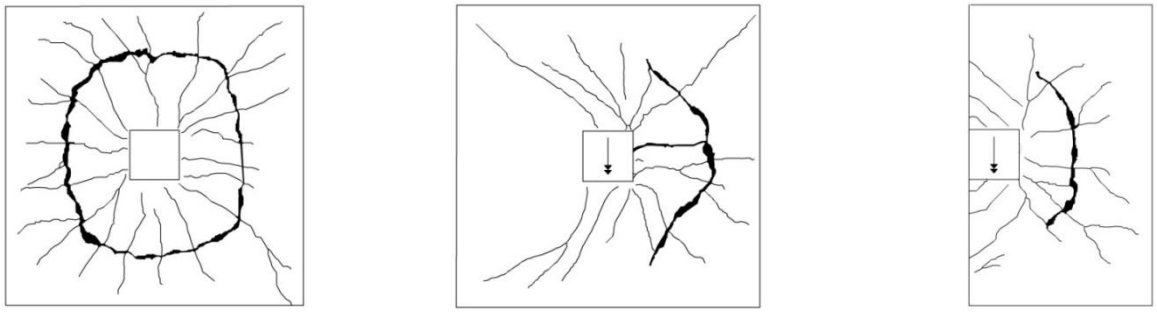

a) Interior – shear only b) Interior – shear and moment c) Edge

Figure 2.7: Different locations of punching cones

2.3.2.3. Analysis based on linear variation of shear stress

Different analysis methods have been used in the literature. The current design codes and standards in North America (CSA 2017, 2019a; ACI 2015, 2019a) implement an analysis based on linear

variation of shear stresses at the critical perimeter. The shear stresses at a critical perimeter located a distance away from the column face is assumed to vary linearly with the distance from the centroidal axis of the perimeter as shown in Figure 2.8. Shear stresses are induced by the vertical shear force and a portion of the unbalanced moment transferred through the connection. The remainder portion of the unbalanced moment is assumed to be resisted by flexure in the slab. The maximum factored shear stress, v_f, is calculated by Equation 2.3, where V_f is the factored shear force, b_o is the perimeter of the critical section, d is the slab average effective depth, γ_v is the fraction of the unbalanced moment transferred between slab and column, M_f, and resisted by shear (Equation 2.4), e is the distance from the centroid of the critical perimeter to the point where shear stress is being calculated and J is a property of the critical perimeter analogous to the polar moment of inertia calculated from Equation 2.5 and Equation 2.6 for interior and edge connections, respectively, where b_1 and b_2 are the widths of the critical perimeter measured in the direction of the span for which moments are determined and in the perpendicular direction, respectively.

$$v_f = \frac{V_f}{b_o d} + \frac{\gamma_v M_f e}{J} \qquad \text{Equation 2.3}$$

$$\gamma_v = 1 - \frac{1}{1 + \frac{2}{3}\sqrt{\frac{b_1}{b_2}}} \qquad \text{Equation 2.4}$$

$$J = \frac{b_1^3 d + d^3 b_1}{6} + \frac{b_2 d b_1^2}{2} \qquad \text{Equation 2.5}$$

$$J = 2\left(\frac{b_1^3 d}{3} + \frac{d^3 b_1}{12}\right) - b_o d e^2 \qquad \text{Equation 2.6}$$

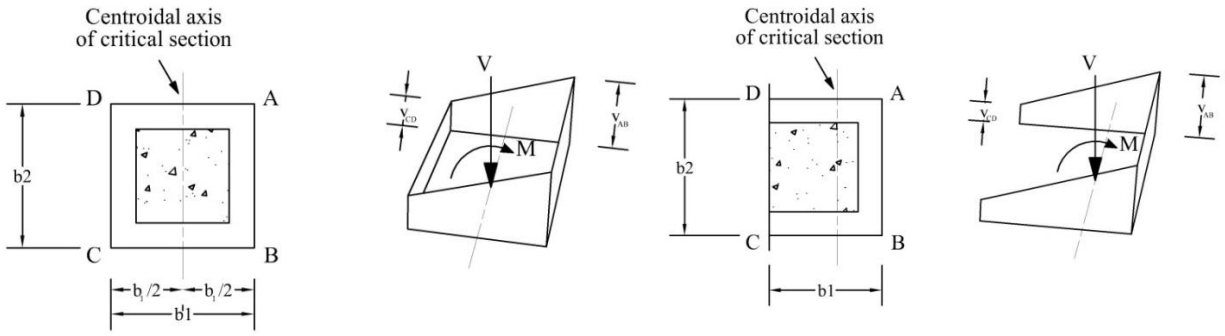

a) Interior connection b) Edge connection

Figure 2.8: Linear shear stress distribution at slab-column connections

2.4. Shear Reinforcement for Slabs

As mentioned earlier, if the shear strength provided by concrete in a slab-column connection is not adequate to resist the applied shear stress, the punching shear capacity of the connection must be increased to insure a ductile flexural failure rather than the brittle punching failure. This can be achieved by different methods such as: 1) increasing the area of concrete resisting shear stresses, e.g., increasing the slab thickness, providing a drop panel or a column head, increasing the column size, or a combination thereof; 2) increasing the concrete compressive strength; and 3) using shear reinforcement. Although all these methods provide an increase in the punching shear capacity, only properly anchored shear reinforcement increases the ductility (Megally and Ghali 2000a). Well-anchored shear reinforcement ties the tension and compression zones of the slab and prevents the widening and extension of inclined shear cracks. This results in an increase in the punching shear capacity and may allow the connection to reach its flexural capacity, which will change the mode of failure to a ductile flexural mode of failure.

The Canadian standard CSA A23.3-19 (CSA 2019b) and the American code ACI 318-19 (ACI 2019a) allow the use of three different types of shear reinforcement in slabs: 1) bars, wires, and

single/multiple leg stirrups; 2) structural steel sections (shear-heads); and 3) headed shear studs. Dilger and Ghali (1981) showed that stirrups do not reach their yield strength before punching shear failure due to the slippage caused by inadequate anchorage. On the other hand, the bends in the stirrups leave only a small vertical height that can be fully effective in controlling shear cracks. In addition, the bends exert high compressive stresses against concrete leading to localized concrete crushing. Furthermore, placement of stirrups within the congested area at the column vicinity creates a construction difficulty. This construction problem is also present when shear-heads are used especially in thin slabs, where the distance between the top and bottom reinforcement mats is too small to allow for the placement of the shear-heads (Polak et al. 2005). The use of shear stud reinforcement has overcome all these disadvantages. Shear studs are easy to install and do not interfere with the flexural reinforcement. Furthermore, unlike stirrups, they are straight vertical stems, which allows them to be anchored as close as possible to the slab top and bottom surfaces (maximum tension and compression zones, respectively). Moreover, the use of shear studs allows for more effective depth, *d*, for the flexural reinforcement than that in the case of stirrups (Dilger and Ghali 1981; Mokhtar et al. 1985).

2.5. Effect of Cyclic Lateral Load on Punching Shear Strength

Megally (1998) demonstrated that, when slab-column connections are subjected to cyclic lateral loads, the reversed nature of the loading accelerates the degradation of the concrete shear resistance due to the considerable increase in widths of diagonal cracks and loss of shear resistance by aggregate interlock. Reversed-cyclic lateral loads will also result in the propagation of flexural cracks in the total slab thickness; thus, weakening the compressive zone. However, this shear strength deterioration is limited to the zone of the slab in the column vicinity, while the surrounding

concrete confines the connection region. As such, the concrete shear resistance under reversed-cyclic lateral loads is expected to be lower than that under static loading.

2.6. Experimental Setup for Connections Subjected to Cyclic Lateral Loading

Numerous experimental studies have been conducted to investigate the seismic response of steel-RC slab-column connections in the last five decades with a variety of boundary conditions and testing configurations. While some studies comprised the testing of slab-column subassemblies (Robertson and Durrani 1991, 1992; Durrani et al. 1995; Hwang and Moehle 2000; Dilger et al. 2005; Kang and Wallace 2005; Rha et al. 2014), the majority of the tests were conducted on isolated connections.

2.6.1. Boundary conditions

Isolated slab-column connections subjected to cyclic lateral loading were idealized in most cases as shown in Figure 2.9 (Pan and Moehle 1989; Wey and Durrani 1992; Robertson et al. 2002; Stark et al. 2005; Tan and Teng 2005; Robertson and Johnson 2006; Anggadjaja and Teng 2008; Cheng and Giduquio 2014; Matzke et al. 2015; Giduquio et al. 2019). In these tests, the columns extended above and below the surfaces of the slabs to storey mid-heights, i.e., the assumed points of contraflexure for lateral loads. A hinge support was attached to the bottom of the column to allow rotation in the direction perpendicular to the free edge (will be referred to as the perpendicular direction), while preventing rotation in the direction parallel to the free edge (will be referred to as the parallel direction) and translation in all directions. At the top, the columns were pinned to the lateral load applying actuator to allow for rotation and translation in the perpendicular direction, while preventing them in the parallel direction. Similarly, the slabs extended around the columns to the lines of contraflexure for lateral loads, which were assumed

to be at mid-spans of the slabs. Although the contraflexure lines are likely to shift during loading, they were reasonably assumed to be stationary. Wey and Durrani (1992) and Dovich (1994), due to space constraints, delineated the slab in the parallel direction at 35 and 25% of the span length, respectively, instead of 50% as in the perpendicular direction. In all these tests, the slabs were simply supported along the edges running in the parallel directions. Roller supports were used at these edges to allow rotation and translation in the perpendicular direction, while preventing vertical deflection. The edges running in the perpendicular direction were left free except in tests designed to investigate the effects of bi-axial cyclic lateral loading, where they were simply supported in the same manner as the ones running in the parallel directions (Pan and Moehle 1989; Tan and Teng 2005; Anggadjaja and Teng 2008; Cheng and Giduquio 2014; Matzke et al. 2015; Giduquio et al. 2019).

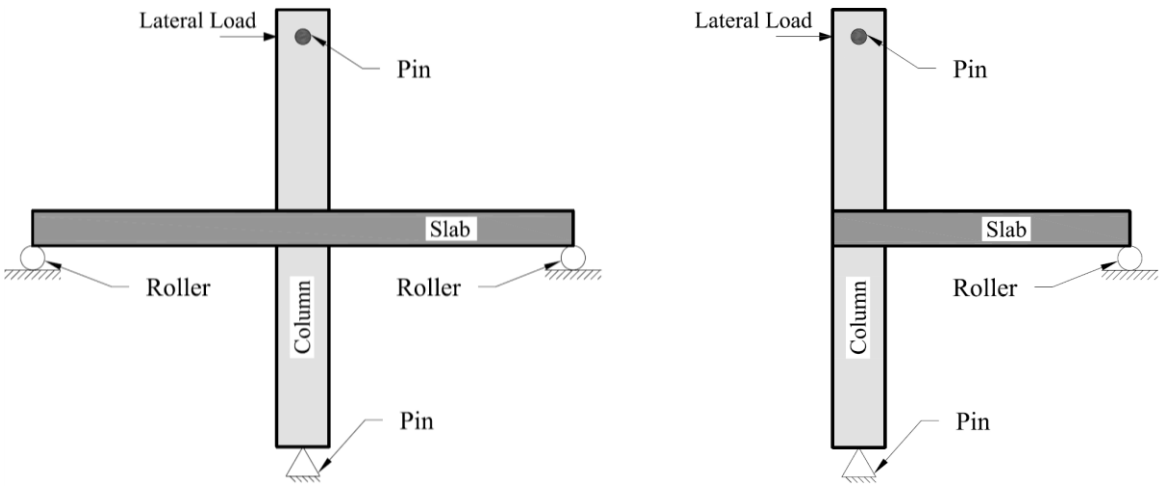

a) Interior connection b) Edge connection

Figure 2.9: Idealization of isolated connections subjected to cyclic loading applied at column tip

Different boundary conditions were employed in earlier studies (Carpenter et al. 1973; Hawkins et al. 1974, 1975; Islam and Park 1976). In these studies, pinned supports were used at both top

and bottom tips of the column to totally prevent the column from translation. Two slab edges were left free, while two equal and opposite vertical cyclic loads were applied at two opposite edges to simulate the cyclic lateral loading effects as shown in Figure 2.10.

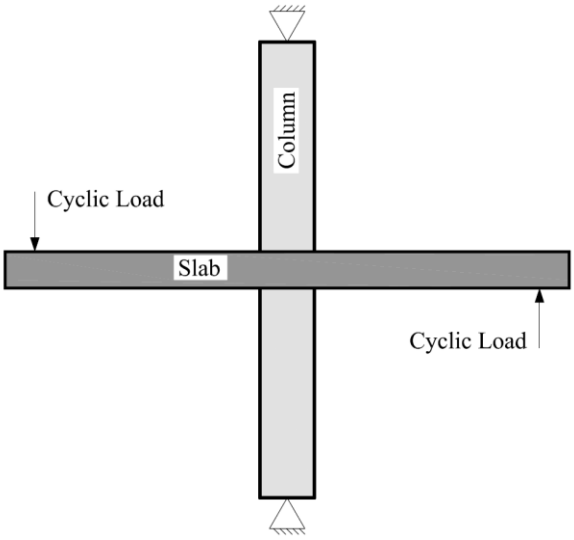

Figure 2.10: Idealization of interior connections with cyclic loading applied to slab edges

2.6.2. Gravity load application

The application of gravity loads has always been a challenge in testing isolated slab-column connections under cyclic lateral loading. Gravity loads are typically simulated by one of two techniques as shown in Figure 2.11. In the first technique (Figure 2.11a), vertical loads are applied at discrete points on the slab surface by one of three mechanisms: 1) distributing weights on the slab (Anggadjaja and Teng 2008), 2) hanging weights from holes in the slab (Hawkins et al. 1975; Islam and Park 1976; Wey and Durrani 1992; Robertson et al. 2002; Robertson and Johnson 2006), or 3) stressing the slab to the laboratory's strong floor (Cheng et al. 2010; Cheng and Giduquio 2014; Matzke et al. 2015; Giduquio et al. 2019). The latter mechanism seems the most convenient as the applied gravity load can be efficiently controlled depending on the hydraulic machine used to apply it. In the second technique, a vertical upward jacking force is applied at the lower column

stub, while the slab edges are pinned as shown in Figure 2.11b (Stark et al. 2005; Broms 2007). This technique, however, is not convenient in the case of edge connections as the connection might become unstable. Furthermore, some researchers employed both techniques, i.e., applying a part of the gravity load by jacking the column up and another part by adding weights to the slab (Pan and Moehle 1989; Tan and Teng 2005; Anggadjaja and Teng 2008).

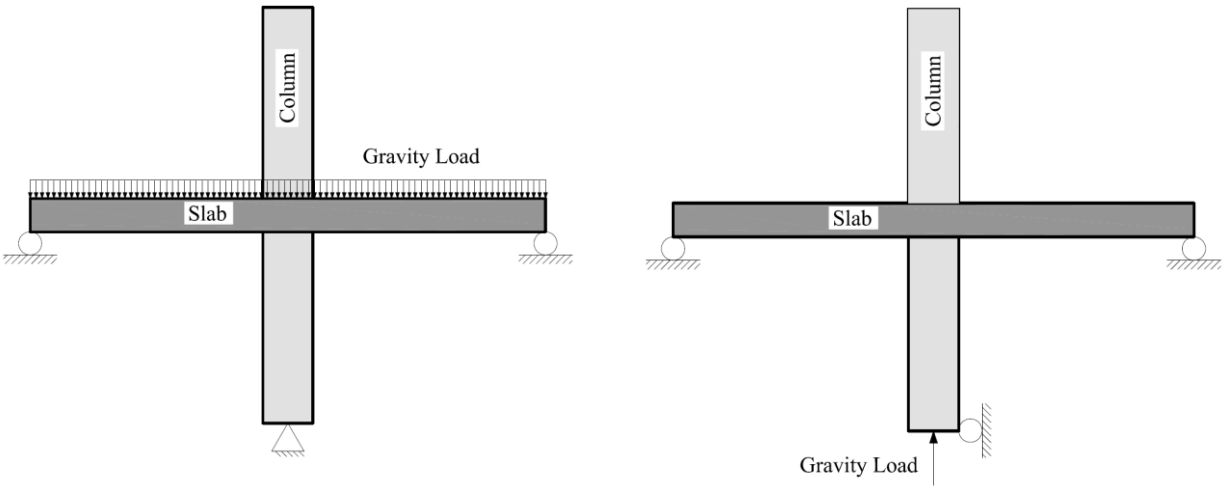

a) Distributing weights on the slab b) Jacking the column

Figure 2.11: Gravity load simulation

2.7. Research on Punching Shear Behaviour of Flat Plates

2.7.1. Steel-RC slab-column connections under cyclic lateral loading

In general, three main factors have been used in the literature to quantify the response of steel-RC slab-column connections subjected to reversed-cyclic lateral loading: drift capacity, lateral displacement ductility and stiffness. The drift capacity is the maximum interstory drift ratio a connection can withstand without losing its gravity load carrying capacity, while the lateral displacement ductility is the ratio between the drift at failure to the drift at yielding of steel reinforcement. The latter factor, however, cannot be precisely estimated for slab-column

connections because there is no distinct yielding point as yielding spreads gradually across the reinforcement at the column vicinity. Accordingly, Pan and Moehle (1989) proposed an arbitrary procedure to define an equivalent yield displacement as illustrated in Figure 2.12. In this procedure, the relationship between lateral displacement (drift) and lateral load is drawn and then idealized by an elastoplastic relationship (bi-linear relation). The elastic portion of the idealized relationship is a secant passing through the origin and a point on the actual curve at a load equal to two-thirds of the maximum capacity. Subsequently, the plastic portion of the idealized relation passes through the point of maximum load and maximum displacement. The intersection of these two straight lines defines the equivalent yield displacement, D_y. Stiffness, on the other hand, is calculated at each loading cycle as the slope of the straight line connecting the two peaks of the hysteretic response as shown in Figure 2.13 (Hawkins et al. 1975). The following sections discuss the influence of different parameters on the seismic response of steel-RC slab-column connections.

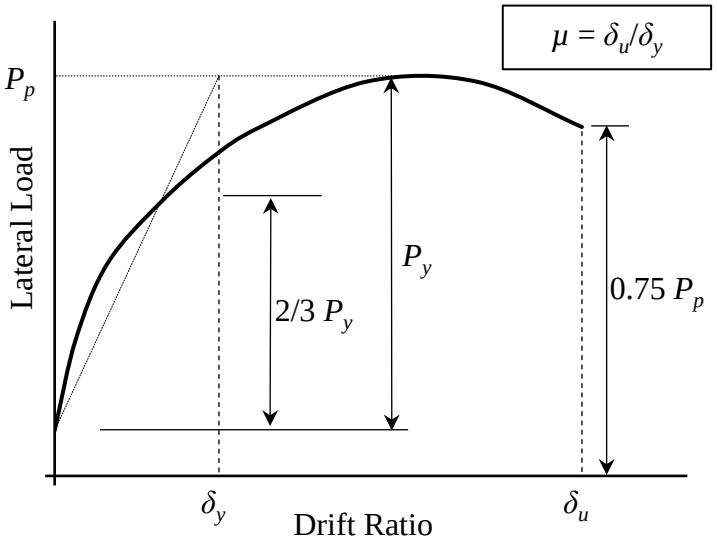

Figure 2.12: Definition of lateral displacement ductility by Pan and Moehle (1989)

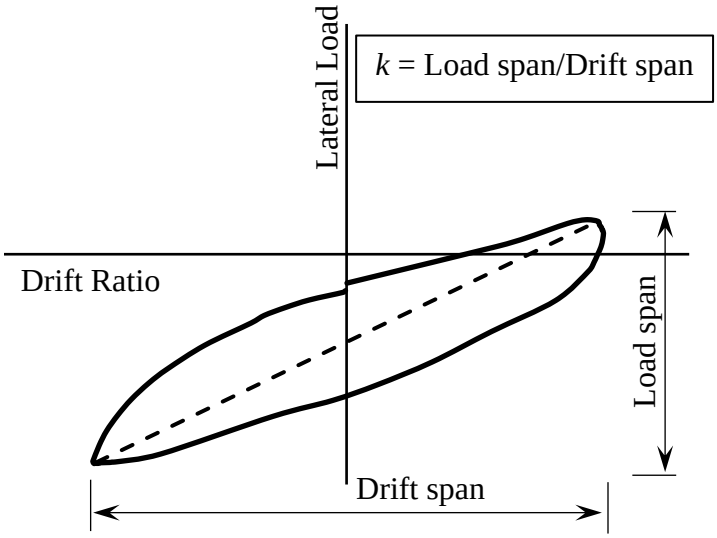

Figure 2.13: Definition of stiffness by Hawkins et al. (1975)

2.7.1.1. Effect of gravity shear ratio

Pan and Moehle (1989) analyzed experimental data from several research studies conducted on isolated slab-column interior connections without shear reinforcement to identify the parameters that influence the seismic response of such connections. The authors showed that the magnitude of the gravity shear transferred to the slab is a primary parameter affecting the drift capacity and lateral displacement ductility of the connections. It was concluded that both the drift capacity and lateral displacement ductility decrease as the gravity shear ratio (V_g/V_c) increases. They reported approximately no lateral displacement ductility when the gravity shear ratio exceeded 0.4, i.e., the connections failed in punching before yield is detected. Accordingly, the authors recommended a maximum value of the gravity shear ratio of 0.4 in order for the connections to possess minimal ductility and to satisfy the minimum 1.5% lateral drift suggested by Sozen (1980). This limit was confirmed by other researchers (Megally and Ghali 1994).

Megally and Ghali (2000a) tested full-scale isolated slab-column edge connections under gravity and simulated cyclic lateral loading. It was reported that the drift capacity, stiffness and lateral ductility decreased with increasing the gravity shear ratio. The ultimate drift ratio, i.e., the drift ratio reached when 20% of the lateral load capacity is lost, decreased from 3.1 to 2.3 and 1.2% when the gravity shear ratio increased from 0.29 to 0.42 and 0.58. The authors proposed a 0.45 limit of the gravity shear ratio for the connections without shear reinforcement in order to satisfy the 2.0% drift ratio limit specified by the National Building Code of Canada at that time (NRCC 1995).

Hueste and Wight (1999) used experimental data from the literature to approximate the relationship between the lateral drift ratio and the gravity shear ratio into a segmented linear envelope as shown in Figure 2.14. At low drift ratios (less than 0.5%), the contribution of unbalanced moments to the total punching shear stress is not significant. As such, they assumed that a connection would fail when it reaches its full gravity shear capacity ($V_g/V_c = 1.0$). The second segment incorporates the 0.4 limiting gravity shear ratio proposed by Pan and Moehle (1989). It represents a linear reduction in the allowable gravity shear ratio from 1.0 to 0.4 as the drift increases from 0.5 to 1.5%. The third segment defines a slower decrease in the gravity shear ratio as the drift ratio increases from 1.5 to 4.0%. Finally, the connection is expected to undergo 4% lateral drift ratio when the gravity shear ratio is less than 0.2.

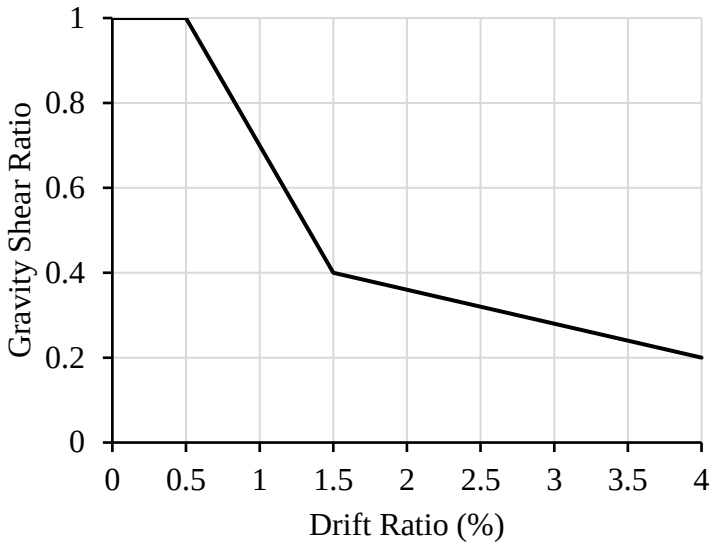

Figure 2.14: Tri-linear drift envelope proposed by Hueste and Wight (1999)

Robertson and Johnson (2006) tested interior connections with discontinuous bottom reinforcement. They subjected the slabs to three different gravity shear ratios (0.25, 0.37 and 0.48) and, consistent with connections with continuous bottom reinforcement in the literature, reported reductions in the drift capacity from 4 to 3 and 1.5%, respectively. The author proposed a more conservative segmented linear envelope than the one proposed by Hueste and Wight (1999) to account for the likelihood of progressive collapse associated with discontinuous bottom reinforcement. This envelope, shown in Figure 2.15, provides a lower bound for almost all prior test results. The proposed trilinear envelope assumes that the connection has no lateral drift capacity when it carries a gravity shear ratio of 1.0. A connection with 0.4 gravity shear ratio can undergo only 1% drift ratio. When the gravity shear ratio is 0.15 or less, the connection is capable of reaching at least 4% lateral drift ratio before punching.

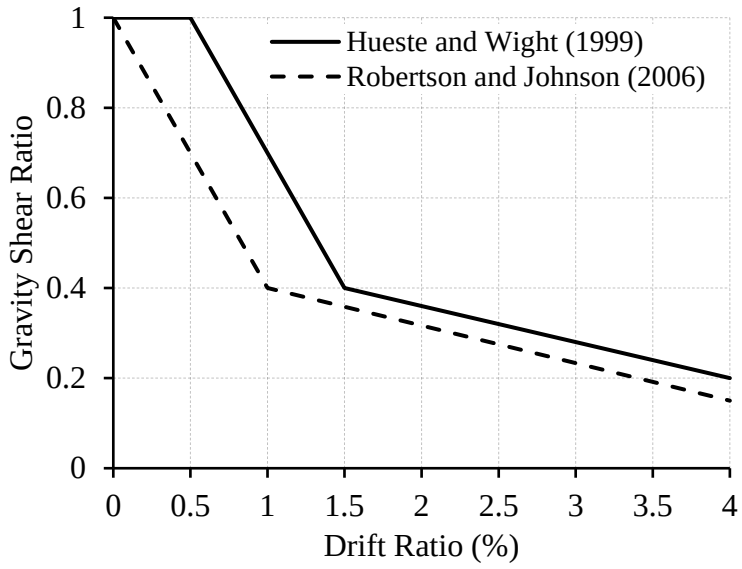

Figure 2.15: Linear envelopes for gravity shear ratio and drift ratio relationship (Robertson and Johnson 2006)

2.7.1.2. Effect of shear reinforcement

In an early investigation by Hawkins et al. (1975), nine full-scale interior connections were tested under combined gravity and cyclic lateral loading. Five connections had closed hoop stirrups as shear reinforcement at different layouts, while the other four acted as control connections without shear reinforcement. They reported that properly designed and detailed stirrups will significantly increase the ductility, energy absorption and capacity of the connections. Similar results of connections with closed stirrups were obtained by other researchers (Islam and Park 1976).

Megally and Ghali (1994) analyzed experimental data from several investigations to study the effect of shear reinforcement on the lateral drift capacity. The authors concluded that slabs with shear reinforcement, whether stirrups of studs, can satisfy the minimum drift requirement (1.5%) for any gravity shear ratio. However, connections with stud shear reinforcement attained higher

ductility and drift capacity than those with conventional stirrups due to the superior anchorage of the studs compared to that of stirrups.

Megally and Ghali (2000a, 2000b, 2000c) tested edge connections with and without stud shear reinforcement under gravity and cyclic lateral loading. Again, the authors reported that the presence of shear studs significantly enhanced the ductility, drift capacity and punching capacity of the connections. In addition, they reported that reducing the stud spacing from 0.75*d* to 0.44*d* enhanced the ductility and drift capacity by only 8 and 11%, respectively. Since this enhancement is not significant, it was concluded that using shear studs with 0.75*d* spacing is efficient for ductile design. It was concluded that no limit on the gravity shear ratio applied to edge connections is required to achieve the 1.5% minimum drift when shear stud reinforcement is provided.

Based on work done by Moehle (1996) and Megally and Ghali (2000b), ACI Committee 318 introduced provisions for shear reinforcement in slab-column connections that are not considered a part of the SFRS in the 2005 code (ACI 2005a). Shear reinforcement is required unless the connection can resist the shear stress due to the factored shear force and induced moment transferred under the design displacement, or if the design drift ratio does not exceed the larger of 0.005 and $[0.035 - 0.05(V_g/V_c)]$ (Figure 2.16). In the 2014 version of the ACI 318 code, the former requirement was omitted and calculations of the induced moments due to the design displacement are no longer required (ACI 2014a).

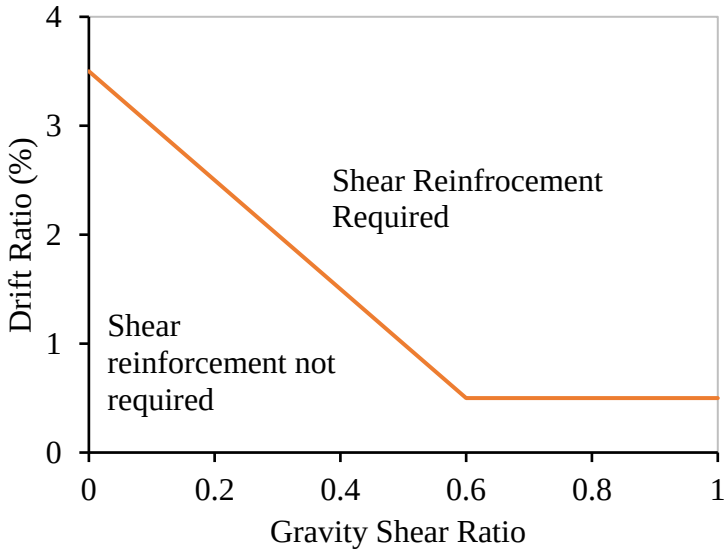

Figure 2.16: ACI Committee 318 requirement for shear reinforcement (ACI 2005a, 2014a)

2.7.1.3. Effect of flexural reinforcement ratio

As mentioned earlier, the main concern when designing slab-column connections in seismic zones is their ductility. It is well demonstrated that increasing the flexural reinforcement ratio in steel-RC connections, although increases their capacity, considerably decreases the ductility of the connections. Accordingly, limited research studies have investigated the influence of flexural reinforcement ratio on the seismic response of slab-column connections.

Emam et al. (1997) tested four interior slab-column connections under cyclic lateral loads to investigate the influence of flexural reinforcement ratio on the seismic response of slab-column connections made with normal strength concrete (NSC) and high strength concrete (HSC). They reported that doubling the reinforcement ratio (from 0.5 to 1.0%) increased the lateral load capacity by 27 and 21% for connections made of NSC and HSC, respectively. It also increased the stiffness of the connections and, subsequently, reduced their stiffness degradation. However, it did not affect the drift capacity of the connections. Furthermore, increasing the flexural reinforcement

ratio had unfavorable effects on the ductility the connections. Doubling the reinforcement ratio decreased the ductility by 53 and 52% for connections made of NSC and HSC, respectively. This was considered a warning against implementing high reinforcement ratios in slabs expected to experience seismic events unless other solutions to guarantee satisfactory seismic performance are provided, e.g., shear reinforcement is provided. Similar results were obtained by Marzouk et al. (2001) for connections made of light-weight NSC and HSC.

2.7.2. FRP-RC slabs under concentric shear force

Several experimental studies were conducted in the last two decades to investigate the punching shear behaviour of FRP-RC flat plates subjected to concentric shear force applied through a steel plate or a column stub (Matthys and Taerwe 2000; El-Ghandour et al. 2003; Ospina et al. 2003; Lee et al. 2009; Dulude et al. 2013; Hassan et al. 2013b, 2015; Nguyen-Minh and Rovňák 2013). It was demonstrated that FRP-RC slabs have considerably lower stiffness and punching capacity than their steel-RC counterparts with similar flexural strength. In addition, it was concluded that the FRP shear reinforcement enhanced the deformation capacity and punching shear capacity of the connections (Hassan et al. 2015).

2.7.3. FRP-RC slab-column connections under shear force and unbalanced moment

Recently, the behaviour of FRP-RC slab-column connections subjected to simultaneous concentric shear force and unbalanced moment transfer has attracted researchers. Gouda and El-Salakawy (2016a) have conducted a pioneer test program to investigate the behaviour of full-scale GFRP-RC interior slab-column connections under a combination of shear forces and unbalanced moments. Similarly, the GFRP-RC connection exhibited lower post-cracking stiffness and punching capacity than those of the steel-RC counterpart with the same flexural reinforcement

ratio. It was also reported that increasing the GFRP reinforcement ratio from 0.65 to 0.98 and further to 1.3% increased the post-cracking stiffness by 51 and 110% and the punching capacity by 8 and 20%, respectively. Furthermore, Gouda and El-Salakawy (2016b) used a new type of GFRP shear studs with headed ends (Figure 2.17) in interior connections under the same load combination. Again, the presence of the well-anchored shear reinforcement resulted in increasing the ultimate deflection and punching capacity of the shear-reinforced connections.

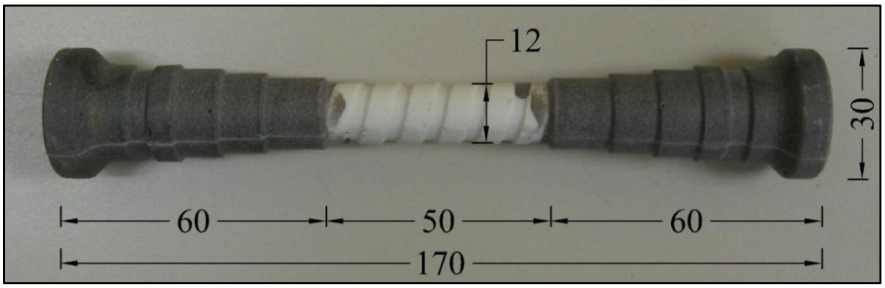

Figure 2.17: GFRP shear stud (El-Gendy and El-Salakawy 2016a; Gouda and El-Salakawy 2016b)

Hussein and El-Salakawy (2018) investigated the effect of flexural reinforcement ratio on interior connections made with HSC. They also introduced a new type of GFRP shear reinforcement in the form of corrugated bars, which are sand-coated bent bars with a 90^{o} angle between the vertical stems and the horizontal portions. Each corrugated bar comprised five vertical stems spaced at 120 mm centre-to-centre. Furthermore, they tested a modified type of GFRP shear studs with a considerably higher design capacity. It was demonstrated that increasing the concrete strength by 111% (from 38 to 80 MPa) increased the punching capacity by only 22% with a considerable reduction in the deflections at the same load level. It was also concluded that both types of shear reinforcement managed to control the widening and propagation of shear cracks, which significantly enhanced the post-cracking stiffness and punching capacity of the connections.

The first experimental investigation on full-scale edge connections reinforced with GFRP bars was conducted by El-Gendy and El-Salakawy (2016), where they used the same type of GFRP headed studs used by Gouda and El-Salakawy (2016b) (Figure 2.17) in GFRP-RC edge connections. The authors reported that the headed ends of the GFRP shear studs provided adequate anchorage, which allowed the studs to reach their recommended design strain (2,175 με) with no apparent signs of slippage; thus, the punching capacities of the shear-reinforced connections were increased. Furthermore, the presence of GFRP studs spaced at 120 mm (0.75 *d*) changed the mode of failure to a mixed flexural-punching mode, while reducing the spacing to 80 mm (0.50 *d*) allowed the connection to reach its full flexural capacity. As a result, increases as high as 46 and 128% in the ultimate capacity and the deformability, respectively, were reported when the GFRP shear studs were spaced at 0.50 *d*. In another study, El-Gendy and El-Salakawy (2018a) reported that a steel-RC connection had approximately three times the post-cracking stiffness of that of a GFRP-RC counterpart with the same reinforcement ratio due to the higher axial stiffness of steel compared to that of GFRP. In addition, it was concluded that increasing the GFRP reinforcement ratio from 0.9 to 1.35 and further to 1.8% increased the post-cracking stiffness by 62 and 119% and the punching capacity by 14 and 21%, respectively.

Mostafa and El-Salakawy (2018) extended the scope of research on GFRP-RC edge connections to include the effect of high strength concrete and type and ratio of GFRP shear reinforcement. The authors reported a relatively low increase of 7 and 15% in the punching capacity of connections made of HSC when the reinforcement ratio was increased by 50 and 100%, respectively. They also emphasized the rule of well-anchored shear reinforcement in enhancing both the punching capacity and deformability of edge connections. Regardless of the shear reinforcement type, a minimum shear reinforcement ratio of 0.4% was recommended to ensure

flexural failure. Recently, Salama et al. (2019) investigated the behaviour of edge connections reinforced with closed and spiral GFRP stirrups. It was concluded that both types of GFRP shear reinforcement offered sufficient confinement to control the development of shear cracks. It was reported that spiral stirrups provided better performance than that of the closed stirrups. The specimen with spiral stirrups experienced 9, 33, and 36% increase in the punching capacity, deformation capacity and energy absorption, respectively, than its counterpart with closed stirrups.

2.8. Research on FRP-RC Members Subjected to Cyclic Lateral Loading

In the last two decades, few experimental studies have been conducted to investigate the seismic response of GFRP-RC beam-column joints (Hasaballa et al. 2011; Mady et al. 2011; Ghomi and El-Salakawy 2016, 2019), GFRP-RC columns (Sharbatdar and Saatcioglu 2009; Ali and El-Salakawy 2015; Tavassoli et al. 2015; Naqvi et al. 2017; AlAjarmeh et al. 2019), and GFRP-RC shear walls (Mohamed et al. 2014; Arafa et al. 2018; Hassanein et al. 2019). It was concluded that the combination of low modulus of elasticity and high tensile strength of GFRP bars allowed GFRP-RC elements to undergo significantly large lateral drifts without exhibiting brittle failure, which indicates the feasibility of using GFRP reinforcement in such members when subjected to seismic loading.

In addition, the low stiffness of GFRP reinforcement compared to that of steel reinforcement results in a lower natural frequency (longer natural period) and, consequently, a higher damping ratio of the GFRP-RC structures. Therefore, GFRP-RC structures will attract less seismic load compared to that attracted by steel-RC counterpart structures, with a faster decay in the amplitude of the seismic vibrations. Furthermore, due to the elastic nature of GFRP reinforcement, GFRP-RC structures possess considerable self-centering capabilities. As such, they will require

significantly less repair efforts to restore their original functionality after surviving a seismic event. To date, however, no research has been conducted to investigate the seismic response of FRP-RC slab-column edge connections.

2.9. Punching Shear Design Models

Based on the aforementioned experimental studies, several empirical models have been introduced by different researchers to predict the punching capacity of FRP-RC slabs (Matthys and Taerwe 2000; Ospina et al. 2003; El-Gamal et al. 2005; Hassan et al. 2014, 2017; El-Gendy and El-Salakawy 2016; Salama et al. 2019). These models, as well as the current design provisions for FRP-RC slabs in codes and guidelines (JSCE 1997; ACI 2015; CSA 2017), are empirical in nature; they are based on statistical fitting of the test results available at the time they were developed. This section reviews the models predicting punching shear capacity of FRP-RC slabs incorporated in current provisions and proposed by researchers.

2.9.1. Eccentric shear stress model

Both CSA A23.3-19 (CSA 2019b) and ACI 318-19 (ACI 2019a) adopt the eccentric shear stress model to estimate the shear stress applied to a connection. In this model, the factored unbalanced moment, M_f, at a connection is assumed to be transferred by both flexure and eccentric shear on a critical section. This critical section, for connections without shear reinforcement, is assumed to be located at a distance $d/2$ from the column face in both codes, where d is the average effective depth of the top (tension) reinforcement in the slab. The portion of the unbalanced moment transferred by shear, $\gamma_v M_f$, is given by Equation 2.7, where b_1 is the width of the critical section in the direction of the unbalanced moment, and b_2 is the width of the critical section perpendicular to b_1.

$$\gamma_v = 1 - \frac{1}{1 + (2/3)\sqrt{b_1/b_2}} \qquad \text{Equation 2.7}$$

This portion of the moment is assumed to be transferred by linear variation of shear around the critical section as shown in Figure 2.18. Thus, the factored shear stress on the critical section, v_f, can be estimated by Equation 2.8, where V_f is the factored shear force transferred between the slab and the column, b_o is the perimeter of the critical section, e is the distance from the centroid of the critical section to the point where shear stress is being calculated, and J_c is a property of the critical section analogous to the polar moment of inertia. On the other hand, the nominal shear resistance, v_n, is typically estimated as a combination of the concrete (v_c) and shear reinforcement (v_s) capacities as given in Equation 2.9**.**

$$v_f = \frac{V_f}{b_o d} + \frac{\gamma_v M_f}{J} e \qquad \text{Equation 2.8}$$

$$v_n = v_c + v_s \qquad \text{Equation 2.9}$$

2.9.2. Slabs without shear reinforcement (code provisions)

2.9.2.1. Canadian Standards Association (CSA)

According to CSA S806-12 (CSA 2017), the factored punching shear stress resistance provided by concrete shall not exceed the smallest of Equation 2.10 to Equation 2.12, where β_c is the ratio of the long side to the short side of the column, λ is a factor to account for concrete density, ϕ_c is the resistance factor for concrete, E_F is the modulus of elasticity of FRP reinforcement (MPa), ρ_F is the longitudinal FRP reinforcement ratio, f_c' is the concrete compressive strength (MPa) and shall not be taken greater than 60 MPa, α_s is a coefficient equal to 4, 3 or 2 for interior, edge and

corner connections, respectively, and $b_{o,0.5d}$ is the perimeter of the critical section located at a distance 0.5d from the column face.

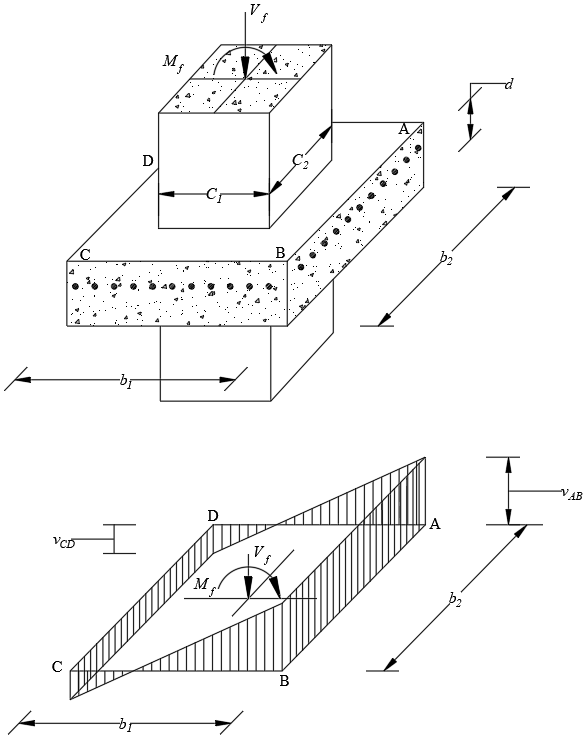

Figure 2.18: Eccentric shear stress model (ACI 2019a; CSA 2019b)

$$v_c = \left(1 + \frac{2}{\beta_c}\right) 0.028 \lambda \phi_c \left(E_F \rho_F f_c'\right)^{1/3} \qquad \text{Equation 2.10}$$

$$v_c = \left[\left(\frac{\alpha_s d}{b_{o,0.5d}}\right) + 0.19\right] 0.147 \lambda \phi_c \left(E_F \rho_F f_c'\right)^{1/3} \qquad \text{Equation 2.11}$$

$$v_c = 0.056 \lambda \phi_c \left(E_F \rho_F f_c'\right)^{1/3} \qquad \text{Equation 2.12}$$

While Equation 2.11 considers the effect of the shear perimeter-to-slab depth ratio, Equation 2.10 considers the effect of column rectangularity on the strength. However, Equation 2.10 will not

govern the design unless the column aspect ratio exceeds 2 (i.e., $\beta_c > 2$). Thus, for most columns, where the column aspect ratio is less than 2, Equation 2.12 governs the design. The slab size effect is then considered if the effective depth of the slab exceeds 300 mm by multiplying the governing value of v_c by $\left(300/d\right)^{0.25}$.

2.9.2.2. American Concrete Institute (ACI)

According to ACI 440.1R-15 (ACI 2015), the nominal shear strength provided by concrete at a critical section located at a distance $d/2$ from the column face can be estimated by Equation 2.13, where f_c' is the concrete compressive strength (MPa) and the term kd represents the depth of the neutral axis assuming elastic cracked conditions (mm), where k is calculated by Equation 2.14 and n_F is the modular ratio (i.e., the ratio between the modulus of elasticity for FRP to that for concrete).

$$v_c = \frac{4}{5}\sqrt{f_c'}\frac{\left(kd\right)}{d} \qquad \text{Equation 2.13}$$

$$k = \sqrt{2\rho_F n_F + \left(\rho_F n_F\right)^2} - \rho_F n_F \qquad \text{Equation 2.14}$$

2.9.2.3. Japan Society of Civil Engineers (JSCE)

The shear strength provided by concrete recommended by JSCE (JSCE 1997) is given by Equation 2.15, where γ_b is a factor of safety generally taken as 1.3, while β_d, β_p, β_r, f_{pcd}, and α are factors considering the slab size effect, the reinforcement axial stiffness, the column perimeter-to-slab depth ratio, the concrete strength, and the load eccentricity, respectively. These factors are estimated by Equation 2.16 to Equation 2.20, respectively, where E_s is the modulus of elasticity of steel (200,000 MPa), u is the perimeter of the loaded area, e.g., the column (mm), e_x and e_y are the

load eccentricities in the x and y directions (mm), respectively, and b_x and b_y are the critical section dimensions in the x and y directions (mm), respectively.

$$v_c = \beta_d \beta_p \beta_r \frac{f_{pcd}}{\gamma_b} \times \frac{1}{\alpha} \quad \text{Equation 2.15}$$

$$\beta_d = \sqrt[4]{1/d} \leq 1.5 \quad \text{Equation 2.16}$$

$$\beta_p = \sqrt[3]{100 \rho_F E_F / E_s} \leq 1.5 \quad \text{Equation 2.17}$$

$$\beta_r = 1 + \left[1/\left(1 + 0.25u/d\right) \right] \quad \text{Equation 2.18}$$

$$f_{pcd} = 0.2\sqrt{f_c'} \leq 1.2 \text{ MPa} \quad \text{Equation 2.19}$$

$$\alpha = 1 + 1.5\left[\left(e_x + e_y\right) / \sqrt{b_x b_y} \right] \quad \text{Equation 2.20}$$

2.9.3. Slabs without shear reinforcement (models proposed in literature)

2.9.3.1. Model by Matthys and Taerwe (2000)

In an early effort by Matthys and Taerwe (2000), the punching shear model for steel-RC slabs in the British Standard, BS8110 (BSI 1997), was modified to account for the lower stiffness of FRP by multiplying the reinforcement ratio by the ratio of modulus of elasticity of FRP to that of steel, E_F/E_S as shown in Equation 2.21. This model considers the influence of the main parameters known to affect the punching behaviour of FRP-RC slabs, i.e., reinforcement ratio and modulus of elasticity, concrete strength and effective slab depth. Unlike the aforementioned code provisions, this model considers the critical section at a distance of 1.5*d* from the column face, similar to the approach followed in BS8110 (BSI 1997).

$$v_c = \left(100\rho_F \frac{E_F}{E_S} f_c^{'}\right)^{1/3} \times \frac{1.36}{d^{0.25}} \qquad \text{Equation 2.21}$$

2.9.3.2. Model by Ospina et al. (2003)

According to Ospina et al. (2003), the model by Matthys and Taerwe (2000) overestimates the effect of FRP reinforcement stiffness. Thus, they modified it by using the square root of E_F/E_S, instead of the cubic one. In addition, based on the available results at that time, it was suggested that the slab size effect was not evident on the punching strength of FRP-RC slabs; thus, it was ignored in their proposed model (Equation 2.22). This model also considers the critical section at a distance of 1.5*d* from column face.

$$v_c = 2.77\left(\rho_F f_c^{'}\right)^{1/3} \sqrt{\frac{E_F}{E_S}} \qquad \text{Equation 2.22}$$

2.9.3.3. Model by El-Gamal et al. (2005)

A new parameter was considered in this model, which was proposed based on punching tests conducted on FRP-RC bridge deck slabs. The effect of slab restraining action, developed by transverse diaphragms and the in-plane stiffness of deck slabs in adjacent panels, was introduced in Equation 2.23. For simplicity, this effect was considered in the form of a factor *N*, which is taken as 0, 1, or 2 for simple slabs in both directions, slabs continuous in one direction, and slabs continuous in both directions, respectively. This model was one of the early models to consider the effect of shear perimeter-to-slab depth ratio.

$$v_c = 0.33\sqrt{f_c^{'}}\left[0.62\left(\rho_F E_F\right)^{1/3}\left(1+\frac{8d}{b_{o,0.5d}}\right)\right](1.2)^N \qquad \text{Equation 2.23}$$

2.9.3.4. Model by Hassan et al. (2017)

This model (Equation 2.24) is an incremental modification of the one incorporated in CSA S806-12 (CSA 2017) by combining the three equations (Equation 2.10 to Equation 2.12) into a single formula. This was done by performing a regression analysis on 69 slabs from the literature.

$$v_c = 0.065\lambda\phi_c\left(\frac{4d}{b_{o,0.5d}} + 0.65\right)\left(E_F\rho_F f_c'\right)^{1/3}\left(125/d\right)^{1/6} \qquad \text{Equation 2.24}$$

2.9.4. Slabs with shear-reinforcement (models proposed in the literature)

2.9.4.1. Model by Hassan et al. (2014)

This model (Equation 2.25 and Equation 2.26**)** estimates the punching capacity of FRP-RC slabs with FRP stirrups. Similar to the approach followed in ACI 318-19 (ACI 2019a), this model assumes that the concrete contribution to shear strength within the shear-reinforced zone is 50% less than that when no shear reinforcement is provided. However, it does not give any guidance regarding the shear strength outside the shear-reinforced zone. In this model, the allowable stress in FRP stirrups**,** f_{Fv}, is taken as the smaller of the two values calculated by Equation 2.27 and Equation 2.28, where r_b is the bend radius, d_b is the stirrup diameter, f_{uv} is the ultimate strength of the straight portion of FRP stirrups, and f_{fbend} is the strength of the bend.

$$v_{c,inner} = 0.028\lambda\phi_c\left(E_F\rho_F f_c'\right)^{1/3} \qquad \text{Equation 2.25}$$

$$v_{sF} = \frac{0.7\phi_F A_{Fv} f_{Fv}}{b_{o,0.5d}\, s} \qquad \text{Equation 2.26}$$

$$f_{Fv} = 0.004E_{Fv} \qquad \text{Equation 2.27}$$

$$f_{Fv} = \frac{\left(0.05 r_b / d_b + 0.3\right) f_{uv}}{1.5} \leq f_{fbend} \qquad \text{Equation 2.28}$$

2.9.4.2. Model by El-Gendy and El-Salakawy (2016)

This model estimates the capacity of FRP-RC connections with GFRP stud shear reinforcement (Equation 2.29 to Equation 2.31**)**, where $v_{c,inner}$ and $v_{c,outer}$ are the shear stress resistance provided by concrete at the inner and outer critical sections located at distance *d*/2 from the column face and from the outermost peripheral shear reinforcement row (MPa), respectively, v_{sF} is the shear stress resistance provided by FRP shear reinforcement (MPa), ϕ_F is the resistance factor for FRP shear reinforcement, A_{Fv} is the area of FRP shear reinforcement (mm^2), ε_{Fv} is the allowable strain in FRP shear reinforcement taken as the smaller of 5,000 με or the maximum usable strain of the used shear reinforcement, E_{Fv} is the modulus of elasticity of FRP shear reinforcement (MPa), and *s* is the spacing of FRP shear reinforcement measured perpendicular to the critical section. This model was then refined to consider different types of GFRP shear reinforcement (Mostafa and El-Salakawy 2018; Hussein and El-Salakawy 2018).

$$v_{c,inner} = 0.041 \lambda \phi_c \left(E_F \rho_F f_c^{'}\right)^{1/3} \qquad \text{Equation 2.29}$$

$$v_{c,outer} = 0.028 \lambda \phi_c \left(E_F \rho_F f_c^{'}\right)^{1/3} \qquad \text{Equation 2.30}$$

$$v_{sF} = \frac{\phi_F A_{Fv} \left(\varepsilon_{Fv} E_{Fv}\right)}{b_{o,0.5d} s} \qquad \text{Equation 2.31}$$

2.9.4.3. Model by Salama et al. (2019)

In a recent effort, Salama et al. (2019) proposed to reduce the shear strength provided by concrete to half the value recommended by CSA S806-12 (CSA 2017). As such, the strength provided by

concrete at the inner and outer critical sections is given by Equation 2.30, while that provided by shear reinforcement is given by Equation 2.31 with a maximum strain limit of 5,000 με.

CHAPTER 3. RESEARCH PROGRAM

3.1. General

Based on the literature review, it was demonstrated that three of the main parameters influencing the seismic response of slab-column connections are the gravity shear ratio, the presence of shear reinforcement and the flexural reinforcement ratio. This research program consists of three phases: experimental, analytical, and numerical. The experimental phase involves the construction and testing of seven full-scale slab-column edge connections in the W. R. McQuade Structures Laboratory at the University of Manitoba to study the effects of the aforementioned parameters on the seismic response of such connections. The analytical phase involves the assessment of different punching shear design models incorporated in current standards and guidelines or proposed in the literature. Based on the assessment, a universal design model is proposed to predict the capacity of both interior and edge connections subjected to gravity or cyclic loads. The numerical phase, on the other hand, comprises the construction and validation of a FEM to simulate the seismic behaviour of the connections. This validated FEM is then used to conduct a parametric study on several key parameters.

3.2. Experimental Study

3.2.1. Materials

3.2.1.1. Concrete

All test specimens were constructed using normal-weight, ready-mix concrete with a target compressive strength of 40 MPa at 28 days. The actual compressive strength of concrete was determined by testing standard cylinders (100 × 200 mm) on the day of slab testing according to CSA A23.1-19/A23.2-19 (CSA 2019c).

3.2.1.2. Slab flexural reinforcement

Two types of reinforcing bars were used as flexural reinforcement for the slabs: No. 15M conventional deformed steel bars for one steel-RC control specimen and No. 15 sand-coated GFRP bars for the rest of the specimens. For the negative (top) orthogonal reinforcement assembly, straight bars were used in the parallel direction, while single-end hooked bars were used in the perpendicular direction with the hooked end coinciding with the location of maximum negative moment (i.e., the free edge of the slab) to provide the required anchorage.

On the other hand, for the positive (bottom) reinforcement assembly, straight bars were used in both orthogonal directions. A particular flexural reinforcement detailing is required when slab-column edge connections are employed in intermediate moment frames as part of the SFRS (ACI 2019a; CSA 2019b). This includes requirements for bottom reinforcement at discontinuous slab edge to be developed at the column face, which will likely require bottom reinforcement perpendicular to the free edge to be hooked. Nonetheless, such reinforcement detailing is not explicitly required when the flat plate system does not form part of the SFRS. Therefore, it was decided to use straight bottom reinforcement perpendicular to the free edge to provide a worst-case scenario when the flat plat system is only employed as a GFRS.

The mechanical properties of the straight and hooked GFRP bars were obtained from standard tests carried out according to ASTM D7205-06 (ASTM 2016) and ASTM D7914-14 (ASTM 2014), respectively, while those of steel bars were obtained from standard tests carried out according to ASTM A370-19 (ASTM 2019). The reinforcement properties are listed in Table 3.1.

Table 3.1: Mechanical properties of the used reinforcing bars

Bar material	Bar size (Number)	Diameter (mm)	Area (mm^2)	Tensile strength [a] (MPa)	Elastic modulus (GPa)	Ultimate strain (%)
Steel (straight and hooked)	15M	15.9	200	400 [b]	200	0.20 [b]
GFRP (straight)	15	15.9 [c]	199 [c] (234) [d]	1,712	66	2.60
GFRP (hooked - straight portion)	15	15.9 [c]	199 [c] (227) [d]	1,405	52	2.70
GFRP (hooked - bent portion)	15	15.9 [c]	199 [c] (227) [d]	725	-	-
GFRP (shear studs)	13	12.8	129	551 [d]	68	0.81 [e]
GFRP (corrugated bars)	13	12.8	129	1,281 [f]	52	2.50 [f]

[a] Calculated using nominal area
[b] Yield stress and strain for steel bars
[c] Nominal area according to CSA S807-19 (CSA 2019d)
[d] Measured area according to Annex A in CSA S806-12 (CSA 2017)
[e] Usable design stress/strain provided by the manufacturer (corresponds to a pull-out load capacity of 70 kN)
[f] Properties of straight portion as provided by the manufacturer

3.2.1.3. Slab shear reinforcement

Two recently developed types of GFRP shear reinforcement were used: shear studs and corrugated bars. The shear studs were 170-mm long No.13 bars with 70-mm long cast-on tapered headed ends. The tapered heads were made of a thermoplastic matrix reinforced with short discrete glass fibres. The heads had an outer diameter of 25 mm (2 times the bar diameter) and were tapered in five steps towards the bar as shown in Figure 3.1. The pullout load capacity of the shear studs were 70 kN as provided by the manufacturer (Pultrall Inc., personal communication, 2017). This value corresponds to a tensile stress of 551 MPa (approximately 30% of the ultimate tensile strength of the bar, 1,848 MPa) and a tensile strain of 8,100 με. The failure of the studs was expected to occur when the heads shear off at the head-bar interface. On the other hand, the corrugated bars were No. 13 sand-coated bent bars with a 90^{o} angle between the vertical stems and the horizontal portions and a total height of 170 mm. Each corrugated bar comprised nine vertical stems spaced at 80 mm centre-to-centre (half the average slab depth, *d*) as shown in Figure 3.2. The mechanical properties of the shear reinforcement as provided by the manufacturer are listed in Table 3.1.

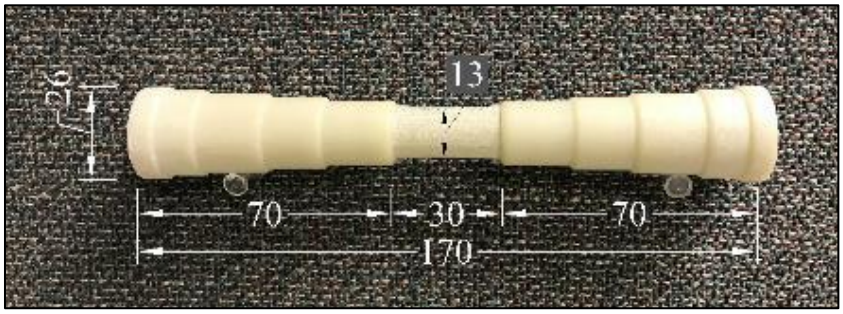

Figure 3.1: GFRP shear stud with headed ends (dimensions in mm)

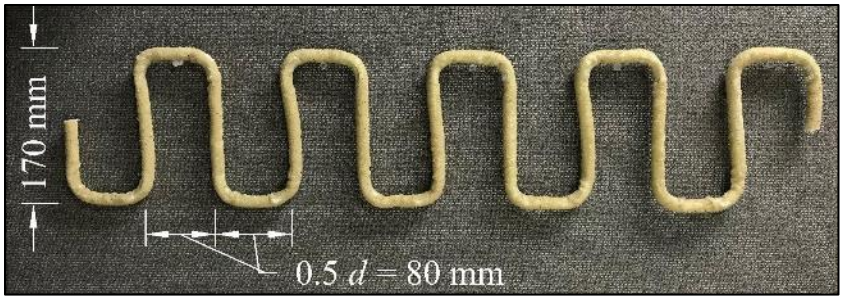

Figure 3.2: GFRP corrugated bar (dimensions in mm)

3.2.1.4. Column reinforcement

The columns of all specimens were reinforced with No. 25M and No. 10M deformed steel bars and stirrups, respectively.

3.2.2. Test specimens

The test specimens, in this study, were isolated full-scale slab-column edge connections. This section outlines the progression of developing the specimens including the design of a typical flat plate parking structure and the extraction of the isolated specimens from the full flat plate system. The details of the specimens and the construction process are then described.

3.2.2.1. Prototype design

Experimental specimens are usually modeled assuming a prototype structure, which is designed for specified loads corresponding to the use and location of the building. In this study, the prototype structure was a typical flat plate parking garage building in the city of Winnipeg, MB, Canada. Therefore, the design was carried out according to the applicable design codes and standards in Canada, i.e., the National Building Code of Canada, NBCC 2015 (NRCC 2015), the Canadian standards for steel-RC structures, CSA A23.3-19 (CSA 2019b), and FRP-RC structures, CSA S806-12 (CSA 2017).

The prototype structure was a multistory flat plate building (neither drop panels nor column heads were incorporated) with a 3.0 m storey height. It consisted of five 5.5 m-long bays in each direction with 300-mm square columns and two I-shaped shear walls running vertically through the south-west side of the building as shown in Figure 3.3. No spandrel beams were designed at the slab perimeter in order to simulate a worst-case configuration at edge connections. Section 21.11.4 in the CSA A23.3-19 (CSA 2019b) was followed and the flat plate system was not considered a part of the SFRS; accordingly, it was designed to carry only the specified gravity loads, while the shear walls would control the lateral deformations. The design was carried out according to the Direct Design Method as described in the CSA A23.3-19 (CSA 2019b) and CSA S806-12 (CSA 2017), where applicable. The flat plate system was designed to carry its self-weight besides a superimposed dead load of 1.0 kN/m^2 (partition allowance), and a specified live load of 2.4 kN/m^2 (NRCC 2015). The design of the prototype structure was carried out twice; the slab of the building was reinforced with steel bars in one design and with GFRP bars in the other. The resulting slabs were 200-mm thick with negative flexural reinforcement ratios at the column strips of edge connections of 0.7 and 1.4% for the steel-RC and GFRP-RC slabs, respectively. Details of the flexural design of both steel and GFRP-RC structures are provided in Appendices A and B, respectively.

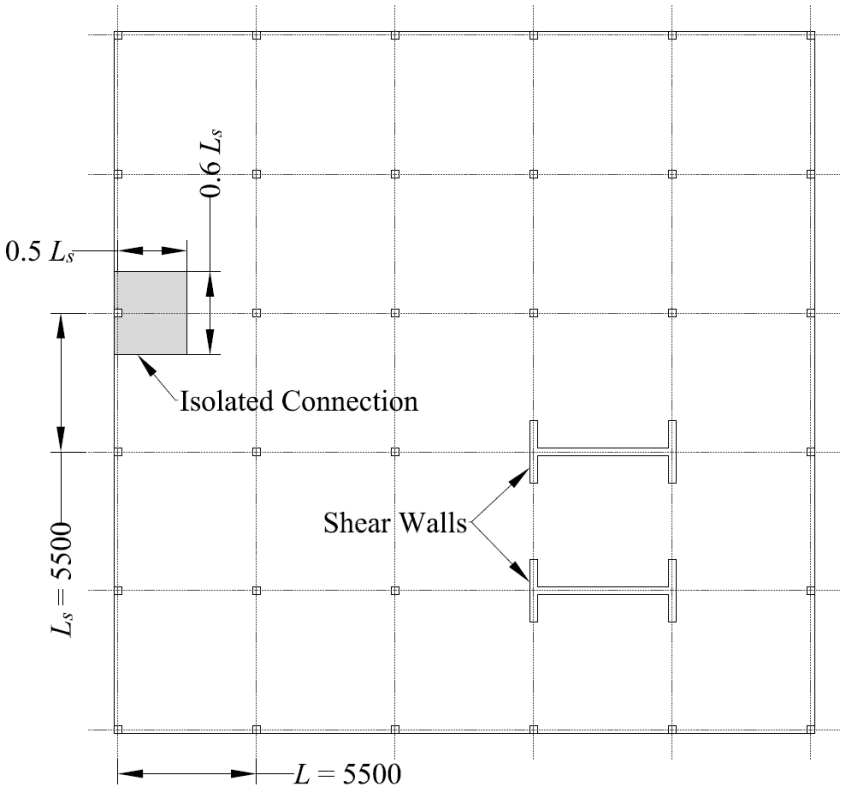

Figure 3.3: Layout of the prototype flat plate structure

3.2.2.2. Extraction of the isolated experimental specimens

The isolated experimental specimens were extracted from the prototype building by delineating the boundaries at the assumed contra-flexure lines corresponding to the type of loading applied to the building. As shown in Figure 3.4, when a building is subjected to gravity load only, it is reasonable to assume the contra-flexure lines for edge connections to be located at a distance of 0.2 L from the centrelines of the edge column, where L is the span between the centrelines of the columns (El-Gendy and El-Salakawy 2016).

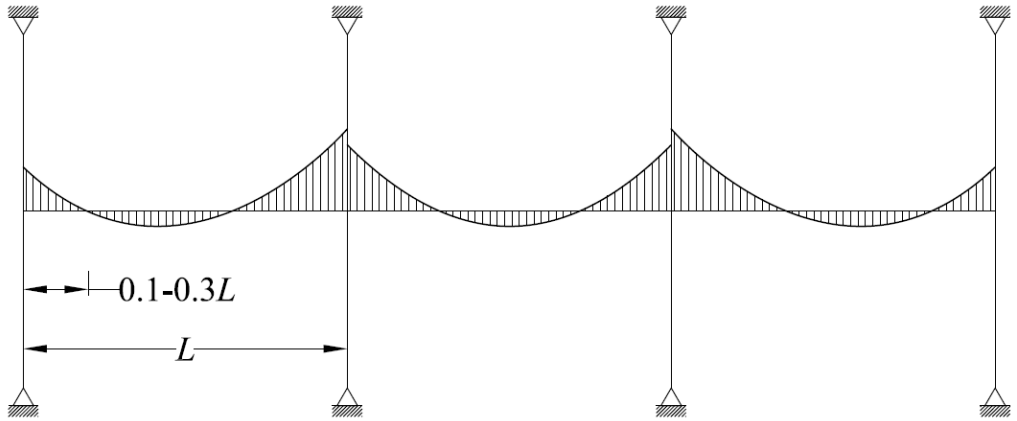

Figure 3.4: Typical bending moment diagram for slab subjected to gravity load only

On the other hand, if the building is hypothetically subjected to uniaxial cyclic lateral load only (no gravity load), the contra-flexure lines in the direction of the lateral load are located at mid-span of the slab regardless of the magnitude and direction of the lateral load as shown in Figure 3.5. Subsequently, when the building is subjected to combined gravity and cyclic lateral loading, the location of contra-flexure lines shift depending on the magnitude and direction of the lateral load as shown in Figure 3.6. That is, when the lateral load (perpendicular to the free edge) is causing negative bending moment at the edge connection, the contra-flexure line shifts away from the edge column towards the mid-span. On the contrary, when the lateral load is causing positive bending moment at the edge connection, the contra-flexure line shifts towards the edge column until it diminishes and the resultant moment changes its direction. In this case, the contra-flexure line farther from the edge column shifts towards the column and approaches mid-span. Accordingly, because they shift in the prototype building during an earthquake excitation, contra-flexure lines cannot be accurately represented in an isolated slab-column connection. Therefore, it was reasonable to assume the location of the contra-flexure line in the direction of the lateral load to be located at mid-span of the slab when testing isolated edge connections. This assumption was

adopted by several researchers (Pan and Moehle 1989; Wey and Durrani 1992; Robertson et al. 2002). In the parallel direction (i.e., relative to the free edge), the slab is subjected to gravity loads only. Accordingly, the contra-flexure lines for the edge connection were assumed at a distance of 0.3*L* from the centrelines of the edge column (Figure 3.4). On the other hand, the contra-flexure lines for the columns are located at mid-heights of the columns.

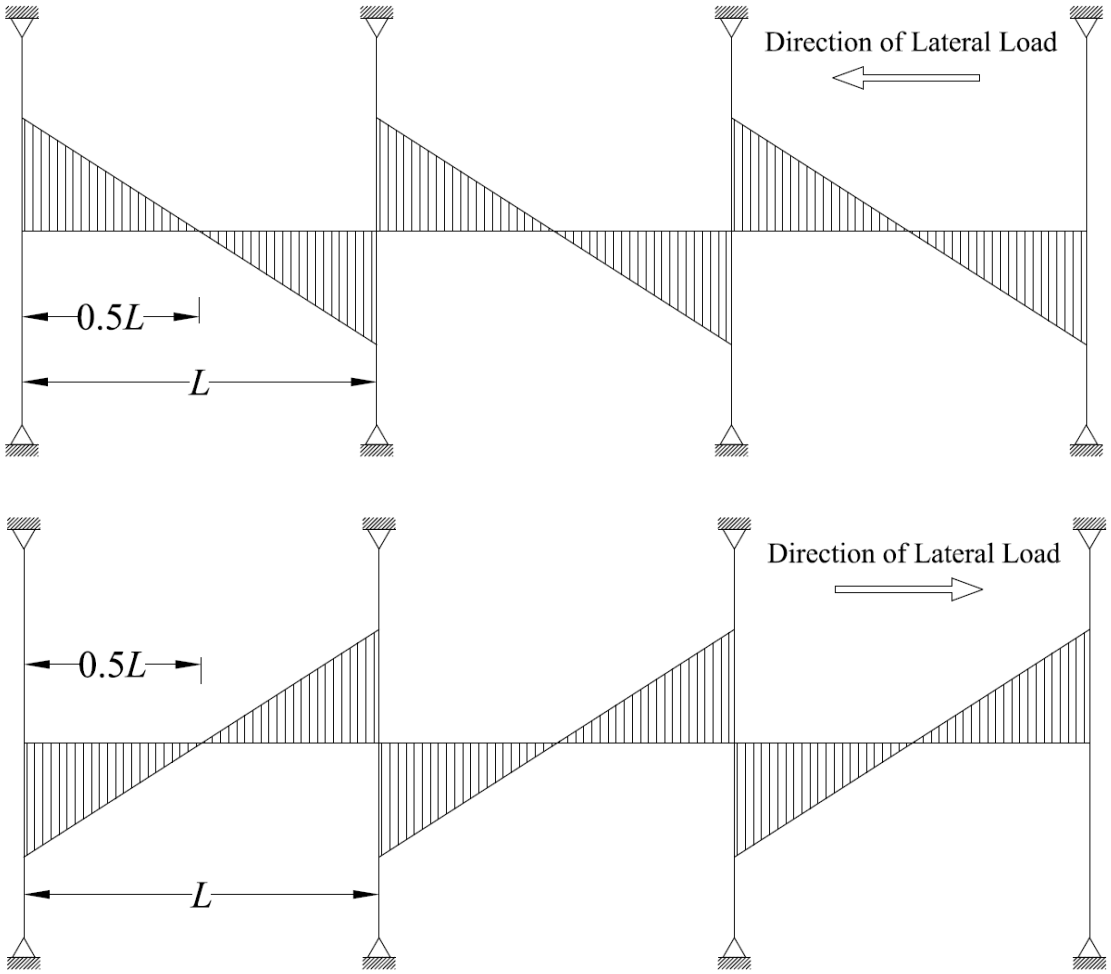

Figure 3.5: Bending moment diagrams for slab subjected to cyclic lateral load only

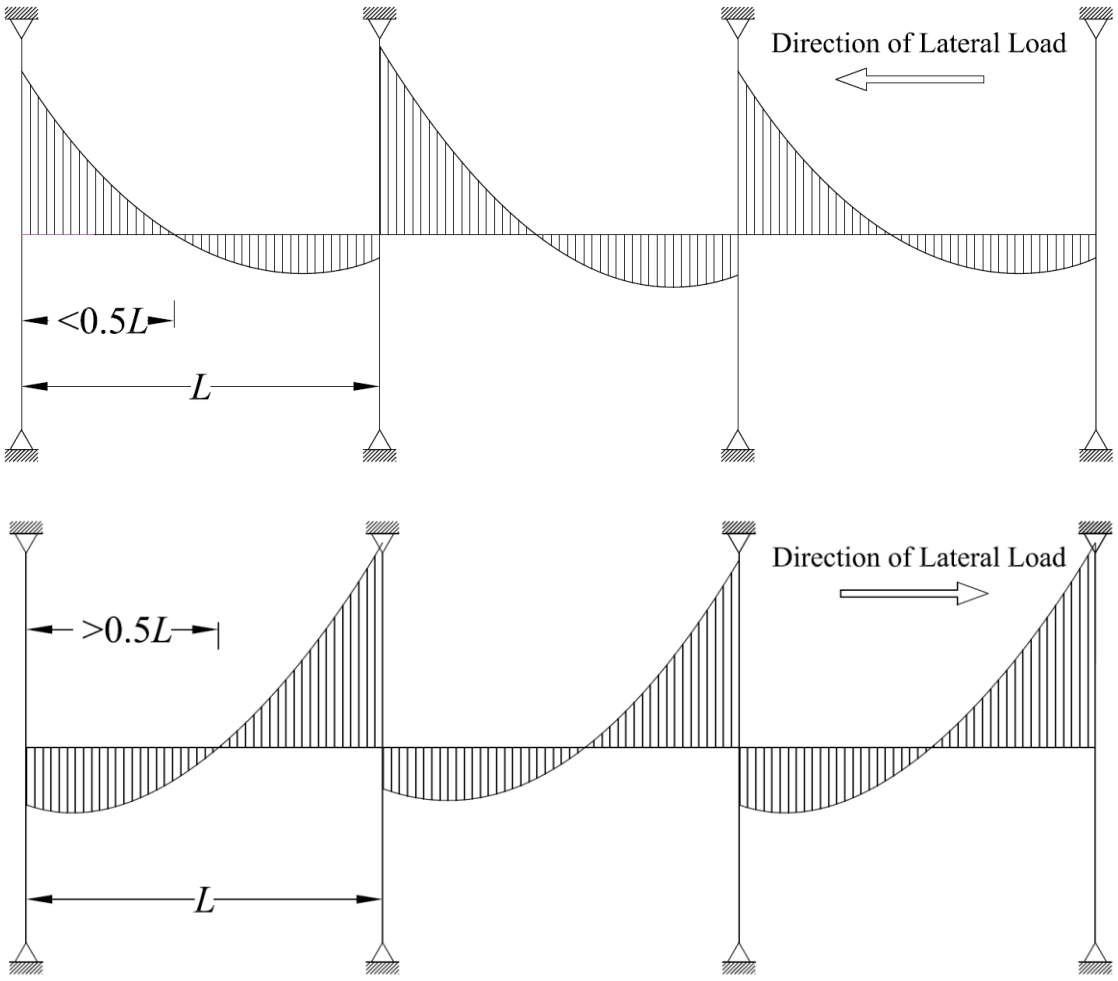

Figure 3.6: Bending moment diagrams for slab subjected to gravity and cyclic lateral load

Figure 3.7 shows the prototype building and the extracted isolated connection. The gravity loads applied to the upper floor are lower than those applied to the lower ones. Accordingly, in order to emphasize the worst case scenario for gravity loads, the isolated connections were extracted from a typical lower floor as shown in Figure 3.7a. The delineating contra-flexure lines at mid-span of the slab and mid-height of the column at the isolated connections were modelled as pinned supports since, by definition, the bending moments at these locations are approximately zero. However, because cyclic lateral loading is not being applied in the parallel direction, the slab edges perpendicular to the free edge were left free. A set of roller supports and a hinged support were

used to simulate the pinned supports for the slab and the column, respectively, as shown in Figure 3.7b. Details of these pinned supports and other test setup elements are discussed in Section 3.2.4.

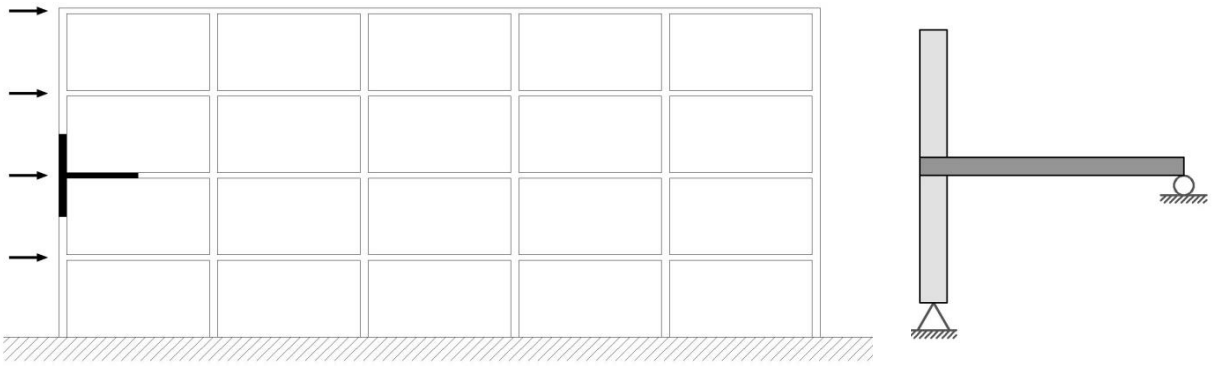

a) Prototype building b) Isolated connection

Figure 3.7: Prototype building and extracted isolated connection

3.2.2.3. Description of the isolated experimental specimens

The slabs of the extracted isolated connections had dimensions of 3,300 × 2,900 × 200 mm with 300-mm wide square columns extending 1,400 mm above and below the slab. However, as shown in Figure 3.8, slabs with dimensions of 3,300 × 3,100 × 200 mm were cast to allow for slab supporting clearance. Similarly, both the upper and lower columns had a nominal height of 1,360 mm so that the distance between the centreline of the slab and the tip of each column is 1,460 mm, i.e., approximately half the storey height. However, to permit the attachment of the column support and the hydraulic actuator, as will be discussed in Section 3.2.4, the upper and lower column heights were adjusted to 1,900 and 970 mm, respectively.

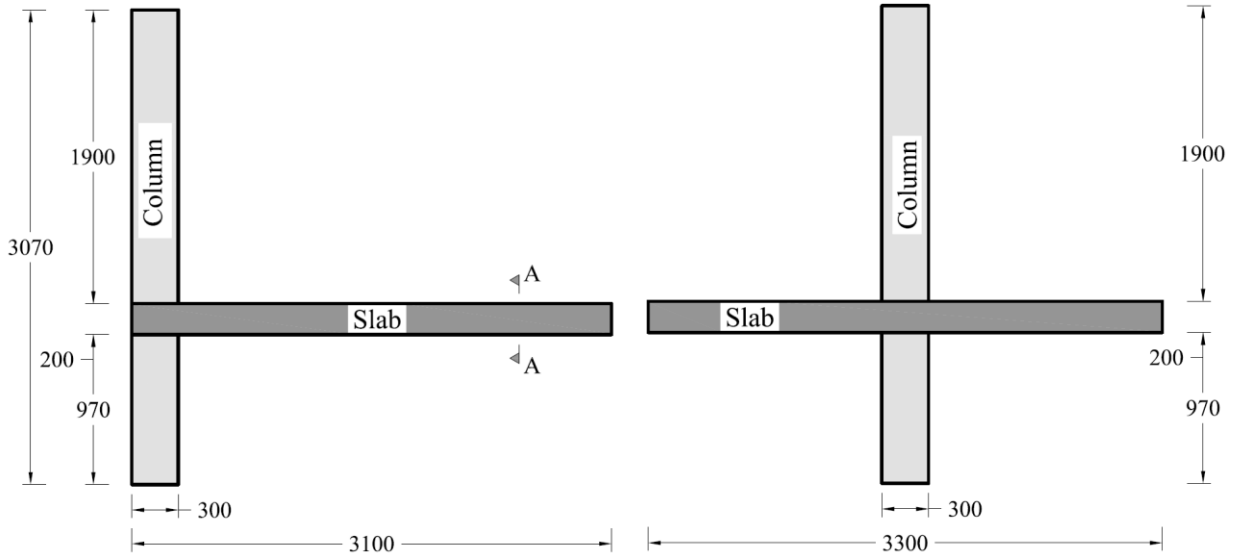

a) Slab-column edge connection b) Section A-A

Figure 3.8: Typical dimensions of isolated slab-column edge connections (dimensions in mm)

Seven full-scale isolated slab-column edge connections were constructed and tested to failure under gravity and uniaxial cyclic lateral loading. The tested parameters were the flexural reinforcement type and ratio, the gravity shear ratio, and the presence and type of GFRP shear reinforcement. The slabs of the connections were reinforced in flexure with deformed steel bars in one connection and GFRP bars with different reinforcement ratios in six connections. Two GFRP-RC slabs were reinforced with GFRP shear reinforcement; one with shear studs and the other with corrugated bars. Flexural reinforcement was provided to resist negative and positive moments in all connections, i.e., two orthogonal reinforcement assemblies (top and bottom) were employed in each connection. The columns for all connections were adequately reinforced with 6-25M longitudinal steel bars and No.10M steel stirrups spaced at 150 mm. The details of the test connections and their designation in different thesis chapters are listed in Table 3.2 and Table 3.3, respectively. The reinforcement configurations for all connections are shown in Figure 3.9 to Figure 3.14.

Table 3.2: Details of test connections

<table>
<tr><th rowspan="3">Specimen number</th><th rowspan="3">Flexural reinf. type</th><th colspan="4">Reinforcement ratio (%)</th><th rowspan="3">Gravity shear ratio</th><th rowspan="3">Shear reinf. type</th></tr>
<tr><th colspan="2">Top assembly</th><th colspan="2">Bottom assembly</th></tr>
<tr><th>Perpend. direction</th><th>Parallel direction</th><th>Perpend. direction</th><th>Parallel direction</th></tr>
<tr><td>1</td><td>Steel</td><td>0.7</td><td>0.70</td><td>0.30</td><td>0.40</td><td rowspan="3">0.4</td><td rowspan="4">NA</td></tr>
<tr><td>2</td><td rowspan="5">GFRP</td><td>0.7</td><td>0.70</td><td>0.40</td><td>0.40</td></tr>
<tr><td>3</td><td rowspan="4">1.4</td><td rowspan="4">1.40</td><td rowspan="4">0.80</td><td rowspan="4">0.80</td></tr>
<tr><td>4</td><td>0.5</td></tr>
<tr><td>5</td><td>0.6</td><td rowspan="2">Shear Studs</td></tr>
<tr><td>6</td><td rowspan="2">0.6</td></tr>
<tr><td>7</td><td>Corrugated Bars</td></tr>
</table>

Table 3.3: Specimens designations

Specimen number	Designation in thesis chapters				
	Ch. 4	Ch. 5	Ch. 6	Ch. 7	Ch. 8
1	ES-0.7	-	-	-	-
2	EG-0.7	-	-	E-0.7-40	E-0.7-40
3	EG-1.4	E40	-	E-1.4-40	E-1.4-40
4	-	E50	-	E-1.4-50	E-1.4-50
5	-	E60	EXX	E-1.4-60	E-1.4-60
6	-	-	ESS	-	-
7	-	-	ECB	-	-

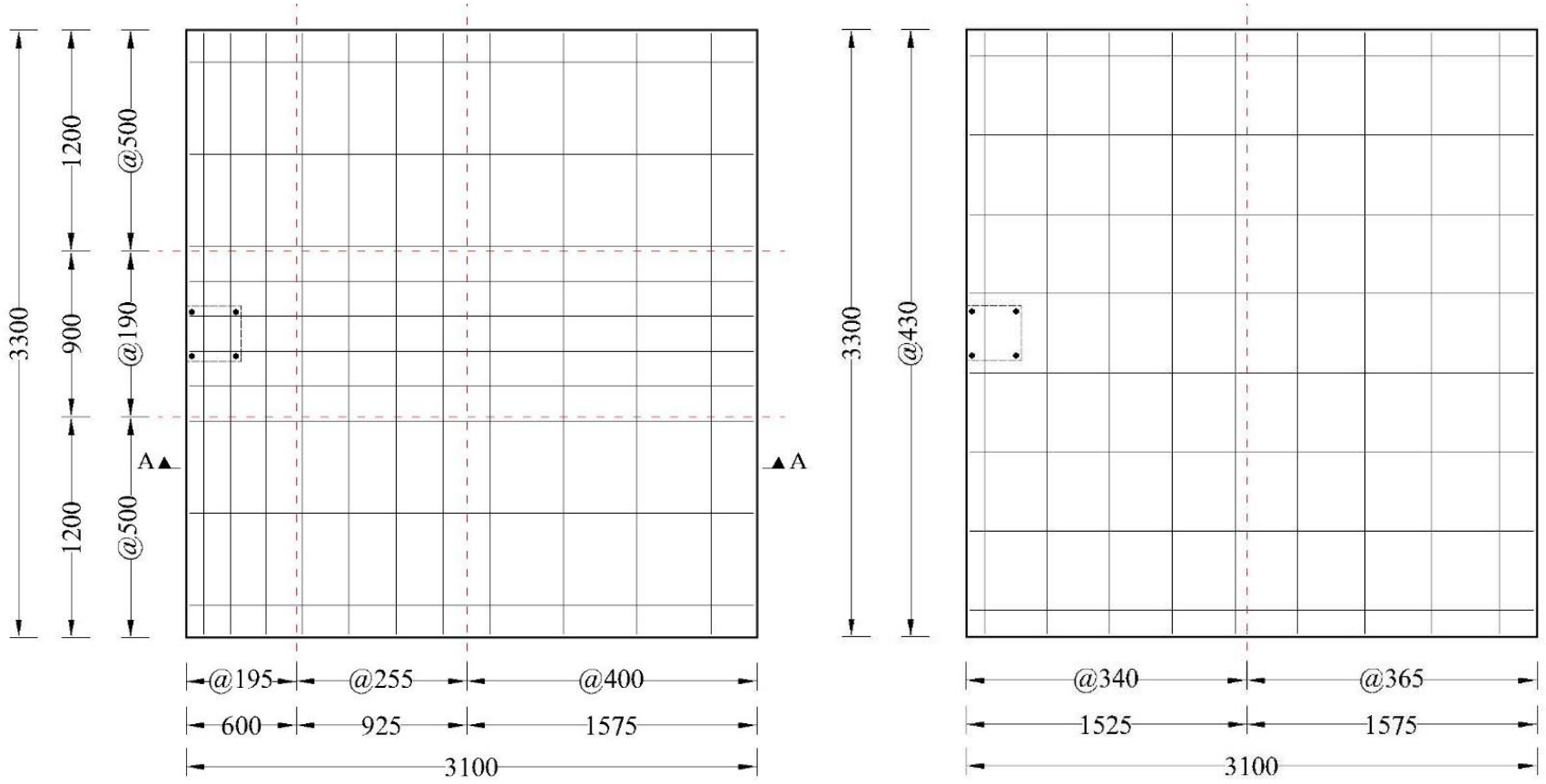

a) Negative moment reinforcement (top assembly)

b) Positive moment reinforcement (bottom assembly)

Figure 3.9: Flexural reinforcement layout for Specimen 1 (dimensions in mm)

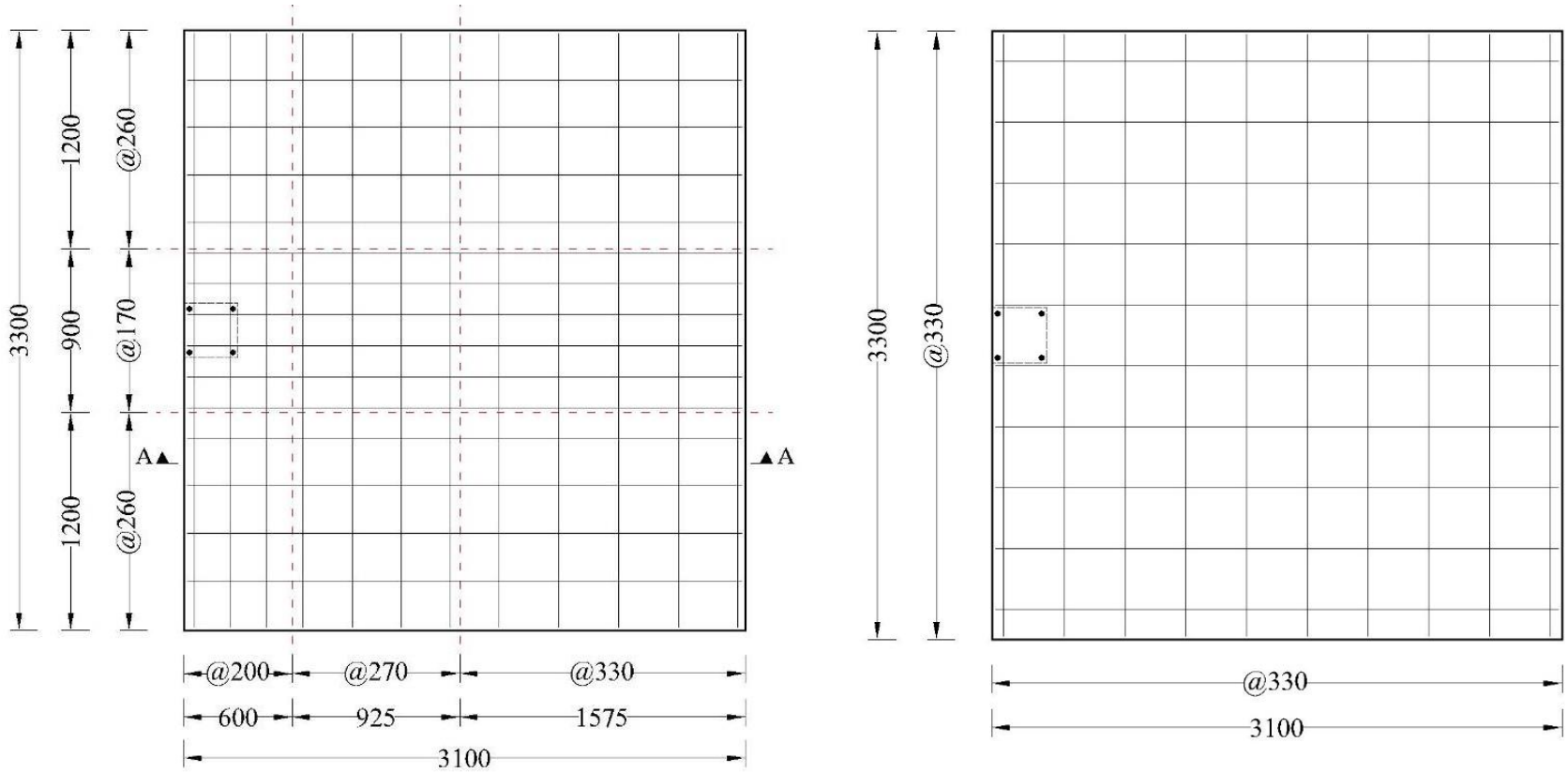

a) Negative moment reinforcement (top assembly)

b) Positive moment reinforcement (bottom assembly)

Figure 3.10: Flexural reinforcement layout for Specimen 2 (dimensions in mm)

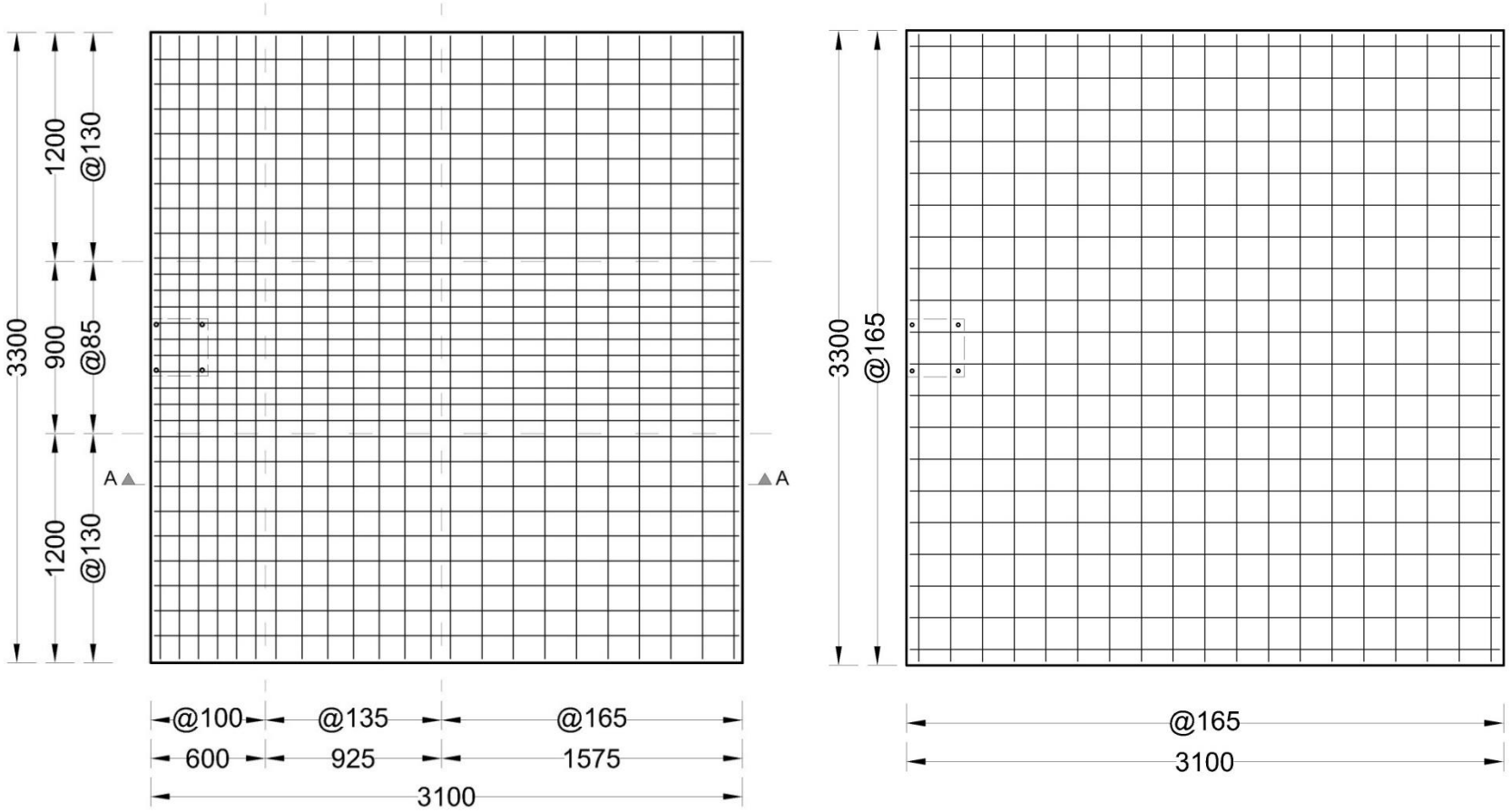

a) Negative moment reinforcement (top assembly)

b) Positive moment reinforcement (bottom assembly)

Figure 3.11: Flexural reinforcement layout for specimens 3 to 7 (dimensions in mm)

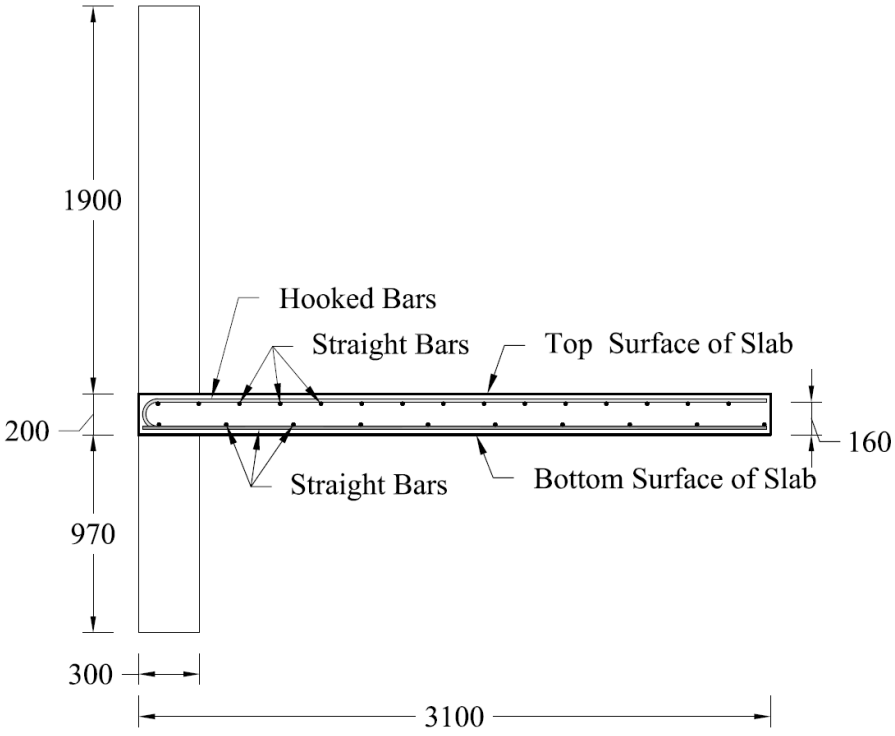

Figure 3.12: Typical cross section A-A (dimensions in mm)

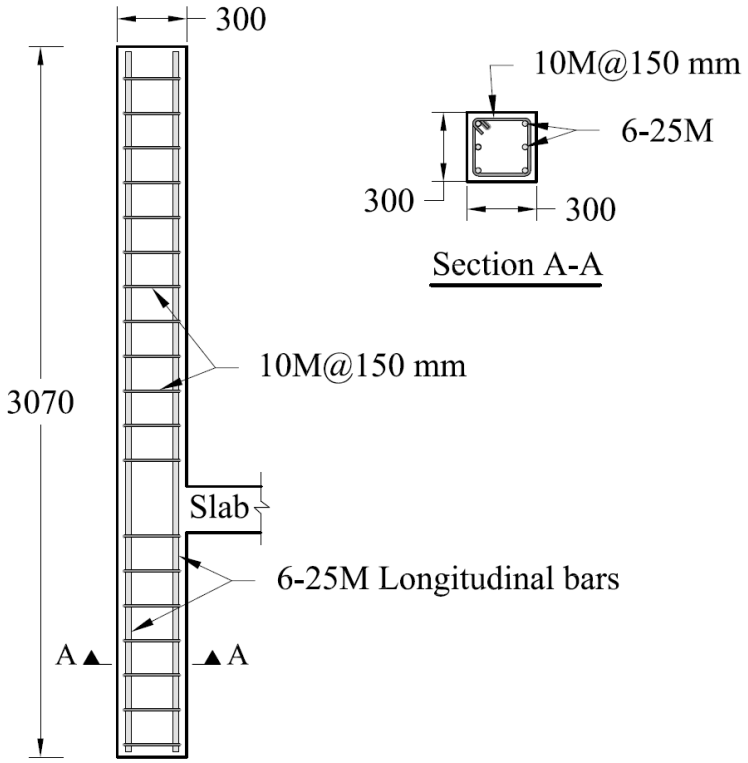

Figure 3.13: Typical column details (dimensions in mm)

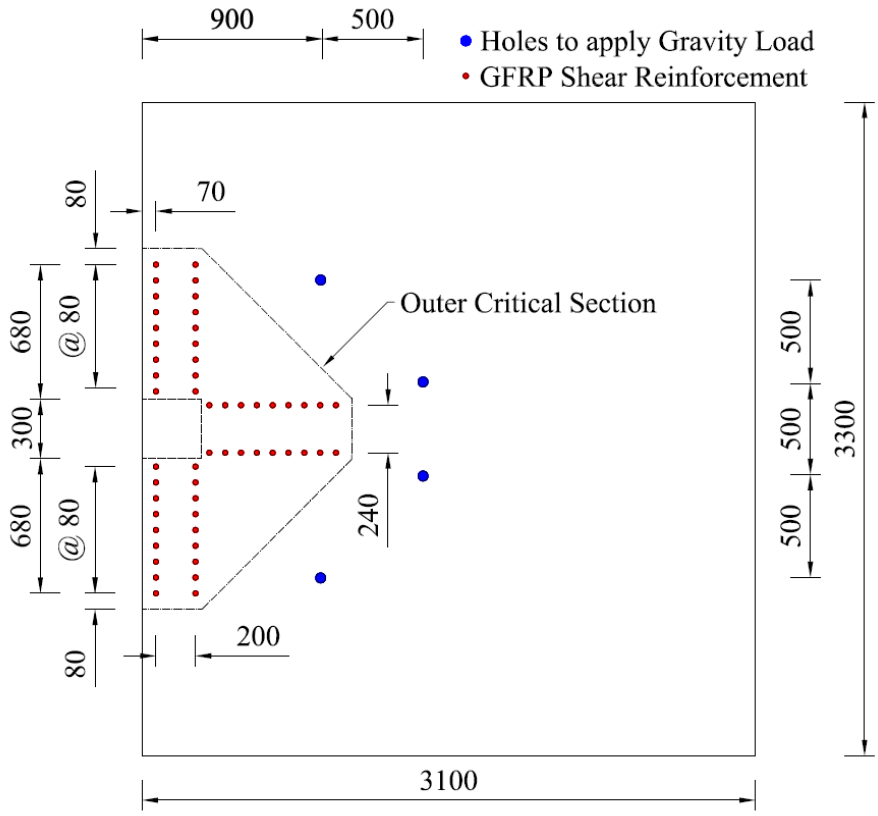

Figure 3.14: Shear reinforcement layout in specimens 6 and 7 (dimensions in mm)

3.2.2.4. Construction of isolated specimens

All specimens were constructed in the laboratory on a flat 4,800×3,700 mm wooden platform. The platform consisted of six 1-inch thick plywood sheets fixed to an assembly of 2×6 wood decking boards. The entire assembly was supported on two 3.0-m long, 1.0-m high concrete blocks, which were resting on the laboratory's strong floor as shown in Figure 3.15. For all specimens, the slab and the lower column were cast on the same day, while the upper column was cast on a following day similar to the common practice. The specimens were then wet cured for at least 7 days. Figure 3.16 to Figure 3.24 show the different stages of construction of test specimens.

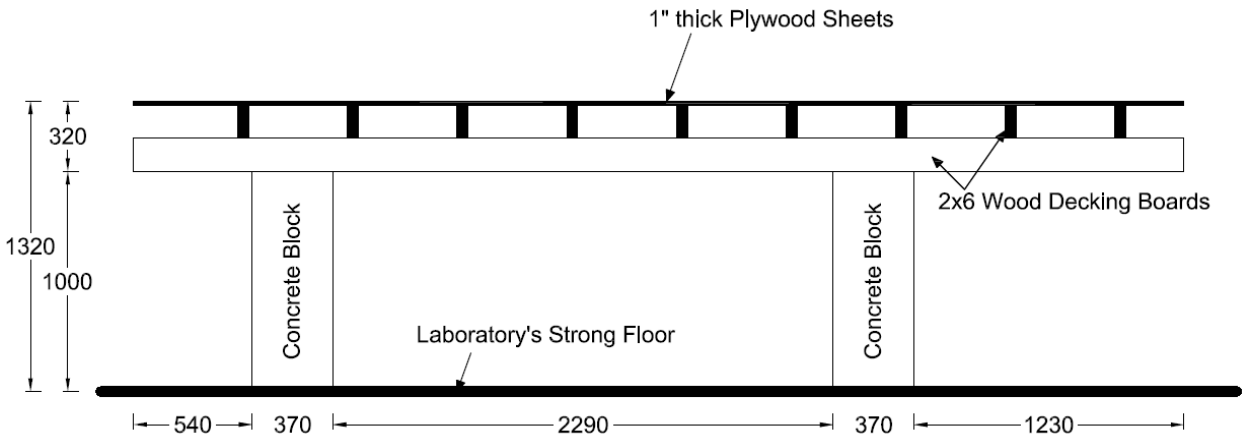

Figure 3.15: Details of formwork (dimensions in mm)

Figure 3.16: Assembled GFRP reinforcement assemblies

Figure 3.17: Column steel reinforcement cage

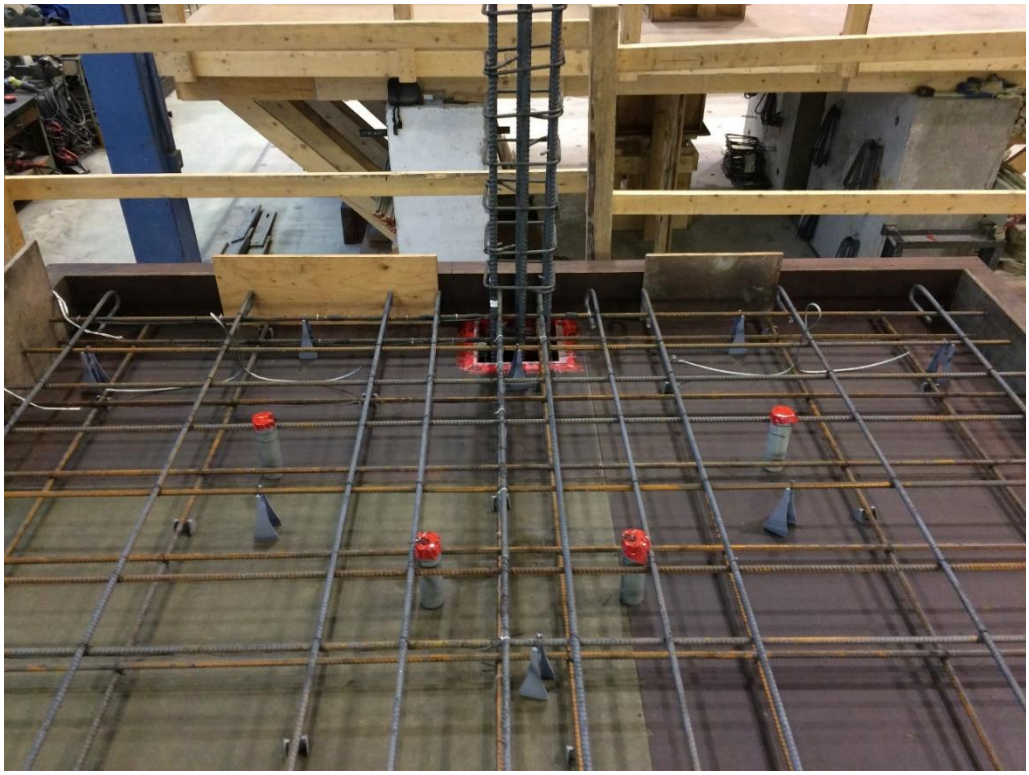

Figure 3.18: Specimen 1 (steel-RC) before casting

Figure 3.19: Specimen 2 (GFRP-RC with reinforcement ratio of 0.7%) before casting

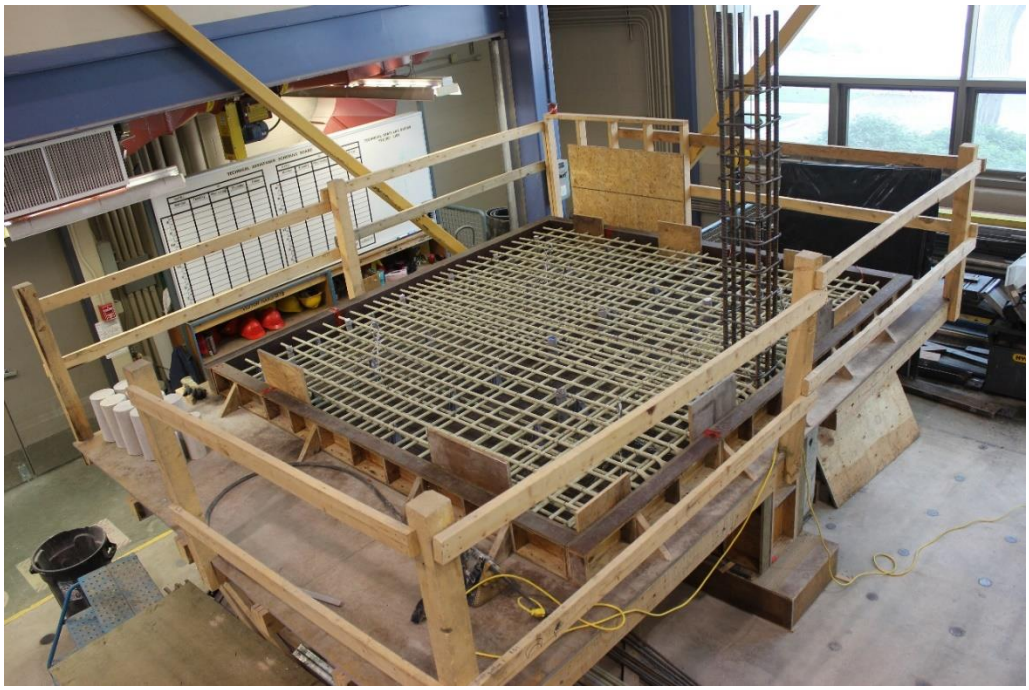

Figure 3.20: Specimen 3 (GFRP-RC with reinforcement ratio of 1.4%) before casting

a) Shear studs' rail assembled

b) A single rail installed

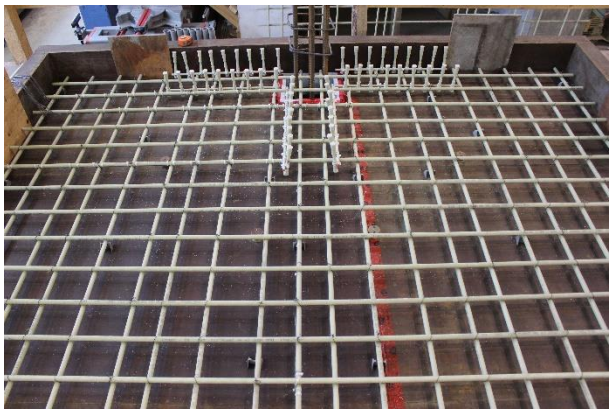

c) All six rails installed

d) All reinforcement assembled

Figure 3.21: Flexural and shear reinforcement assemblies in specimen 6

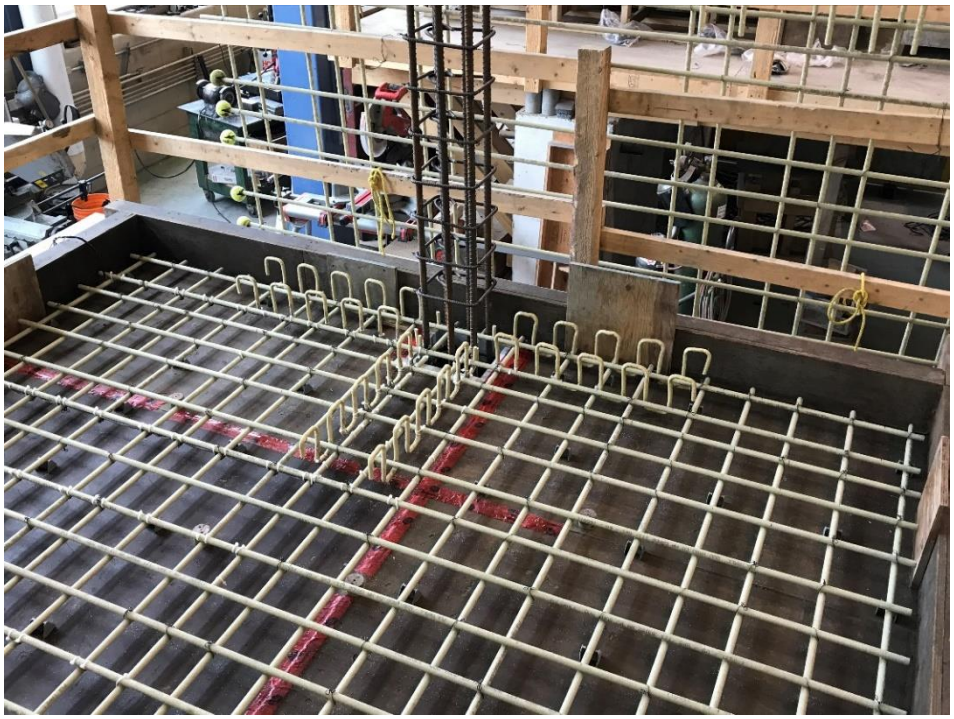

a) Corrugated bars installed

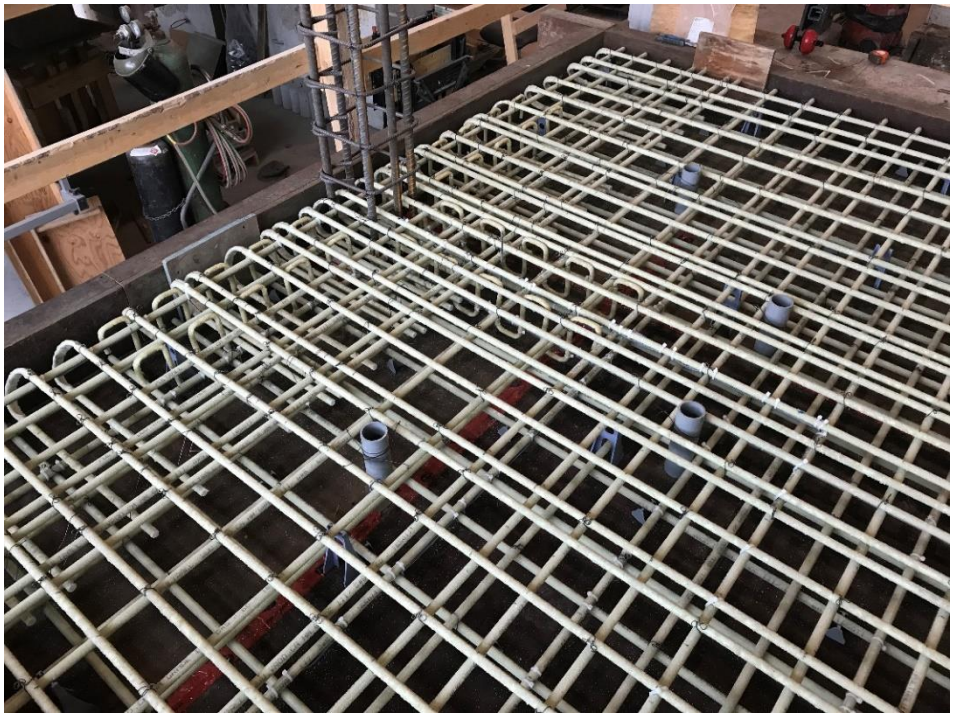

b) All reinforcement installed

Figure 3.22: Flexural and shear reinforcement assemblies in specimen 7

a) Specimen 1 (steel-RC)

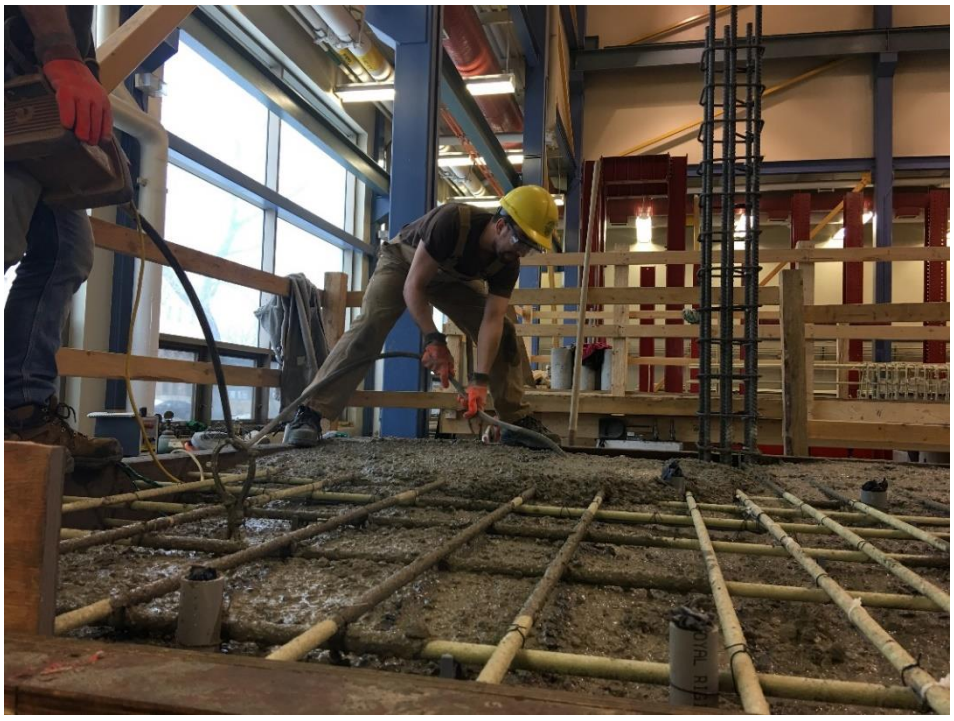

b) Specimen 3 (GFRP-RC)

Figure 3.23: Concrete casting

Figure 3.24: Moving specimen to setup

3.2.3. Instrumentation

In each connection, twelve 6-mm long electrical-resistance strain gauges (ESG) were attached to the top slab flexural reinforcement to measure the strains as shown in Figure 3.25. In addition, in the shear-reinforced specimens, twelve 6-mm long ESGs were attached to the vertical stems of the shear reinforcement at critical locations**.** On the other hand, four load cells were used to monitor gravity loads. Three cells were attached to the hydraulic jacks applying the gravity load to the slab, while the fourth one was installed at the bottom of the column to record the vertical reaction at the support. All instrumentation was connected to a computerized data acquisition (DAQ) system to record the readings during the test.

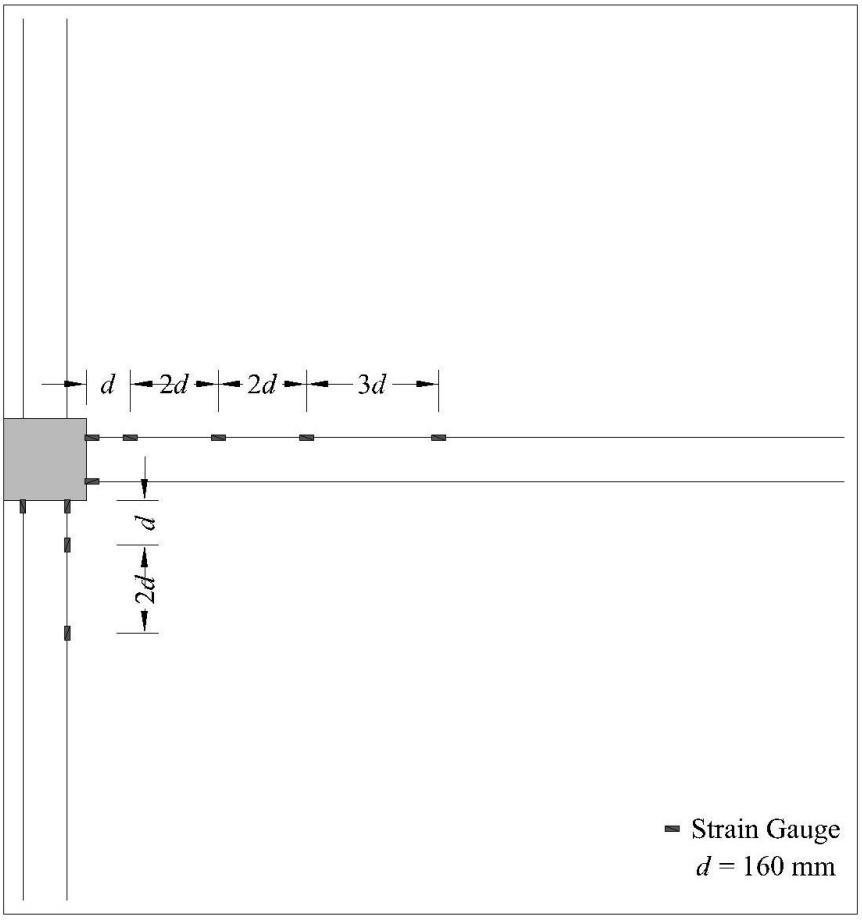

Figure 3.25: Typical strain gauges layout on the flexural reinforcement

3.2.4. Test setup

Figure 3.26 to Figure 3.28 show schematic drawings of the test setup. This setup was designed to test slab-column connections under uniaxial cyclic lateral load with a constant level of gravity load. All connections were supported at the column base and at the slab edge parallel to the free end, while the two slab edges perpendicular to the free edge were left unrestrained. The slab edge parallel to the free edge was clamped by two horizontal 100 × 100 × 6.25 mm hollow structural sections (HSS) from both top and bottom to prevent out-of-plane slab displacement. The clamped edge was supported by a series of roller supports in the form of three vertical 100 × 100 × 6.25 mm HSS link supports. These link supports were pinned at the top to the horizontal HSS at the

soffit of the slab edge and pinned at the bottom to a set of horizontal 100 × 100 × 6.25 mm HSSs, which were fixed to the laboratory's strong floor. The pinned connections were realized by clevis and unthreaded rod assemblies welded to the horizontal HSSs as shown in Figure 3.29. These link supports simulated a roller support at the slab edge; they allowed rotation and horizontal displacement in the perpendicular direction with negligible vertical displacement.

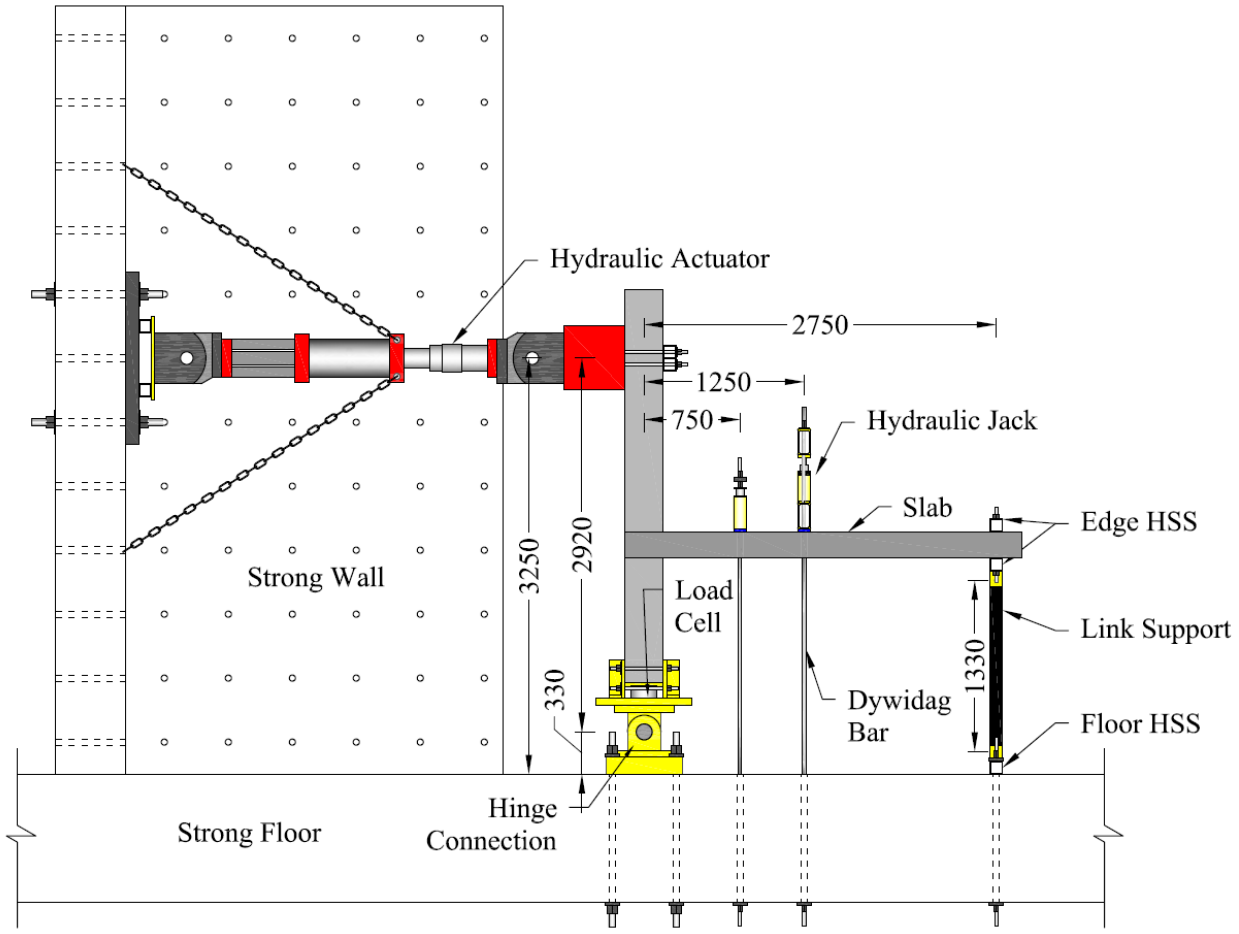

Figure 3.26: Schematic drawing of the test setup – elevation view (dimensions in mm)

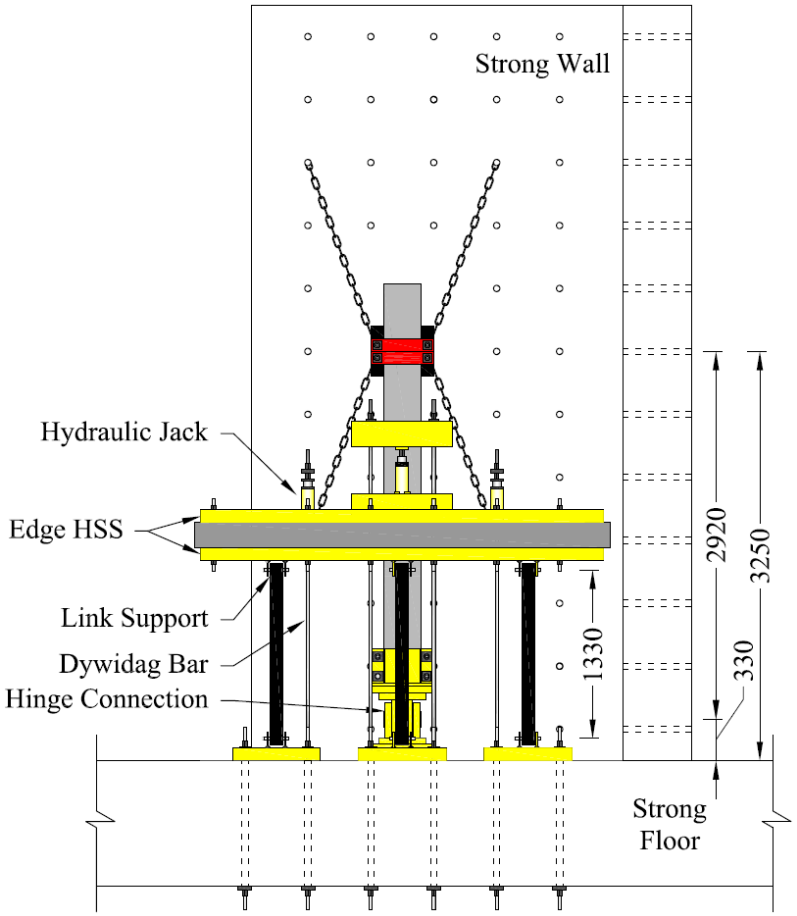

Figure 3.27: Schematic drawing of the test setup – side view (dimensions in mm)

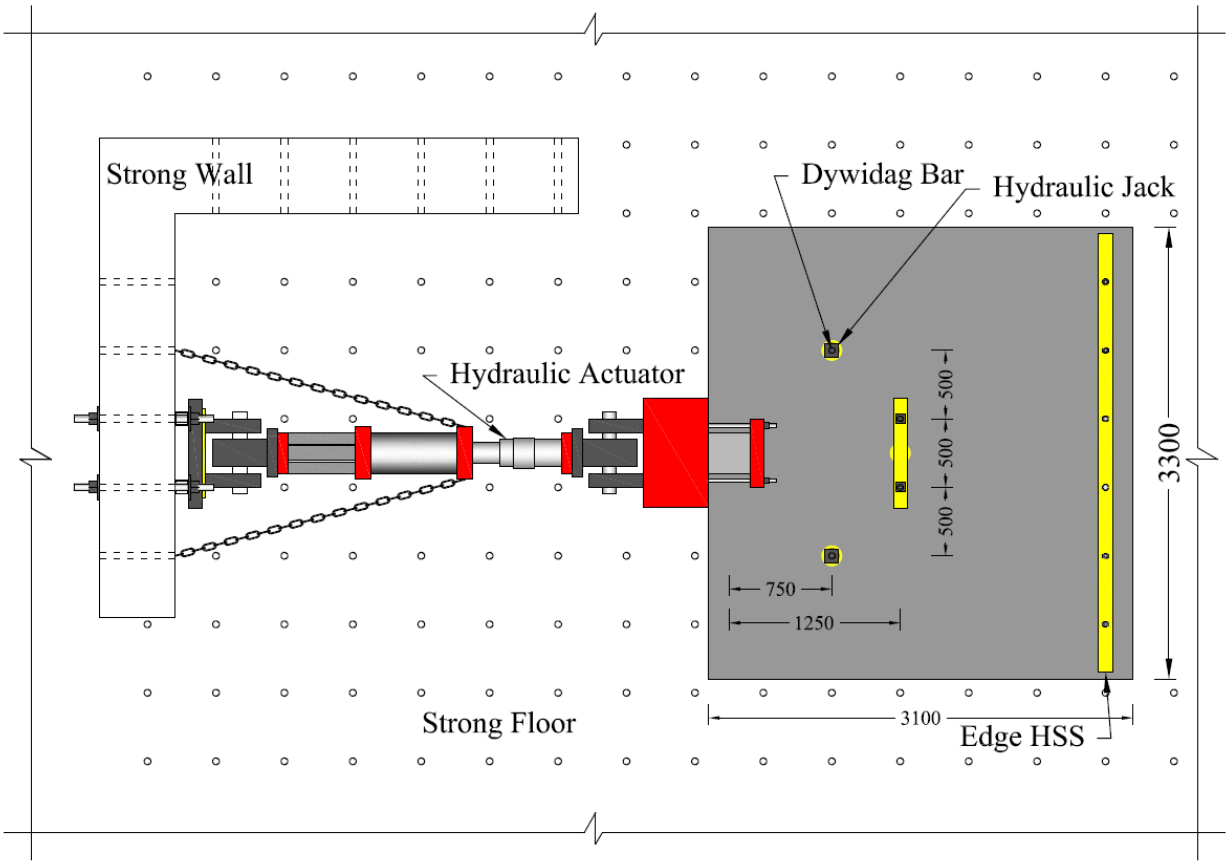

Figure 3.28: Schematic drawing of the test setup – plan view (dimensions in mm)

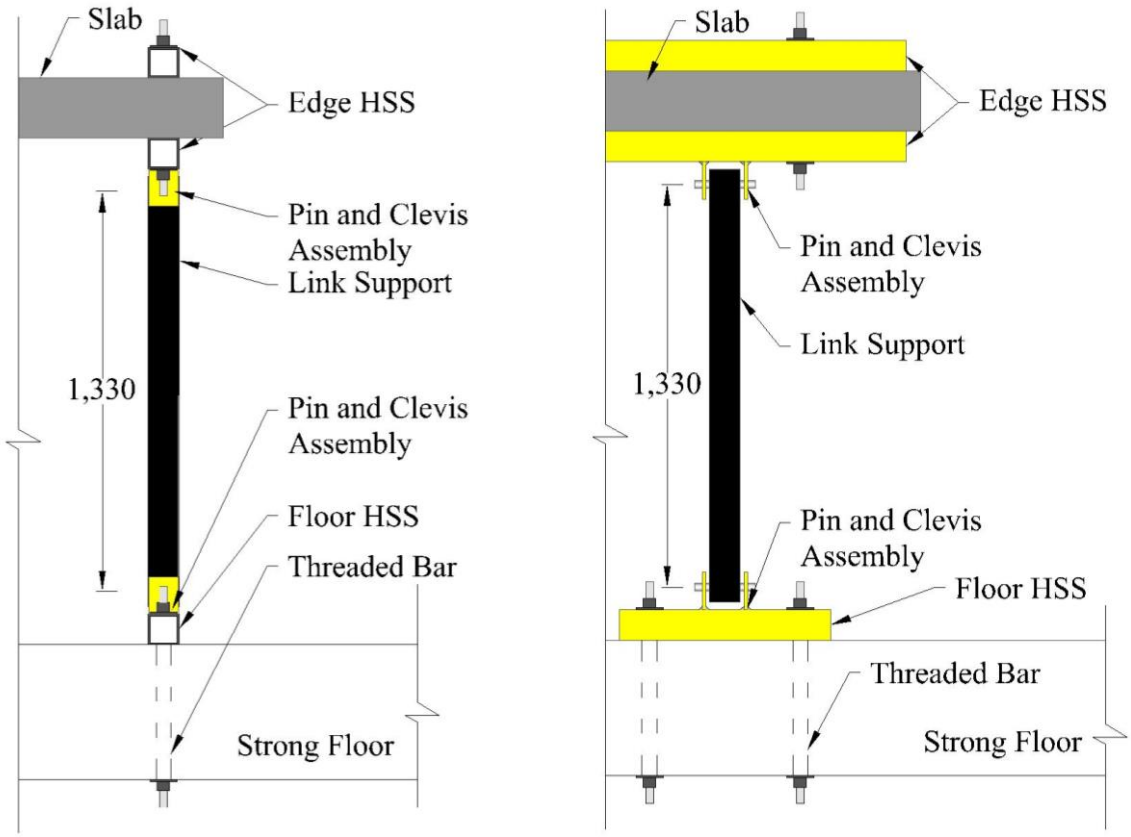

a) Elevation view b) Side view

Figure 3.29: Details of link support (Dimensions in mm)

Zee and Moehle (1984) discussed errors associated with modelling the roller support with links. When the slab displaces horizontally, the links rotate about the floor clevises and, accordingly, a vertical displacement will occur at the slab edge parallel to the free edge as shown in Figure 3.30. This vertical displacement (δ_v) is a function of the imposed drift ratio (assuming rigid links) and the length of the link (l) as shown by Equation 3.1, where δ_h is the horizontal displacement of the link at the slab level. Accordingly, at drift ratios (δ_h/l) as high as 0.03, the ratio δ_v/δ_h is only 0.015, which is small enough that the vertical displacement does not affect the overall behaviour of the connections. At higher drift ratios, the vertical displacement increases in magnitude; however,

since the connections are cracked and behave non-linearly at these high drift ratios, there is no significant effect on the overall behaviour.

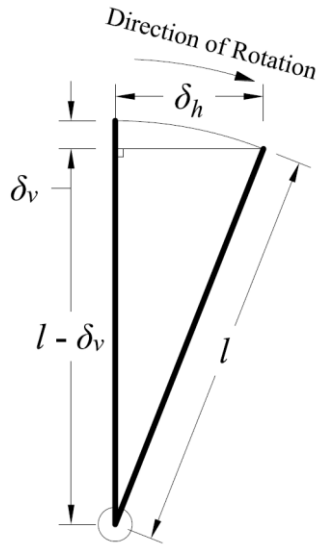

Figure 3.30: Statics of rotated edge link

$$\frac{\delta v}{\delta h} = \frac{1-\sqrt{1-\left(\delta h / \ell\right)^2}}{\left(\delta h / \ell\right)} \qquad \text{Equation 3.1}$$

A steel hinge connection (Figure 3.31) was used at the column base to allow rotation in the perpendicular direction only. A load cell was inserted between the hinge and the column in order to measure the vertical reaction of the column. The hinge connection was prestressed to the laboratory's strong floor in order to transfer its reactions to the strong floor. On the other hand, the top of the column was pinned to a horizontally placed, fully dynamic MTS hydraulic actuator (1,000 kN capacity and 500 mm stroke), which was used to apply the cyclic lateral load. The actuator transferred its horizontal reaction forces to a rigid L-shaped RC reaction wall (3.5 m wide × 6.0 m high per leg) as shown in Figure 3.28. The distance between the axis of lateral load application (the centreline of the actuator) and the axis of rotation of the hinge support was set to

2,920 mm, with the vertical distance between the centreline of the actuator and the centreline of the slab being 1,460 mm. This is the same distance as the vertical distance between the axis of rotation of the bottom hinge support and the centreline of the slab. To keep these two distances the same, the upper column was cast slightly longer to allow for the attachment of the actuator, while the lower column was cast slightly shorter to accommodate the height of the hinge connection.

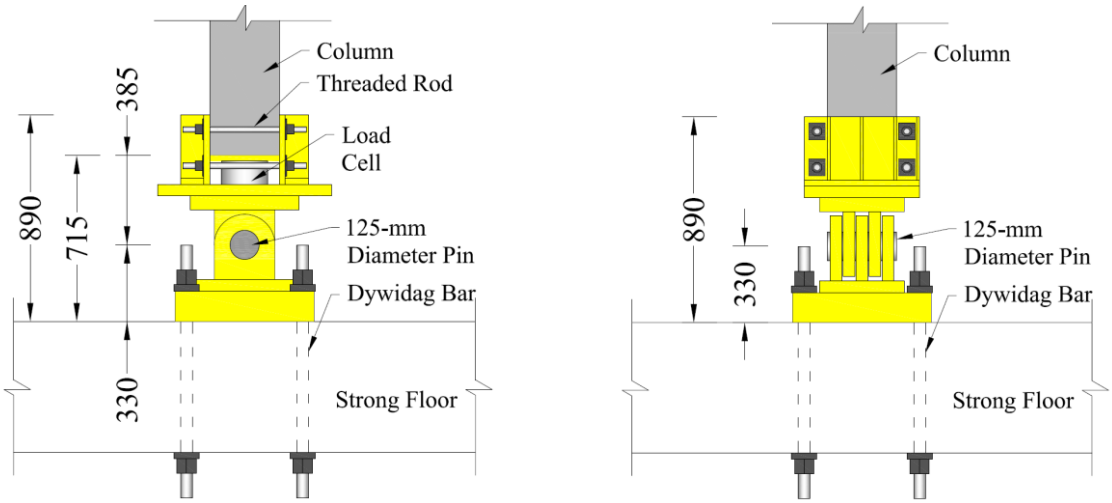

a) Elevation view b) Side view

Figure 3.31: Details of hinge connection (dimensions in mm)

As mentioned earlier, the application of gravity load has always been a challenge in testing isolated slab-column edge connections subjected to lateral cyclic load. In this study, the gravity load was simulated by pulling down the slab at four discrete points. This was carried out through an assembly of three hydraulic jacks and two spreader beams, as shown in Figure 3.32. The assembly was used to tension four threaded steel bars running through pre-made holes in the slab and anchored at the laboratory's floor. One jack and the two spreader beams were used to tension the two middle bars, while each of the other two jacks was used to tension a bar; all jacks were pumped simultaneously. Figure 3.33 to Figure 3.36 show pictures of different elements of the setup.

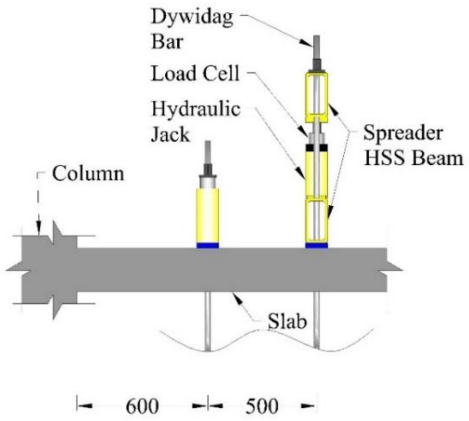

a) Elevation view

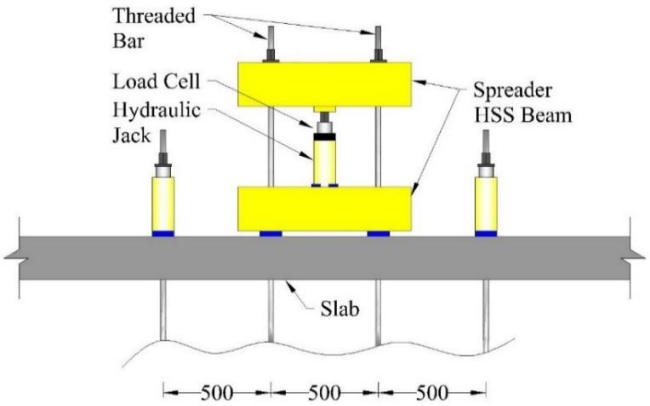

b) Side view

Figure 3.32: Details of gravity load assembly

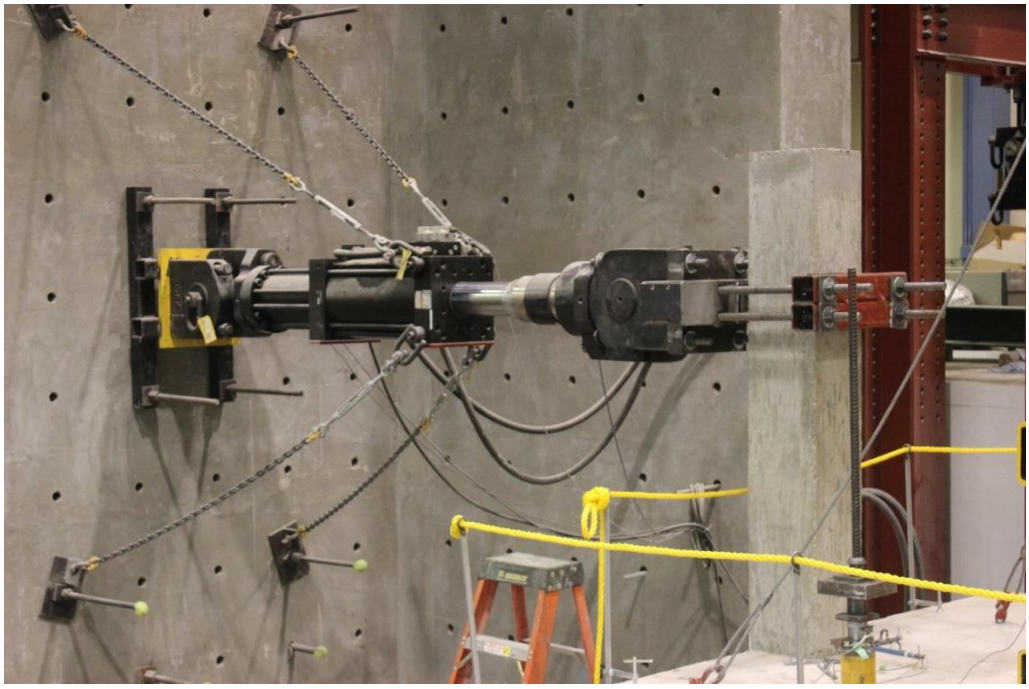

Figure 3.33: Hydraulic actuator connected to column

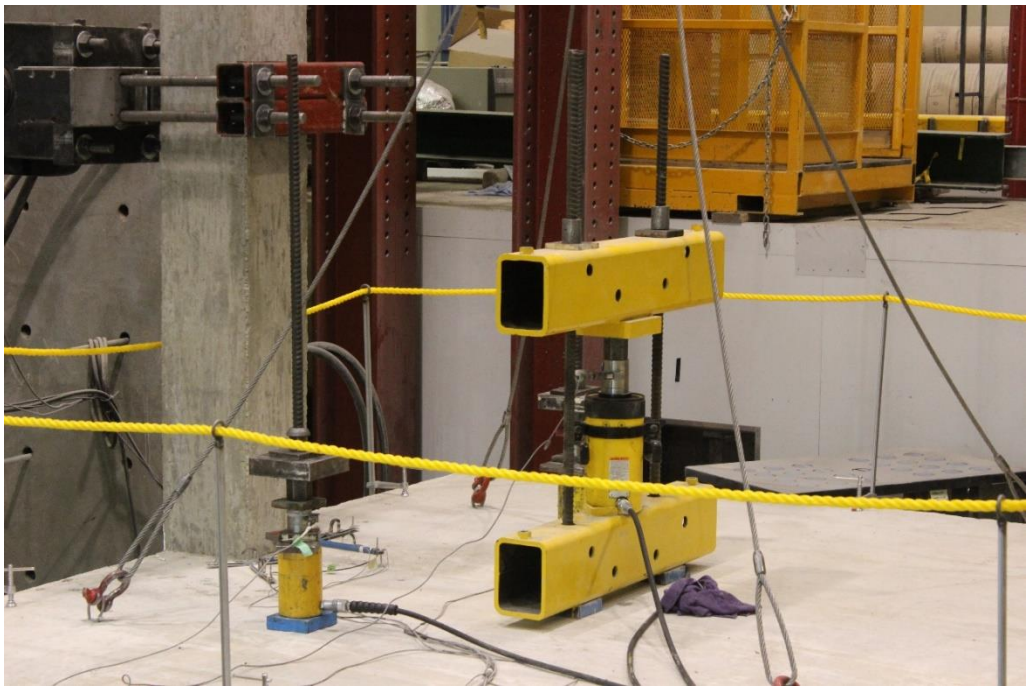

Figure 3.34: Gravity load assembly

a) Elevation

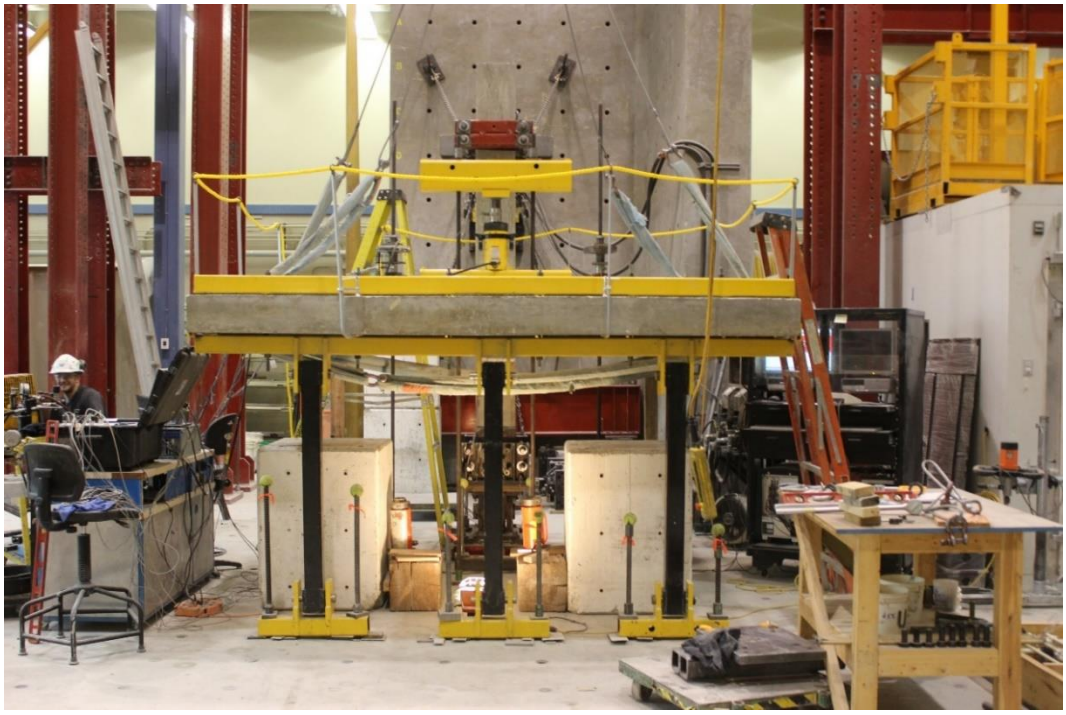

b) Side view

Figure 3.35: Test setup

Figure 3.36: Slab edge link support

3.2.5. Test procedure

The test started by locking the horizontal hydraulic actuator in place while applying the gravity load on the slab using the four hydraulic jacks. This resulted in a vertical reaction at the column hinge support (bottom end) and a lateral reaction at the actuator (top end), with no lateral

displacement of the column. The applied vertical load was distributed between the slab edge support and the column hinge support. Therefore, the vertical reaction at the bottom of the column (hinge support) was monitored until the specified gravity load transferred from the slab to the column was reached. This specified gravity load was a function of the punching shear capacity provided by concrete, V_c, which was obtained based on the concrete strength on the day of testing. Values of the initial gravity load transferred to the column (column vertical reaction) and the lateral reaction at the actuator are listed in Table 3.4. Once the specified gravity load (column reaction) was reached, it was maintained constant throughout the remainder of the test. At this point, the horizontal actuator started to apply the cyclic lateral drifts and the applied gravity load was closely monitored and adjusted during the application of the lateral load, maintaining a constant gravity load throughout the test. Due to the lateral reactions generated in the actuator during the initial application of gravity load, the hysteretic loops do not originate from the zero-load point. Instead, they originate from a point that corresponds to zero drift and the lateral reaction at the actuator listed in Table 3.4.

Table 3.4: Details of gravity load

Connection	Theoretical punching capacity, V_c (kN)	Gravity shear		Lateral reaction (kN)
		Ratio	Initial load, V_g (kN)	
1	498	0.4	199	21.6
2	298	0.4	119	13.1
3	383	0.4	153	14.2
4	378	0.5	189	16.9
5	381	0.6	228	24.6
6	382	0.6	229	29.9
7	362	0.6	217	28.1

The lateral load was simulated by a displacement-controlled uniaxial quasi-static cyclic loading at the top of the column at a rate of 0.01 Hz. The test protocol shown in Figure 3.37 was followed for all specimens. This protocol was adopted from the ACI 374.1-05 report (ACI 2019b) and is expressed in terms of drift ratios. In this loading scheme, the specimen was subjected to increasing predefined drift ratios in several steps. Each step comprised three fully reversed cycles with the same drift ratio in order to ensure stable formation of cracks. All drift ratios were specified so that the ratio between a drift in any step and its predecessor lies between 1.25 and 1.5. The tests stopped when punching failure occurred or when at least 25% of the lateral load capacity was lost. The drift was considered positive when the actuator was pushing the column and negative when it was pulling it.

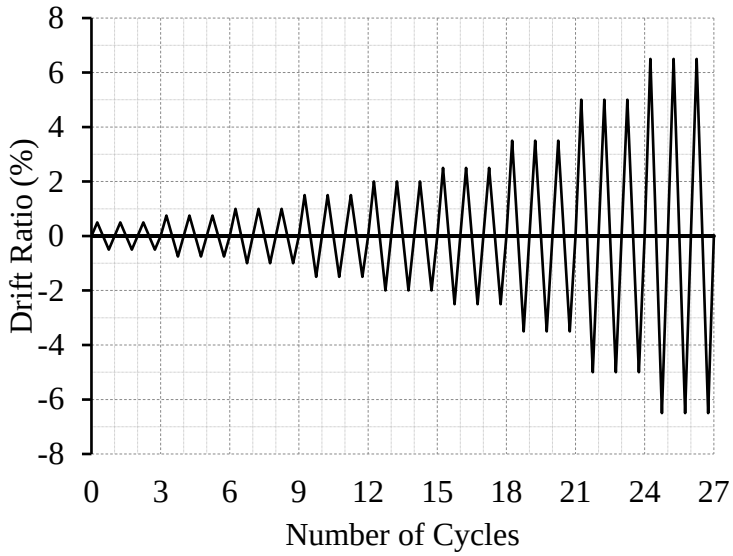

Figure 3.37: Lateral drift scheme

3.3. Analytical Study

3.3.1. Database of experimental research on FRP-RC connections

Data from 66 FRP-RC slab-column connections or two-way slabs without shear reinforcement reported in the literature (including 56 interior and 10 edge specimens) are compiled. Moreover, data from 21 shear-reinforced FRP-RC slab-column connections or two-way slabs from the literature (including 12 interior and 9 edge specimens) are assembled. These 87 specimens, in addition to the six GFRP-RC connections tested in the experimental phase of this study, cover a large spectrum of material and geometrical properties with a wide range of slab dimension (1,000 to 2,800 mm), column size (71 to 450 mm), slab thickness (120 to 350 mm), effective depth of slab (89 to 284 mm), concrete strength (28.9 to 118.0 MPa), average flexural reinforcement ratio (0.19 to 3.76%), average modulus of elasticity of flexural reinforcement (28.4 to 147.6 GPa), moment-to-shear ratio (0 to 0.4 m), type of FRP flexural reinforcement (GFRP bars; CFRP bars and grids; hybrid grids), type of FRP shear reinforcement (GFRP studs, corrugated bars, stirrups and spirals; CFRP stirrups and spirals), and modulus of elasticity of shear reinforcement (44.8 to 130.4 GPa).

3.3.2. Assessment of punching shear models

As mentioned earlier, the available punching shear design models for FRP-RC connections are empirical in nature. They are based on statistical fitting of the test results available at the time they were developed. The bulk of the experimental studies conducted before the development of these models focused on slab specimens subjected to concentric gravity loads only. Furthermore, none of the available models were calibrated against test results of slab-column connections subjected to reversed-cyclic lateral loads.

Therefore, the accuracy of the ten available models (Section 2.9) is assessed against the compiled database. Subsequently, refinement of the models to better predict the punching capacity of different types of connections subjected to different types of load are proposed. A universal model capable of accurately estimating the capacity of different connection types, regardless of the type of load, is proposed.

3.4. Numerical Study

3.4.1. Introduction

A non-linear FEM was constructed to simulate the seismic response of FRP-RC slab-column edge connections using a commercial finite element analysis software package, ATENA-3D, version 5.3.4 (Červenka et al. 2018). The efficiency of this FEM was validated against the experimental results obtained from the experimental phase. Subsequently, the validated FEM was used to conduct a parametric study to investigate the influence of key parameters on the seismic response of FRP-RC slab-column edge connections. The following sections describes the basic characteristics of the constructed FEM.

3.4.2. Finite elements

Three major types of elements are implemented in ATENA-3D: 1) plane elements (for 2D, 3D and axisymmetric analysis); 2) solid 3D elements; and 3) special elements (for modeling external cables, springs and gaps). Plane elements include truss elements, quadrilateral elements, and triangular elements as shown in Figure 3.38. In this study, 2D truss elements with a single node at each end were used to model all types of reinforcement. Solid 3D elements, on the other hand, include tetrahedral elements with 4 to 10 nodes, brick elements with 8 to 20 nodes, and wedge

elements with 6 to 15 nodes as shown in Figure 3.39. In this study, tetrahedral elements were used to model concrete and steel plates.

3.4.3. Concrete modelling

Several constitutive models, besides a user-defined one, are incorporated in ATENA-3D to model the behaviour of different materials. Modeling of concrete requires an advanced and comprehensive constitutive model, especially where extensive damage is expected. The behaviour of concrete is highly nonlinear with a compressive strength that depends on crack width in addition to low tensile strength and shear stiffness. Furthermore, cyclic loading induces opening and closing of cracks and can lead to further degradation of concrete properties.

To provide a comprehensive description of the concrete behaviour, the powerful fracture-plastic constitutive model implemented in ATENA-3D was adopted to model concrete behaviour. It combines constitutive models for the tensile (fracture) and compressive (plastic) behaviour of concrete. The fracture model, which is based on the classical orthotropic smeared crack formulation and crack band model, employs Rankine failure criterion with exponential softening as shown in Figure 3.40. This model implements both fixed and rotated crack orientation and allows for reducing the shear stiffness after cracking. In addition, it considers the effect of tension stiffening, i.e., the contribution of cracked concrete to the tensile stiffness of reinforcing bars when cracks do not fully develop along the section. In ATENA-3D, tension stiffening is accounted for by a tension-stiffening factor that represents the relative limiting value of tensile strength in the tension softening diagram as shown in Figure 3.41. In this study, this factor was set to 0.3 in all specimens, which means that tensile strength of concrete does not drop below 30% of its maximum value after cracking.

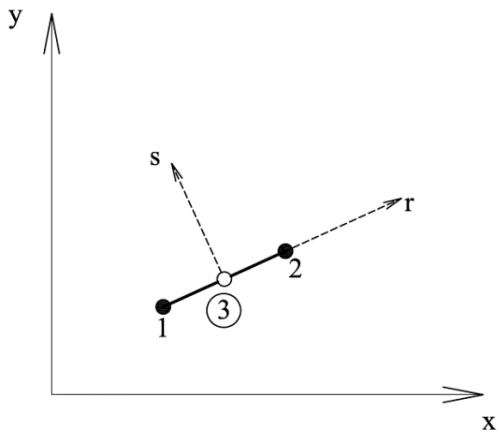

a) Truss element

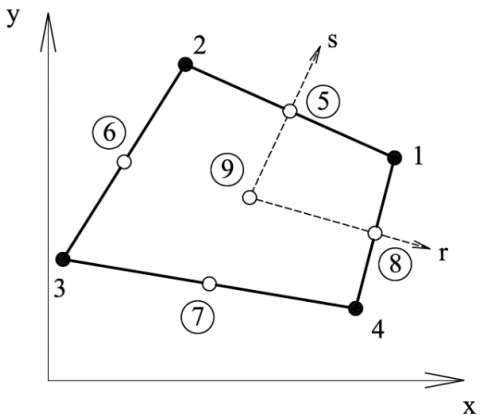

b) Quadrilateral element

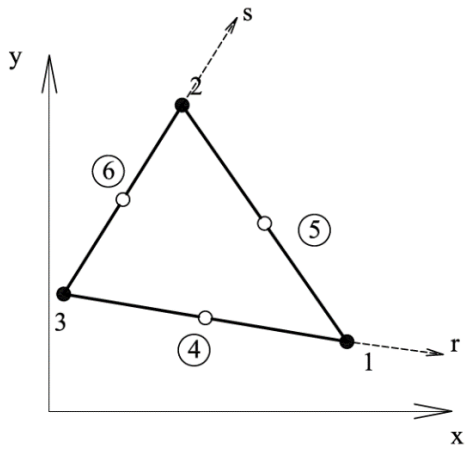

c) Triangular element

Figure 3.38: Geometry of plane elements

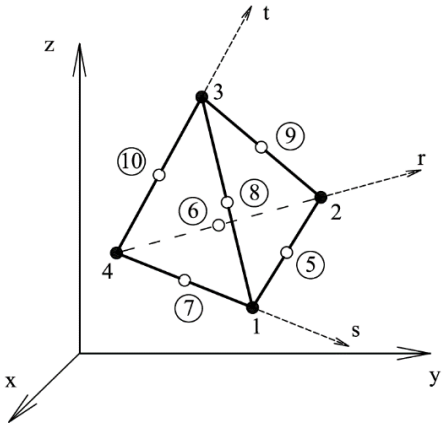

a) Tetrahedral element

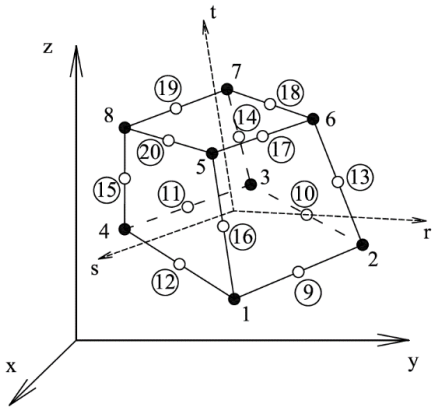

b) Brick element

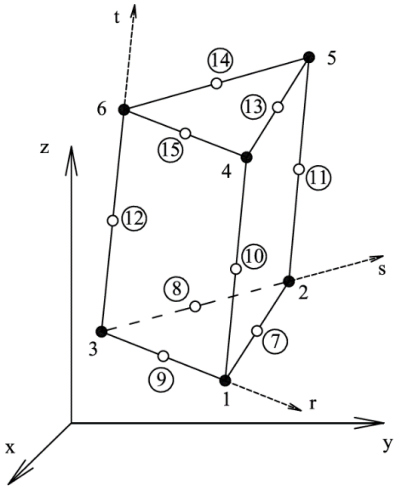

c) Wedge element

Figure 3.39: Solid 3D elements incorporated in ATENA-3D (Červenka et al. 2018)

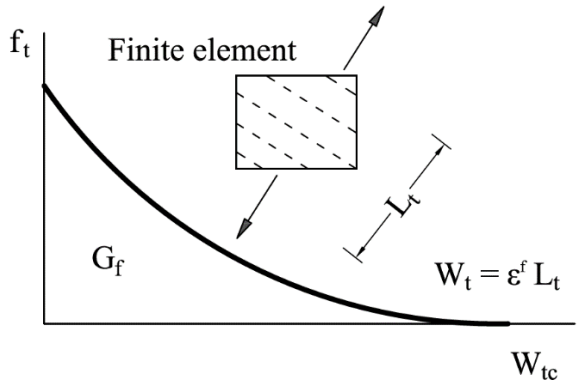

Figure 3.40: Exponential tensile softening

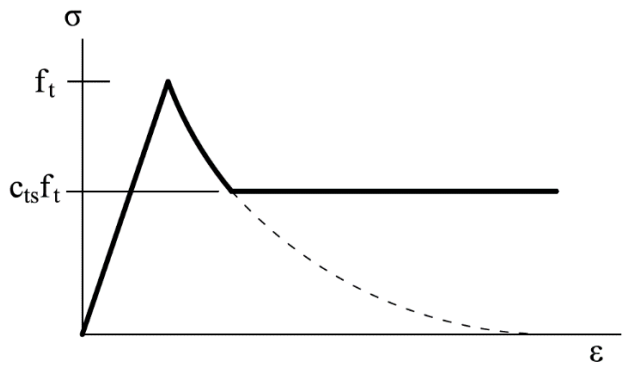

Figure 3.41: Tension stiffening

On the other hand, the plastic model simulates both hardening and softening of concrete under compression based on the Menétrey-Willam failure surface (Menétrey and Willam 1995). As shown in Figure 3.42, this hardening/softening law consists of an elliptical hardening curve and a linear softening one (described in Equation 3.2 to Equation 3.5). In addition, this model allows for reducing concrete compressive strength after cracking as described by Vecchio and Collins (1986). In ATENA-3D, this reduction is accounted for by a factor representing the relative limiting value of compressive strength in the direction of cracks as shown in Figure 3.43. In this study, this factor was set to 0.7 in all specimens, which means that the compressive strength in the direction of cracks may be reduced to a minimum of 70% its maximum value.

$$\sigma = f_{co} + \left(f_c - f_{co}\right)\sqrt{1 - \left[\left(\varepsilon_c - \varepsilon_{eq}^p\right)/\varepsilon_c\right]^2} \qquad \text{Equation 3.2}$$

$$f_{co} = 2 f_t^{'} \qquad \text{Equation 3.3}$$

$$\varepsilon_c^p = f_c^{'}/E \qquad \text{Equation 3.4}$$

$$W_d = \left(\varepsilon_{eq}^{p} - \varepsilon_{c}^{p}\right) L_C \qquad \text{Equation 3.5}$$

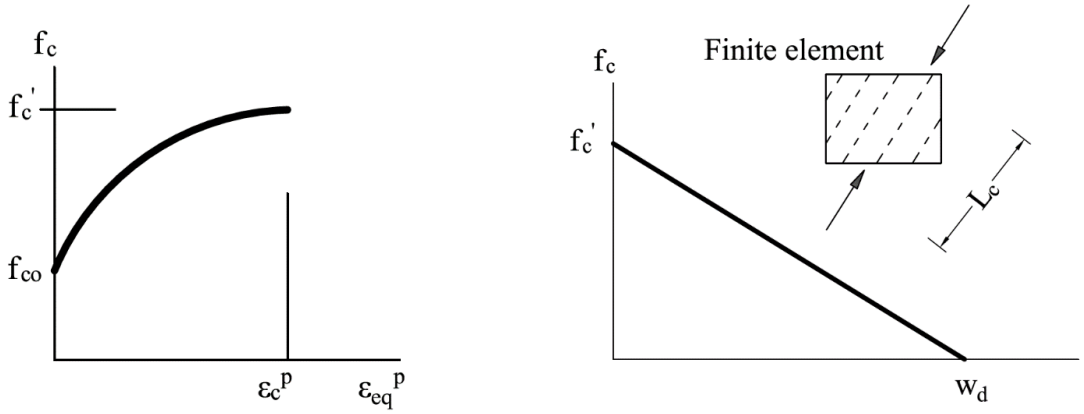

Figure 3.42: Characteristics of plastic model

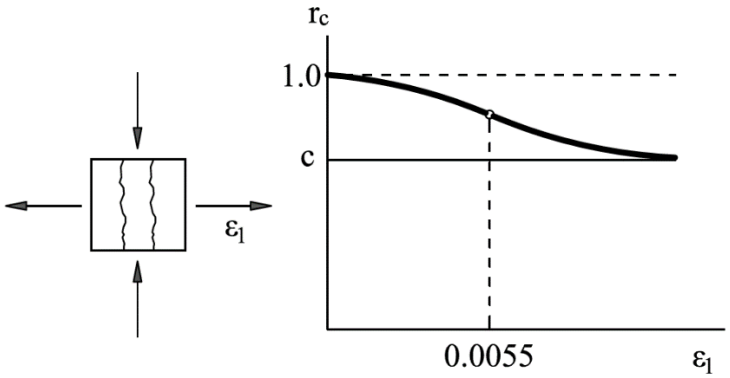

Figure 3.43: Reduction factor for compressive strength of cracked concrete

3.4.4. Reinforcement modelling

In general, different types of reinforcement can be modeled as either smeared or discrete reinforcement. In both forms, the state of uniaxial stress is assumed and the same stress-strain laws can be used. Smeared reinforcement is considered a component of a composite material. In this case, reinforcement is uniformly distributed inside concrete in a layer form with a certain reinforcement ratio and direction angle. On the other hand, discrete reinforcement is modelled as individual truss elements; the exact location, stiffness and area of each bar must be defined. When

the analysis starts, each bar is decomposed into individual truss finite elements embedded into the generated mesh of the concrete macro element. In this study, the discrete reinforcement model was selected to model different types of reinforcement.

Three different reinforcement stress-strain laws are incorporated in ATENA-3D: 1) a bi-linear law, which is an elastic-perfectly plastic relationship suitable for modelling the idealized yielding behaviour of steel reinforcement; 2) a user-defined multi-line law, which is suitable to model the four stages of steel reinforcement behaviour (i.e., elastic state, yielding plateau, hardening, and fracture); and 3) a cyclic reinforcement law, which is suitable for modelling steel reinforcement in RC elements subjected to cyclic loading. The latter model (Menegotto and Pinto 1973), shown in Figure 3.44, was used in this study to model the behaviour of steel reinforcement. The yield strength and modulus of elasticity were taken as 400 MPa and 200 GPa, respectively. On the other hand, a perfectly elastic relationship was adopted for the GFRP reinforcement as shown previously in Figure 2.1. The GFRP reinforcement properties listed in Table 3.1 were used to model GFRP reinforcement.

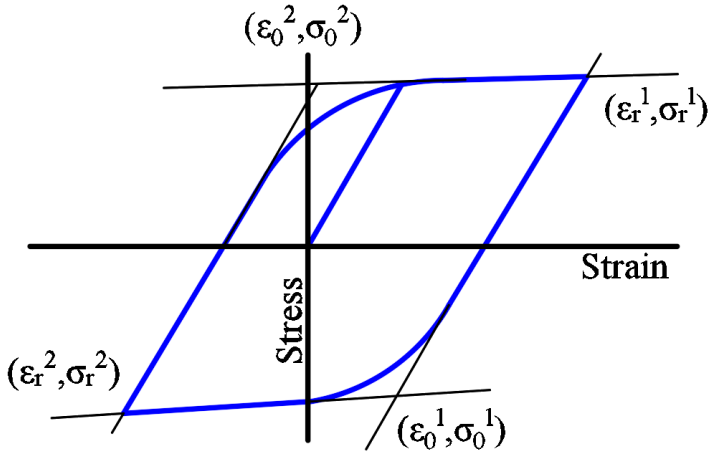

Figure 3.44: Cyclic reinforcement model

3.4.5. Bond modelling

The bond between reinforcement and the surrounding concrete is crucial to ensure integral composite behaviour of RC elements. This is modelled by defining a bond-slip relationship for the used reinforcement. Although a perfect bond between the reinforcement and the surrounding concrete can typically be assumed in finite element modelling, this approach is considered unrealistic since slippage of reinforcement is often inevitable with the development of significant drifts and cracks. In addition to a user-defined model, two built-in models are implemented in ATENA-3D. The first model is the CEB-FIB 1990 model (CEB 1993), which defines the bond-slip relationship as a function of concrete compressive strength, reinforcement type, and confinement condition. The bond-slip relationship of the CEB-FIB 1990 model is given by Equation 3.6 to Equation 3.9 and shown in Figure 3.45. The second built-in model is based on the work by Bigaj (1999). This model depends on the concrete compressive strength, reinforcement bar diameter, and quality of bond between bar and surrounding concrete. This bond-slip relationship is shown schematically in Figure 3.46.

$$\tau_b = \tau_{\max}\left(\frac{s}{s_1}\right)^{\alpha},\ 0 \le s \le s_1 \qquad \text{Equation 3.6}$$

$$\tau_b = \tau_{\max},\ s_1 \le s \le s_2 \qquad \text{Equation 3.7}$$

$$\tau_b = \tau_{\max} - \left(\tau_{\max} - \tau_f\right)\left(\frac{s - s_2}{s_3 - s_2}\right),\ s_2 \le s \le s_3 \qquad \text{Equation 3.8}$$

$$\tau_b = \tau_f,\ s_3 < s \qquad \text{Equation 3.9}$$

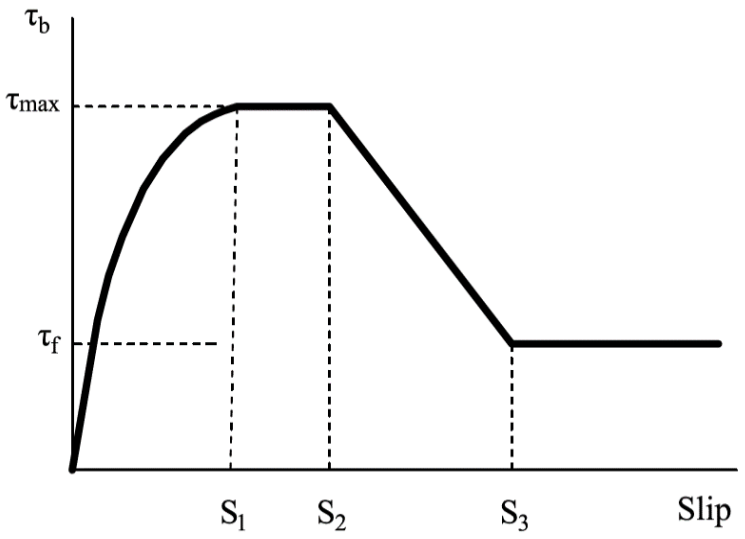

Figure 3.45: CEB-FIB bond-slip model (CEB 1993)

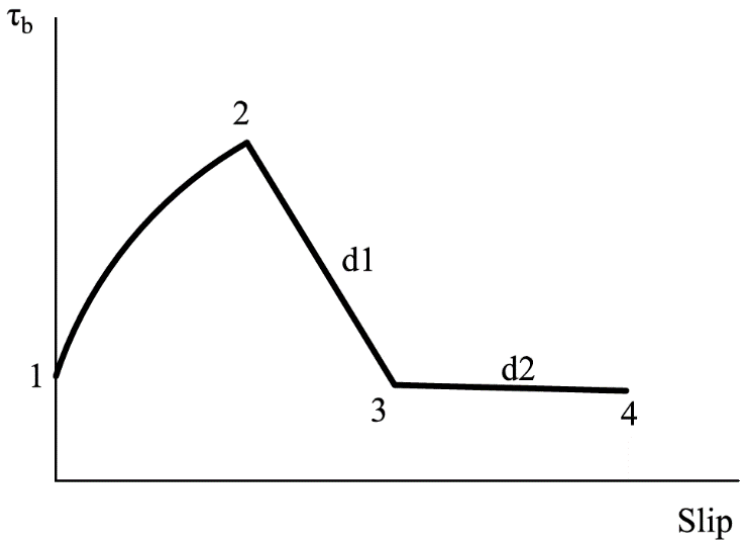

Figure 3.46: Bigaj (1999) bond-slip model

In this study, the CEB-FIB 1990 model was used to model the bond-slip relationship between steel reinforcement and the surrounding concrete. For the used ribbed steel bars embedded in confined concrete with good bond condition, the values listed in Table 3.5 were used to define the bond-slip relationship. Nonetheless, for GFRP reinforcement, a user-defined model based on the work by Alves et al. (2011) was used as shown in Figure 3.47.

Table 3.5: Parameters used to define the bond-slip relationship for steel reinforcement

Parameter	S_1	S_2	S_3	α	τ_{max}	τ_f
Value	1.0 mm	3.0 mm	8.0 mm	0.4	$2.5\sqrt{f_c'}$	0.4 τ_{max}

Note: S_1, S_2, and S_3 = characteristic slip values based on bond condition and concrete confinement; α = coefficient ranging between 0 and 1; τ_{max} = maximum bond strength; τ_f = bond stress at failure.

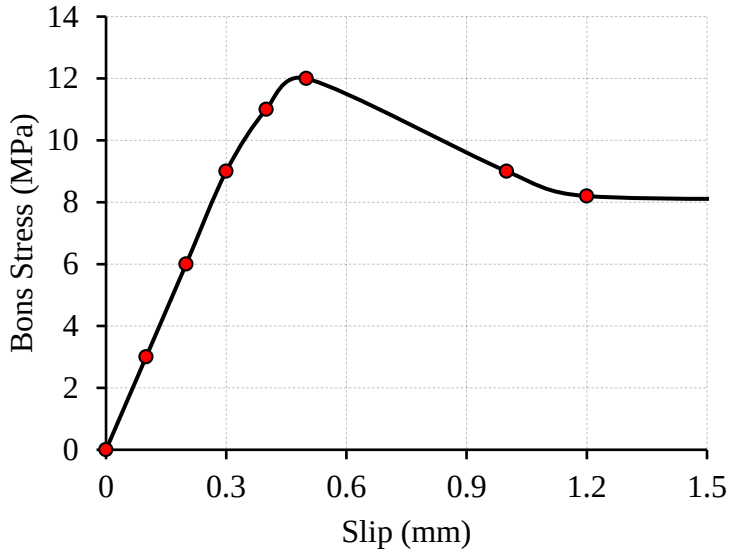

Figure 3.47: Bond-slip model used for GFRP reinforcement (Alves et al. 2011)

3.4.6. Model validation and parametric study

The constructed FEM was validated against the experimental results of the GFRP-RC connections tested in the experimental phase of this study. The four GFRP-RC connections without shear reinforcement were selected for the validation process. The validation process was carried out with respect to failure load, hysteretic response, drift envelope, slab reinforcement strains, and cracking pattern.

The validated model was employed to conduct an extensive parametric study to investigate the effect of several parameters on the seismic response of FRP-RC slab-column edge connections. The tested parameters are the gravity shear ratio, flexural reinforcement type, column aspect ratio, slab thickness, and flexural reinforcement ratio. Figure 3.48 shows a flow chart for the test matrix

used in the parametric study. The designation of the FEMs consist of five parts representing the five parameters. The first part indicates the reinforcement type (G for GFRP, C for CFRP), the second part indicates the flexural reinforcement ratio (e.g., 0.9 for ρ = 0.875%), the third part indicates the applied gravity shear ratio, V_g/V_c (e.g., 20 for V_g/V_c = 0.2), the fourth part indicates the column width perpendicular to the free edge of the slab, C_1 (e.g., 36 for C_1 = 360 mm), and the fifth part indicates the slab thickness (e.g., 20 for thickness of 200 mm).

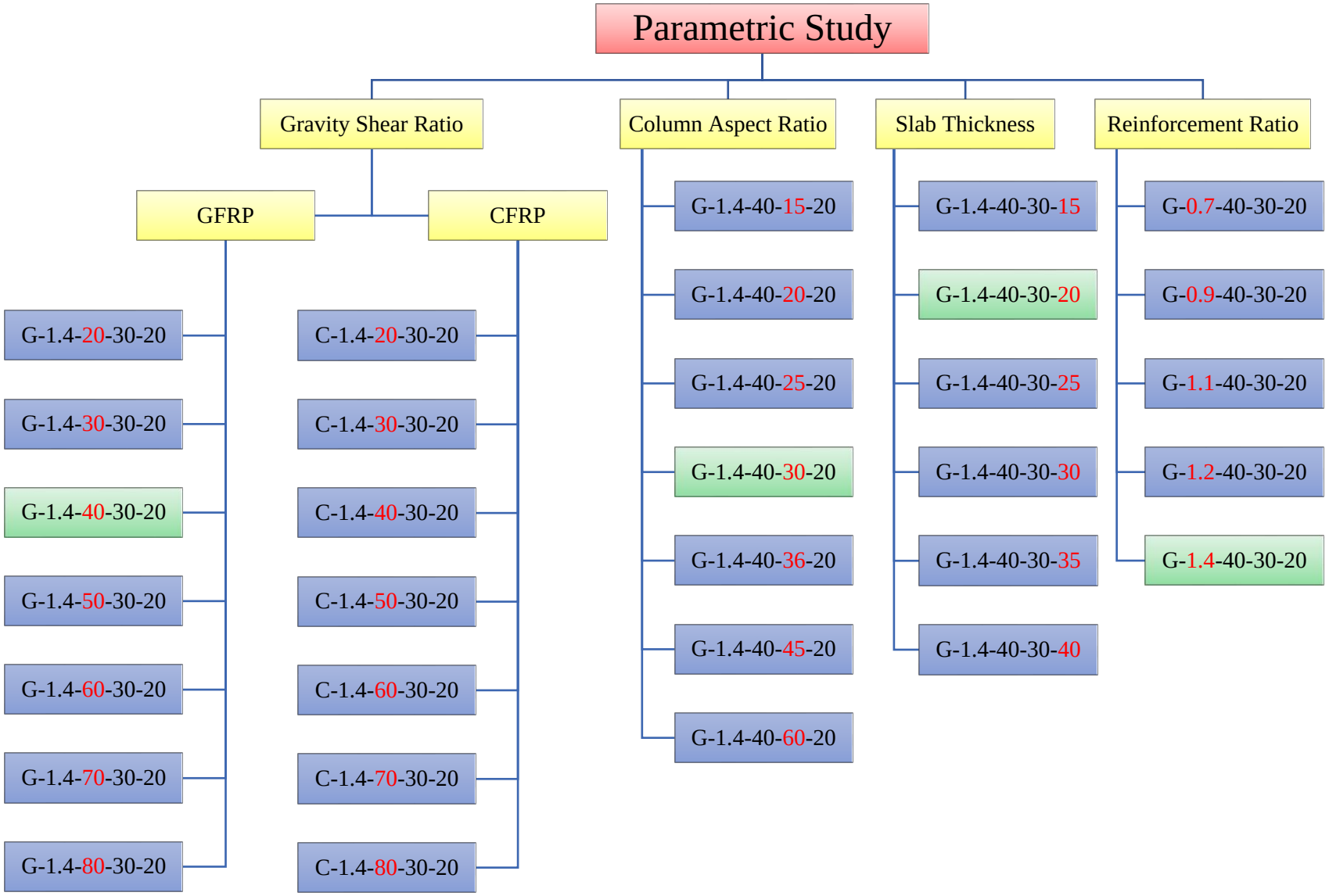

Figure 3.48: Test matrix of the parametric study

CHAPTER 4. EFFECT OF FLEXURAL REINFORCEMENT TYPE AND RATIO ON THE PUNCHING BEHAVIOR OF RC SLAB-COLUMN EDGE CONNECTIONS SUBJECTED TO REVERSED-CYCLIC LATERAL LOADS

Authors and Affiliation:

- Mohammed G. El-Gendy, PhD Candidate, Department of Civil Engineering, University of Manitoba
- Ehab F. El-Salakawy, Professor, Department of Civil Engineering, University of Manitoba

Journal and Status:

Elsevier Journal of Engineering Structures, published on September 26, 2019.

Reference:

El-Gendy, M., and El-Salakawy, E. 2019. "Effect of flexural reinforcement type and ratio on the punching behavior of RC slab-column edge connections subjected to reversed-cyclic lateral loads." *Eng. Struct.*, 200, 109703, https://doi.org/10.1016/j.engstruct.2019.109703.

Note:

The manuscript had been slightly altered from the original paper by renumbering the tables and figures to include the chapter number. In addition, the reference list and list of notations have been moved to the appropriate sections in the thesis as indicated in the table of contents.

Abstract

Three full-scale reinforced-concrete (RC) slab-column edge connections were constructed and tested to failure under a combination of gravity load and uniaxial reversed-cyclic lateral load. The main test parameters were the flexural reinforcement type [steel or glass fiber-reinforced polymer (GFRP)] and flexural reinforcement ratio [0.7 or 1.4%]. The performance of the connections was evaluated in terms of mode of failure, hysteretic response, stiffness, energy dissipation and strains in the reinforcement. It was demonstrated that GFRP-RC connections are able to safely achieve or exceed the minimum 1.50% drift capacity before punching failure with adequate deformability. The low modulus of elasticity and high tensile strength of GFRP bars allowed GFRP-RC connections to experience comparable reinforcement strains to those in the steel-RC counterpart. In addition, the linear nature of GFRP reinforcement resulted in lower stiffness degradation and lower residual damage in GFRP-RC connections compared to the steel-RC connection.

Keywords: Cyclic loading; deformability; drift ratio; flat plate; glass fiber-reinforced polymer (GFRP); punching shear; seismic loading; slab-column edge connection.

4.1. Introduction

Reinforced concrete (RC) flat plate systems are utilized extensively for construction of both low and high-rise buildings. The numerous advantages of flat plate systems include the simple formwork, which results in fast and economical construction; the possible lower storey heights, which reduces the total building height and, in turn, reduces lateral loads; and the possibility to increase number of floors in areas where height restriction applies. The absence of beams, however, results in a flexible system and makes slab-column connections prone to punching shear failure. When subjected to seismic activity, the seismic excitation results in the transfer of excessive shear forces and unbalanced moments at slab-column connections. In addition, the reversed nature of the cyclic load results in the propagation of flexural cracks in the full slab thickness, thus weakening the otherwise undisturbed compression zone and, consequently, reducing the punching shear capacity provided by concrete. In addition, due to the lack of ductility, the connections will not be able to undergo significant lateral drifts prior to punching failure.

Therefore, the Canadian standard CSA A23.3-14 (CSA 2014a) and the American code ACI 318-14 (ACI 2014a) allow the use of steel-RC flat plate systems in regions of high seismic risk as a gravity force resisting system (GFRS) only. In this case, a stiffer structural system, such as shear walls or moment-resistant frames, shall be provided to function as a seismic force resisting system (SFRS). Nevertheless, the presence of the stiffer structural system does not completely eliminate the seismic forces applied to the flat plate system. In addition, as the entire structure drifts, the flat plate system will undergo the same lateral drifts of the SFRS. Therefore, flat plate systems in such structures must be designed for deformation compatibility with the SFRS to ensure they can maintain their gravity load capacity with a minimum level of ductility, which makes the system able to accommodate the seismically induced lateral displacements (ACI 2011).

On the other hand, steel-RC flat plate systems constructed in regions of harsh environmental conditions are vulnerable to corrosion of the steel reinforcement, which results in the deterioration of RC elements and, in turn, requires several rehabilitations during the service life of the structure. The use of the non-corrodible glass fiber-reinforced polymer (GFRP) composites as an alternative to steel reinforcement has been proven as an effective solution to the corrosion problem.

Despite the initial higher material cost associated with GFRP reinforcement compared to conventional steel reinforcement, the savings in construction labor cost and the long-term cost savings due to the anticipated superior durability make GFRP a more cost-effective reinforcement option. Berg et al. (2006) demonstrated that using FRP reinforcement instead of conventional steel resulted in 57% savings in the construction labor cost of an RC bridge deck due to the low weight and prefabricated profile of GFRP reinforcement. Younis et al. (2018) conducted a life cycle cost analysis (LCCA) of three design alternatives using three types of reinforcement, i.e., black steel, stainless steel, and GFRP. It was concluded that using stainless steel and GFRP resulted in approximately 15 and 50% savings based on a 100-year lifetime. However, the differences in the mechanical properties of steel and GFRP reinforcement raise concerns about the feasibility of using the elastic GFRP reinforcement in seismic zones. To date, no research has been conducted on FRP-RC slab-column connections subjected to reversed-cyclic load. The main objective of this paper is to investigate the effect of flexural reinforcement type and ratio on the seismic response of RC slab-column edge connections.

4.2. Literature Review

Several experimental studies were conducted on steel-RC slab-column connections subjected to cyclic loads during the last few decades. In an early investigation by Hawkins et al. (1974), it was

reported that slab-column interior connections subjected to reversed-cyclic lateral loads had 20% lower shear strength than their counterparts subjected to monotonically-increased load. Ghali et al. (1976) investigated the effect of varying the flexural reinforcement ratio on the dynamic response of interior slab-column connections. Although doubling the reinforcement ratio from 0.5 to 1.0% led to a 26% increase in the lateral load capacity, it resulted in substantial reductions of 56 and 50% in the ductility and energy absorption of the connections, respectively. This was considered a warning against implementing high reinforcement ratios in slabs constructed in seismic zones.

Similar results were obtained in a more recent study by Emam et al. (1997), who demonstrated that increasing the flexural reinforcement ratio from 0.5 to 1.0% resulted in a 27% increase in the lateral load capacity and a 53% reduction in the displacement ductility, which was defined as the ratio between the column displacement at failure and at first yielding of slab reinforcement. However, they found that the drift capacity was unaffected with the increase in the reinforcement ratio. Furthermore, to ensure deformation compatibility with the SFRS, Sozen (1980) recommended that a steel-RC flat plate system without shear reinforcement must be able to undergo at least 1.50% drift ratio without punching failure, where the drift ratio is defined as the ratio of the relative lateral displacement of two successive floors to the floor height. This drift ratio could not be sustained if the gravity shear ratio applied to a slab-column connection without shear reinforcement exceeds 0.4, where the gravity shear ratio is the ratio of the gravity shear transferred between the slab and the column to the theoretical punching shear strength provided by concrete (Pan and Moehle 1989; Megally and Ghali 1994; Hueste and Wight 1999).

On the other hand, GFRP bars have a relatively low elastic stiffness compared to steel bars. This results in GFRP-RC slab-column connections subjected to monotonic load having lower punching

shear capacity than their counterparts reinforced with the same reinforcement ratio of steel reinforcement (Ospina et al. 2003; El-Gendy and El-Salakawy 2018a). In addition, due to their elastic nature, GFRP bars do not undergo a yielding plateau prior to their brittle rupture. Normally, yielding of steel reinforcement is relied on as the main source of ductility of RC elements.

Research conducted in the last two decades on GFRP-RC elements, however, showed a promising potential for using GFRP reinforcement as longitudinal and transverse reinforcement in elements subjected to seismic loads. Experimental studies on GFRP-RC short columns (Tavassoli et al. 2015; Ali and El-Salakawy 2016), shear walls (Mohamed et al. 2014; Arafa et al. 2018) and beam-column joints (Hasaballa et al. 2011; Ghomi and El-Salakawy 2016) demonstrated that the unique combination of low modulus of elasticity and high tensile strength of GFRP bars will allow GFRP-RC elements to undergo significantly large lateral drifts without exhibiting brittle failure. It was also reported that, although they dissipated relatively lower energy than their steel-RC counterparts, GFRP-RC elements experienced considerably less permanent damage due to the elastic behavior of the FRP reinforcement; thus, requiring minimum repair work after surviving a seismic event (Hasaballa et al. 2011; Mohamed et al. 2014; Ghomi and El-Salakawy 2016; Arafa et al. 2018).

4.3. Experimental Program

4.3.1. Design of the prototype structure

Two elastic analyses of a typical parking garage building consisting of five 5.5-m long bays in both directions and a 3.0 m storey height were performed to obtain the flexural reinforcement ratios of the test specimens. As shown in Figure 4.1, the building consisted of flat plate floors supported on 300-mm square columns, while two I-shaped shear walls represented the SFRS. The slabs of

the building were reinforced with steel bars in one analysis and GFRP bars in the other. As per the National Building Code of Canada (NRCC 2015), a specified gravity load of 8.2 kN/m^2, which includes a specified dead load of 5.8 kN/m^2 (i.e., self-weight and 1.0 kN/m^2 partition allowance) and a specified live load of 2.4 kN/m^2, was applied to the flat plate system.

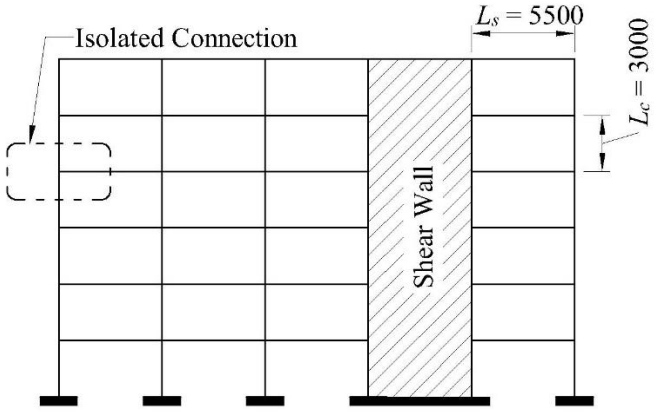

a) Prototype structure

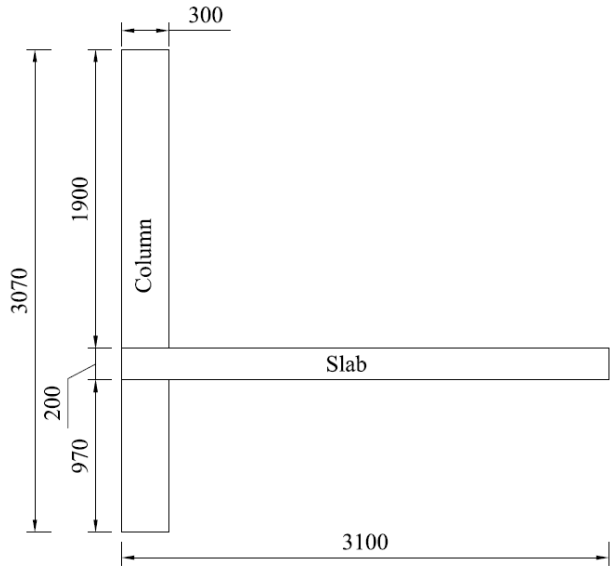

b) Specimen elevation view

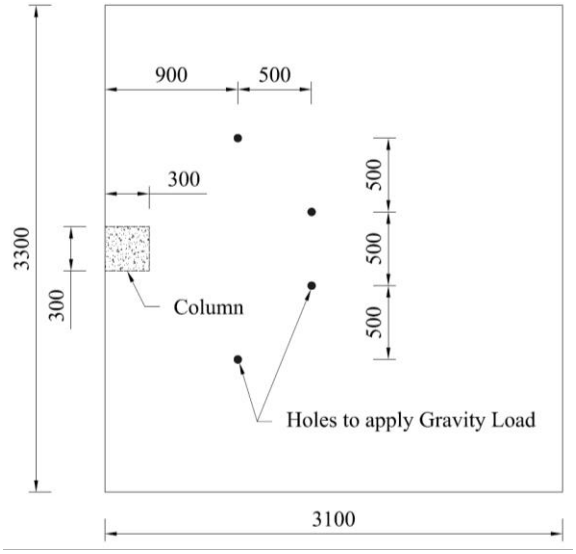

c) Specimen plan view

Figure 4.1: Prototype structure and test specimens (dimensions in mm)

The analyses, carried out according to CSA A23.3-14 (CSA 2014a) and CSA S806-12 (CSA 2017), where applicable, resulted in a 200-mm thick slab reinforced with negative (top) and positive (bottom) flexural reinforcement assemblies (average slab depth, *d*, of 160 mm). For the GFRP-RC system, the resulting reinforcement ratio of the top assembly in the column strip perpendicular to the free edge (in the perpendicular direction) was 1.40%, which is approximately twice that of the steel-RC system (0.66%) although both systems were subjected to the same specified loads. This is attributed to the significantly lower modulus of elasticity of the GFRP bars compared to that of the steel bars; thus, a higher GFRP reinforcement ratio was required to satisfy the serviceability requirements.

4.3.2. Isolated test specimens

Three isolated, full-scale, slab-column edge connections were constructed and tested to failure under a combination of a gravity load and a uniaxial reversed-cyclic lateral load. As shown in Figure 4.1, the specimens represent a typical edge connection in the prototype flat plate parking garage building designed previously. The isolated connections were bounded by the contra-flexure lines. When a flat plate system is subjected to gravity load only, these lines are assumed between 0.1 L_s and 0.3 L_s in the slab, where L_s is the center-to-center spacing between columns. On the other hand, when a system is subjected to gravity and lateral loads, contra-flexure lines are assumed at 0.5 L_s (Pan and Moehle 1989; Robertson et al. 2002). For the test specimens, since the lateral load is applied in the perpendicular direction only, the contra-flexure lines were assumed at mid-heights of the columns and at distances of 0.30 L_s and 0.50 L_s from the centerlines of edge columns in the parallel direction and the perpendicular direction, respectively. Accordingly, the isolated connections had slab dimensions of 3,300 × 2,900 mm with a square edge column extending 1,400 mm above and below the slab surfaces. However, 3,300 × 3,100 mm slabs were cast to allow for

support clearance. Similarly, both the upper and lower columns had a nominal height of 1,360 mm such that the distance between the centerline of the slab and the tip of each column is 1,460 mm, i.e., approximately half the storey height. However, to permit the attachment of the column support and the hydraulic actuator, the upper and lower column heights were changed to 1,900 and 970 mm, respectively, as will be discussed later.

The slabs were reinforced with deformed steel bars in one connection (ES-0.7) and with sand-coated GFRP bars in two connections (EG-0.7 and EG-1.4). The 0.7 and 1.4% reinforcement ratios resulting from the elastic analyses of the steel- and GFRP-RC systems were utilized in connections ES-0.7 and EG-1.4, respectively. To be able to study the effect of flexural reinforcement type and ratio, the 1.4% GFRP reinforcement ratio resulting from the elastic analysis was divided by two and employed in connection EG-0.7. The reinforcement configurations of the test specimens are shown in Figure 4.2.

4.3.3. Materials

All test specimens were constructed using normal-weight, ready-mix concrete provided by a local supplier with a target 28-day compressive strength of 40 MPa. The actual concrete compressive strength was determined by testing standard 100 × 200 mm cylinders on the day of testing according to CSA A23.1-14/A23.2-14 (CSA 2014b) as listed in Table 4.1. The connections and the cylinders were cast in the laboratory and wet-cured for 7 days.

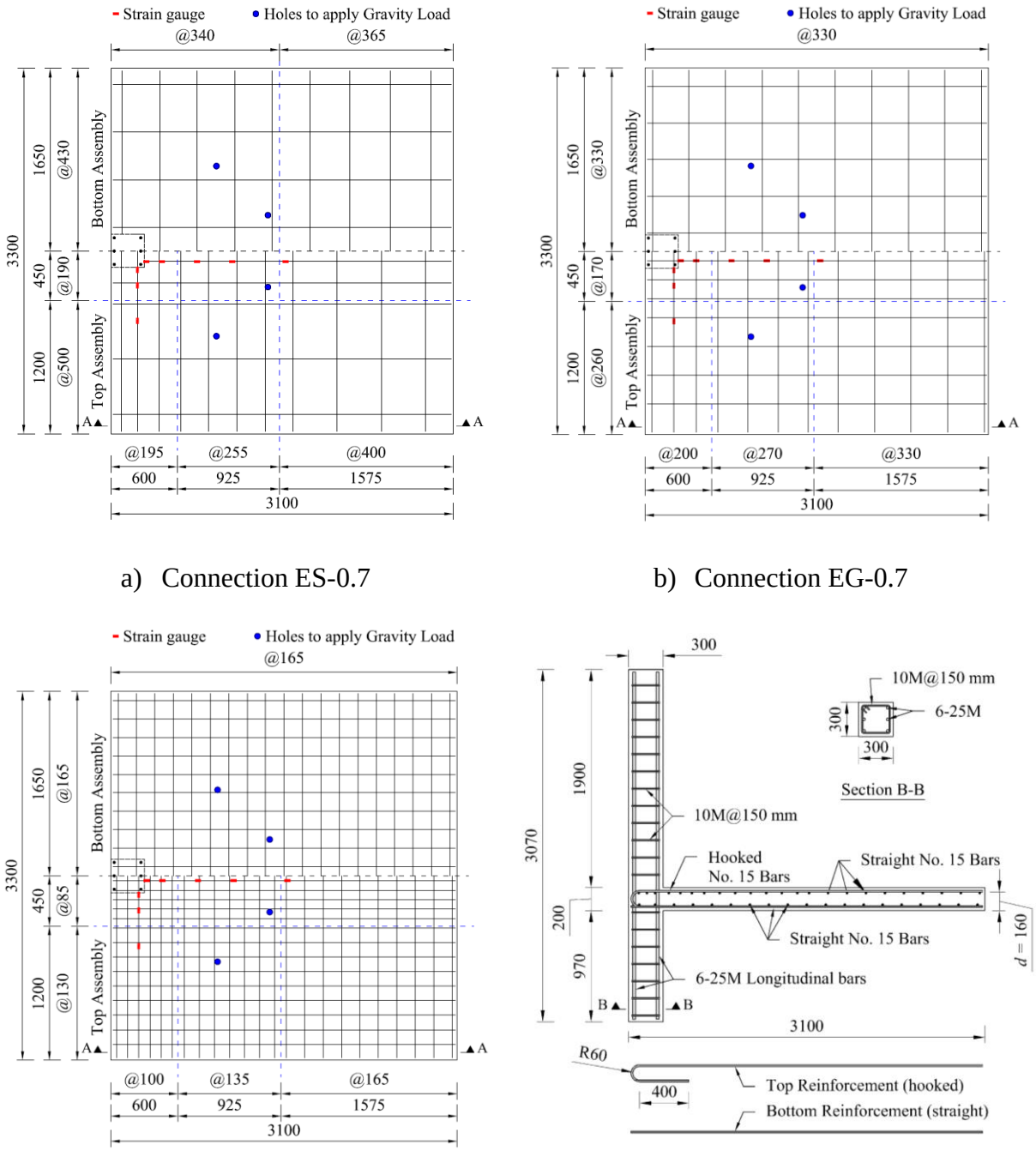

a) Connection ES-0.7

b) Connection EG-0.7

c) Connection EG-1.4

d) Section A-A and reinforcement details

Figure 4.2: Reinforcement configuration (dimensions in mm)

Table 4.1: Details of test connections

Connection	Reinforcement			f_c'	V_g/V_c	V_c	V_g
	Type	Ratio, ρ (%)	Effective ratio (%)				
ES-0.7	steel	0.7	0.7	45	0.4	498[a]	199
EG-0.7	GFRP	0.7	0.2	46	0.4	298[b]	119
EG-1.4	GFRP	1.4	0.4	49	0.4	383[b]	153

Note: f_c' = concrete compressive strength; V_g = gravity shear force transferred between the slab and the column; V_c = punching shear strength provided by concrete. All columns are 300-mm square columns.

[a] According to CSA A23.3-14 (CSA 2014a)
[b] According to CSA S806-12 (CSA 2017)

Two types of reinforcing bars were used as longitudinal reinforcement for the slabs: size No. 15M deformed steel bars for connection ES-0.7 and size No. 15 sand-coated GFRP bars for connections EG-0.7 and EG-1.4. For all specimens, hooked bars were used in the perpendicular direction of the top assembly to provide the required anchorage, while straight bars were used elsewhere as shown in Figure 4.2. On the other hand, the columns were adequately reinforced with 6-25M steel bars and No. 10M steel stirrups. Since columns are expected to remain uncracked during testing, the effect of the column reinforcement on the behavior of the connections is believed to be minimal and can be reasonably ignored. The mechanical properties of the used steel and GFRP bars were obtained from standard tests carried out according to ASTM A370-17 (ASTM 2017), ASTM D7205-06 (ASTM 2016), and ASTM D7914-14 (ASTM 2014), as applicable. The properties of the used slab reinforcement are listed in Table 4.2.

Table 4.2: Mechanical properties of the slab reinforcement

Bar Type	Bar size	Nominal diameter (mm)	Area (mm^2)	Tensile strength (MPa)	Modulus of elasticity (GPa)	Ultimate strain (%)
Steel	No. 15M	15.9	199	400[a]	200	0.2[a]
Straight GFRP	No. 15	15.9	199[b]	1,712[c]	66	2.6
Hooked GFRP (straight portion)	No. 15	15.9	199[b]	1,405[c]	52	2.7
Hooked GFRP (bent portion)	No. 15	15.9	199[b]	725	-	-

[a] Yield stress/strain for steel reinforcement
[b] Nominal area according to CSA S807-10 (CSA 2015)
[c] Calculated using nominal area

4.3.4. Test setup and instrumentation

Figure 4.3 shows a schematic drawing of the test setup. The setup was designed such that a test connection is pinned at top and bottom of the column (i.e. approximately storey mid-heights), while the slab has a roller support along the edge parallel to the free edge. The supported slab edge was stiffened by two horizontal 100 × 100 × 6.25 mm hollow structural sections (HSS) at the top and bottom of the slab to prevent out-of-plane displacement. The stiffened edge was then supported by three vertical 100 × 100 × 6.25 mm pin-ended HSS link assemblies to simulate a roller support. These vertical links were pinned at the top to the horizontal HSS at the soffit of the slab edge and pinned at the bottom to a set of horizontal 100 × 100 × 6.25 mm HSSs, which were prestressed to the laboratory's floor. This way the links provide negligible resistance to the horizontal translation, prevent the vertical translation and allow rotation in the direction of the lateral load application.

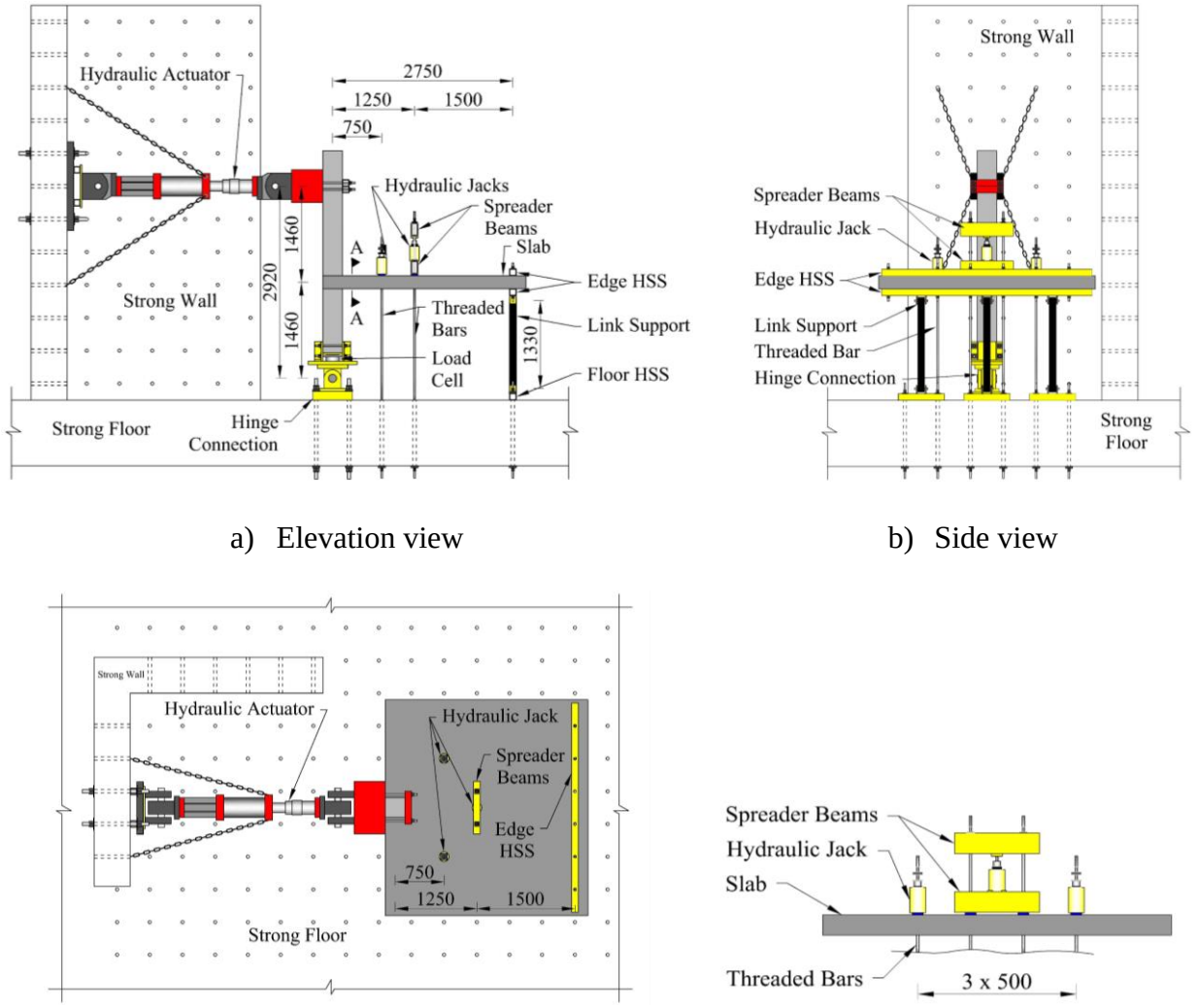

a) Elevation view

b) Side view

c) Plan view

d) Gravity load assembly (Section A-A)

Figure 4.3: Schematic drawing of the test setup (dimensions in mm)

The idealized pinned support at the bottom of the lower column was modeled by a pin and clevis assembly, which was prestressed to the laboratory's floor. This steel hinge support restricted the vertical and horizontal translations of the column base, while allowing rotation in the direction of the lateral load application only. The top of the upper column was pinned to a horizontally-placed fully-dynamic MTS hydraulic actuator with load and stroke capacities of 1,000 kN and 500 mm,

respectively. This actuator was used to apply and monitor the reversed-cyclic lateral load/drift and transferred its horizontal reaction forces to a rigid L-shaped RC reaction wall (3.5-m wide × 6.0-m high per leg). The vertical distance between the axis of lateral load application (point of contra-flexure of the upper column) and the centerline of the slab was 1,460 mm, which is the same as the vertical distance between the axis of rotation of the bottom hinge support (point of contra-flexure of the lower column) and the centerline of the slab, as shown in Figure 4.3. Therefore, the unbalanced moment transferred between the slab and the upper column is the same as that transferred between the slab and the lower column. In order to keep these two distances the same, the upper column was cast slightly longer to allow for the attachment of the actuator head while the lower column was cast slightly shorter to accommodate the height of the hinge connection.

On the other hand, the application of gravity load has always been a challenge in testing isolated slab-column edge connections under cyclic load. One of the commonly accepted practices in structural testing of slab-column connections since the 1960s is simulating the distributed gravity load on the slab by discrete point loads (Corley and Hawkins 1968; Ospina et al. 2003; Cheng et al. 2010; Giduquio et al. 2019). In this study, the gravity load was simulated by pulling down the slab at four discrete points. This was achieved through an assembly of three hydraulic jacks and two spreader beams, as shown in Figure 4.3. The assembly was used to tension four threaded steel bars running through pre-made holes in the slab and anchored at the laboratory's floor. One jack and the two spreader beams were used to tension the two middle bars, while each of the other two jacks was used to tension a single bar; the three jacks were pumped simultaneously. The location of the gravity load application points was determined by a finite element analysis using ATENA 3D software package (Červenka et al. 2018) to produce a moment-to-shear ratio similar to that resulting from a uniform distributed load.

Several 6-mm long electrical-resistance strain gauges (ESG) were attached to the top reinforcement assemblies in the slabs of the connections to measure flexural reinforcement strains as shown in Figure 4.2. On the other hand, four load cells were used to monitor gravity loads. Three cells were attached to the hydraulic jacks applying the gravity load, while the fourth one was installed at the bottom of the lower column to record the vertical reaction at the hinge support.

4.3.5. Loading procedure

All connections were tested under uniaxial reversed-cyclic lateral load with a constant level of gravity load. The test commenced by applying the gravity load, while the movement of the horizontal actuator was locked to prevent lateral displacement of the connection during the application of gravity load. The 0.4 maximum gravity shear ratio recommended in the literature for steel-RC connections without shear reinforcement was used in all connections. Consequently, the specified gravity load for each connection, V_g, was calculated using the concrete compressive strength on the day of testing as listed in Table 4.1. Once the specified gravity load was reached, the load in the jacks was kept constant during the remainder of the test, while the horizontal actuator started to apply the cyclic lateral load. The applied gravity load was closely monitored and adjusted during the application of the lateral load to keep a constant gravity shear ratio throughout the test.

The lateral load was simulated by a displacement-controlled uniaxial quasi-static reversed-cyclic loading at the top of the upper column at a rate of 0.01 Hz following the scheme shown in Figure 4.4, which is adopted from ACI 374.1-05 (ACI 2014b). In this scheme, the connections were subjected to increasing predetermined drift ratios in several steps, where each step comprised three fully-reversed cycles with the same drift ratio to ensure stable formation of cracks. All drift ratios

were determined such that the ratio of each one to its predecessor lies between 1.25 and 1.5. Eventually, the tests were stopped when punching failure occurs or when at least 25% of the lateral load capacity is lost.

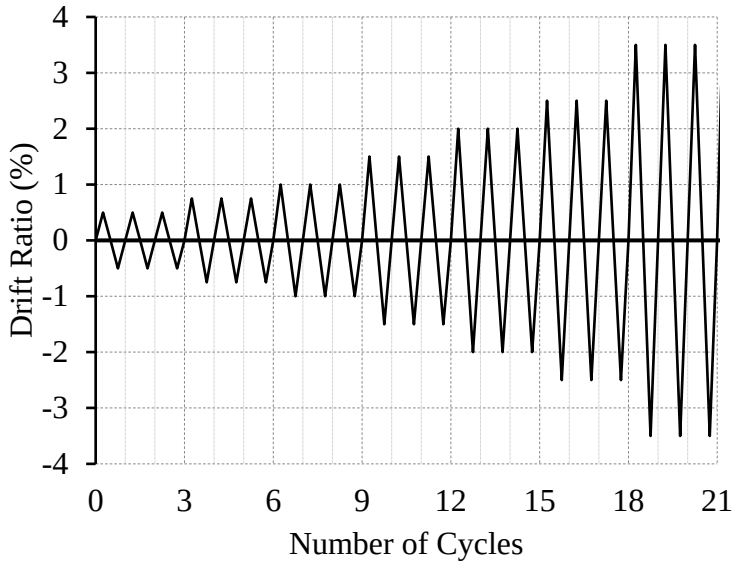

Figure 4.4: Lateral displacement history

4.4. Experimental Results and Discussion

4.4.1. Mode of failure and cracking pattern

To consider the low stiffness of GFRP reinforcement, the effective reinforcement ratio is calculated as the product of the actual reinforcement ratio, ρ, and the ratio between the modulus of elasticity of the used GFRP reinforcement and steel, E_{GFRP}/E_s. Regardless of the reinforcement type and ratio, all connections failed in a brittle punching shear mode with no signs of flexural failure, e.g., concrete crushing at the compression face of the slab. However, the degree of failure brittleness was different for each specimen. Specimen EG-0.7, with 0.7% GFRP reinforcement ratio and the lowest effective reinforcement ratio of 0.2%, experienced the most brittle failure at 2.50% drift ratio with minimal warning.

As can been seen in Figure 4.5, no significant concrete spalling or wide cracks were observed in connection EG-0.7 before the sudden failure at 2.50% drift ratio. Specimen ES-0.7, with 0.7% steel reinforcement ratio and the highest effective reinforcement ratio of 0.7, experienced a less brittle punching failure, where multiple cracks started to widen after the 0.75% and until failure due to reinforcement yielding. However, sudden failure occurred once the drift ratio increased to 2.00%. Doubling the GFRP reinforcement ratio to 1.4% in specimen EG-1.4 allowed the connection to undergo further drifts and resulted in the least brittle punching failure, where significant concrete spalling and crack widening took place before failure, i.e., during the application of 2.50% drift ratio. Complete punching shear failure was not observed, however, until the 3.50% drift ratio was applied.

4.4.2. Load-drift relationship (hysteretic response)

The relationship between the applied lateral load and the corresponding drift ratio, i.e., hysteresis diagram, is shown in Figure 4.6, where the drift was considered positive when the hydraulic actuator was pushing the column. The main test results are summarized in Table 4.3, where the gravity lateral load (P_g) is the lateral load after the application of gravity loads; the peak lateral load (P_p) is the maximum measured lateral load; the peak drift ratio (δ_p) is the drift ratio corresponding to P_p and the ultimate drift ratio (δ_u) is the maximum drift ratio the connection was able to sustain before failure. Regardless of the reinforcement type and ratio, all connections were able to safely undergo or exceed the required drift ratio of 1.5% associated with the applied gravity shear ratio of 0.4 before punching failure. Doubling the GFRP reinforcement ratio from 0.7 to 1.4%, however, increased the drift capacity of the connections.

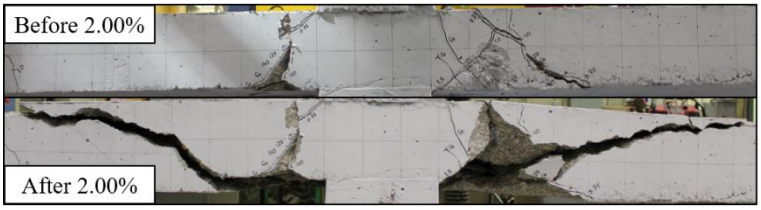

a) Connection ES-0.7

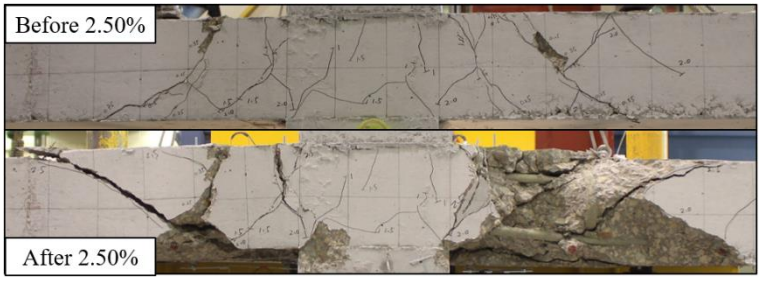

b) Connection EG-0.7

c) Connection EG-1.4

Figure 4.5: Cracking pattern on the free edge of the slab

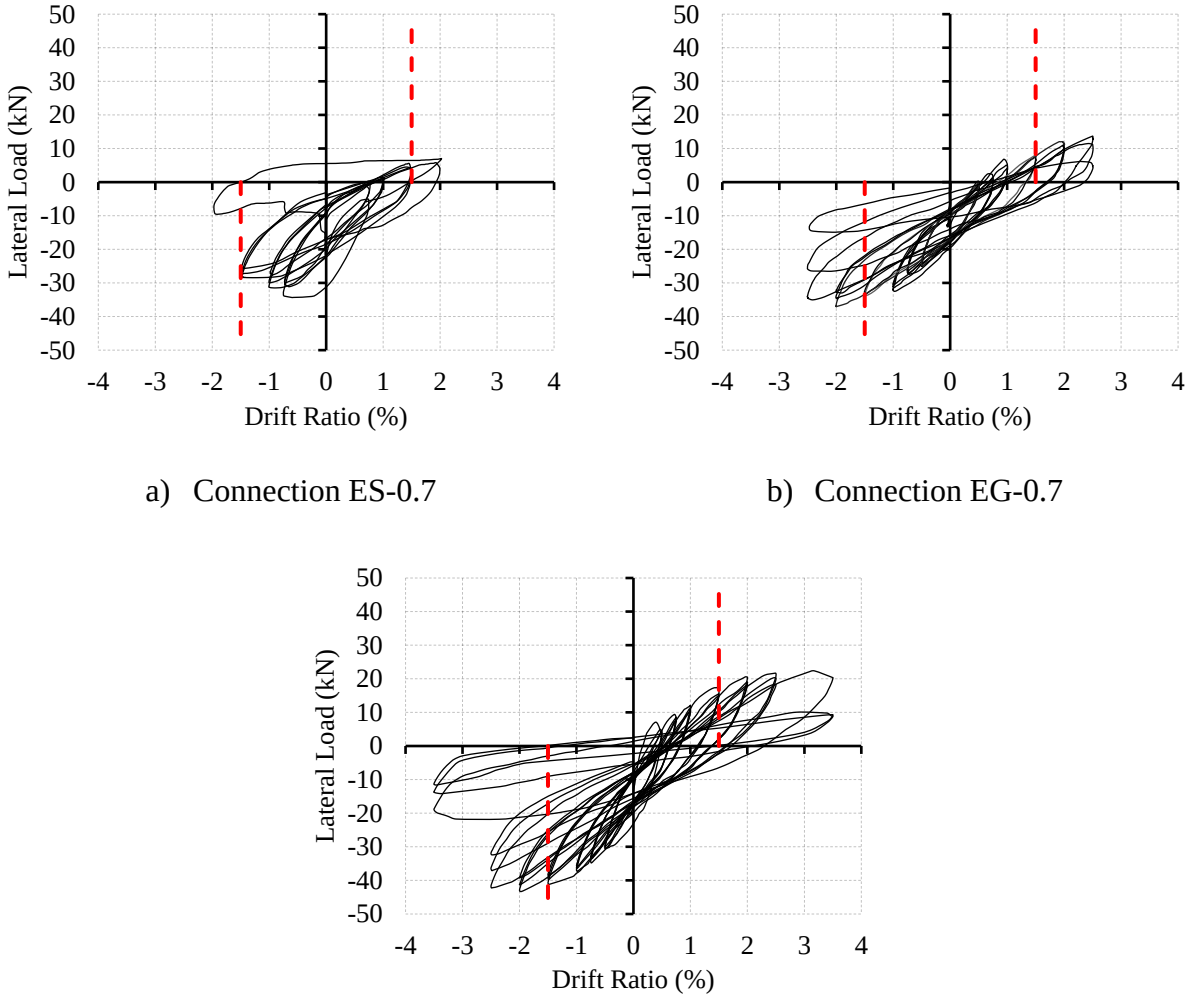

a) Connection ES-0.7

b) Connection EG-0.7

c) Connection EG-1.4

Figure 4.6: Hysteresis diagrams

Due to the elastic nature of the GFRP reinforcement, specimen EG-0.7 exhibited consistent increase in the lateral load capacity with increasing the applied drifts up to a maximum of 37.1 kN at 2.00% drift ratio. At this point, there were no signs of punching shear failure yet. Once the applied drift ratio increased to 2.50%, complete punching occurred and the connection rapidly lost its lateral load capacity. By the end of the 2.50% drift ratio, the lateral load had dropped to 14.9 kN, which represent a 60% reduction in the lateral load capacity. Similarly, the lateral load capacity of specimen EG-1.4 continued to increase up to a maximum of 43.3 kN at 2.00% drift ratio. By

the end of the 2.50% drift ratio, the lateral load had dropped to 32.4 kN, which represent a 25% reduction in the lateral load capacity. As mentioned earlier, however, complete punching was not observed until the 3.50% drift ratio was applied. This was not the case for specimen ES-0.7, reinforced with steel reinforcement, where reinforcement yielding occurred at the first cycle of 0.75% drift ratio and resulted in a plateau in the hysteretic response at a maximum lateral load of 34.3 kN. Consequently, the specimen experienced considerable inelastic deformations while the lateral load kept decreasing gradually until it reached 25.7 kN at the third cycle of the 1.50% drift ratio. The lateral load capacity was entirely lost and punching failure occurred at the first cycle of the 2.00% drift ratio.

Table 4.3: Test results

Connection	Lateral load (kN)		Drift ratio (%)			Deformability factor, μ	Reinforcement strain, ε_f (micro-strain)		
	P_g	P_p	δ_p	δ_u	δ_y		After gravity load	At failure	Residual [a]
ES-0.7	21.6	34.3	0.75	1.50	0.75	2.00	1,200	10,140	8,070
EG-0.7	13.1	37.1	2.00	2.00	1.22	1.64	650	9,370	3,080
EG-1.4	14.2	43.3	2.00	2.50	1.05	2.38	190	7,300	1,770

Note: P_g = gravity lateral load; P_p = peak lateral load; δ_p = peak drift ratio; δ_u = ultimate drift ratio; δ_y = equivalent yield drift ratio; ε_f = flexural reinforcement strain at failure.

[a] After 1.00% drift ratio

In order to quantify the ability of the connections to undergo inelastic deformations, envelopes of the hysteresis diagrams shown in Figure 4.7 were used to calculate the lateral displacement deformability factor, μ. For specimen ES-0.7, with steel reinforcement, this factor was calculated as the ratio of the ultimate drift ratio at failure (δ_u) to the drift ratio at yielding of steel reinforcement. Since there is no distinct yielding point in slabs, as opposed to beams, because

yielding spreads gradually across the slab reinforcement, the equivalent drift ratio at yielding (δ_y) is defined by the graphical construction shown in Figure 4.8 as suggested by Pan and Moehle (1989). In this procedure, the envelope of the hysteresis diagram is idealized by an elasto-plastic relationship. The plastic portion of the idealized relationship passes through the peak lateral load point (P_p). On the other hand, the elastic portion passes through the point of zero drift ratio and a point on the actual curve at a load equal to two-thirds of P_y, which equals P_p minus the lateral load caused by gravity loads. The intersection of these two straight portions defines the equivalent yield drift ratio, δ_y. Since GFRP-RC connections are expected to undergo significant deformations before failure due to the combination of high strength and low modulus of elasticity of the GFRP reinforcement, the aforementioned procedure was used to calculate the lateral displacement deformability factor for the GFRP-RC specimens as well.

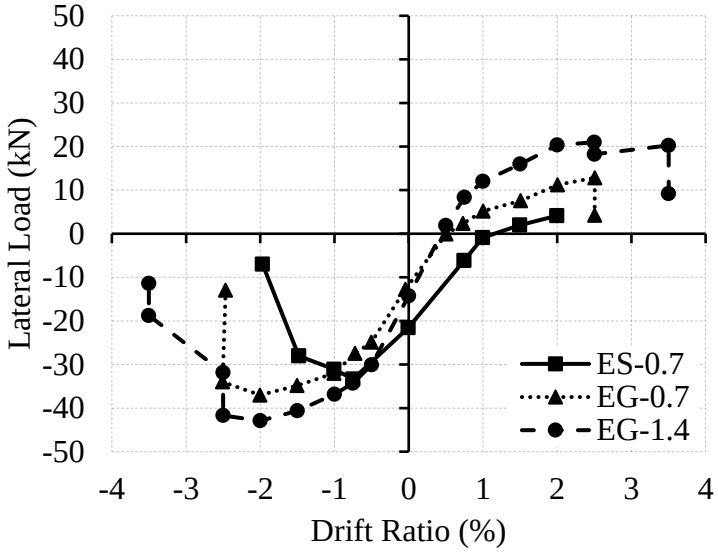

Figure 4.7: Envelopes of hysteresis diagrams

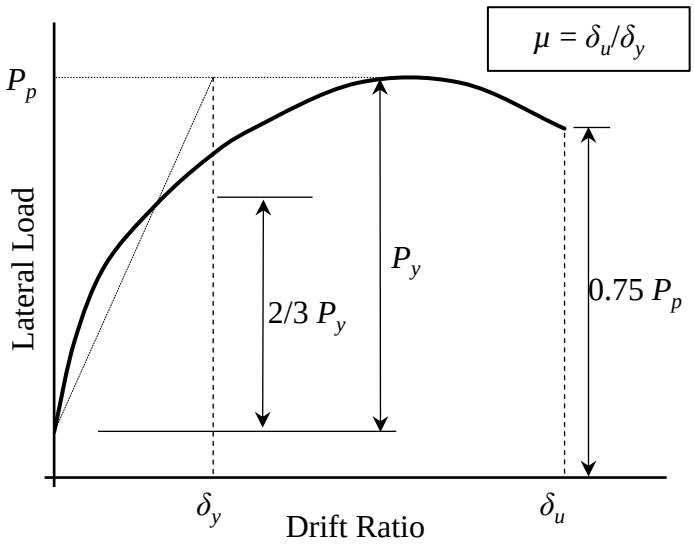

Figure 4.8: Definition of deformability

The values of the lateral displacement deformability factor are listed in Table 4.3**.** Due to their inherent brittleness, slab-column connections in general are expected to have limited deformability. Pan and Moehle (1989) suggested that, if the interstory drift ratio is limited to 1.5%, the lateral displacement ductility factor of slab-column connections should not be less than 1.2. Specimen ES-0.7 had an adequate deformability factor of 2.00 due to the early yielding of the steel reinforcement, which allowed the specimen to undergo considerable inelastic deformations before failure. On the other hand, specimen EG-0.7 with elastic GFRP reinforcement, had a deformability factor of only 1.64. Nonetheless, increasing the GFRP reinforcement ratio increased the punching capacity of the connections and allowed connection EG-1.4 to undergo large drifts before failure, thus, increasing the deformability factor by 45%. All connections had deformability factors higher than 1.2.

4.4.3. Stiffness degradation and energy dissipation

The stiffness factor, *k*, of the specimens at different loading stages are compared in Figure 4.9 as an indication of the level of damage after each loading cycle. It was calculated as the slope of the straight line connecting the two peaks of the third hysteresis loop at each loading cycle. The stiffness factors for the test connections at different drift ratios are listed in Table 4.4. Increasing the GFRP reinforcement ratio increased the stiffness of the connection at all drift ratios. The initial stiffness, at 0.50% drift ratio, of connection EG-1.4 was 43% higher than that of connection EG-0.7. This increase is relatively lower than that associated with connections subjected to gravity load only when GFRP reinforcement ratio is doubled.

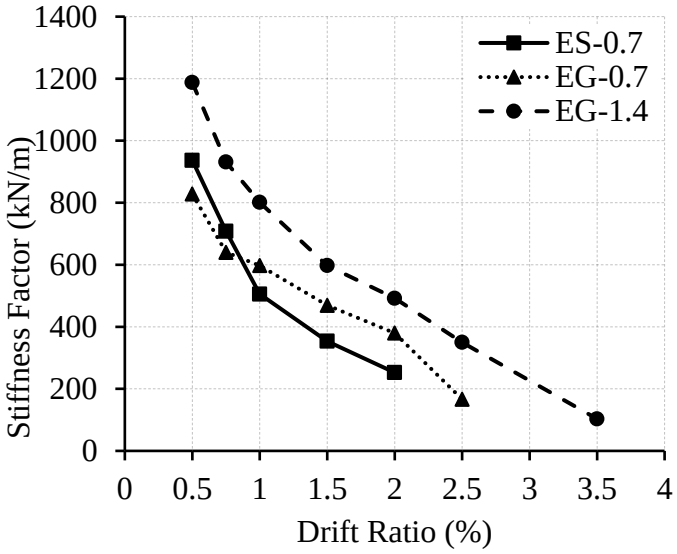

Figure 4.9: Stiffness degradation

Table 4.4: Stiffness and energy dissipation factors

Connection	Stiffness factor, k (kN/m)		Stiffness degradation factor	Accumulative dissipated energy (kN-m)	
	at 0.50%	at 1.50%		at 1.50%	at δ_u
ES-0.7	937	354	0.38	6.7	6.7
EG-0.7	828	469	0.57	4.6	7.6
EG-1.4	1,188	598	0.50	5.1	12.4

Note: δ_u = ultimate drift ratio.

Research on GFRP-RC slab-column interior and edge connections subjected to monotonically-increased vertical load and unbalanced moment revealed that the stiffness factor increases approximately linearly with increasing the GFRP reinforcement ratio. Gouda and El-Salakawy (2016a) reported an increase in the post-cracking stiffness factor of 110% when the 0.65% reinforcement ratio was doubled in GFRP-RC interior connections. Likewise, El-Gendy and El-Salakawy (2018a) demonstrated that doubling the reinforcement ratio from 0.9 to 1.8% in GFRP-RC edge connections increased the post-cracking stiffness factor by 119%. The relatively low increase in the initial stiffness of connection EG-1.4, 43%, despite utilizing double the GFRP reinforcement ratio of connection EG-0.7 is attributed to the higher gravity load applied to connection EG-1.4, which resulted in significant cracking under gravity load before the application of lateral drifts and, in turn, reduced its lateral load stiffness.

On the other hand, although having 13% higher initial stiffness than that of connection EG-0.7, connection ES-0.7 experienced a more severe stiffness degradation with the application of subsequent drifts due to the yielding of steel reinforcement. This resulted in connection ES-0.7 having 25% lower stiffness than that of connection EG-0.7 after 1.50% drift ratio. In order to assess the stiffness degradation of the specimens with the application of subsequent drifts, the stiffness degradation factor is used, which is the ratio between the stiffness factor at 1.50% drift ratio to the

initial stiffness factor (at 0.50% drift ratio) as listed in Table 4.4. While connection ES-0.7 (with steel reinforcement) lost approximately two-thirds of its initial stiffness after 1.50% drift ratio, both GFRP-RC connections were able to retain at least 50% of their initial stiffness. This is an indication of the higher level of damage associated with steel-RC connections due to yielding of the steel reinforcement.

Regardless of the reinforcement type and ratio, energy dissipation is not one of the main attributes of flat plate systems due to the brittle nature of the punching failure associated with the flexible connections. Moreover, the elastic nature of GFRP reinforcement would further reduce the energy dissipation capacity of GFRP-RC connections compared to steel-RC counterparts. Figure 4.10 shows the relationship between the accumulative dissipated energy and drift ratio for all connections, where the energy dissipated during a drift cycle was calculated as the area enclosed by the hysteresis loop of this cycle.

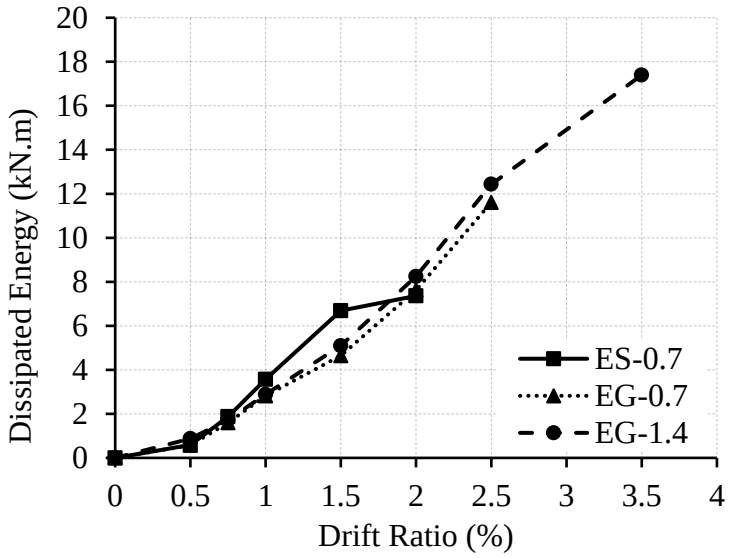

Figure 4.10: Energy dissipation

As expected, connection ES-0.7 dissipated higher energy than both GFRP-RC connections at the same drift ratio. At 1.50% drift ratio, connection ES-0.7 had dissipated 46 and 31% higher energy than connections EG-0.7 and EG-1.4, respectively. Nonetheless, at ultimate drift ratio, connections EG-0.7 and EG-1.4 had dissipated 13 and 85% higher energy, respectively, than connection ES-0.7 due to their higher drift capacity. Although increasing flexural reinforcement ratio would decrease the energy dissipation capacity of slab-column connections (Ghali et al. 1976), connection EG-1.4 dissipated 7.0% higher energy than connection EG-0.7 at the same drift ratio of 2.50%. This is attributed to the higher gravity load applied to connection EG-1.4 (153 kN) compared to that applied to connection EG-0.7 (119 kN). The values of the accumulative dissipated energy at different drift ratios for all connections are listed in Table 4.4.

4.4.4. Flexural reinforcement strains

Figure 4.11 shows the relationship between the drift ratio and the strain in top flexural reinforcement assembly measured at the column face in the perpendicular direction. For connection ES-0.7, flexural reinforcement did not yield under the application of gravity load. A strain value of 1,200 με was recorded, which is 60% of the theoretical yield strain of the used reinforcement. Yielding was not detected until the first cycle of the 0.75% drift ratio, where the strain readings jumped to 8,620 με (approximately four times the yielding strain). The strain gauge malfunctioned at the third cycle of the 1.00% drift ratio after recording a maximum strain of 10,140 με. The GFRP reinforced connections, on the other hand, had a more stable hysteresis response. Insignificant strains of 660 and 190 με were recorded in connections EG-0.7 and EG-1.4, respectively, after the application of gravity load. Then, strains kept increasing linearly with increasing drifts until failure. The maximum reinforcement strain recorded in connection EG-0.7 was 9,370 με. This value, despite the absence of yielding in GFRP reinforcement, is 92% of the

maximum measured strain in connection ES-0.7, which indicates that the large elastic deformations of GFRP may allow GFRP-RC connections to undergo considerable deformations before failure. The ultimate reinforcement strain was reduced to 7,300 με when the GFRP flexural reinforcement ratio was doubled in connection EG-1.4.

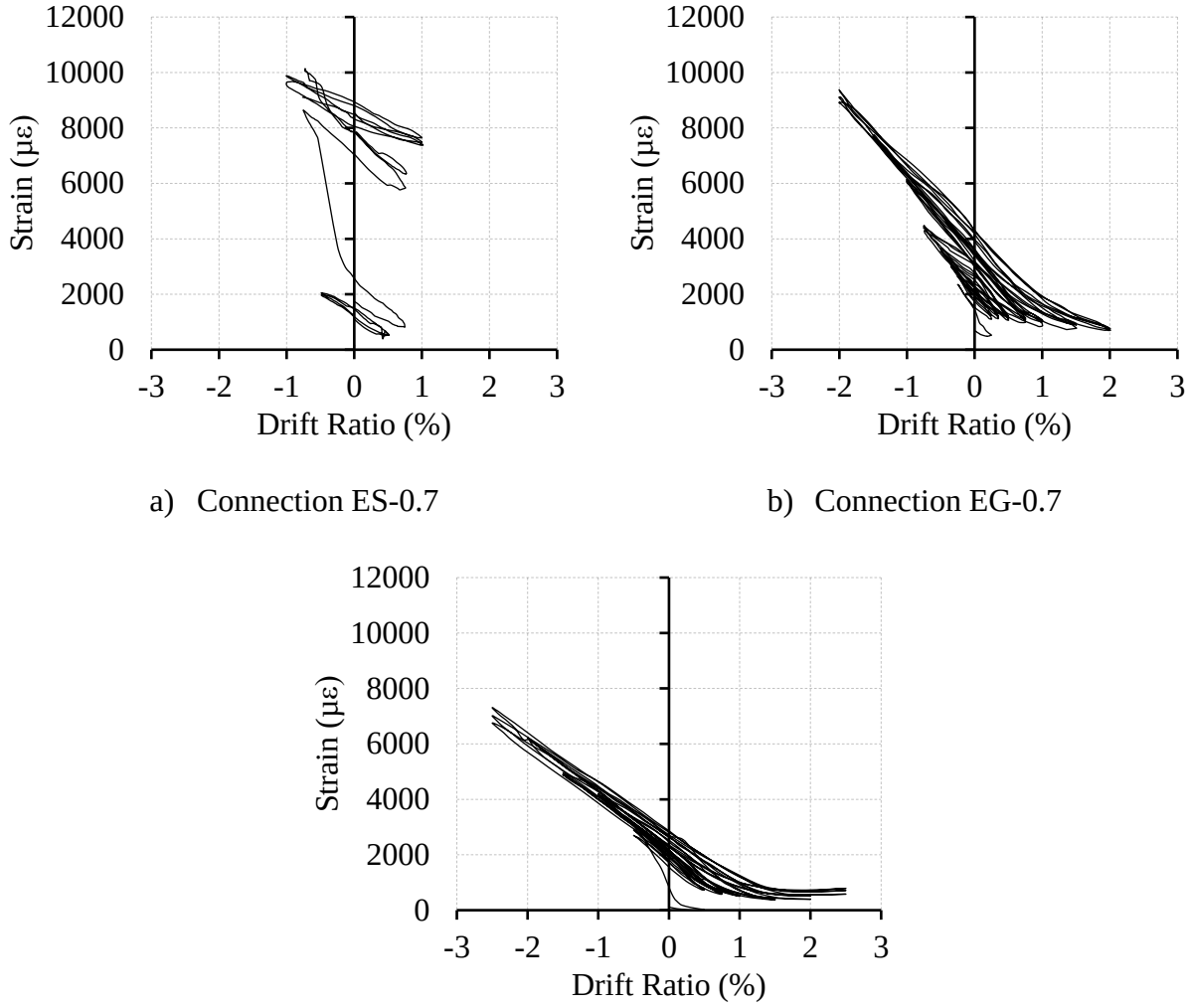

a) Connection ES-0.7

b) Connection EG-0.7

c) Connection EG-1.4

Figure 4.11: Reinforcement strain-drift ratio relationship

The linear elastic behavior of the GFRP reinforcement is evident when residual strains in the reinforcement at the end of each drift step are compared as shown in Figure 4.12. After 1.00% drift

ratio, the residual reinforcement strain in connection ES-0.7 was 2.6 times higher than that in connection EG-0.7. Also, doubling the GFRP reinforcement ratio resulted in 43% reduction in the residual reinforcement strain after 1.00% drift ratio. The increase in the residual reinforcement strains with increasing drift was minimal for the GFRP-RC connections. The ratio between the residual strain after 2.00% drift ratio and that after 0.50% drift ratio was only 1.74 and 1.32 for connections EG-0.7 and EG-1.4, respectively. This ratio could not be calculated for connection ES-0.7 since the strain gauge malfunctioned after the 1.00% drift ratio; however, the ratio between the residual strain after 1.00% drift ratio and that after 0.50% drift ratio was 4.75 due to the permanent yielding of the steel reinforcement. This behavior resulted in significantly less residual damage in the GFRP-RC connections, regardless of the reinforcement ratio, after surviving the seismic excitation.

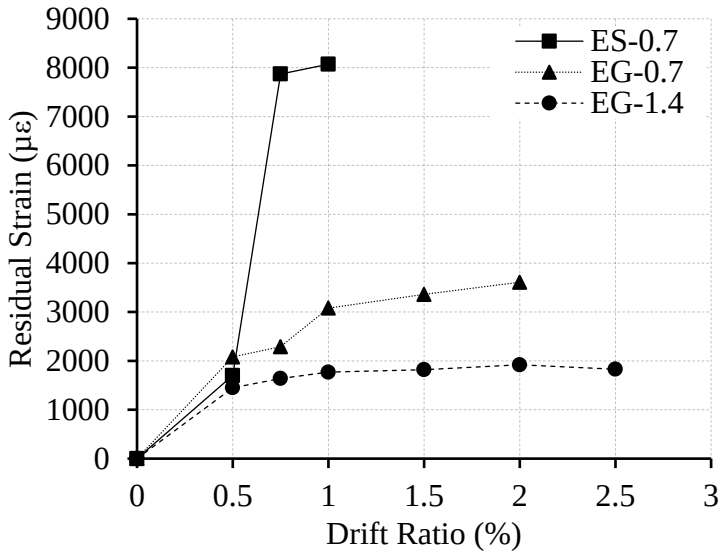

Figure 4.12: Residual reinforcement strains

4.5. Conclusions

The tests discussed in this study are part of an ongoing extensive research program at the University of Manitoba to investigate the behavior of GFRP-RC slab-column connections with different configurations under different types of loading. Based on the limited number of tests conducted in this study, the following conclusions can be drawn:

1. All connections exhibited a brittle punching shear failure. However, they were able to safely achieve or exceed the minimum 1.50% drift capacity before punching failure. While connection EG-0.7 (with GFRP reinforcement) experienced a more brittle failure than its counterpart connection ES-0.7 with the same steel reinforcement ratio, doubling the GFRP reinforcement ratio in connection EG-1.4 allowed the connection to undergo larger drifts and reduced the brittleness of the failure.
2. Doubling the GFRP reinforcement ratio from 0.7 to 1.4% slightly increased the drift capacity of the GFRP-RC connections by 25% (from 2.00 to 2.50%). However, it resulted in an enhancement of 45% in the deformability of the connections. All connections had deformability factors higher than the minimum 1.2 recommended in the literature.
3. Although connection ES-0.7 had 13% higher initial stiffness than that of connection EG-0.7, connection ES-0.7 experienced a more severe stiffness degradation due to the yielding of steel reinforcement. While connection EG-0.7 was able to retain 57% of its initial stiffness after 1.50% drift ratio, connection ES-0.7 lost approximately two-thirds of its initial stiffness at the same drift level. This is an indication of the higher level of damage associated with steel-RC connections due to yielding of the steel reinforcement.

4. Doubling the GFRP reinforcement ratio from 0.7 to 1.4% resulted in 43 and 63% enhancement in the initial stiffness and energy dissipation capacity of the connections, respectively. However, it did not significantly affect the stiffness degradation.
5. While steel reinforcement yielding allowed connection ES-0.7 to experience reinforcement strains higher than 10,140 με before punching, the unique combination of low modulus of elasticity and high tensile strength of GFRP bars allowed connections EG-0.7 and EG-1.4 to experience reinforcement strains of 9,370 and 7,300 με, respectively. These values are 92 and 72% of the maximum measured steel reinforcement strain, which indicates that GFRP reinforcement can undergo comparable deformations to steel reinforcement before failure.
6. The residual reinforcement strain in connection ES-0.7 after 1.00% drift ratio was 2.6 times higher than that in connection EG-0.7 due to the permanent yielding of steel reinforcement. In addition, the residual strain after 2.00% drift ratio was only 74 and 32% higher than that after 0.50% drift ratio for connections EG-0.7 and EG-1.4, respectively. Thus, GFRP-RC connections will sustain significantly less residual damage after surviving the seismic excitation.

The findings are encouraging to expand the scope of testing to include various design parameters, such as lateral load configuration (e.g., bi-axial loading and uniaxial loading parallel to free edge), column aspect ratio, and slab thickness. This will help in developing the much-needed numerical models, and design formulas and guidelines for GFRP-RC flat plate systems in seismic zones.

CHAPTER 5. GRAVITY LOAD EFFECT ON SEISMIC RESPONSE OF GLASS FIBER REINFORCED POLYMER-REINFORCED CONCRETE SLAB-COLUMN EDGE CONNECTIONS

Authors and Affiliation:

- Mohammed G. El-Gendy, PhD Candidate, Department of Civil Engineering, University of Manitoba
- Ehab F. El-Salakawy, Professor, Department of Civil Engineering, University of Manitoba

Journal and Status:

American Concrete Institute (ACI) Structural Journal, published on August/September 2020 issue.

Reference:

El-Gendy, M., and El-Salakawy, E. 2020. "Gravity load effect on seismic response of glass fiber-reinforced polymer-reinforced concrete slab-column edge connections." *ACI Struct. J.*, 117 (5), https://doi.org/10.14359/51724665.

Note:

The manuscript had been slightly altered from the original paper by renumbering the tables and figures to include the chapter number. In addition, the reference list and list of notations have been moved to the appropriate sections in the thesis as indicated in the table of contents.

Abstract

When reinforced concrete (RC) flat plate systems are used as gravity force resisting systems in regions of high seismic activities, they are required to accommodate at least 1.50% drift ratio without jeopardizing their gravity load capacity. The current codes and standards in North America limit the allowable gravity shear ratio in steel-RC flat plate systems without shear reinforcement to 0.4 for the system to be able to sustain the 1.50% drift capacity. This paper reports the results of an inaugural experimental study investigating the effect of gravity shear ratio on the drift capacity of slab-column edge connections reinforced with glass fiber-reinforced polymers (GFRP) reinforcement. Three full-scale GFRP-RC edge connections were tested under a combination of gravity and uniaxial reversed-cyclic lateral loads. It was concluded that the 0.4 limit on the gravity shear ratio can be relaxed in the case of GFRP-RC connections.

Keywords: Cyclic loading; drift capacity; edge connection; flat plate; glass fiber-reinforced polymer (GFRP); gravity shear ratio; punching shear; seismic loading; slab-column connection.

5.1. Introduction

Reinforced concrete (RC) flat plate systems are widely favored by designers for both low- and high-rise buildings due to their functional form and construction economy. One serious issue with flat plate systems, however, is their susceptibility to brittle punching shear failure due to the concentration of shear stresses at slab-column connections. This brittle failure is further prompted by the excessive shear forces and unbalanced moments transferred between the slab and the column at slab-column connections due to the significant horizontal displacements associated with seismic activities. Consequently, in regions of high seismic activities, the high flexibility and low energy dissipation capacity of flat plate systems make it necessary to combine them with a stiffer structural system, such as shear walls or moment-resistant frames, to function as a seismic force resisting system (SFRS), whereas the flat plate system resists gravity loads only. Nevertheless, the presence of the stiffer structural system does not completely eliminate the seismic forces applied to the flat plate system. In addition, as the entire structure drifts, the flat plate system will undergo the same lateral drifts of the SFRS. Therefore, flat plate systems must be designed for deformation compatibility with the SFRS. In other words, the flat plate system must have adequate drift capacity to be able to accommodate the seismically induced lateral drifts without experiencing punching failure of the slab-column connections. Accordingly, a minimum drift capacity of 1.50% interstory drift ratio, which is defined as the ratio of the relative lateral drift of two successive floors to the floor height, was recommended by Sozen (1980).

One of the main parameters affecting the drift capacity of steel-RC slab-column connections is the magnitude of the gravity shear carried by the slab. This parameter is represented by the gravity shear ratio, which is the ratio of the gravity shear force transferred between the slab and the column, V_g, to the theoretical punching shear capacity provided by concrete, V_c. Pan and Moehle

(1989) reviewed test results of 18 slab-column interior connections subjected to simulated seismic loading. They concluded that both the drift capacity and lateral displacement ductility decrease as the gravity shear ratio increases. Megally and Ghali (2000c) tested full-scale isolated edge connections under gravity and simulated cyclic lateral load. They reported that increasing the gravity shear ratio by 45 and 100% (from 0.29 to 0.42 and 0.58) decreased the drift capacity by 26 and 61% (from 3.1 to 2.3 and 1.2%), respectively.

Different limits on the gravity shear ratio that a slab-column connection without shear reinforcement can withstand before punching shear failure were set by different researchers. Pan and Moehle (1989) recommended a maximum gravity shear ratio of 0.4 for connections without shear reinforcement to possess a drift capacity of at least 1.50%. This limit was later supported by other researchers (Megally and Ghali 1994; Hueste and Wight 1999). Robertson and Durrani (1991, 1992) tested three slab-column subassemblies consisting of two edge and one interior connection each. They suggested revising the maximum gravity shear ratio recommended by Pan and Moehle (1989) to become 0.35 and 0.50 for interior and edge connections, respectively. The latter limit for edge connections was also recommended by Megally and Ghali (2000b). Currently, the Canadian standard CSA A23.3-19 (CSA 2019b) and American code ACI 318-19 (ACI 2019a) incorporate the 0.4 limit on gravity shear ratio without distinction between interior and exterior connections. According to CSA A23.3-19 (CSA 2019b), the gravity shear ratio applied to connections without shear reinforcement should not exceed the value calculated by Equation 5.1; otherwise, shear reinforcement must be used. Similarly, according to ACI 318-19 (ACI 2019a), the maximum drift ratio a slab-column connection without shear reinforcement can withstand, δ, is a function of the gravity shear ratio as calculated by Equation 5.2**,** where ϕ is the strength

reduction factor. A graphical representation of the requirements of both codes is shown in Figure 5.1.

$$\frac{V_g}{V_c} \leq \left(\frac{0.005}{\delta}\right)^{0.85} \quad \text{, where } \delta \geq 0.005 \qquad \text{Equation 5.1}$$

$$\delta \leq 0.035 - 0.05\left(\frac{V_g}{\phi V_c}\right) \quad \text{, where } \delta \geq 0.005 \qquad \text{Equation 5.2}$$

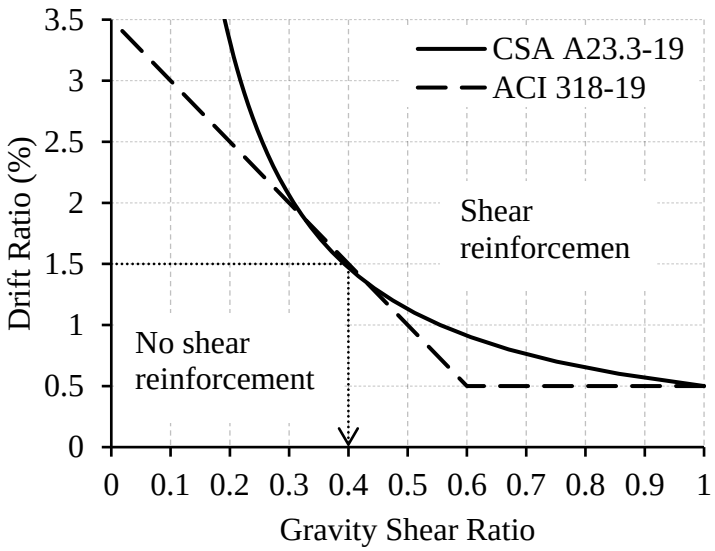

Figure 5.1: Drift requirements of the current codes in North America

On the other hand, in addition to expensive repairs, corrosion of internal steel reinforcement can lead to fatal consequences. A parking garage floor collapsed in Montreal, Quebec in November 2008 killing at least one person (Canadian Consulting Engineer 2008). The failure was attributed to the corrosive effects of deicing salts. Many alternatives to conventional steel reinforcement have been proposed to overcome the corrosion problem. These alternatives include epoxy-coated steel, stainless steel, and fiber-reinforced polymer (FRP) composites. According to the Canadian standard CSA 413-14 (CSA 2019e), epoxy-coated steel is not allowed in parking structures due to

durability concerns. Stainless steel, on the other hand, is substantially expensive. Younis et al. (2018) conducted a life cycle cost analysis of three design alternatives using three types of reinforcement, i.e., black steel, stainless steel, and glass fiber-reinforced polymer (GFRP). It was concluded that using stainless steel and GFRP will result in approximately 15 and 50% savings based on a 100-year lifetime. Thus, GFRP is a far more cost-effective option to replace conventional black steel. When GFRP bars are used as internal flexural reinforcement for flat plate systems, their low modulus of elasticity and high strength will result in large elastic deformations that would replace the yielding plateau of steel bars and allow the slab-column connections to undergo considerable seismically induced lateral drifts without punching failure (El-Gendy and El-Salakawy 2018b).

The tests discussed in this paper are part of an extensive ongoing research study at the University of Manitoba aimed at investigating the punching shear behavior of GFRP-RC slab-column connections with different configurations under different types of loading. The first phase of this study started in 2011 by studying the behavior of interior and edge connections subjected to monotonically increased axial load and unbalanced moment (Gouda and El-Salakawy 2015, 2016a, 2016b; El-Gendy and El-Salakawy 2016, 2018a; Hussein and El-Salakawy 2018; Mostafa and El-Salakawy 2018). Compared to interior connections, relatively higher unbalanced moments transfer between the slab and column at edge connections. In addition, less confinement is provided to the concrete in the column vicinity due to the disruption of the slab, which may also result in lack of slab negative reinforcement anchorage. Thus, slab-column edge connections are more critical to punching shear failure than interior ones. Therefore, this paper presents the first attempt to investigate the effect of gravity shear ratio on the seismic response of GFRP-RC slab-

column edge connections and to recommend a limit on the maximum gravity shear ratio a GFRP-RC slab-column edge connection can carry, while experiencing the minimum 1.50% drift ratio.

5.2. Research Significance

Recently, the seismic behavior of GFRP-RC elements, e.g., shear walls, columns and beam-column joints, has been investigated (Sharbatdar and Saatcioglu 2009; Hasaballa et al. 2011; Tavassoli et al. 2015; Arafa et al. 2018). However, no studies have investigated the seismic response of the flexible GFRP-RC slab-column connections when subjected to different gravity shear ratios. This pioneer experimental study provides a valuable insight on the seismic response of GFRP-RC slab-column edge connections subjected to simulated seismic loading conditions, with a focus on the maximum gravity shear ratio a connection can carry, while having a minimum level of deformability and drift capacity.

5.3. Experimental Investigation

A series of tests (refer to Figure 5.2 for test setup) were conducted on full-scale isolated slab-column edge connections by first applying a desired level of gravity load and then applying a sequence of cyclic lateral displacements until failure.

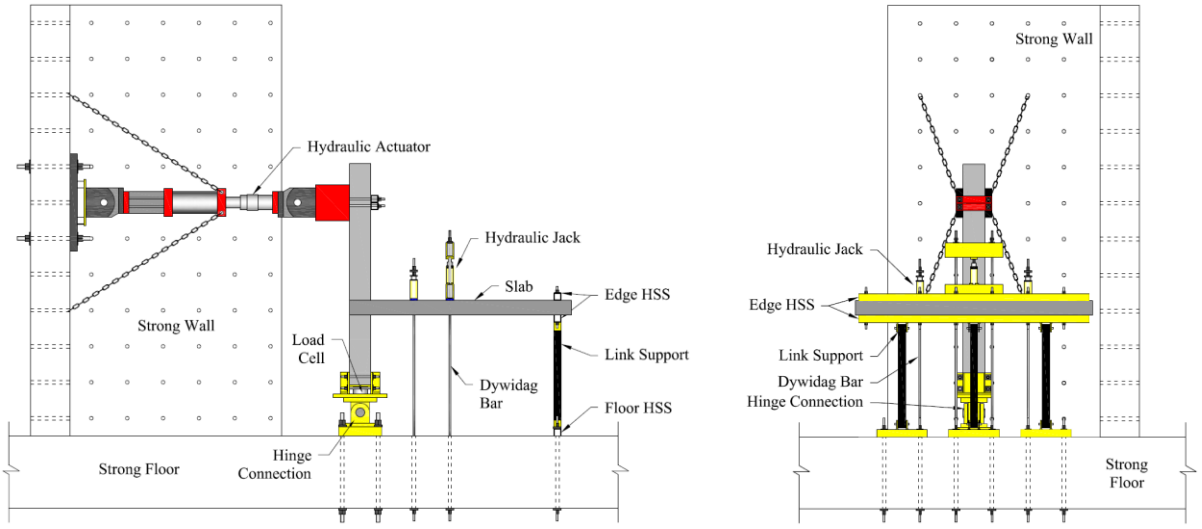

a) Elevation view b) Side view

Figure 5.2: Schematic drawing of the test setup

5.3.1. Prototype structure

A multistory prototype GFRP-RC flat plate building with a 3.0 m storey height was designed as a parking garage structure according to the Canadian standards CSA A23.3-19 (CSA 2019b) and CSA S806-12 (CSA 2017), where applicable. As shown in Figure 5.3, the prototype building consisted of five 5.5-m long bays in each direction with 300-mm square columns and two I-shaped shear walls to control the lateral deformations, i.e., work as the SFRS. The design live load was 2.4 kN/m^2, while the dead load included the self-weight in addition to a partition allowance of 1.0 kN/m^2 according to the National Building Code of Canada (NRCC 2015). The design resulted in a 200-mm thick slab reinforced with top and bottom flexural reinforcement assemblies. Due to the lower stiffness of GFRP bars compared to that of steel, serviceability requirements governed the design of the slab and resulted in a column strip reinforcement ratio in the perpendicular direction of 1.4 and 0.7% for the top and bottom assemblies, respectively.

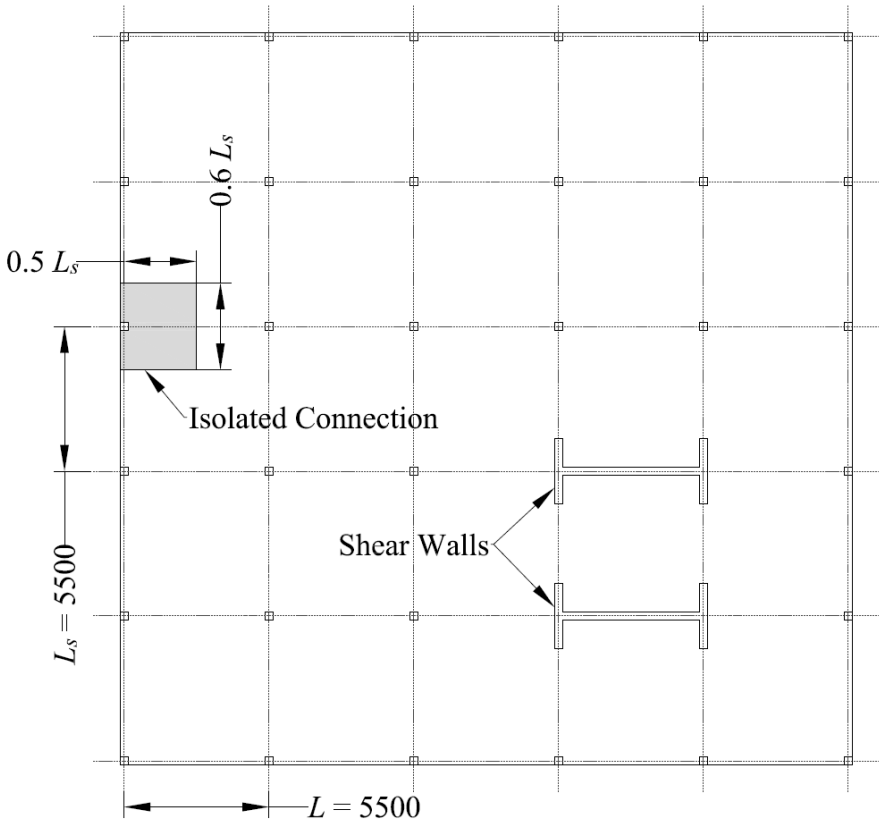

Figure 5.3: Prototype flat plate system

5.3.2. Test specimens

The dimensions of the isolated connections were determined by delineating the boundaries at the contra-flexure lines. These lines were assumed at mid-heights of the edge column. For the slab, however, they were assumed at distances of 0.30 L_s and 0.50 L_s from the centerlines of the edge column in the directions parallel and perpendicular to the free edge, respectively, where L_s is the center-to-center spacing between columns as shown in Figure 5.3. This resulted in an edge connection with 3,300 × 2,900 mm slab dimensions and a 300-mm square edge column extending 1,400 mm above and below the slab surfaces. However, the dimensions of the slab were increased to 3,300 × 3,100 mm to allow for a slab supporting clearance. Similarly, both the top and bottom columns had a nominal height of 1,360 mm so that the distance between the centerline of the slab

and the tip of each column is 1,460 mm, i.e., approximately half the storey height. However, to permit the attachment of the column support and the hydraulic actuator, as discussed later, the top and bottom column heights were changed to 1,900 and 970 mm, respectively. Typical dimensions and reinforcement details of a test connection are shown in Figure 5.4.

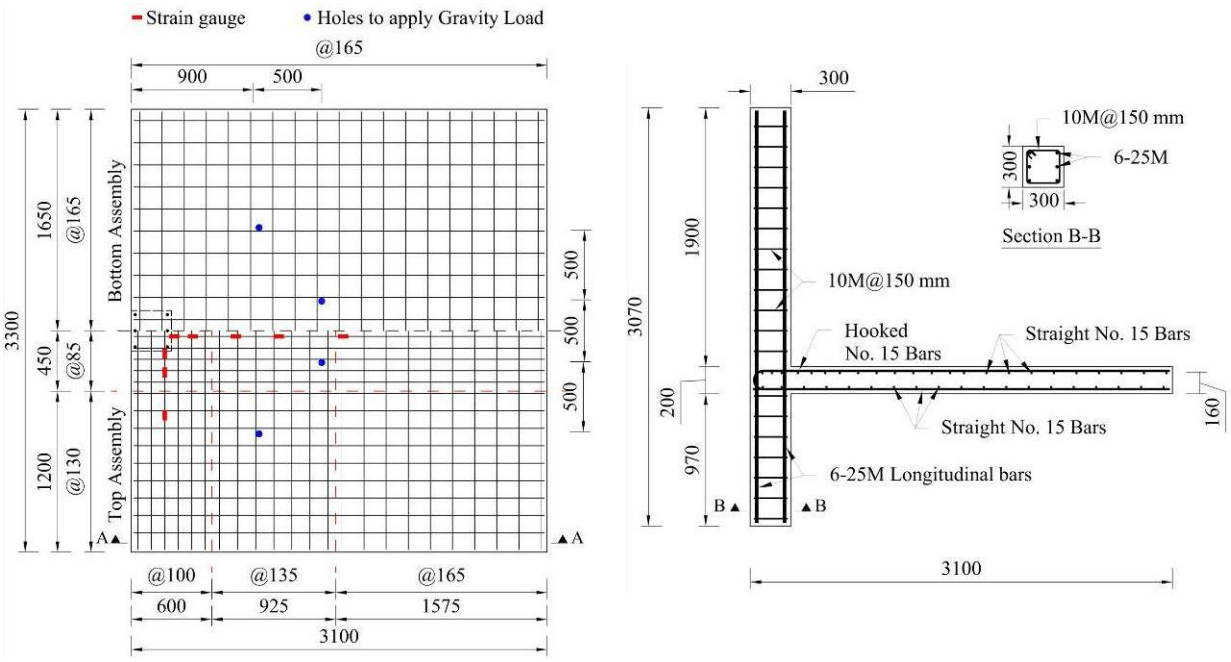

a) Slab reinforcement b) Section A-A

c) Connection before casting

Figure 5.4: Typical connection details

Three full-scale isolated slab-column edge connections were constructed and tested to failure under gravity and uniaxial reversed-cyclic lateral loads. The three connections were identical in all aspects (i.e., dimensions, flexural reinforcement ratio and the absence of shear reinforcement) with minor variations in the actual concrete compressive strength as listed in Table 5.1. The test parameter was the amount of gravity shear applied to the connections. The 0.4 maximum gravity shear ratio recommended in the literature for steel-RC connections without shear reinforcement was applied to the first connection (connection E40). Based on the results of this test, the gravity shear ratio applied to the second connection (connection E50) was increased to 0.5. Eventually, a high gravity shear ratio of 0.6 was applied to the third connection (connection E60).

Table 5.1: Details of test connections

Connection	V_g/V_c	V_c (kN)	V_g (kN)	f_c' (MPa)
E40	0.4	383	153	49
E50	0.5	378	189	47
E60	0.6	381	228	48

Note: V_g/V_c = applied gravity shear ratio; V_c = theoretical punching shear capacity provided by concrete calculated by Equation 5.5; V_g = gravity shear force transferred between slab and column; f_c' = actual concrete compressive strength on day of testing.

For all connections, the gravity shear ratio was calculated as a function of the punching shear capacity provided by concrete, V_c, which is calculated in CSA S806-12 (CSA 2017) as the smallest of the three values described in Equation 5.3 to Equation 5.5. Several research studies on GFRP-RC interior and edge connections subjected to gravity load concluded that this model, unlike the ACI 440.1R one (ACI 2015), provides reasonable predictions of the punching shear strength provided by concrete. It was demonstrated that the ACI 440.1R model ignores the contributions of the aggregate interlock and reinforcement dowel action to the punching shear strength; thus, it consistently underestimates the punching shear strength provided by concrete (Dulude et al. 2013;

El-Gendy and El-Salakawy 2018a). The values of the theoretical punching shear capacity provided by concrete, V_c, and the actual gravity loads applied to the connections, V_g, are listed in Table 5.1.

$$V_c = \left(1 + \frac{2}{\beta_c}\right)\left[0.028\lambda\phi_c\left(E_F\rho_F f_c^{'}\right)^{\frac{1}{3}}\right]\left(b_o d\right) \quad \text{Equation 5.3}$$

$$V_c = \left[\left(\frac{\alpha_s d}{b_o}\right) + 0.19\right]\left[0.147\lambda\phi_c\left(E_F\rho_F f_c^{'}\right)^{\frac{1}{3}}\right]\left(b_o d\right) \quad \text{Equation 5.4}$$

$$V_c = \left[0.056\lambda\phi_c\left(E_F\rho_F f_c^{'}\right)^{\frac{1}{3}}\right]\left(b_o d\right) \quad \text{Equation 5.5}$$

5.3.3. Materials

Size No. 15 sand-coated GFRP bars were used in the top and bottom orthogonal reinforcement assemblies of the slabs. For the top assembly, single-end hooked bars were used in the direction perpendicular to the free edge of the slab with the hooked end coinciding with the location of maximum top (negative) moment (i.e., the free edge of the slab) to provide the required anchorage, while straight bars were used elsewhere as shown in Figure 5.4. On the other hand, the columns were adequately reinforced with six 25M steel bars and No. 10M steel stirrups. The mechanical properties of the straight and hooked GFRP bars were obtained from standard tests carried out according to ASTM D7205-06 (ASTM 2016) and ASTM D7914-14 (ASTM 2014), as applicable (Table 5.2).

Normal-weight, ready-mix concrete with a target 28-day compressive strength of 40 MPa was used in all connections. The actual concrete compressive strength was determined by testing standard 100 × 200 mm cylinders on the day of slab testing according to CSA A23.1-19/A23.2-19 (CSA

2019b) as listed in Table 5.1. The connections and the cylinders were cast in the laboratory and wet-cured for 7 days.

Table 5.2: Mechanical properties of the used GFRP reinforcement

Bar shape	Bar size	d_b (mm)	A_b (mm^2)	f_F (MPa)	E_F (GPa)	ε_{Fu} (%)
Straight	No. 15	15.9	199[a] (234)[b]	1,712	66	2.6
Hooked (straight portion)			199[a] (227)[b]	1,405	52	2.7
Hooked (bent portion)			199[a] (227)[b]	725	-	-

Note: d_b = bar diameter; A_b = bar area; f_{Fu} = tensile strength; E_F = modulus of elasticity; ε_{Fu} = ultimate strain.

[a] Nominal area according to CSA S807-19 (CSA 2019d)
[b] Measured area according to Annex A in CSA S806-12 (CSA 2017)

5.3.4. Test setup and instrumentation

The test setup shown in Figure 5.2 was designed to test the connections under uniaxial reversed-cyclic lateral load with a constant level of gravity load. The connections were supported at the column base and at the slab edge running parallel to the slab's free edge, while the other two slab edges were unrestrained. The column base was connected to a steel hinge support modeled by a pin and clevis assembly, which was prestressed to the laboratory's floor. This support was intended to restrict the vertical and horizontal translations of the column base, while allowing rotation in the direction of the lateral load application only. The supported slab edge was stiffened by two horizontal 100 × 100 × 6.25 mm hollow structural sections (HSS) at the top and bottom of the slab to prevent out-of-plane displacement. The stiffened edge was then supported by three vertical 100 × 100 × 6.25 mm pin-ended HSS link assemblies to simulate a roller support. These vertical links were pinned at the top to the horizontal HSS at the soffit of the slab edge and pinned at the bottom to a set of horizontal 100 × 100 × 6.25 mm HSS, which were prestressed to the laboratory's floor.

This way the links prevent the vertical translation of the slab edge, while allowing horizontal translation and rotation in the direction of the lateral load application.

The reversed-cyclic lateral load was applied by means of a horizontally placed, fully dynamic hydraulic actuator with load and stroke capacities of 1,000 kN and 500 mm, respectively. This actuator was pinned to the top of the column and was transferring its horizontal reaction forces to a rigid 500-mm thick L-shaped RC reaction wall (3.5-m wide × 6.0-m high per leg). Accordingly, the distance between the centerline of the actuator and the axis of rotation of the hinge support was 2,920 mm. On the other hand, the gravity load was applied to the slab by a set of three hydraulic jacks. The jacks were used to tension four steel threaded bars (dywidag bars) running through pre-made holes in the slab and anchored at the laboratory's floor. Figure 5.5 shows a connection in the setup during testing. In each connection, twelve 6-mm long electrical-resistance strain gauges (ESG) were attached to the top slab flexural reinforcement to measure the strains as shown in Figure 5.4. On the other hand, four load cells were used to monitor gravity loads. Three cells were attached to the hydraulic jacks applying the gravity load, while the fourth one was installed at the bottom of the column to record the vertical reaction at the hinged support.

5.3.5. Loading procedure

The test started by applying the gravity load, while the movement of the horizontal actuator was locked to prevent lateral displacement of the connection during the application of gravity load. The specified gravity load for each connection was calculated using the concrete compressive strength on the day of testing. Once the specified gravity load was reached, it was kept constant during the remainder of the test, while the horizontal actuator started to apply the lateral load.

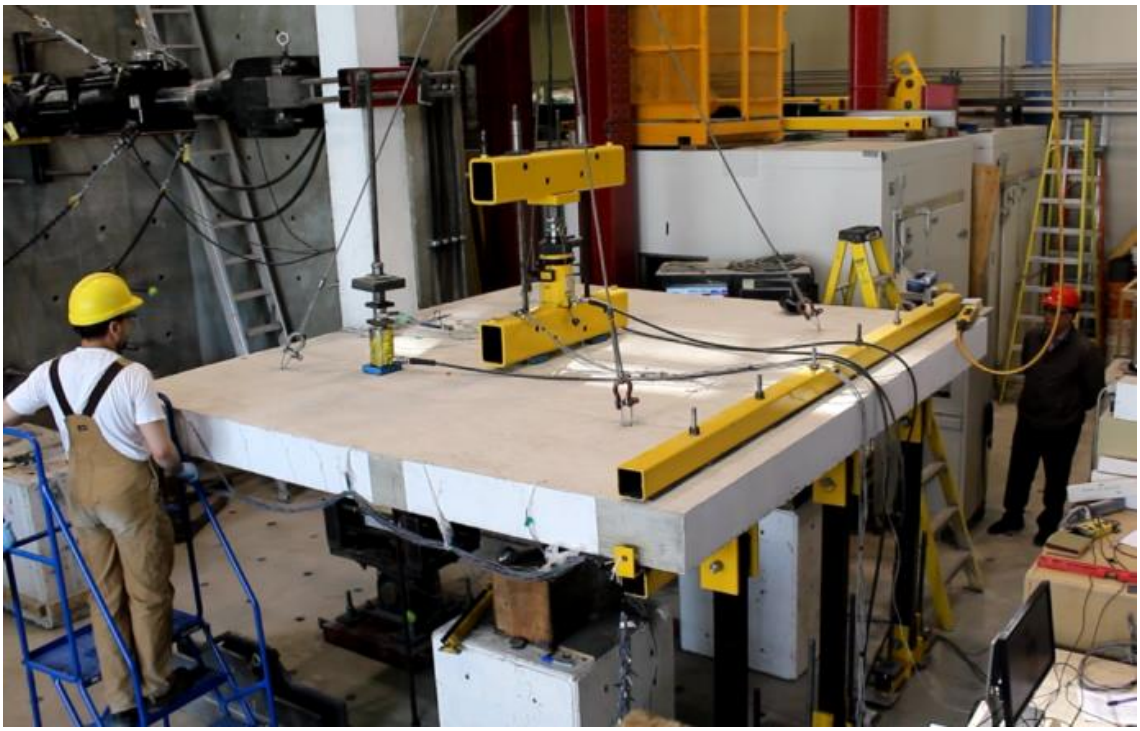

Figure 5.5: An overview of a connection during testing

The lateral load was simulated by a displacement-controlled uniaxial quasi-static reversed-cyclic load at the column tip at a rate of 0.01 Hz following the scheme shown in Figure 5.6, which was adopted from ACI 374.1-05 (ACI 2014b). In this scheme, the connections were subjected to increasing specified drift ratios in several steps, where each step comprised three fully reversed cycles with the same drift ratio to ensure stable formation of cracks. All drift ratios were determined such that the ratio of each one to its predecessor lays between 1.25 and 1.5. Eventually, the test was stopped when punching failure occurs or when at least 25% of the lateral load capacity is lost.

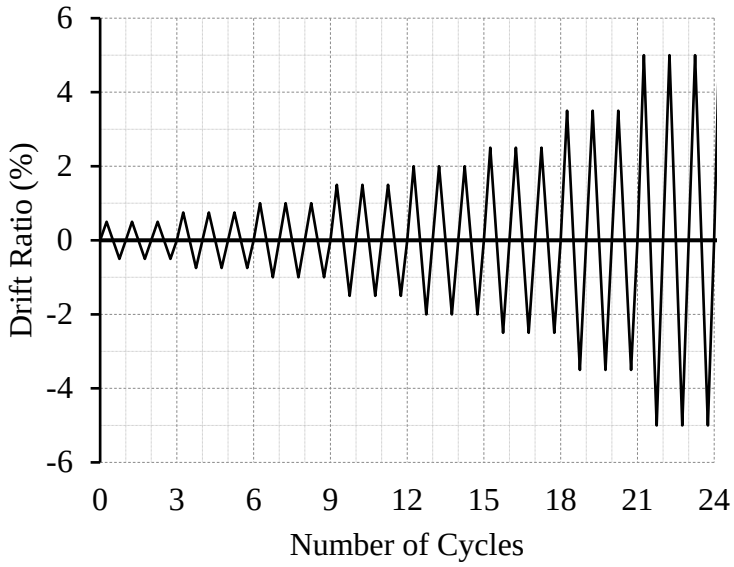

Figure 5.6: Lateral drift scheme

5.4. Experimental Results and Discussion

5.4.1. Mode of failure and cracking pattern

All connections failed by punching shear of the slab in the column vicinity, with the failure of connection E40 being less sudden than that of the other two connections subjected to higher gravity shear ratios. During the application of gravity loads, the first flexural crack, which was a circumferential flexural crack at the slab-column interface, was observed when the gravity load transferred to the column was ranging between 80 and 110 kN for all connections. This represents a maximum of 72, 58 and 48% of the specified gravity load for connections E40, E50 and E60, respectively. No more cracks were observed in connection E40 after the relatively low specified gravity load was reached. Nevertheless, with increasing the gravity loads applied to connections E50 and E60, several radial flexural cracks and diagonal shear cracks developed on the slab top surface and free edge, respectively. These cracks continued to propagate, and more cracks were developed with the application of lateral drifts in all connections until the final cracking pattern was established.

As shown in Figure 5.7, significant concrete spalling and crack widening took place in connection E40 before failure, i.e., during the application of 2.50% drift ratio, which resulted in a considerably less brittle failure. Complete punching shear failure was not observed, however, until the 3.50% drift ratio was applied. This was not the case for connections E50 and E60, where the failure was considerably sudden with minimal warning. As can be seen in Figure 5.7, no concrete spalling or significantly wide cracks were observed in connections E50 and E60 before failure. Connection E60 experienced the most brittle punching shear failure with the most damage to the connection. For all connections, despite their relatively low transverse stiffness, the bottom integrity bars passing through the column managed to prevent the complete collapse of the slabs after punching. Figure 5.8 shows the cracking pattern on the top surface of the slab before and after punching for all connections.

5.4.2. Load-drift relationship (hysteretic response)

Figure 5.9 shows the relationship between the applied lateral load and the corresponding drift ratio, i.e., hysteresis diagrams. It is to be noted that the drift and lateral load were considered positive when the hydraulic actuator was pushing the column. The main test results are summarized in Table 5.3, where the gravity lateral load (P_g) is the lateral load after the application of gravity loads on the slab; the peak lateral load (P_p) is the maximum measured lateral load; the peak drift ratio (δ_p) is the drift ratio corresponding to P_p; and the ultimate drift ratio (δ_u) is the maximum drift ratio the connection was able to sustain before failure. Increasing the applied gravity shear ratio significantly decreased the drift capacity of the connections. Connection E40 was able to safely experience the 1.50% drift ratio, with a lateral load of 41.1 kN, while fully carrying the applied gravity loads. The lateral load then increased to a maximum of 43.3 kN during the 2.00% drift ratio before slightly decreasing to 42.2 kN during the first cycle of the 2.50% drift ratio, where

punching shear failure started to occur. By the end of the 2.50% drift ratio, the lateral load had dropped to 32.4 kN, which represent a 25% reduction in the lateral load capacity.

a) Connection E40

b) Connection E50

c) Connection E60

Figure 5.7: Cracking pattern on the free edge of the slab

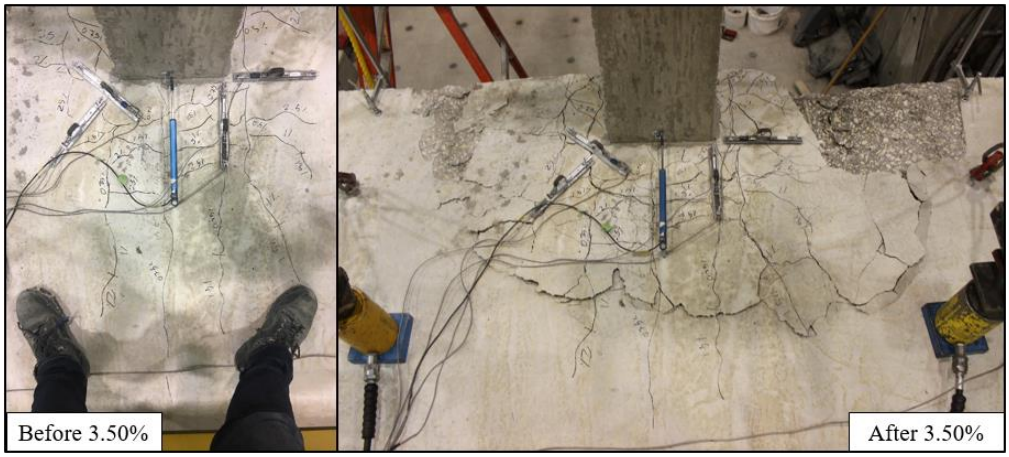

a) Connection E40

b) Connection E50

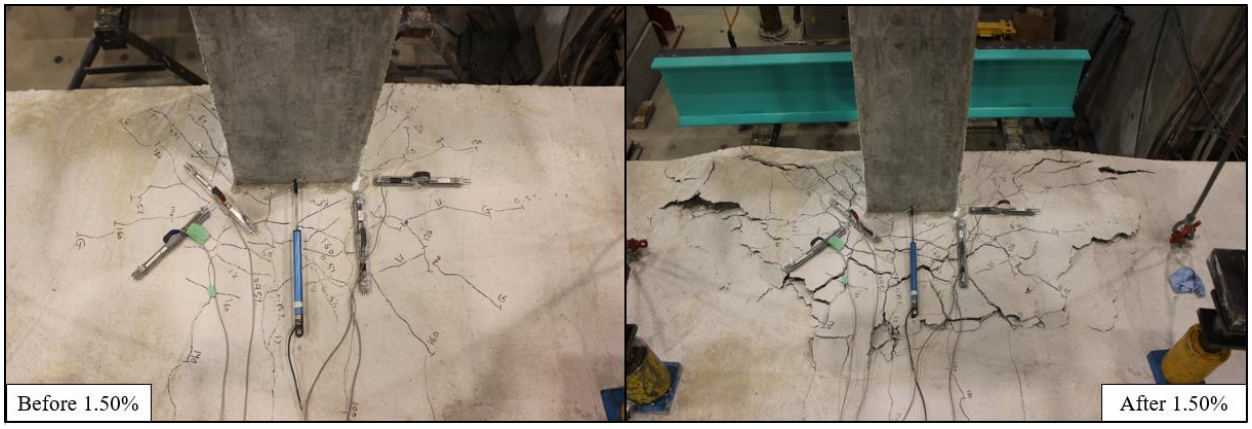

c) Connection E60

Figure 5.8: Cracking pattern on the top surface of the slab

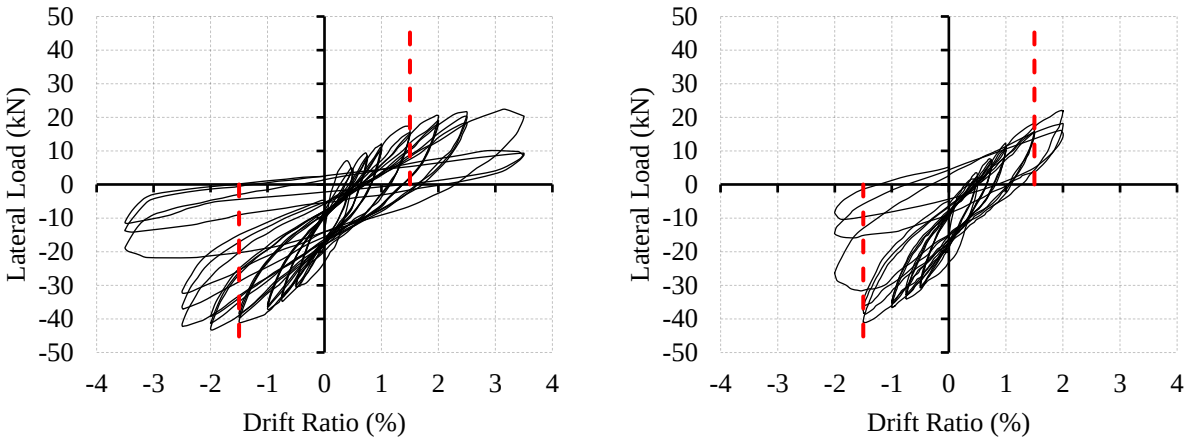

a) Connection E40

b) Connection E50

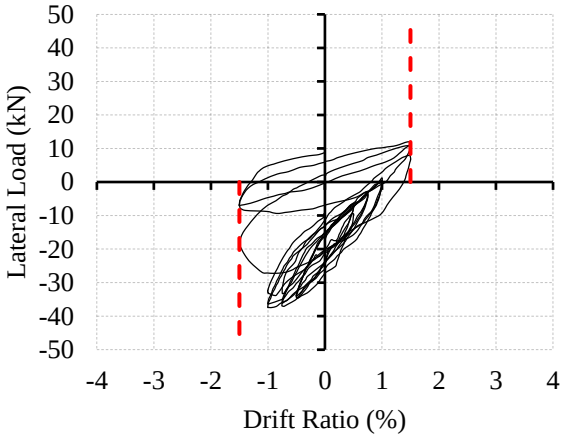

c) Connection E60

Figure 5.9: Hysteresis diagrams

Table 5.3: Test results

Connection	P_g (kN)	P_p (kN)	δ_p (%)	δ_u (%)	δ_y (%)	μ	ε_f (με)
E40	14.2	43.3	2.00	2.50	1.05	2.38	7,300
E50	16.9	41.1	1.50	1.50	0.94	1.60	5,570
E60	24.6	37.4	1.00	1.00	0.68	1.47	5,350 [a]

Note: P_g = gravity lateral load; P_p = peak lateral load; δ_p = peak drift ratio; δ_u = ultimate drift ratio; δ_y = equivalent yield drift ratio; μ = deformability factor; ε_f = flexural reinforcement strain at failure.

[a] Recorded at a distance *d* from column face

When the applied gravity shear ratio was increased to 0.5 in connection E50, the connection was able to sustain the 1.50% drift ratio without losing its gravity load-capacity. The lateral load reached a maximum of 41.1 kN at the first cycle of the 1.50% drift ratio. This value gradually decreased to 36.0 kN after the end of the 1.50% drift ratio, which indicates only a 12.4% reduction in the lateral load capacity. At this point, there were no signs of a punching shear failure yet. Complete punching failure took place and the lateral load capacity was entirely lost when the drift ratio increased to 2.00%. Consequently, when the gravity shear ratio was increased to 0.6, connection E60 was not able to reach the 1.50% drift ratio under this relatively high gravity shear ratio. The connection reached a maximum lateral load of 37.4 kN at the first cycle of the 1.00% drift ratio and lost only 9.4% of its lateral load capacity by the third cycle. Nevertheless, the lateral load capacity was lost when complete punching occurred at the first cycle of the 1.50% drift ratio. Figure 5.10 shows the effect of gravity load on the drift capacity of the test connections. For properly designed GFRP-RC edge connections with a flexural reinforcement ratio of 1.4% and without shear reinforcement to sustain a drift ratio of 1.50% without punching failure, the gravity shear ratio can reach up to 0.5. This value is higher than the 0.4 gravity shear ratio limit associated with steel-RC connections.

5.4.3. Lateral displacement deformability

Figure 5.11 shows envelopes of the hysteresis diagrams of all connections. These envelopes were used to calculate the lateral displacement deformability factor, μ, which quantifies the ability of a GFRP-RC slab-column connection to undergo inelastic deformations before failure. This factor is calculated, for steel-RC connections, as the ratio of the ultimate drift ratio at failure (δ_u) to the drift ratio at yielding of steel reinforcement, where the equivalent drift ratio at yielding (δ_y) is defined by the graphical construction shown in Figure 5.12 as suggested by Pan and Moehle (1989). In

this procedure, the envelope of the hysteresis diagram is idealized by an elasto-plastic relationship. The plastic portion of the idealized relationship passes through the peak lateral load point (P_p). On the other hand, the elastic portion passes through the point of zero drift ratio and a point on the actual curve at a load equal to two-thirds of P_y, which equals P_p, i.e., the peak lateral load, minus the lateral load caused by gravity loads (P_g). The intersection of these two straight portions defines the equivalent yield drift ratio, δ_y. Since GFRP-RC connections are expected to undergo significant deformations before failure due to the low modulus of elasticity of the GFRP reinforcement, the procedure was used to calculate the lateral displacement deformability factor for the test connections.

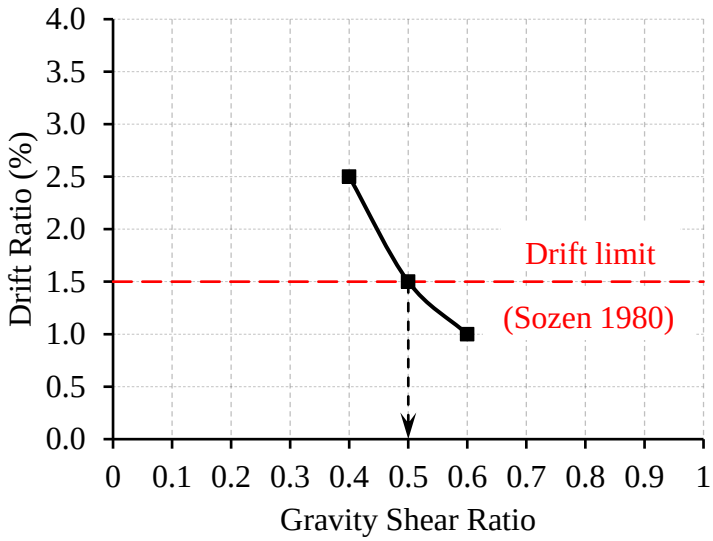

Figure 5.10: Effect of gravity shear ratio on the drift capacity

The values of the lateral displacement deformability factor are listed in Table 5.3**.** In general, slab-column connections without shear reinforcement are expected to have limited deformability. Pan and Moehle (1989) suggested that, if a flat plate system is accompanied by an SFRS that is sufficiently stiff to restrain the interstory drift ratio to 1.5%, a lateral displacement ductility factor

of the slab-column connections of 1.2 would be sufficient. However, Marzouk et al. (2001) mentioned that a ductility factor greater than 2.0 must be achieved before a connection can be considered to behave in a deformable manner. Although these values are low compared to values often considered acceptable in seismic design, the relatively high flexibility of slab-column connections reduces the ductility demands (Pan and Moehle 1989). Connection E40, subjected to the lowest gravity shear ratio, showed the highest deformability with a deformability factor of 2.38, which is slightly higher than the adequate deformability factor of 2.0 suggested by Marzouk et al. (2001). Increasing the applied gravity shear ratio, however, would further reduce the deformability of the connections. Therefore, when the gravity shear ratio was increased to 0.5 and 0.6, the deformability of the connections was reduced by 33 and 38%, respectively. Nevertheless, all connections had deformability factors higher than 1.2 (Pan and Moehle 1989).

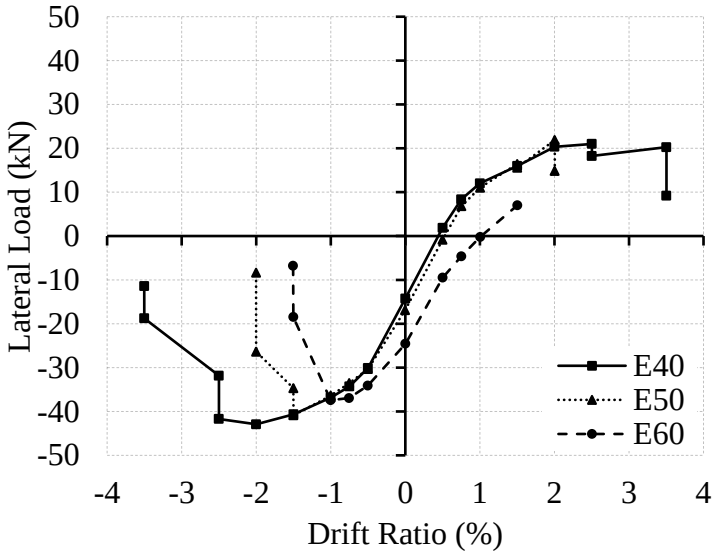

Figure 5.11: Envelopes of hysteresis diagrams

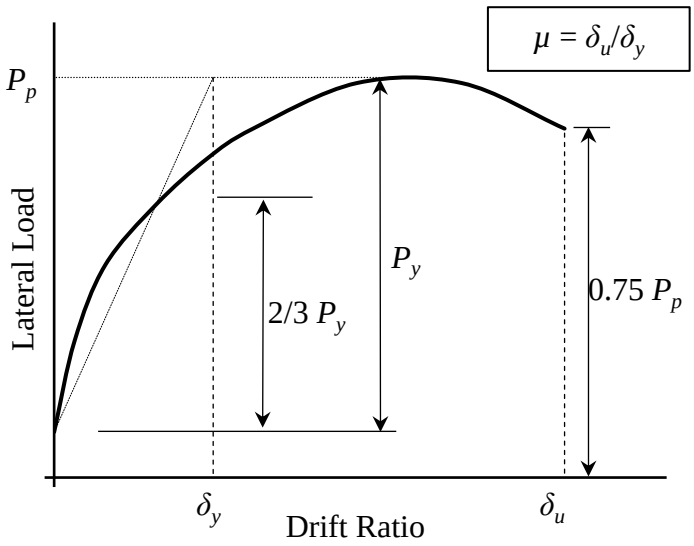

Figure 5.12: Definition of deformability

5.4.4. Stiffness degradation

The peak-to-peak stiffness factor, *k*, which is calculated as the slope of the straight line connecting the two peaks of the third hysteresis loop at each loading cycle as shown in Figure 5.13, is used to assess the stiffness degradation of the connections. The stiffness factors for the test connections at different drift ratios are tabulated in Table 5.4 and are plotted against the drift ratio in Figure 5.14. Increasing the gravity shear ratio decreased the stiffness of the connections at all drift ratios. The initial stiffness, at 0.50% drift ratio, of connections E50 and E60 was 10 and 23% less than that of connection E40. This is attributed to the fact that higher vertical loads resulted in more cracks under gravity loads before the application of lateral loads and, therefore, led to a reduced stiffness. For all connections, the stiffness decreased rapidly with the successive cycles of increasing drifts. Once punching failure occurred, the stiffness dropped dramatically to 29, 34 and 34% of its value prior to failure for connections E40, E50 and E60, respectively.

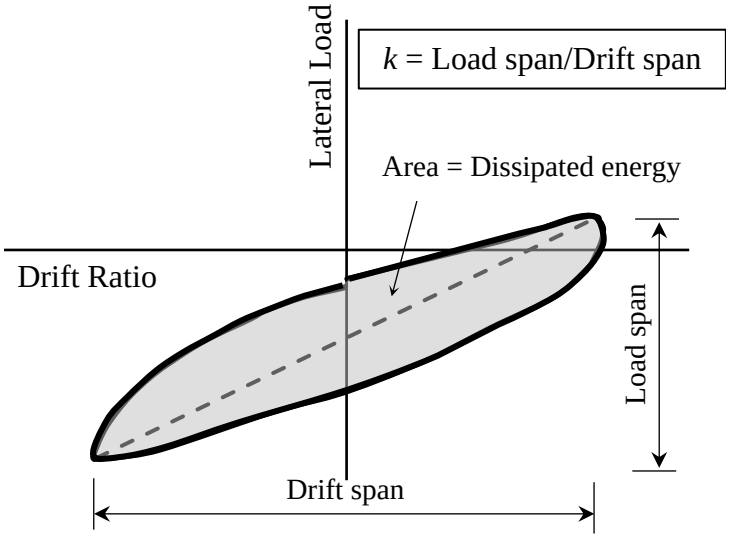

Figure 5.13: Definition of stiffness and energy dissipation factors

Table 5.4: Stiffness and energy dissipation factors

Connection	*k* (kN/m)			E_D (kN.m)
	at 0.50%	at 1.50%	at δ_u	
E40	1,188	598	350	12.4
E50	1,075	550	550	5.8
E60	918	219	640	3.0

Note: *k* = stiffness factor; E_D = accumulative dissipated energy at δ_u; δ_u = ultimate drift ratio.

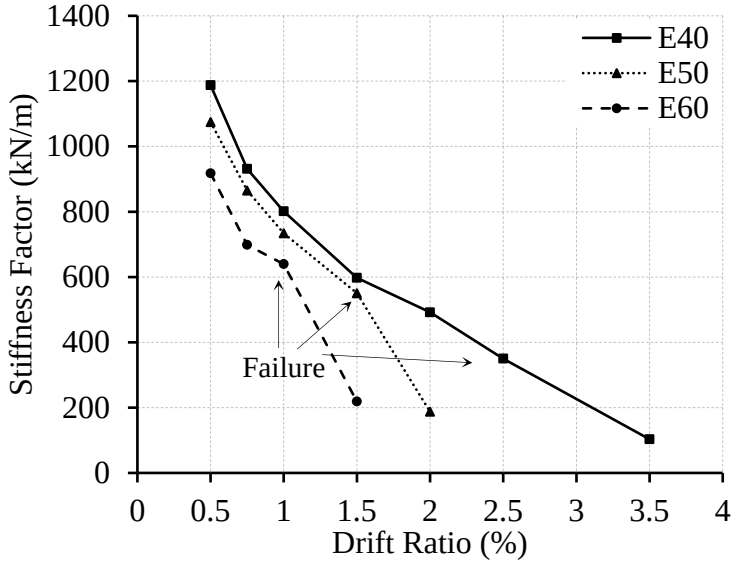

Figure 5.14: Stiffness degradation

5.4.5. Energy dissipation

The energy dissipated during a drift cycle is represented by the area enclosed by the hysteresis loop of this cycle as shown in Figure 5.13, while the accumulative dissipated energy, E_D, was calculated by summing up the energy dissipated in successive drift cycles. Figure 5.15 shows the relationship between the accumulative dissipated energy and drift ratio for all connections. Regardless of the gravity shear ratio, all connections dissipated similar amounts of energy up to 1.00% drift ratio; however, the amount of energy dissipation was different for each connection at failure. Increasing the gravity shear ratio resulted in a more abrupt punching shear failure at relatively lower drift ratios, which decreased the amount of dissipated energy. At the ultimate drift ratio, δ_u, connection E40 dissipated 12.4 kN.m of the seismic energy, which is 2.1 and 4.1 times higher than that dissipated by connections E50 and E60, respectively. The values of the accumulative dissipated energy at the ultimate drift ratio for all connections are listed in Table 5.4.

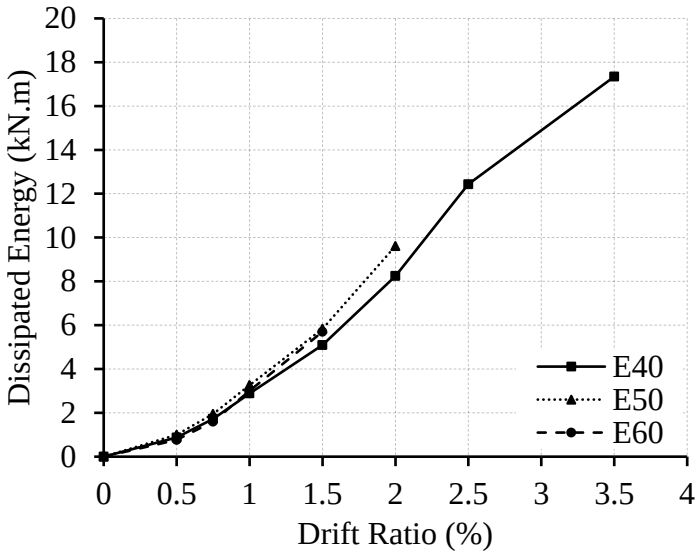

Figure 5.15: Energy dissipation

5.4.6. Flexural reinforcement strains

Figure 5.16 shows the strain profiles of the slab flexural reinforcement passing through the column in the direction perpendicular to the free edge for all connections. These profiles were plotted using the maximum measured tensile strains at each drift ratio. Increasing the gravity shear ratio increased the reinforcement strains before the application of the lateral drifts. At this level, connection E40 experienced strains less than 200 με in all locations, which is consistent with the scarcity of observed cracks in the column vicinity after the application of gravity loads. However, the strain gauge at the column face in connection E50 showed a strain reading of 2,190 με due to the increase in the gravity shear ratio, while all other gauges recorded strains less than 600 με. In connection E60, the strain gauge at the column face showed a strain reading of 2,190 με and strain readings higher than 1,900 με were recorded up to a distance *d* from the column face, where *d* is the average slab depth.

At failure, the maximum measured strains in all connections were well below the rupture strain of the used GFRP bars. This was expected because the connections failed in punching shear well before they develop their full flexural capacities. In addition, should flexural failure have taken place, the failure would have been initiated by concrete crushing rather than rupturing of reinforcing bars as the slabs were over-reinforced. A maximum strain of 7,300 με was measured at the column face in connection E40, which represents approximately 27% of the rupture strain of the used bars. The maximum measured strains for all connections are listed in Table 5.3. For steel-RC connections, maximum strain readings ranging between 6,000 and 7,500 με were reported in edge connections without shear reinforcement (Durrani et al. 1995; Anggadjaja and Teng 2008). Accordingly, the relatively high strain reading of 7,300 με in connection E40, which

is comparable to those experienced by steel reinforcement after yielding, confirms that the large elastic deformations of GFRP can replace the yielding of steel.

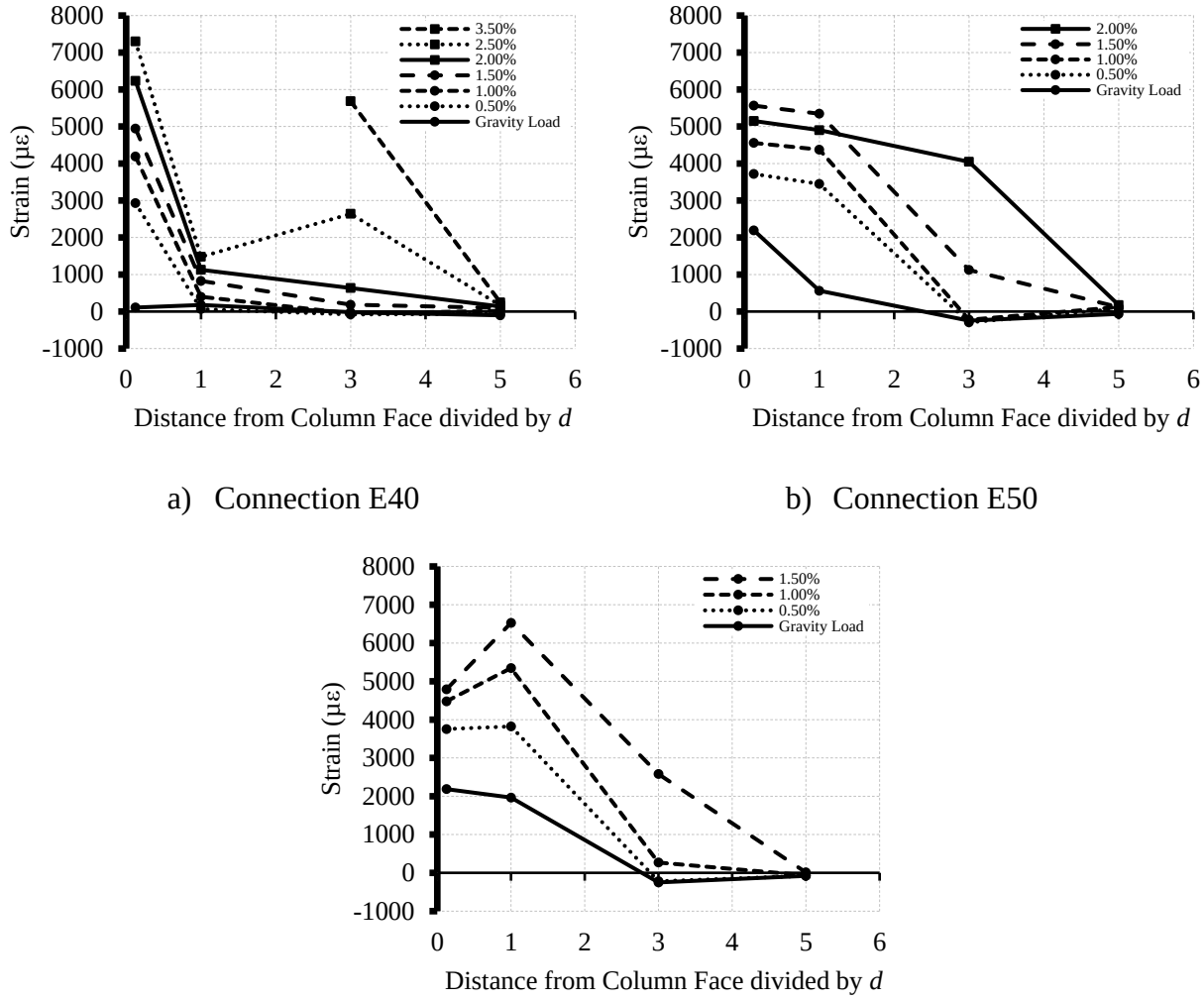

a) Connection E40

b) Connection E50

c) Connection E60

Figure 5.16: Strain profiles of the flexural reinforcement

5.5. Summary and Conclusions

A pioneer experimental investigation was conducted to evaluate the effect of gravity shear ratio on the seismic response of GFRP-RC slab-column edge connections. Three identical full-scale isolated connections were constructed and tested to failure under a combination of gravity and

uniaxial reversed-cyclic lateral loads using a sophisticated test setup. Based on the observed response of the connections, the following conclusions are drawn:

1. The gravity shear ratio (V_g/V_c) is a primary factor affecting the seismic response of GFRP-RC slab-column connections. While connection E40, subjected to V_g/V_c = 0.4, was able to attain a drift ratio of 2.50%, increasing the gravity shear ratio decreased the drift and lateral load capacities of the connections and resulted in a more brittle punching shear failure without sufficient amble warning.
2. The magnitude of the gravity shear ratio must be controlled to ensure the integrity of slab-column connections under simulated seismic loading. Based on the limited number of tests conducted in this study, for properly designed GFRP-RC connections with a flexural reinforcement ratio of 1.4% and without shear reinforcement to achieve a minimum drift capacity of 1.50% without punching failure, the applied gravity shear ratio must not exceed 0.5. This value is higher than the 0.4 limit in ACI 318-19 (2019a) for steel-RC connections.
3. Lateral displacement deformability of GFRP-RC slab-column connections can be quantified using an equivalent yield drift ratio approach. Although increasing the gravity shear ratio significantly decreased the deformability of the connections, all connections had deformability factors higher than 1.2. Only connection E40, subjected to V_g/V_c = 0.4, had a deformability factor higher than 2.0.
4. The stiffness of the connections decreased as the gravity shear ratio increased due to the excessive slab cracking in the column vicinity as a result of the increased gravity loads. Increasing the gravity shear ratio from 40 to 50 and 60% reduced the initial stiffness of the connections by 10 and 23%, respectively.

5. The GFRP-RC slab-column connections dissipated moderate levels of energy, especially when the applied gravity shear ratio is low. When subjected to $V_g/V_c = 0.4$, connection E40 dissipated energy in the order of 2.1 and 4.1 times that dissipated by connections E50 ($V_g/V_c = 0.5$) and E60 ($V_g/V_c = 0.6$), respectively.
6. The connections did not collapse after the punching failure because the bottom GFRP slab reinforcement running through the column (integrity bars), despite their relatively low transverse stiffness, held the slab after punching.

The findings are encouraging to expand the scope of testing to include various design parameters, which will help in developing the much-needed numerical models, and design formulas and guidelines for GFRP-RC flat plate systems in seismic zones.

CHAPTER 6. GFRP SHEAR REINFORCEMENT FOR SLAB-COLUMN EDGE CONNECTIONS SUBJECTED TO REVERSED-CYCLIC LATERAL LOAD

Authors and Affiliation:

- Mohammed G. El-Gendy, PhD Candidate, Department of Civil Engineering, University of Manitoba
- Ehab F. El-Salakawy, Professor, Department of Civil Engineering, University of Manitoba

Journal and Status:

American Society of Civil Engineers (ASCE) Journal of Composites for Construction, published on January 14, 2020.

Reference:

El-Gendy, M., and El-Salakawy, E. 2020. "GFRP shear reinforcement for slab-column edge connections subjected to reversed-cyclic lateral load." *J. Compos. Constr.*, ASCE, 24(2), 04020003, https://doi.org/10.1061/(ASCE)CC.1943-5614.0001000.

Note:

The manuscript had been slightly altered from the original paper by renumbering the tables and figures to include the chapter number. In addition, the reference list and list of notations have been moved to the appropriate sections in the thesis as indicated in the table of contents.

Abstract

In regions of high seismic activity, flat plate systems can be used as gravity force resisting systems, where special moment frames are provided as seismic force resisting systems. Nevertheless, all elements of the reinforced concrete (RC) structure must have sufficient deformability to be capable of deforming into the inelastic range. An efficient method of enhancing the deformability of flat plate systems is providing slab shear reinforcement. This paper presents the results of an experimental program evaluating the efficiency of two new types of glass fiber-reinforced polymer (GFRP) shear reinforcement in enhancing the deformability of GFRP-RC slab-column edge connections. Three full-scale connections were tested under gravity and uniaxial reversed-cyclic lateral loading, one connection was reinforced with GFRP shear studs, one with GFRP corrugated bars, and one had no shear reinforcement. The use of GFRP shear studs and corrugated bars increased the lateral load capacity of the connections by 47 and 44%, respectively. In addition, both types of GFRP shear reinforcement were able to enhance the deformability of the connections significantly, whereas the connection with shear studs was able to sustain deformations associated with 3.50% drift ratio without jeopardizing its gravity load capacity.

Keywords: Cyclic loading; deformability; edge connection; flat plate; GFRP; punching; shear reinforcement; slab-column connection.

6.1. Introduction

Under seismic loads, reinforced concrete (RC) slab-column connections are relatively flexible, which may cause extensive structural and non-structural damage as excessive lateral drifts occur. In addition, the transfer of shear forces and excessive unbalanced moments due to the significant horizontal displacement would promote punching shear failure leading to, in the worst case, a progressive collapse of the entire structure (Mitchell et al. 1990). Accordingly, in regions of high seismic activity, the Canadian Standards Association (CSA) Standard A23.3-14 (CSA 2014a) and the American Concrete Institute (ACI) code ACI 318 (ACI 2014a) allow the use of steel-RC flat plate systems only as gravity force resisting systems (GFRS), where special moment frames or shear walls are provided as the seismic force resisting system (SFRS). Nevertheless, as the entire structure drifts, the flat plate system will undergo the same lateral drifts of the SFRS and, thus, it must be designed for deformation compatibility with the SFRS. This will ensure that the flat plate system can maintain its gravity load capacity with a minimum level of deformability, which makes it able to accommodate the seismically induced lateral drifts without punching shear failure of the slab-column connections.

Sozen (1980) recommended that an RC flat plate system without shear reinforcement should withstand a minimum of 1.50% drift ratio, which is defined as the ratio of the relative lateral drift of two successive floors to the floor height, without punching failure. It was demonstrated that steel-RC slab-column connections can accommodate the minimum 1.50% drift ratio when they are subjected to a gravity shear ratio of no more than 40% (Pan and Moehle 1989; Megally and Ghali 1994). The gravity shear ratio is defined as the ratio of the gravity shear transferred between the slab and the column to the theoretical punching shear strength provided by concrete. When the gravity shear ratio exceeds 40%, shear reinforcement must be used to increase the deformability

and drift capacity of the slabs. Experimental research was conducted on shear-reinforced connections since the 1970s (Carpenter et al. 1973; Hawkins et al. 1975; Durrani et al. 1995; Megally and Ghali 2000c; Matzke et al. 2015). It was demonstrated that shear reinforcement with adequate mechanical anchorage, i.e., stud shear reinforcement, provides more deformability and drift capacity than conventional stirrups. However, both types of reinforcement will allow the connections to satisfy the 1.50% drift ratio at any level of gravity shear ratio (Megally and Ghali 1994; ACI 2010).

On the other hand, fiber-reinforced polymer (FRP) composites are increasingly used to replace conventional steel reinforcement in RC structures, especially those constructed in regions of harsh environmental conditions, to take advantage of their noncorrodible nature. Unlike steel bars, FRP bars do not yield; instead, they behave elastically up to failure without experiencing a ductile phase prior to their brittle rupture. This behavior raises concerns about the feasibility of using FRP reinforcement in RC flat plate systems subjected to seismic activity, in which significant amounts of energy need to be dissipated by the inelastic behavior of the RC elements. Recently, however, the authors (El-Gendy and El-Salakawy 2018b) demonstrated the feasibility of using GFRP bars as longitudinal slab reinforcement in slab-column edge connections subjected to simulated seismic loading, in which the large elastic deformations of the GFRP reinforcement resulting from their low modulus of elasticity and high strength compensated for the absence of yielding. Furthermore, research conducted on GFRP-RC connections reinforced with GFRP shear studs and GFRP corrugated bars demonstrated the efficiency of both types of shear reinforcement in increasing the deformability and ultimate capacity of connections subjected to monotonically-increased axial load and unbalanced moment (El-Gendy and El-Salakawy 2016; Hussein and El-Salakawy 2018; Mostafa and El-Salakawy 2018). These results encouraged the authors to investigate the efficiency

of such innovative GFRP shear studs and GFRP corrugated bars in connections subjected to simulated seismic loads. In this paper, the behavior of both types of GFRP shear reinforcement in slab-column edge connections subjected to gravity and uniaxial reversed-cyclic lateral loading is examined.

6.2. Experimental Program

6.2.1. Materials

Normal-weight, ready-mix concrete with a target 28-day compressive strength of 40 MPa was used for all connections. The actual concrete compressive strength was determined by testing standard cylinders (100 × 200 mm) on the day of testing according to CSA A23.1-14/A23.2-14 (CSA 2014b). The concrete strength for all connections on the day of testing is given in Table 6.1.

Table 6.1: Details of test connections

Connection	Shear reinforcement		Gravity shear		Concrete strength (MPa)
	Type	Spacing (mm)	Ratio (%)	Load (kN)	
EXX	-	-	60	228	48
ESS	Shear studs	80	60	229	49
ECB	Corrugated bars	80	60	217	41

The slabs of all connections were reinforced with top and bottom orthogonal reinforcement assemblies of No. 15 sand-coated GFRP bars. For the top assembly, straight bars were used in the direction parallel to the free edge (the parallel direction) whereas single-end hooked bars were used in the direction perpendicular to the slab's free edge (the perpendicular direction). The hooked end coincided with the location of maximum negative moment (i.e., the free edge of the slab) to provide the required anchorage. Alternatively, for the bottom assembly, straight bars were used in both directions. In addition, Nos. 25M and 10M deformed steel bars and stirrups, respectively,

were used to reinforce the columns in all connections. The mechanical properties of the straight and hooked GFRP bars obtained from standard tests carried out according to ASTM D7205/D7205M (ASTM 2016) and ASTM D7914/ D7205M (ASTM 2014), as applicable, are given in Table 6.2.

Table 6.2: Mechanical properties of the used GFRP reinforcement

Bar shape	Bar size	Nominal diameter (mm)	Area (mm^2)	Tensile strength (MPa)	Modulus of Elasticity [a] (GPa)	Ultimate strain (%)
Straight	No. 15	15.9	199[b] [234][c]	1,712	66	2.60
Hooked (straight portion)	No. 15	15.9	199[b] [227][c]	1,405	52	2.70
Hooked (bent portion)	No. 15	15.9	199[b] [227][c]	725	-	-
Shear stud	No. 13	12.8	129[b] [135][c]	551[d]	68	0.81[d]
Corrugated bar (straight portion)	No. 13	12.8	129[b] [149][c]	1,281[e]	52	2.50[e]

[a] Calculated using nominal area
[b] Nominal area according to CSA S807-10 (CSA 2015)
[c] Measured area according to Annex A in CSA S806-12 (CSA 2017)
[d] Usable design stress/strain provided by the manufacturer (corresponds to a pull-out load capacity of 70 kN)
[e] Properties of straight portion as provided by the manufacturer

For the shear reinforcement, two recently developed types of GFRP shear reinforcement were used: shear studs with headed ends and corrugated bars. The shear studs comprised 170-mm long, No. 13 bars with 70-mm long, cast-on tapered heads. The tapered heads, which were made of a thermoplastic matrix reinforced with discrete short fibers, had an outer diameter of 25 mm (two times the bar diameter) tapered in five steps toward the bar as shown in Figure 6.1. The pullout capacity of the shear studs was 70 kN as provided by the manufacturer (Pultrall Inc., personal communication, 2017). This value corresponds to a tensile stress of 551 MPa (30% of the ultimate

tensile strength of the bar, 1,848 MPa) and a tensile strain of 8,100 με. On the other hand, the corrugated bars were No. 13 sand-coated bent bars with a 90° angle between the vertical stems and the horizontal portions and a total height of 170 mm. Each corrugated bar comprised nine vertical stems spaced at 80 mm center-to-center, which is half the average slab depth, *d*, as shown in Figure 6.1. The mechanical properties of the shear studs and corrugated bars were provided by the manufacturer and are given in Table 6.2.

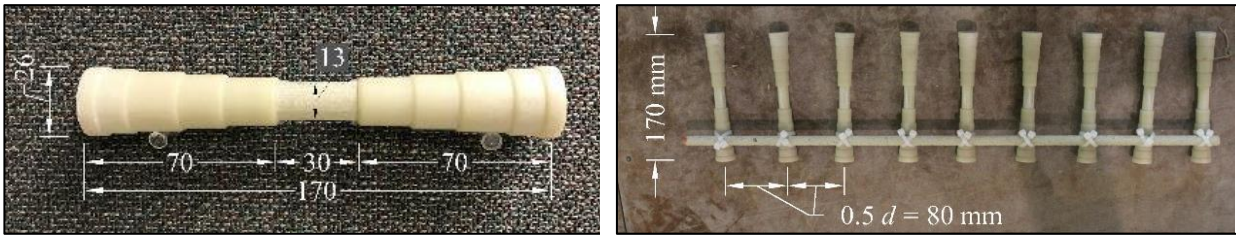

a) Shear stud b) Shear studs' rail

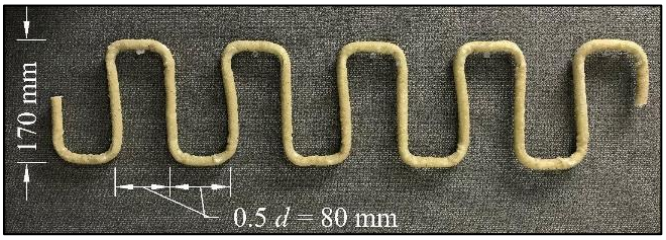

c) Corrugated bar

Figure 6.1: GFRP shear reinforcement (dimensions in mm)

6.2.2. Test specimens

Three full-scale isolated slab-column edge connections were constructed and tested under gravity and uniaxial reversed-cyclic lateral loading. All connections were similar in all aspects except the shear reinforcement type; one control connection had no shear reinforcement (Connection EXX), one was reinforced with GFRP shear studs (Connection ESS), and one was reinforced with GFRP corrugated bars (Connection ECB). The specimens were modeled after a multistory GFRP-RC flat

plate parking garage structure with a story height of 3.0 m. The prototype building consisted of five 5.5-m long bays in each direction with 300-mm square columns and two I-shaped shear walls running vertically through it in order to control the lateral deformations, i.e., work as the SFRS. The design was carried out according to CSA A23.3-14 (CSA 2014a) and CSA S806-12 (CSA 2017), where applicable. The resulting slab was 200-mm thick and was reinforced with negative (top) and positive (bottom) flexural reinforcement assemblies, in which the reinforcement ratio of the top assembly in the column strip in the perpendicular direction was 1.40%.

The isolated connections were extracted from the prototype building by delineating the boundaries at the contra-flexure lines. When a flat plate system is subjected to gravity load only, these lines are assumed between $0.1L_s$ and $0.3L_s$, in which L_s is the center-to-center spacing between columns. On the other hand, when a system is subjected to gravity and lateral loads, contraflexure lines are assumed at 0.5 L_s (Pan and Moehle 1989; Wey and Durrani 1992; Robertson et al. 2002). For the test specimens, because the lateral load is applied in the perpendicular direction only, the contraflexure lines were assumed at midheights of the columns and at distances of 0.30 and 0.50 L_s from the centerlines of edge columns in the parallel and perpendicular directions, respectively. Accordingly, the slab of an isolated connection had dimensions of 3,300 × 2,900 × 200 mm with square columns extending 1,400 mm above and below the slab. Nevertheless, slabs with dimensions of 3,300 × 3,100 × 200 mm were cast to allow for slab supporting clearance. Similarly, both the top and bottom columns had a nominal height of 1,360 mm so that the distance between the centerline of the slab and the tip of each column is 1,460 mm, i.e., approximately half the story height. However, to permit the attachment of the column support and the hydraulic actuator, as discussed subsequently, the top and bottom column heights were changed to 1,900 and 970 mm, respectively. The details of the test connections are shown in Figure 6.2 and Figure 6.3.

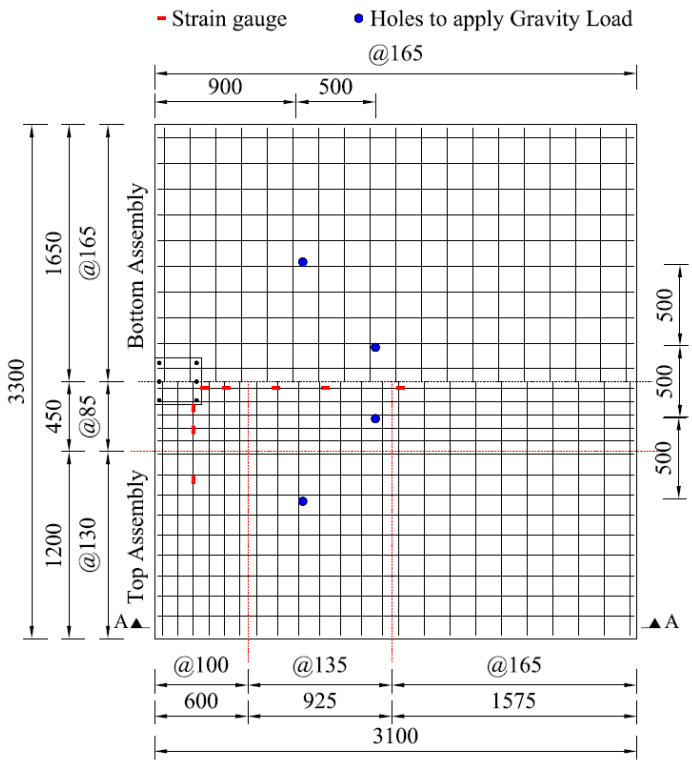

Figure 6.2: Typical slab dimensions and flexural reinforcement (dimensions in mm)

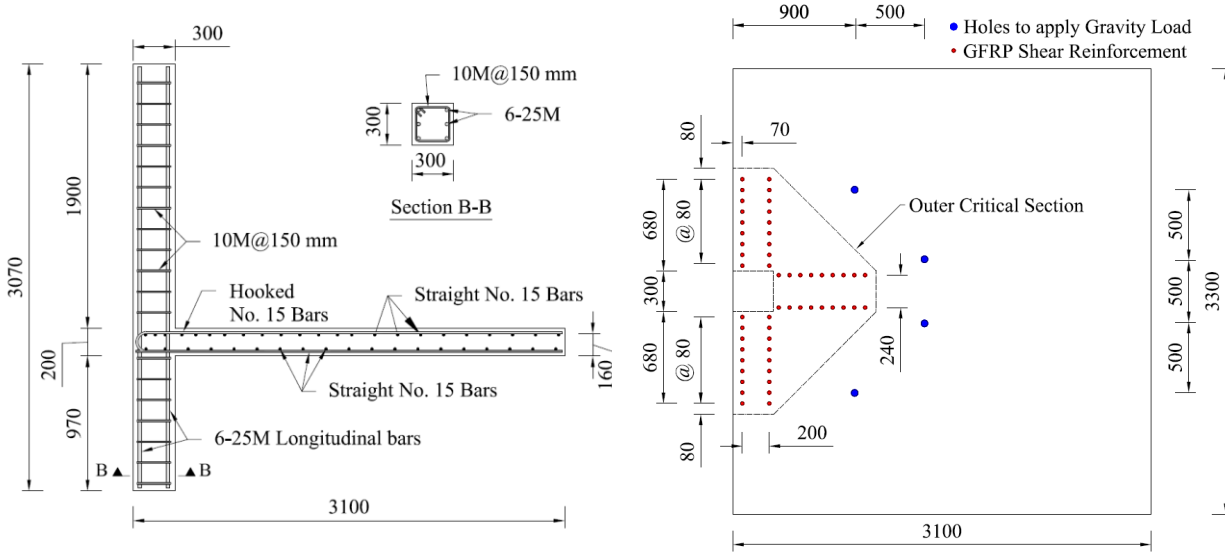

a) Section A-A (from Figure 6.2) b) Shear reinforcement configuration

Figure 6.3: Typical column reinforcement and slab shear reinforcement (dimensions in mm)

Connection ESS contained six concentric rails of shear studs, i.e., two rails were perpendicular to each side of the edge column. Each rail consisted of nine shear studs (as shown in Figure 6.1) spaced at 80 mm (0.50*d*) with the first stud located at a distance of 0.25*d* from the column face, allowing the studs to extend to a distance of 4.25*d* from the column face. This configuration follows CSA A23.3-14 (CSA 2014a), which requires shear reinforcement in steel-RC connections subjected to seismic loading to be spaced no more than 0.50*d* and to extend a minimum of 4.00*d* beyond the column face. Similarly, in Connection ECB, six GFRP corrugated bars were placed in the slab at the column vicinity, with two bars perpendicular to each side of the edge column. Because the corrugated bars comprised nine vertical stems spaced at 80 mm (0.50*d*) center-to-center, placing the corrugated bars with the vertical stem closest to the column at 0.25*d* from the column face resulted in identical configuration of the shear reinforcement to that of Connection ESS. The shear reinforcement configuration of both connections is shown in Figure 6.3.

6.2.3. Test setup

The connections were tested under uniaxial reversed-cyclic lateral loading with a constant level of gravity load. As shown in Figure 6.4, the connections were supported at the column base and at the slab edge running parallel to the slab's free edge, whereas the other two slab edges were unrestrained. The supported slab edge was stiffened by two horizontal 100 × 100 × 6.25 mm hollow structural sections (HSS) at the top and bottom of the slab to prevent out-of-plane displacement. The stiffened edge was supported by three vertical 100 × 100 × 6.25 mm HSS link supports to simulate a roller support. These vertical link supports were pinned at the top to the horizontal HSS at the soffit of the slab edge and pinned at the bottom to a set of horizontal 100 × 100 × 6.25 mm HSS, which were fixed to the laboratory's floor. A steel hinge connection fixed to the laboratory's floor was connected to the column base to allow rotation in the perpendicular

direction only. In addition, the top of the column was pinned to a horizontally placed fully dynamic hydraulic actuator with load and stroke capacities of 1,000 kN and 500 mm, respectively, which was used to apply the reversed-cyclic lateral loading. The distance between the centerline of the actuator and the axis of rotation of the hinge support was set to 2,920 mm. The actuator transferred its horizontal reaction forces to a rigid L-shaped RC reaction wall (3.5-m wide × 6.0-m high per leg). On the other hand, the gravity load was applied to the slab using three hydraulic jacks to tension four threaded steel bars running through premade holes in the slab and anchored at the laboratory's floor.

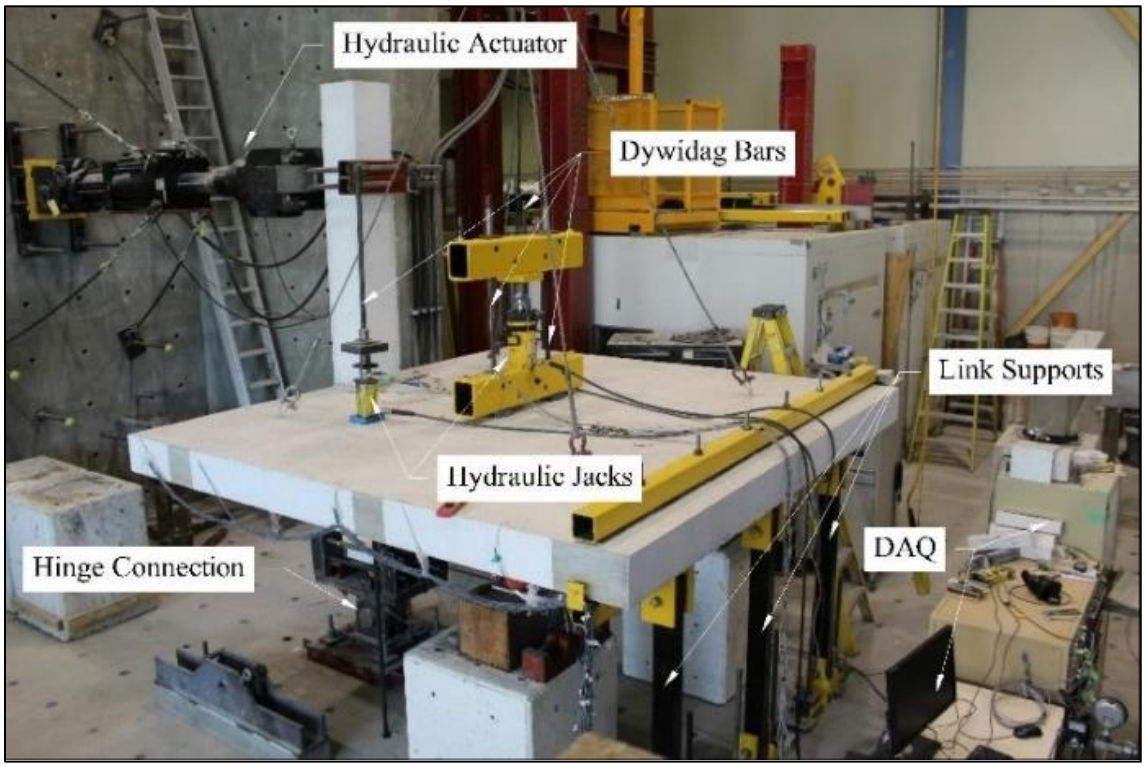

Figure 6.4: Test setup

6.2.4. Instrumentation

In each connection, 12 six-mm long electrical-resistance strain gauges (ESG) were attached to the top slab flexural reinforcement to measure the strains as shown in Figure 6.2. In addition, where

shear reinforcement was present, 12 six-mm long ESGs were attached at critical locations to the vertical stems of the shear reinforcement. Also, four load cells were used to monitor gravity loads. Three cells were attached to the hydraulic jacks applying the gravity load, whereas the fourth one was installed at the bottom of the column to record the vertical reaction at the support.

6.2.5. Loading procedure

The test started by applying the gravity load. All connections were subjected to the same high gravity shear ratio of 60%, i.e., the initial gravity load applied to the connections was 60% of the nominal punching shear strength provided by concrete, V_c. The nominal punching shear strength provided by concrete was calculated by multiplying the shear stress resistance provided by concrete, v_c, by the area $b_o d$, of the critical perimeter located at a distance $d/2$ from the column face. According to CSA S806-12 (CSA 2017), the shear stress resistance provided by concrete, v_c, is calculated as the smallest of the three values described in Equation 6.1 to Equation 6.3, where v_c = shear stress resistance provided by concrete (MPa); β_c = ratio of long side to short side of the column; λ = factor to account for concrete density; ϕ_c = resistance factor for concrete; E_F = modulus of elasticity of FRP reinforcement (MPa); ρ_F = longitudinal FRP reinforcement ratio; f_c' = concrete compressive strength (MPa) and shall not be taken greater than 60 MPa; α_s = dimensionless coefficient equal to three for edge connections; d = average depth of the slab (mm); and b_o = length of the critical perimeter for shear at $d/2$ from column face (mm).

$$V_c = \left(1 + \frac{2}{\beta_c}\right)\left[0.028\lambda\phi_c\left(E_F\rho_F f_c'\right)^{\frac{1}{3}}\right]\left(b_o d\right) \qquad \text{Equation 6.1}$$

$$V_c = \left[\left(\frac{\alpha_s d}{b_o}\right) + 0.19\right]\left[0.147\lambda\phi_c\left(E_F\rho_F f_c^{'}\right)^{\frac{1}{3}}\right]\left(b_o d\right) \qquad \text{Equation 6.2}$$

$$V_c = \left[0.056\lambda\phi_c\left(E_F\rho_F f_c^{'}\right)^{\frac{1}{3}}\right]\left(b_o d\right) \qquad \text{Equation 6.3}$$

Because all three values depend on the compressive strength of concrete, the amount of gravity load transferred to the column slightly varied based on the actual concrete strength on the day of testing. The values of the initial gravity loads transferred to the columns are given in Equation 6.1. The initial gravity load values are considerably higher than the service load typically applied to the flat plate system (approximately 52 kN in this case). Consequently, the slab is expected to experience considerable cracking under the application of gravity load. The gravity load was applied by pumping the jacks simultaneously until the specified gravity load was transferred to the column. This was done while the horizontal actuator was locked to prevent lateral displacement of the connections. Once the specified gravity load was achieved, it was maintained throughout the remainder of the test, while the horizontal actuator started to apply the lateral load.

The lateral load was simulated by a displacement-controlled uniaxial quasi-static reversed-cyclic loading at the column tip at a rate of 0.01 Hz following the scheme shown in Figure 6.5, which was adopted from ACI 374.1 (ACI 2005b). In this scheme, the connections were subjected to increasing specified drift ratios in several steps, in which each step comprised three fully reversed cycles with the same drift ratio in order to ensure stable formation of cracks. All drift ratios were determined such that the ratio of each one to its predecessor fell between 1.25 and 1.5. Eventually, the tests were stopped when punching failure occurred or when at least 25% of the lateral load capacity was lost according to ACI 374.1 (ACI 2005b). The drift and lateral load were considered

positive when the actuator was pushing the column and negative when the actuator was moving in the opposite direction.

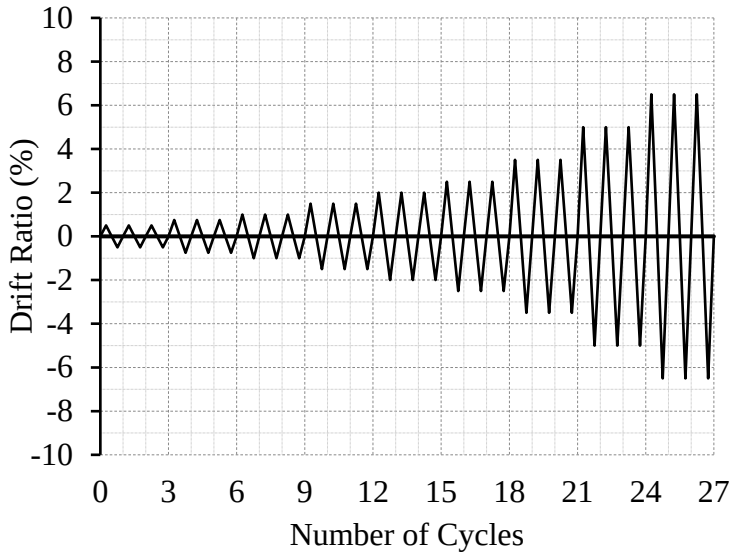

Figure 6.5: Lateral drift scheme

6.3. Experimental Results and Discussion

6.3.1. Mode of failure and cracking pattern

Connection EXX (without shear reinforcement) exhibited an abrupt punching shear failure of the slab in the column vicinity, where the column along with a surrounding part of the slab suddenly punched through the remainder of the slab. On the other hand, Connection ECB (with corrugated bars), encountered significant deformations and crack widening before failing by punching shear inside the shear-reinforced zone after experiencing considerable lateral drifts. In addition to excessive deformations and considerably wide cracks, significant concrete damage and spalling took place in Connection ESS (with shear studs) before punching shear failure occurred inside the shear-reinforced zone at a higher drift ratio than that of Connection ECB. For all connections, the two bottom reinforcing bars passing through the column (integrity bars), and the shear

reinforcement in the shear-reinforced connections, prevented the complete collapse of the slabs after punching.

Figure 6.6 to Figure 6.8 show different cracking patterns for Connections EXX, ESS, and ECB, respectively. In all connections, flexural cracks developed on the slab top and bottom surfaces and on the free edge during the application of gravity loads. The first circumferential flexural crack on the slab top surface was observed at the slab-column interface when the gravity shear transferred to the column was 80 kN for all connections. This value represents 35, 35, and 37% of the specified gravity load for Connections EXX, ESS, and ECB, respectively. Simultaneously, torsional and radial flexural cracks initiated on the slab top surface at the inner corners of the column and propagated symmetrically toward the slab edges. In addition, diagonal shear cracks started to form on the free edge. The second circumferential crack on the slab top surface was observed when the gravity shear was ranging between 160 and 180 kN (70 and 79% of the specified gravity load) for Connections EXX and ESS, respectively. For Connection ECB, however, this crack was not observed until lateral drifts were applied. This cracking behavior under gravity loads is similar to that reported in the literature of GFRP-RC edge connections subjected to monotonically-increased axial load and unbalanced moment (El-Gendy and El-Salakawy 2016, 2018a; Mostafa and El-Salakawy 2018).

During the application of lateral drifts, additional radial flexural cracks and diagonal shear cracks developed on the slab top surface and free edge for all connections. In addition, other diagonal shear cracks on the free edge developed in a perpendicular direction to the ones developed under gravity loading due to the reversed nature of the lateral loading. These cracks spread and opened as the test progressed until the final typical cracking pattern developed.

a) Slab top surface at failure

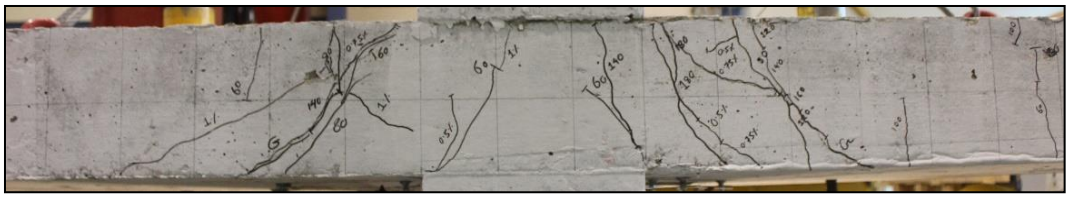

b) Slab free edge after 1.00% drift ratio

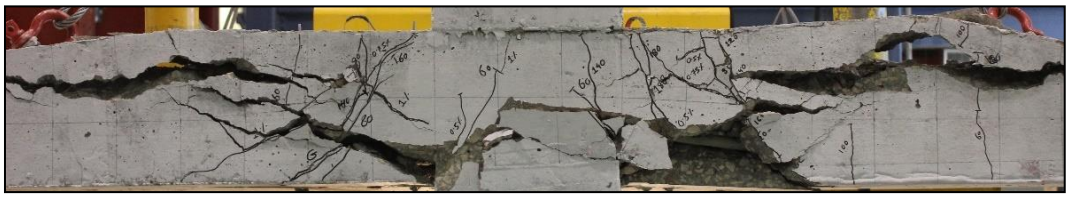

c) Slab free edge after 1.50% drift ratio (at failure)

d) Internal cracking

Figure 6.6: Cracking patterns for connection EXX

a) Slab top surface at failure

b) Slab free edge after 2.50% drift ratio

c) Slab free edge after 6.50% drift ratio (at failure)

d) Internal cracking

Figure 6.7: Cracking patterns for connection ESS

a) Slab top surface at failure

b) Slab free edge after 2.50% drift ratio

c) Slab free edge after 3.50% drift ratio (at failure)

d) Internal cracking

Figure 6.8: Cracking patterns for connection ECB

Connection EXX (without shear reinforcement) punched suddenly, with a dramatic decay of the lateral load capacity, during the first cycle of the 1.50% drift ratio. Before then, there were no considerable signs of failure (e.g., concrete spalling, wide diagonal shear cracks on the free edge, and wide circumferential flexural cracks on the top surface). Figure 6.6b and Figure 6.6c show the free edge of Connection EXX before and after the application of the 1.50% drift ratio. During the application of the 2.50% drift ratio, Connection ESS experienced significant concrete spalling at the free edge as shown in Figure 6.7b. At this level, the bottom heads of the shear studs close to the column at the free edge were exposed and had lost most of the concrete confinement. However, the remaining studs kept functioning and, despite the extensive shear cracks at the free edge, the lateral load capacity was maintained as the lateral drift ratios kept increasing up to 5.00%, when the punching shear failure started to occur and the lateral load capacity started to decrease. Once the lateral drift ratio was increased to 6.50%, complete punching shear failure was observed and the lateral load capacity was lost. At this moment, the slab was severely damaged at the column vicinity as shown in Figure 6.7a and Figure 6.7c. Unlike Connection ESS, Connection ECB did not experience significant concrete spalling before failure. The punching failure occurred during the first cycle of the 3.50% drift ratio without considerable warning in terms of concrete spalling and significantly wide cracks as shown in Figure 6.8b and Figure 6.8c. This cracking behavior under gravity and uniaxial reversed-cyclic lateral loading is similar to that reported in the literature of steel-RC edge connections tested under similar conditions (Robertson and Durrani 1991; Megally and Ghali 2000c; Anggadjaja and Teng 2008).

6.3.2. Hysteretic response

Figure 6.9 shows plots of the hysteresis diagrams for all connections. These diagrams represent the relationship between the applied lateral load at the column and the corresponding drift ratio.

The drift ratio was calculated as the horizontal displacement of the column at the point of lateral load application divided by the distance from that point to the axis of rotation at the column base, i.e., 2,920 mm. When gravity load is applied to an edge connection before the application of lateral drifts, unbalanced moments will be transferred to the column generating lateral loads as the actuator holds the column in place. Subsequently, when lateral drifts are applied, the hysteretic loops do not originate from the zero-load point; instead, they originate from a point that corresponds to zero drift and the lateral load value resulting from the unbalanced moments.

The major test results are given in Table 6.3, in which the peak lateral load (P_p) is the maximum measured lateral load; the peak drift ratio (δ_p) is the drift ratio corresponding to P_p; and the ultimate drift ratio (δ_u) is the maximum drift ratio the connection was able to sustain before failure. Due to the considerably high gravity shear ratio applied during the test, Connection EXX was able to sustain only 1.00% drift ratio at a peak lateral load of 37.4 kN. Once the applied drift ratio was increased to 1.50%, the lateral load drastically dropped to a value of 6.8 kN (18% of the peak lateral load) and punching failure occurred as mentioned previously.

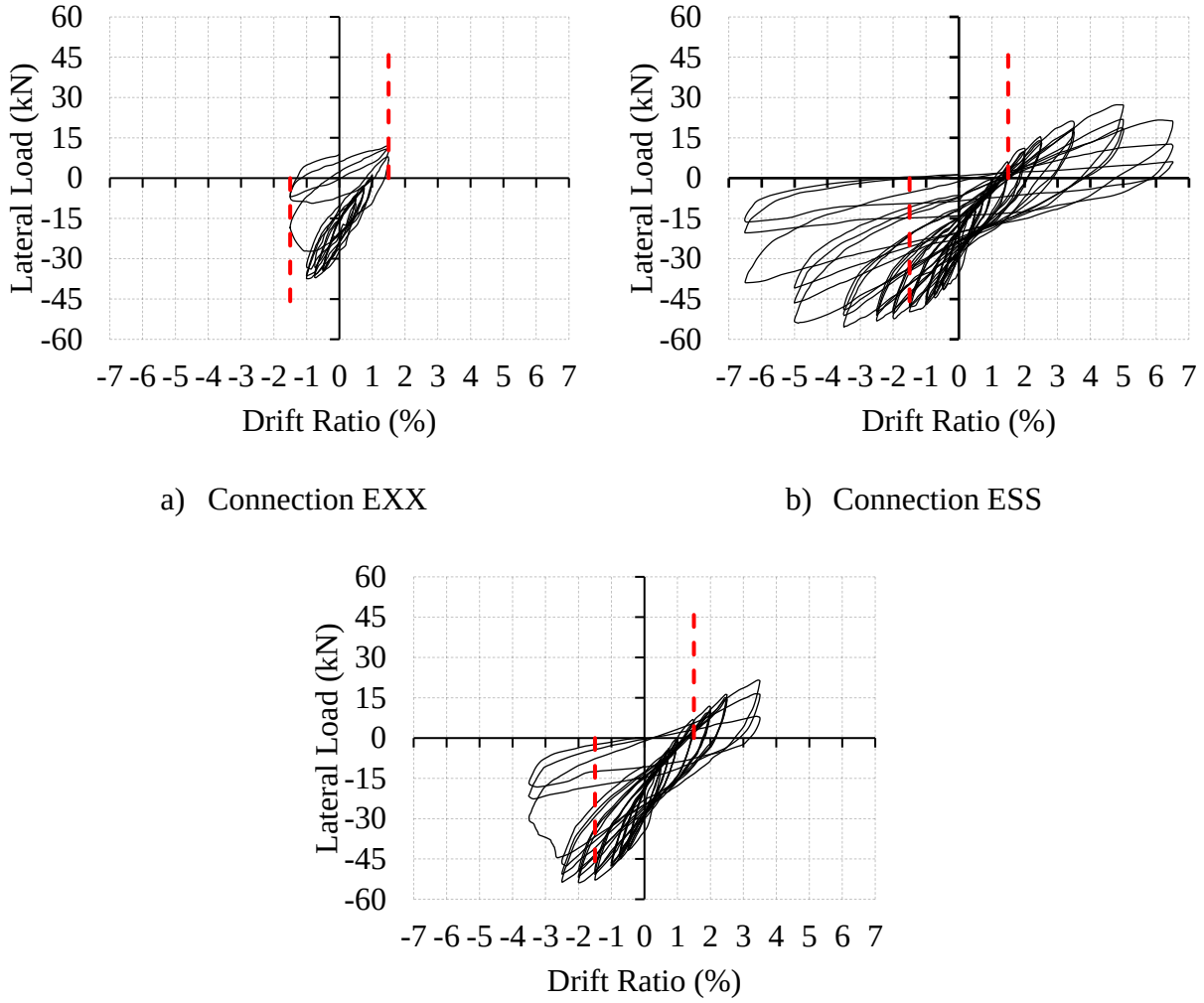

a) Connection EXX

b) Connection ESS

c) Connection ECB

Figure 6.9: Hysteresis diagrams

Table 6.3: Test results

Connection	P_p (kN)	Drift ratio (%)			μ	Maximum strain at failure (με)	
		δ_p	δ_u	δ_y		Flexural reinforcement	Shear reinforcement
EXX	37.4	1.00	1.00	0.68	1.47	6,530	N/A
ESS	55.1	3.50	3.50	1.49	2.35	10,140	3,270
ECB	53.8	2.00	2.50	1.22	2.05	8,470	5,040

Note: P_p = peak lateral load; δ_p = peak drift ratio; δ_u = ultimate drift ratio; δ_y = equivalent yield drift ratio; μ = deformability factor.

The presence of the well-anchored shear studs, however, allowed Connection ESS to sustain much higher drift ratios and lateral loads. The lateral load of Connection ESS continued to increase until it reached a maximum of 55.1 kN (47% higher than that of Connection EXX) at the first cycle of the 3.50% drift ratio. Then, the lateral load gradually decreased until it reached 40.8 kN at the third cycle of the 5.00% drift ratio, at which the punching shear failure started to occur. This value is 74% of the peak lateral load, which indicates more than 25% loss of the lateral load. On the other hand, although the corrugated bars improved the lateral load and drift capacities of the connection, Connection ECB was not able to sustain the same drift ratios as those experienced by Connection ESS. At the first cycle of the 2.00% drift ratio, Connection ECB reached a maximum lateral load of 53.8 kN. Subsequently, this value gradually decreased to 47.6 kN at the third cycle of the 2.50% drift ratio. Once the applied drift ratio was increased to 3.50%, the lateral load dropped to 16.8 kN (31% of the peak lateral load) and punching failure took place. Accordingly, despite being subjected to a high gravity shear ratio of 60%, both shear-reinforced connections were able to reach drift ratios considerably higher than the recommended 1.50%.

6.3.3. Lateral displacement deformability

In order to quantify the ability of a GFRP-RC slab-column connection to undergo inelastic deformations before failure, the lateral displacement deformability factor, μ, was calculated. This factor is analogous to the lateral displacement ductility factor for steel- RC connections, which is calculated as the ratio of the ultimate drift ratio at failure (δ_u) to the drift ratio at yielding of steel reinforcement. In steel-RC connections, yielding spreads gradually across the slab reinforcement and, thus, there is no distinct yielding point. Accordingly, several definitions of an equivalent yielding point were reported in the literature. One of these definitions is the arbitrary procedure proposed by Pan and Moehle (1989) as shown in Figure 6.10. In this procedure, the envelope of

the drift ratio-lateral load relationship is drawn and idealized by an elastoplastic relationship. The elastic portion of the idealized relationship is a secant passing through the point of zero drift ratio and a point on the actual curve at a load equal to two-thirds of P_y, which equals P_p, i.e., the peak lateral load, minus the lateral load caused by gravity loads. Then, the plastic portion of the idealized relationship passes through the peak lateral load. The intersection of these two straight lines defines the equivalent yield drift ratio, δ_y.

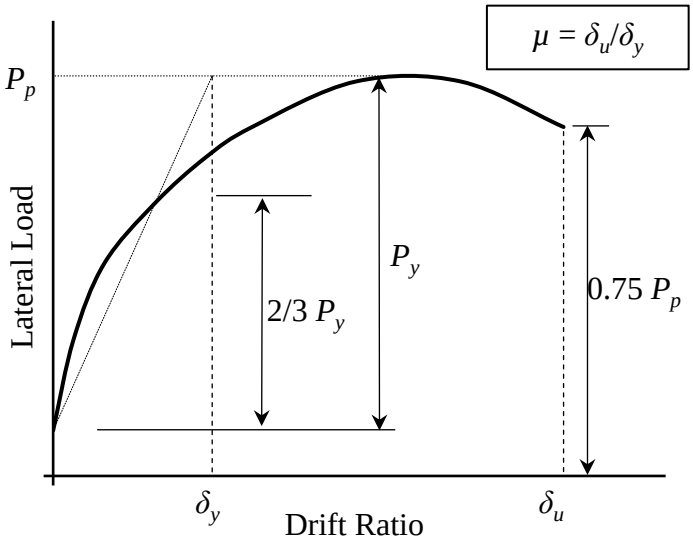

Figure 6.10: Definition of deformability

For GFRP-RC connections, although GFRP reinforcement does not yield, GFRP-RC connections are expected to undergo significant deformations before failure due to the low modulus of elasticity of the GFRP reinforcement. Thus, to assess the ability of a GFRP-RC connection to undergo inelastic deformations before failure, the aforementioned procedure was used to calculate the lateral displacement deformability factor of the GFRP-RC connections as given in Table 6.3. Envelopes of the hysteresis diagrams of all connections are plotted in Figure 6.11. The use of shear reinforcement in the slabs significantly increased the ultimate drift capacity and deformability of

the connections. Using shear studs and corrugated bars increased the deformability of the connection by 60 and 40%, respectively. However, Connection ESS achieved higher ultimate drift ratio (3.50%) than that achieved by Connection ECB (2.50%) with 15% higher deformability. In general, a lateral displacement deformability factor greater than 2.0 must be achieved before a structural member can be considered to behave in a deformable manner (Marzouk et al. 2001). Although the connection without shear reinforcement (Connection EXX) was not able to achieve this level of deformability, both shear-reinforced connections exceeded this minimum required level.

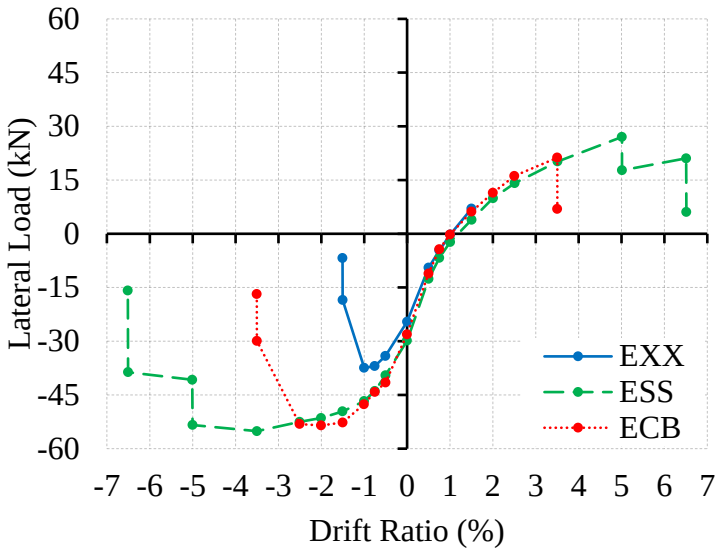

Figure 6.11: Envelopes of hysteresis diagrams

6.3.4. Stiffness degradation

To assess the stiffness degradation of the connections, the peak-to-peak stiffness factor, *k*, was used. This factor was calculated as the slope of the straight line connecting the two peaks of the third hysteresis loop at each loading cycle as shown in Figure 6.12. The values of the stiffness factors for the three connections were plotted against the drift ratio in Figure 6.13. In addition,

Table 6.4 gives the stiffness factors for all connections at different drift ratios along with the stiffness degradation factor, which is the ratio between the stiffness factor at 1.50% drift ratio to the initial stiffness factor (at 0.50% drift ratio). Cracking of the slab due to the application of gravity loads resulted in relatively low initial stiffness of the connections under lateral loading; however, using shear reinforcement enhanced the initial stiffness of the shear-reinforced connections. Connections ESS and ECB had 19 and 23% higher initial stiffness, respectively, than that of Connection EXX. This is attributed to the role of the vertical stems of the shear reinforcement in controlling the propagation of web shear cracks, which start first at the column vicinity before the development of circumferential flexural cracks as described by ASCE-ACI Task Committee 426 (1974). Furthermore, the horizontal portions of the corrugated bars slightly improved the initial stiffness of Connection ECB by controlling the flexural cracks in the column vicinity.

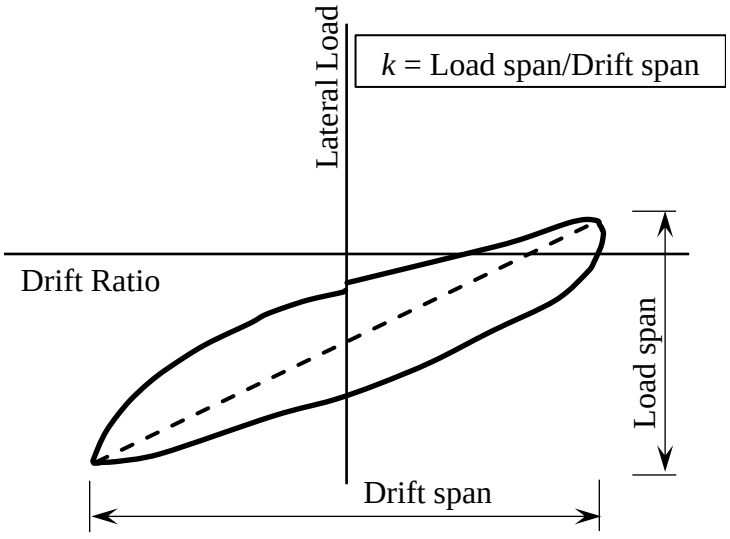

Figure 6.12: Definition of stiffness factor

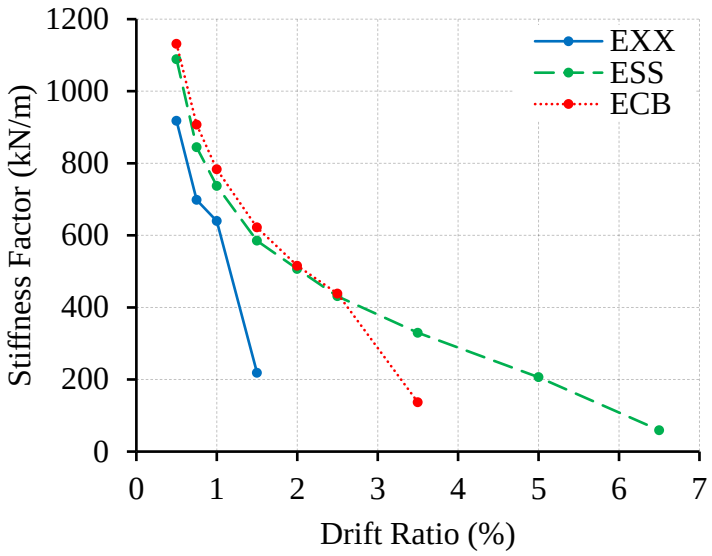

Figure 6.13: Stiffness degradation

Table 6.4: Stiffness and energy dissipation factors

Connection	Stiffness factor, *k* (kN/m)			Stiffness degradation factor	Accumulative dissipated energy (kN-m)
	at 0.50%	at 1.50%	at δ_u		
EXX	918	219	640	0.24	3.0
ESS	1,089	585	206	0.54	20.2
ECB	1,131	622	137	0.55	13.9

As shown in Figure 6.13, the stiffness of all connections decreased rapidly with the application of successive cycles of increasing drifts due to the progression of cracks. Connection EXX (without shear reinforcement) experienced the most drastic stiffness degradation with a stiffness degradation factor of only 0.24. The rate of stiffness degradation was significantly reduced by the use of shear reinforcement, which controlled the development of larger shear cracks and reduced the associated damage in the joint region. Thus, Connections ESS and ECB had a stiffness degradation factor of 0.54 and 0.55, respectively. In addition, they had higher stiffness factors than that of Connection EXX at all drift ratios. Moreover, due to its higher initial stiffness, Connection ECB had a higher stiffness factor than that of Connection ESS at all drift ratios until a drift ratio

of 2.50%. After that drift ratio (at 3.50%), Connection ECB failed and lost 88% of its initial stiffness, whereas Connection ESS had lost only 70% of its initial stiffness.

6.3.5. Energy dissipation

Reinforced concrete elements in seismic zones are expected to dissipate seismic energy. The energy dissipated during a loading cycle was represented by the area enclosed by the hysteresis loop of this cycle as shown in Figure 6.14. The values of the accumulative dissipated energy, which were calculated by summing up the energy dissipated in successive drift cycles, were plotted against the drift ratio for all connections in Figure 6.15. The values of the accumulative dissipated energy at the ultimate drift ratio are given in Table 6.4. Before it fails in punching shear after a 1.00% drift ratio, Connection EXX was able to dissipate 3.0 kN.m of the seismic energy. Its energy dissipation behavior was similar to that of Connections ESS and ECB, which dissipated 3.1 and 3.2 kN.m of the seismic energy up to the same drift ratio of 1.00%, respectively. However, the presence of the shear reinforcement prevented punching failure at low drift ratios, which resulted in a substantial increase in the energy dissipation capacity of the connections. Before failure, Connections ESS and ECB dissipated 20.2 and 13.9 kN.m of the seismic energy, respectively. These values are 6.7 and 4.6 times greater than that dissipated by Connection EXX before failure as well.

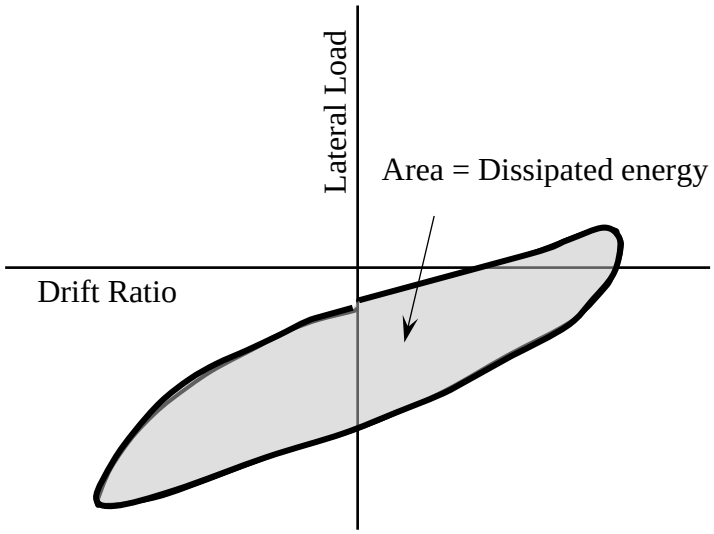

Figure 6.14: Definition of dissipated energy

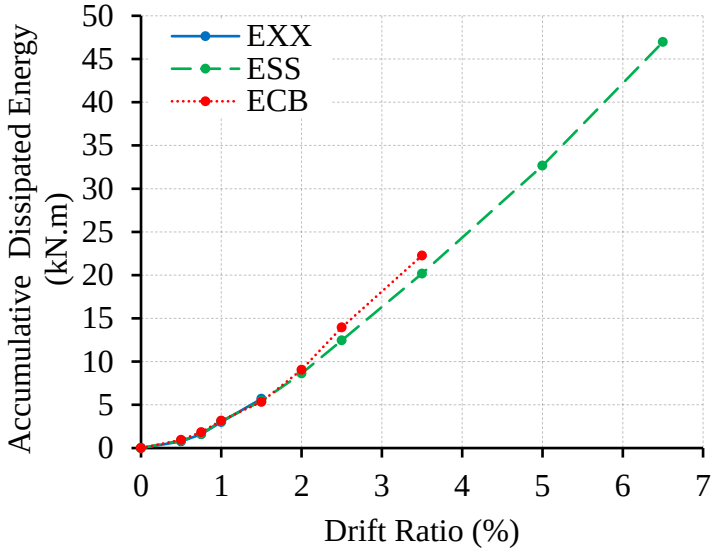

Figure 6.15: Energy dissipation

6.3.6. Flexural reinforcement strain

Figure 6.16 shows the strain profiles of the slab flexural reinforcement passing through the column for all connections. These profiles were plotted using the maximum measured tensile strains at each drift ratio. In the perpendicular direction, the three connections showed similar strain profiles

with a maximum strain reading at 1.50% drift ratio of 6,530, 5,880, and 6,520 με for Connections EXX, ESS, and ECB, respectively. The presence of the shear reinforcement allowed Connections ESS and ECB to sustain higher drift ratios and, in turn, experience higher flexural reinforcement strain levels. At 2.50% drift ratio, Connections ESS and ECB had maximum strain readings of 7,780 and 8,470 με, respectively. With further increases in the applied drift ratios, strain gauges in Connection ECB were damaged instantaneously, whereas those in Connection ESS were able to function until the 5.00% drift ratio with a maximum strain reading of 10,140 με. This value is only 38% of the ultimate strain of the used hooked bars. For steel-RC edge connections, maximum strain readings ranging between 6,000 and 7,500 με were reported under similar conditions (Durrani et al. 1995; Anggadjaja and Teng 2008). Accordingly, the relatively high strain reading of 6,530 με in Connection EXX, which is comparable to those experienced by steel reinforcement after yielding, is an indication that the large elastic deformations of GFRP can replace the yielding of steel. In the parallel direction, the three Connections EXX, ESS, and ECB showed similar behavior until failure with maximum strain readings at failure of 3,830, 4,070, and 3,970 με, respectively.

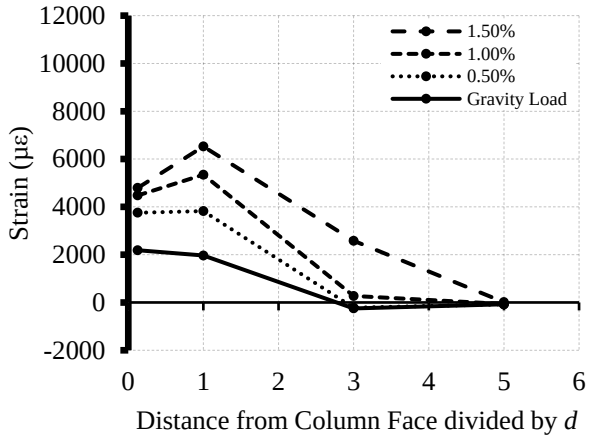

a) Connection EXX (perpendicular)

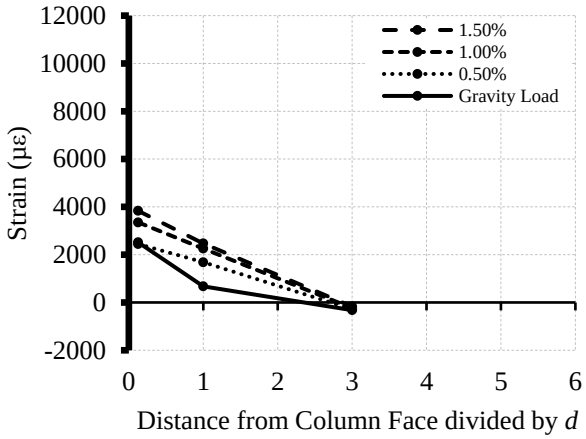

b) Connection EXX (parallel)

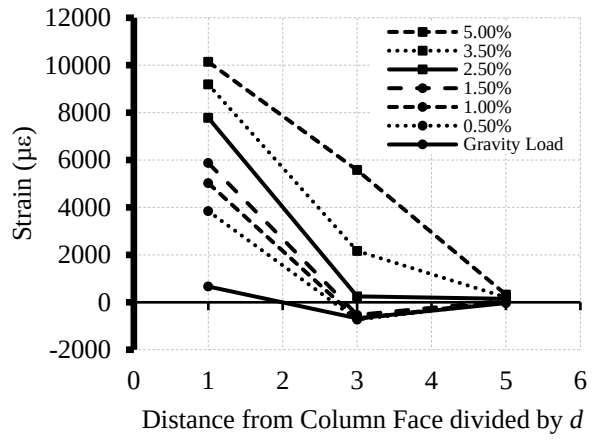

c) Connection ESS (perpendicular)

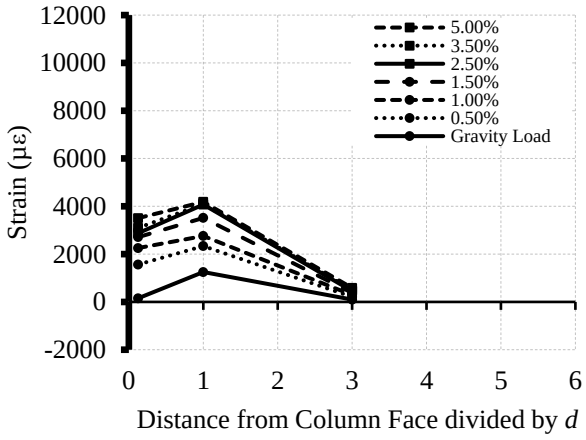

d) Connection ESS (parallel)

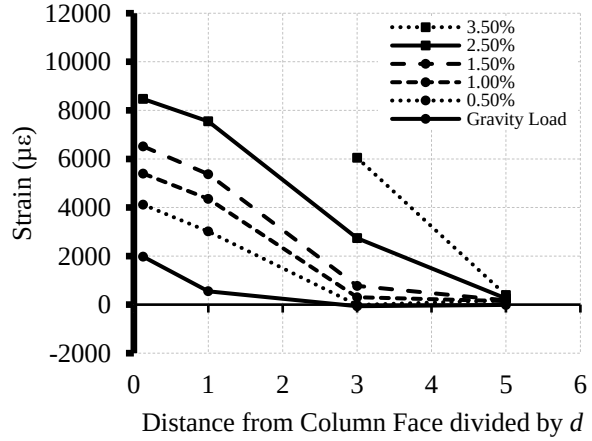

e) Connection ECB (perpendicular)

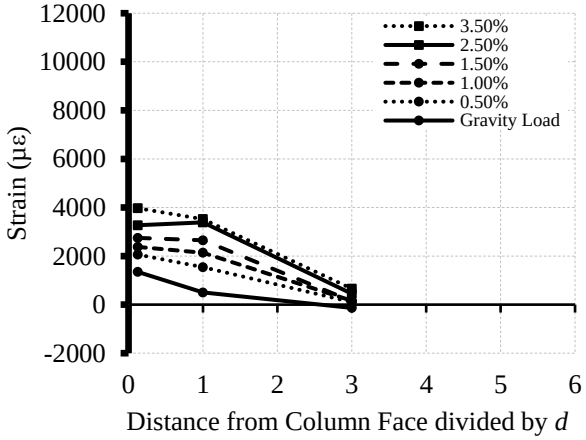

f) Connection ECB (parallel)

Figure 6.16: Strain profiles of the flexural reinforcement

6.3.7. Shear reinforcement strain

Strain profiles of the shear reinforcement for both shear-reinforced connections are shown in Figure 6.17. Despite the relatively high gravity shear ratio applied to all connections, insignificant strains developed in the shear reinforcement under the application of gravity loads. In Connection ESS, the strains in the shear studs slightly increased with increasing the applied drift ratios until the 1.00% drift ratio, with all strains being well below 1,200 με. Once the drift ratio was increased to 1.50%, a drastic hike in the strain reading at Strain gauge 3 took place, with the strain reading increasing from 310 to 1,460 με indicating the formation of a large diagonal shear crack. A similar trend was observed in Connection ECB with the strain hike taking place closer to the column (in Strain gauge 2, rather than Strain gauge 3). The highest strain reading in Connection ESS was 3,270 με and was recorded in Strain gauge 1. This value is 65% of the GFRP shear reinforcement strain limit suggested by Mostafa and El-Salakawy (2018) for GFRP shear-reinforced edge connections and only 40% of the usable design strain provided by the manufacturer as given in Table 6.2.

On the other hand, although failing at a lower drift ratio, a higher strain reading of 5,040 με was captured by Strain gauge 8 in Connection ECB. This is attributed to the low stiffness of the vertical stem of the corrugated bars (52 GPa) compared to that of the shear studs (68 GPa). This relatively high strain value has just exceeded the 5,000 με limit; however, it is only 20% of the ultimate strain of the vertical stem of the corrugated bar. Accordingly, it is recommended that the design strain of GFRP shear reinforcement in slab-column connections be limited to 3,000 με. At failure, Connection ESS experienced significant concrete damage in the column vicinity as shown in Figure 6.7, which allowed the manual extraction of ten shear studs; two of them were instrumented with strain gauges. The two instrumented shear studs, Studs 1 and 7, show a normal strain-drift

ratio relationship until failure as shown in Figure 6.18. In addition, all extracted studs were intact with no signs of damage in the heads or rupture in the bars, which suggests that the punching shear failure was triggered by the loss of confinement around the heads of the studs due to the destruction of the concrete surrounding the studs as a result of the reversed cyclic loading.

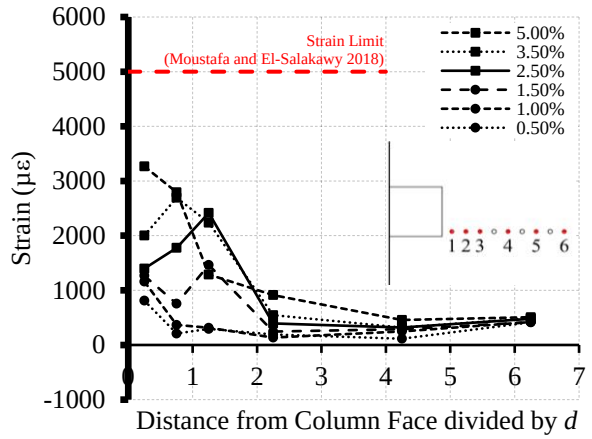

a) Connection ESS (perpendicular)

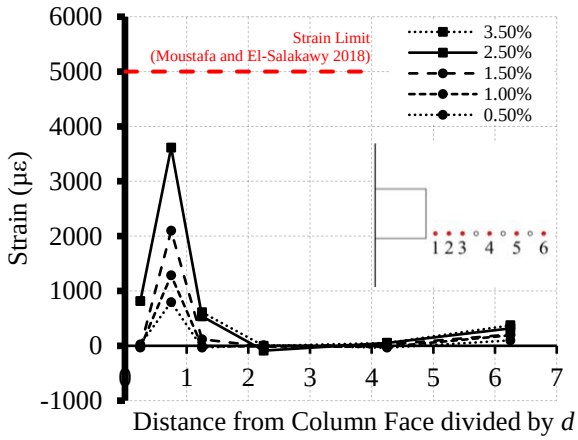

b) Connection ECB (perpendicular)

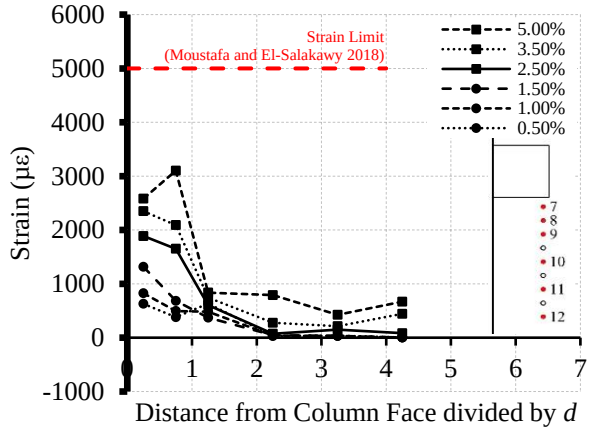

c) Connection ESS (parallel)

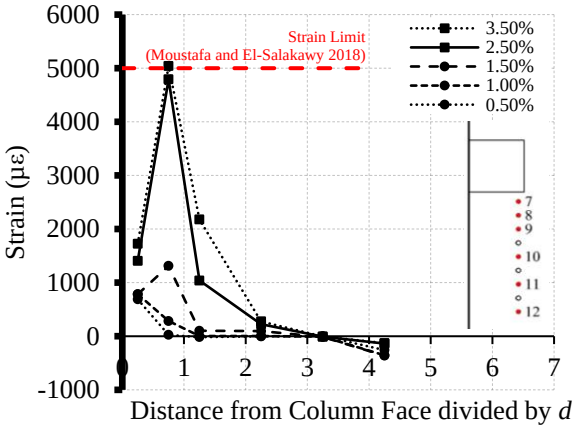

d) Connection ECB (parallel)

Figure 6.17: Strains in shear reinforcement versus distance from column face

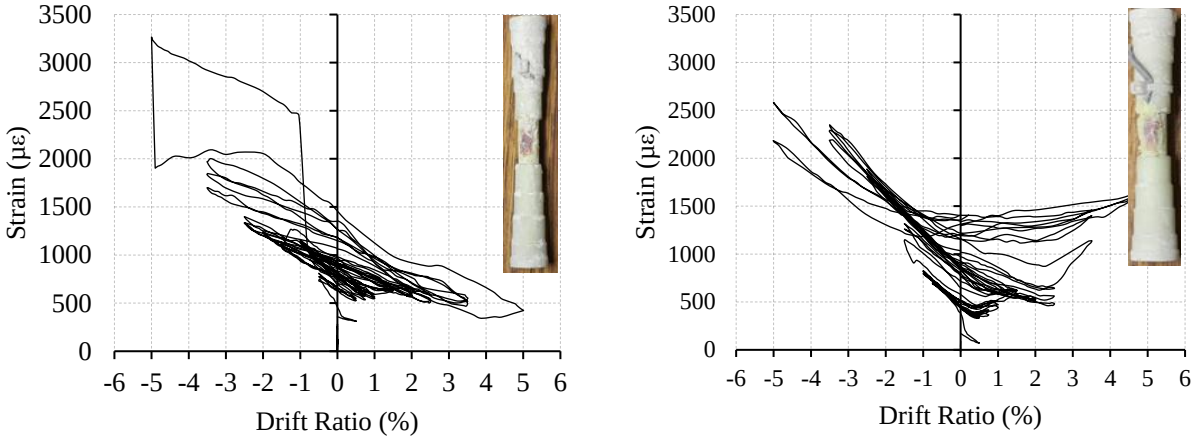

a) Stud number 1 b) Stud number 7

Figure 6.18: Strain versus drift ratio in extracted GFRP shear studs

6.3.8. Ultimate capacity

According to CSA S806-12 (CSA 2017), the ultimate capacity of Connection EXX (without shear reinforcement) was calculated using Equation 6.1 to Equation 6.3. Alternatively, because no design provisions for FRP-RC shear-reinforced slabs are available in any design standard, the equations proposed by the authors (El-Gendy and El-Salakawy 2016) for slab-column connections reinforced by GFRP shear reinforcement were used to calculate the predicted capacities of Connections ESS and ECB with shear reinforcement as shown in Equation 6.4 to Equation 6.6, where v_r = shear stress resistance (MPa); $v_{c,inner}$ = shear stress resistance provided by concrete at the inner critical perimeter located $d/2$ from the column face (MPa); v_{sF} = shear stress resistance provided by FRP shear reinforcement (MPa); ϕ_F = resistance factor for FRP shear reinforcement; A_{Fv} = area of FRP shear reinforcement (mm2); ε_{Fv} = allowable strain in FRP shear reinforcement; E_{Fv} = modulus of elasticity of FRP shear reinforcement (MPa); and s = spacing of FRP shear reinforcement measured perpendicular to critical perimeter (mm).

$$v_r = v_{c,inner} + v_{sF} \quad \text{Equation 6.4}$$

$$v_{c,inner} = \left[0.041 \lambda \phi_c \left(E_F \rho_F f_c^{'} \right)^{\frac{1}{3}} \right] \quad \text{Equation 6.5}$$

$$v_{sF} = \frac{\phi_F A_{Fv} \left(\varepsilon_{Fv} E_{Fv} \right)}{b_o s} \quad \text{Equation 6.6}$$

For all connections, the factored shear stress, v_f, was calculated using Equation 6.7 where V_f = factored shear force transferred between the slab and column (kN); γ_v = fraction of unbalanced moment transferred by eccentricity of shear at slab-column connections; M_f = unbalanced moment transferred between the slab and the column calculated by multiplying the ultimate lateral load by the height of the column, 2.92 m (kN.m); e = distance from centroid of section for critical shear to the point where shear stress is being calculated (mm); and J = property of the critical shear section analogous to the polar moment of inertia.

$$v_f = \frac{V_f}{b_o d} + \frac{\gamma_v M_f}{J} e \quad \text{Equation 6.7}$$

The punching capacities of all test connections were calculated using the aforementioned equations with all material and strength factors set to 1.0 to predict the nominal capacities. In addition, as mentioned previously, the allowable strain in FRP shear reinforcement was set to 3,000 με. Table 6.5 gives the parameters used to calculate the predicted capacities and comparisons between the actual and predicted capacities for all test connections.

Table 6.5: Ultimate capacity parameters

Connection	E_f (GPa)	ρ_f (%)	b_o (mm)	d (mm)	$J \times 10^9$ (mm^4)	e (mm)	γ_v	A_{Fv} (mm^2)	s (mm)	v_f (MPa)	v_r (MPa)	v_f/v_r
EXX	60.7	1.44	1,220	160	3.4	118	0.38	N/A	N/A	2.28	1.95	1.17
ESS	60.7	1.44	1,220	160	3.4	118	0.38	774	80	2.96	3.06	0.97
ECB	60.7	1.44	1,220	160	3.4	118	0.38	774	80	2.91	2.67	1.07

Note: E_f = modulus of elasticity of FRP reinforcement; ρ_f = longitudinal FRP reinforcement ratio; b_o = perimeter of critical section for shear; d = average depth of slab; J = property of the critical shear section analogous to polar moment of inertia; e = distance from centroid of critical section to the point where shear stress is being calculated; γ_v = fraction of unbalanced moment transferred by eccentricity of shear; A_{Fv} = area of FRP shear reinforcement; s = spacing of FRP shear reinforcement measured perpendicular to critical section; v_f = factored shear stress on critical section; v_r = punching shear resistance.

For Connection EXX (without shear reinforcement), CSA S806-12 (CSA 2017) reasonably predicted the actual capacity of the slab with v_f/v_r of 1.19, which is consistent with results from literature for GFRP-RC edge connections subjected to monotonically-increased vertical loads and unbalanced moments (El-Gendy and El-Salakawy 2016; Mostafa and El-Salakawy 2018). For the two connections with shear reinforcement, Equation 6.4 to Equation 6.6 yielded good predictions of the capacities with an average v_f/v_r of 1.04 ± 0.06 (COV = 8.2%).

6.4. Conclusions

Two recently developed types of GFRP shear reinforcement, i.e., shear studs and corrugated bars, were used in slab-column edge connections subjected to gravity and uniaxial reversed-cyclic lateral loading. Three full-scale connections were constructed and tested to investigate the influence of GFRP shear reinforcement on the seismic response of such connections. Both types of GFRP shear reinforcement are very promising as a practical solution to increase the deformability of GFRP-RC connections in seismic zones. Based on the observed behavior of the test connections, the following conclusions can be drawn:

1. When subjected to simulated seismic loading conditions, GFRP-RC slab-column edge connections without shear reinforcement and subjected to high gravity shear ratio of 60% could not sustain 1.50% drift ratio before experiencing brittle punching failure.
2. The use of well-anchored GFRP shear reinforcement resulted in a substantial increase in the drift capacity and deformability of the connections, which allowed them to sustain large seismically-induced deformations without jeopardizing their gravity load capacity.
3. The use of GFRP shear studs and corrugated bars increased the lateral load capacity of the connections by 47 and 44%, respectively, and allowed the connections to undergo large

inelastic deformations associated with 3.50 and 2.50% lateral inter-story drift ratio, respectively, without punching failure.

4. The equivalent yield drift ratio concept can be used to assess the deformability of GFRP-RC slab-column connections. Without shear reinforcement, the GFRP-RC connection was not able to achieve the minimum required level of deformability suggested by Marzouk et al. (2001). However, both types of GFRP shear reinforcement substantially enhanced the deformability of the connections and allowed them to exceed the required level of deformability. Although the use of corrugated bars increased the deformability by 40%, using shear studs resulted in a higher increase of 60%.
5. Both types of GFRP shear reinforcement enhanced the initial stiffness of the connections and resulted in a significantly lower rate of stiffness degradation and, in turn, higher stiffness at the same drift ratio. At 1.50% drift ratio, Connections ESS (with shear studs) and ECB (with corrugated bars) had 2.67 and 2.84 times higher stiffness than Connection EXX (without shear reinforcement).
6. Without shear reinforcement, the GFRP-RC connections were not able to dissipate a sufficient amount of energy. The presence of GFRP shear reinforcement, which prevented punching failure at low drift ratios, resulted in a substantial increase in the energy dissipation capacity of the connections. Connections ESS (with shear studs) and ECB (with corrugated bars) dissipated 6.7 and 4.6 times the energy dissipated by Connection EXX (without shear reinforcement).
7. The significant concrete damage in the column vicinity of Connection ESS along with the absence of damage signs in the individual shear studs extracted from Connection ESS after

failure suggest that the punching failure was triggered by the loss of confinement around the heads of the studs rather than the malfunction of the shear studs.

8. The design strain of GFRP shear stud reinforcement in slab-column connections should be limited to 3,000 με.
9. For the connection without shear reinforcement, CSA S806-12 (CSA 2017) provided reasonable predictions with v_f/v_r of 1.19. On the other hand, the model proposed by the authors (El-Gendy and El-Salakawy 2016) yielded good predictions of the capacities with an average v_f/v_r of 1.04 ± 0.06 (COV = 8.2%).

CHAPTER 7. ASSESSMENT OF PUNCHING SHEAR DESIGN MODELS FOR FRP-RC SLAB-COLUMN CONNECTIONS

Authors and affiliation:

- Mohammed G. El-Gendy, PhD Candidate, Department of Civil Engineering, University of Manitoba
- Ehab F. El-Salakawy, Professor, Department of Civil Engineering, University of Manitoba

Journal and Status:

American Society of Civil Engineers (ASCE) Journal of Composites for Construction, published on July 10, 2020.

Reference:

El-Gendy, M., and El-Salakawy, E. 2020. "Assessment of punching shear design models for GFRP-RC slab-column connections." *J. Compos. Constr.*, ASCE, 24 (5): 04020047, https://doi.org/10.1061/(ASCE)CC.1943-5614.0001054.

Note:

The manuscript had been slightly altered from the original paper by renumbering the tables and figures to include the chapter number. In addition, the reference list and list of notations have been moved to the appropriate sections in the thesis as indicated in the table of contents.

Abstract

Several empirical models have been introduced during the last two decades to estimate the punching capacity of two-way slabs reinforced with fiber-reinforced polymer (FRP) reinforcement. In this study, the applicability of these models on FRP-reinforced concrete (RC) slab-column interior and edge connections subjected to gravity loads is assessed. The models are also calibrated against experiments conducted previously by the authors on FRP-RC edge connections subjected to reversed-cyclic lateral loads. Test results of 68 interior and 25 edge specimens, 6 of which were tested under reversed-cyclic lateral loads, were used to evaluate the available models. Based on the analysis, a universal model capable of accurately predicting the capacity of both interior and edge specimens subjected to gravity or cyclic loads is proposed. The proposed model provided mean test-to-predicted strength of 1.01 ± 0.14 and 1.01 ± 0.09 for interior and edge specimens, respectively. Furthermore, a design model is proposed to estimate the gravity shear limits for FRP-RC connections without shear reinforcement and subjected to cyclic load.

Keywords: Cyclic load; database; drift capacity; empirical model; flat plate; FRP; punching capacity; slab-column connection.

7.1. Introduction

Punching shear strength of reinforced concrete (RC) slab-column connections usually governs the design of flat plate systems. When reinforced with fiber-reinforced polymer (FRP) composite bars, concrete slab-column connections have lower punching strength and lower stiffness than their steel-RC counterparts that have the same flexural reinforcement ratio. This is attributed to the lower axial and transverse stiffness of FRP reinforcement compared to steel bars (Matthys and Taerwe 2000; El-Gendy and El-Salakawy 2018a). The lower axial stiffness reduces the contributions of the uncracked concrete and aggregate interlock to the punching strength, while the lower transverse stiffness reduces that of the dowel action provided by longitudinal reinforcement.

Therefore, design provisions in codes and guidelines pertaining to steel-RC connections cannot be directly applied to FRP-RC counterparts. During the last two decades, several empirical models have been introduced by different researchers to predict the punching capacity of FRP-RC two-way slabs (Matthys and Taerwe 2000; Ospina et al. 2003; El-Gamal et al. 2005; Hassan et al. 2014, 2017; El-Gendy and El-Salakawy 2016; Salama et al. 2019). These models, as well as the current design provisions for FRP-RC two-way slabs in codes and guidelines (JSCE 1997; ACI 2015; CSA 2017), are empirical in nature; they are based on statistical fitting of the test results available at the time they were developed. The bulk of the experimental studies conducted before the development of these models focused on two-way slabs subjected to concentric gravity loads only. Furthermore, none of the available models were calibrated against test results of slab-column connections subjected to reversed-cyclic lateral loads.

On the other hand, in regions of high seismic activities, the use of steel-RC flat plate systems is allowed only as gravity force resisting systems (GFRS), where special moment frames or shear walls are provided as the seismic force resisting system (SFRS) (ACI 2019a; CSA 2019b). Nevertheless, flat plate systems must be designed for deformation compatibility with the SFRS to avoid punching failure when subjected to the design drifts. One of the main parameters affecting the drift capacity of steel-RC connections is the magnitude of the gravity shear carried by the slab (Pan and Moehle 1989). This parameter is represented by the gravity shear ratio, which is the ratio of the gravity shear force transferred between the slab and the column, V_g, to the theoretical punching shear strength provided by concrete, V_c. The current design provisions in North America require the use of shear reinforcement in steel-RC connections when the applied gravity shear ratio exceeds a certain limit, which is based on the design drifts as will be discussed later. Typically, for steel-RC connections without shear reinforcement to be able to undergo a drift ratio of 1.5%, the applied gravity shear ratio shall not exceed 0.4. Otherwise, shear reinforcement must be provided.

In the present study, the FRP-RC punching shear design models available in current codes and guidelines, as well as the empirical models developed by different researchers, are evaluated. The applicability of these models on FRP-RC interior and edge connections subjected to monotonically-increased gravity loads (i.e., concentric shear force and unbalanced bending moment) is investigated. In addition, the models are calibrated against experiments conducted previously by the authors on FRP-RC edge connections subjected to reversed-cyclic lateral load (El-Gendy and El-Salakawy 2019, 2020a, 2020b). Refinement of the existing models to better predict the punching capacity of different types of connections subjected to different types of load are proposed. Furthermore, based on the results of FRP-RC connections subjected to reversed-

cyclic lateral load, a design model is proposed to estimate the gravity shear limits for FRP-RC connections without shear reinforcement.

7.2. Review of Current Punching Shear Design Models

The available punching shear design models for FRP-RC structures are generally based on those for steel-RC ones with modifications to account for the significant differences between FRP and steel, in terms of axial stress-strain relationship, transverse strength and bond behaviour. This section reviews the models predicting punching shear capacity of FRP-RC connections incorporated in current provisions and introduced by researchers.

7.2.1. Eccentric shear stress model

Both CSA A23.3-19 (CSA 2019b) and ACI 318-19 (ACI 2019a) adopt the eccentric shear stress model to estimate the shear stress applied to a connection. In this model, the factored unbalanced moment, M_f, at a connection is assumed to be transferred by both flexure and eccentric shear on a critical section. This critical section, for connections without shear reinforcement, is assumed to be located at a distance $d/2$ from the column face in both codes, where d is the average effective depth of the top (tension) reinforcement in the slab. The portion of the unbalanced moment transferred by shear, $\gamma_v M_f$, is given by Equation 7.1, where b_1 is the width of the critical section in the direction of the unbalanced moment, and b_2 is the width of the critical section perpendicular to b_1.

$$\gamma_v = 1 - \frac{1}{1 + (2/3)\sqrt{b_1/b_2}} \qquad \text{Equation 7.1}$$

This portion of the moment is assumed to be transferred by linear variation of shear around the critical section as shown in Figure 7.1. Thus, the factored shear stress on the critical section, v_f,

can be estimated by Equation 7.2 where V_f is the factored shear force transferred between the slab and the column, b_o is the perimeter of the critical section, e is the distance from the centroid of the critical section to the point where shear stress is being calculated, and J_c is a property of the critical section analogous to the polar moment of inertia. On the other hand, the nominal shear resistance, v_n, is typically estimated as a combination of the concrete (v_c) and shear reinforcement (v_s) capacities as given in Equation 7.3**.**

$$v_f = \frac{V_f}{b_o d} + \frac{\gamma_v M_f}{J} e \qquad \text{Equation 7.2}$$

$$v_n = v_c + v_s \qquad \text{Equation 7.3}$$

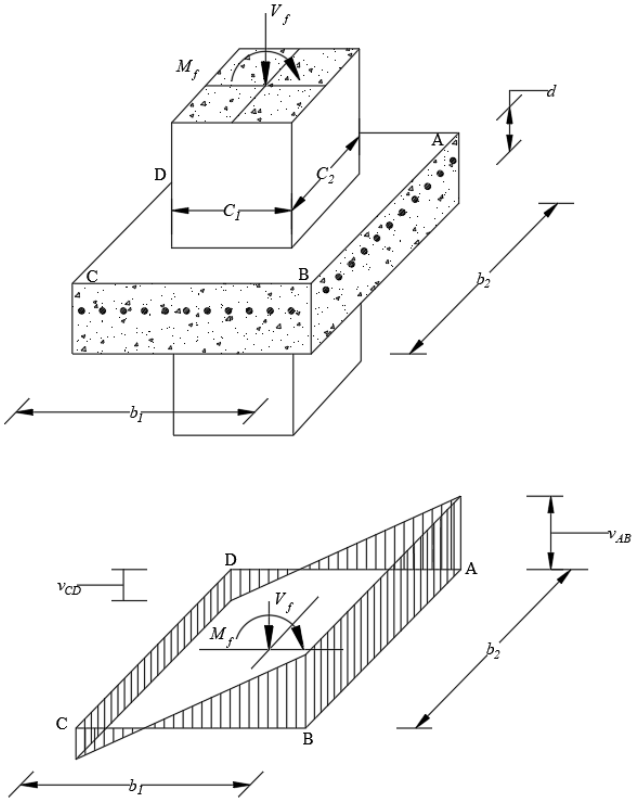

Figure 7.1: Eccentric shear stress model (ACI 2019a; CSA 2019b)

7.2.2. Two-way slabs without shear reinforcement (code provisions)

7.2.2.1. Canadian Standards Association (CSA)

According to CSA S806-12 (CSA 2017), the factored punching shear stress resistance provided by concrete shall not exceed the smallest of the values given by Equation 7.4 to Equation 7.6, where β_c is the ratio of the long side to the short side of the column, λ is a factor to account for concrete density, ϕ_c is the resistance factor for concrete, E_F is the modulus of elasticity of FRP reinforcement (MPa), ρ_F is the longitudinal FRP reinforcement ratio, f_c' is the concrete compressive strength (MPa) and shall not be taken greater than 60 MPa, α_s is a coefficient equal to 4, 3 or 2 for interior, edge and corner connections, respectively, and $b_{o,0.5d}$ is the perimeter of the critical section located at a distance 0.5d from the column face.

$$v_c = \left(1 + \frac{2}{\beta_c}\right) 0.028 \lambda \phi_c \left(E_F \rho_F f_c'\right)^{1/3} \qquad \text{Equation 7.4}$$

$$v_c = \left[\left(\frac{\alpha_s d}{b_{o,0.5d}}\right) + 0.19\right] 0.147 \lambda \phi_c \left(E_F \rho_F f_c'\right)^{1/3} \qquad \text{Equation 7.5}$$

$$v_c = 0.056 \lambda \phi_c \left(E_F \rho_F f_c'\right)^{1/3} \qquad \text{Equation 7.6}$$

While Equation 7.5 considers the effect of the shear perimeter-to-slab depth ratio, Equation 7.4 considers the effect of column rectangularity on the strength. However, Equation 7.4 will not govern the design unless the column aspect ratio exceeds 2 (i.e., $\beta_c > 2$). Thus, for most columns, where the column aspect ratio is less than 2, Equation 7.6 governs the design. The slab size effect is then considered if the effective depth of the slab exceeds 300 mm by multiplying the governing value of v_c by $\left(300/d\right)^{0.25}$.

7.2.2.2. American Concrete Institute (ACI)

According to ACI 440.1R-15 (ACI 2015), the nominal shear strength provided by concrete at a critical section located at a distance $d/2$ from the column face can be estimated by Equation 7.7, where f_c' is the concrete compressive strength (MPa) and the term kd represents the depth of the neutral axis assuming elastic cracked conditions (mm), where k is calculated by Equation 7.8 and n_F is the modular ratio (i.e., the ratio between the modulus of elasticity for FRP to that for concrete).

$$v_c = \frac{4}{5}\sqrt{f_c'}\,\frac{(kd)}{d} \qquad \text{Equation 7.7}$$

$$k = \sqrt{2\rho_F n_F + (\rho_F n_F)^2} - \rho_F n_F \qquad \text{Equation 7.8}$$

7.2.2.3. Japan Society of Civil Engineers (JSCE)

The shear strength provided by concrete recommended by JSCE (JSCE 1997) is given by Equation 7.9, where γ_b is a factor of safety generally taken as 1.3, while β_d, β_p, β_r, f_{pcd}, and α are factors considering the slab size effect, the reinforcement axial stiffness, the column perimeter-to-slab depth ratio, the concrete strength, and the load eccentricity, respectively. These factors are estimated by Equation 7.10 to Equation 7.14, respectively, where E_s is the modulus of elasticity of steel (200,000 MPa), u is the perimeter of the loaded area, e.g., the column (mm), e_x and e_y are the load eccentricities in the x and y directions (mm), respectively, and b_x and b_y are the critical section dimensions in the x and y directions (mm), respectively.

$$v_c = \beta_d \beta_p \beta_r \frac{f_{pcd}}{\gamma_b} \times \frac{1}{\alpha} \qquad \text{Equation 7.9}$$

$$\beta_d = \sqrt[4]{1/d} \le 1.5 \qquad \text{Equation 7.10}$$

$$\beta_p = \sqrt[3]{100\rho_F E_F / E_s} \le 1.5 \qquad \text{Equation 7.11}$$

$$\beta_r = 1 + \left[1/\left(1 + 0.25u/d\right)\right] \qquad \text{Equation 7.12}$$

$$f_{pcd} = 0.2\sqrt{f_c'} \le 1.2 \text{ MPa} \qquad \text{Equation 7.13}$$

$$\alpha = 1 + 1.5\left[\left(e_x + e_y\right)/\sqrt{b_x b_y}\right] \qquad \text{Equation 7.14}$$

7.2.3. Two-way slabs without shear reinforcement (models proposed in literature)

7.2.3.1. Model I (Matthys and Taerwe 2000)

In an early effort by Matthys and Taerwe (2000), the punching shear model for steel-RC connections in the British Standard, BS8110 (BSI 1997), was modified to account for the lower stiffness of FRP by multiplying the reinforcement ratio by the ratio of modulus of elasticity of FRP to that of steel, E_F/E_S as shown in Equation 7.15. This model considers the influence of the main parameters known to affect the punching behavior of FRP-RC two-way slabs, i.e., reinforcement ratio and modulus of elasticity, concrete strength and effective slab depth. Unlike the aforementioned code provisions, this model considers the critical section at distance 1.5*d* from the column face, similar to the approach followed in BS8110 (BSI 1997).

$$v_c = \left(100\rho_F \frac{E_F}{E_S} f_c'\right)^{1/3} \times \frac{1.36}{d^{0.25}} \qquad \text{Equation 7.15}$$

7.2.3.2. Model II (Ospina et al. 2003)

According to Ospina et al. (2003), *Model I* (Matthys and Taerwe 2000) overestimates the effect of FRP reinforcement stiffness. Thus, they modified it by using the square root of E_F/E_S, instead of the cubic one. In addition, based on the available results at that time, it was suggested that the slab size effect was not evident on the punching strength of FRP-RC two-way slabs; thus, it was ignored in their proposed model (Equation 7.16). This model also considers the critical section at distance 1.5*d* from column face.

$$v_c = 2.77\left(\rho_F f_c^{'}\right)^{1/3}\sqrt{\frac{E_F}{E_S}} \qquad \text{Equation 7.16}$$

7.2.3.3. Model III (El-Gamal et al. 2005)

A new parameter was considered in this model, which was proposed based on punching tests conducted on FRP-RC deck slabs. The effect of slab restraining action, which can be contributed by the in-plane stiffness of deck slabs in adjacent panels, was introduced in Equation 7.17. For simplicity, this effect was considered in the form of a factor *N*, which is taken as 0, 1, or 2 for simple slabs in both directions, slabs continuous in one direction, and slabs continuous in both directions, respectively. This model was one of the early models to consider the effect of shear perimeter-to-slab depth ratio.

$$v_c = 0.33\sqrt{f_c^{'}}\left[0.62\left(\rho_F E_F\right)^{1/3}\left(1+\frac{8d}{b_{o,0.5d}}\right)\right](1.2)^N \qquad \text{Equation 7.17}$$

7.2.3.4. Model IV (Hassan et al. 2017)

This model (Equation 7.18) is an incremental modification of the one incorporated in CSA S806-12 (CSA 2017) by combining the three equations (Equation 7.4 to Equation 7.6) into a single

formula. This was done by performing a regression analysis on 69 slab-column interior connections from the literature.

$$v_c = 0.065\lambda\phi_c\left(\frac{4d}{b_{o,0.5d}} + 0.65\right)\left(E_F\rho_F f_c^{'}\right)^{1/3}\left(125/d\right)^{1/6} \qquad \text{Equation 7.18}$$

7.2.4. Shear-reinforced two-way slabs (models proposed in the literature)

7.2.4.1. Model V (Hassan et al. 2014)

This model (Equation 7.19 and Equation 7.20**)** estimates the capacity of FRP-RC two-way slabs with FRP stirrups. Similar to the approach followed in ACI 318-19 (ACI 2019a), this model assumes that the shear strength provided by concrete within the shear-reinforced zone is 50% of that provided by concrete when no shear reinforcement is provided. However, it does not give any guidance regarding the shear strength outside the shear-reinforced zone. In this model, the allowable stress in FRP stirrups**,** f_{Fv}, is taken as the smaller of the two values calculated by Equation 7.21 and Equation 7.22, where r_b is the bend radius, d_b is the stirrup diameter, f_{uv} is the ultimate strength of the straight portion of FRP stirrups, and f_{fbend} is the strength of the bend.

$$v_{c,inner} = 0.028\lambda\phi_c\left(E_F\rho_F f_c^{'}\right)^{1/3} \qquad \text{Equation 7.19}$$

$$v_{sF} = \frac{0.7\phi_F A_{Fv} f_{Fv}}{b_{o,0.5d}s} \qquad \text{Equation 7.20}$$

$$f_{Fv} = 0.004E_{Fv} \qquad \text{Equation 7.21}$$

$$f_{Fv} = \frac{\left(0.05r_b/d_b + 0.3\right)f_{uv}}{1.5} \le f_{fbend} \qquad \text{Equation 7.22}$$

7.2.4.2. Model VI (El-Gendy and El-Salakawy 2016)

A model was proposed by the authors (El-Gendy and El-Salakawy 2016) to estimate the capacity of FRP-RC connections with glass fiber-reinforced polymer (GFRP) stud shear reinforcement (Equation 7.23 to Equation 7.25**)**, where $v_{c,inner}$ and $v_{c,outer}$ are the shear stress resistance provided by concrete at the inner and outer critical sections located at distance $d/2$ from the column face and from the outermost peripheral shear reinforcement row (MPa), respectively, v_{sF} is the shear stress resistance provided by FRP shear reinforcement (MPa), ϕ_F is the resistance factor for FRP shear reinforcement, A_{Fv} is the area of FRP shear reinforcement (mm^2), ε_{Fv} is the allowable strain in FRP shear reinforcement taken as the smaller of 5,000 με or the maximum usable strain of the used shear reinforcement, E_{Fv} is the modulus of elasticity of FRP shear reinforcement (MPa), and s is the spacing of FRP shear reinforcement measured perpendicular to the critical section. This model was then refined to consider different types of GFRP shear reinforcement (Mostafa and El-Salakawy 2018; Hussein and El-Salakawy 2018).

$$v_{c,inner} = 0.041\lambda\phi_c\left(E_F\rho_F f_c^{'}\right)^{1/3} \qquad \text{Equation 7.23}$$

$$v_{c,outer} = 0.028\lambda\phi_c\left(E_F\rho_F f_c^{'}\right)^{1/3} \qquad \text{Equation 7.24}$$

$$v_{sF} = \frac{\phi_F A_{Fv}\left(\varepsilon_{Fv}E_{Fv}\right)}{b_{o,0.5d}s} \qquad \text{Equation 7.25}$$

7.2.4.3. Model VII (Salama et al. 2019)

In a recent effort, Salama et al. (2019) proposed to reduce the shear strength provided by concrete to half the value recommended by CSA S806-12 (CSA 2017). As such, the strengths provided by

concrete at the inner and outer critical sections are both given by Equation 7.24, while that provided by shear reinforcement is given by Equation 7.25 with a maximum strain limit of 5,000 με.

7.3. Flexural Capacity Using Yield-Line Theory

Slab-column connections, especially those containing shear reinforcement, may experience punching or flexural failure. When slab-column connections exhibit a deformable flexural failure, the failure is typically followed by a secondary brittle punching one. Thus, the actual mode of failure may be misinterpreted without proper calculations of the flexural capacity of the connection. Historically, the flexural capacity of steel-RC slab-column connections was estimated by performing a yield-line analysis (Mortin and Ghali 1991; Stein et al. 2007). In this analysis, a failure pattern compatible with the boundary conditions of the connection in the test set-up is postulated. The flexural capacity is then calculated in terms of the bending moment per unit width of the slab at the yielding of flexural reinforcement. To account for the elastic nature of FRP, Gar et al. (2014) suggested the use of an equivalent plastic moment capacity for FRP-RC slabs, M_p, which can be estimated using Equation 7.26**,** where M_n and M_{cr} are the ultimate and cracking moment per unit width of the slab, respectively, and I_{cr} and I_g, are the cracked and gross moments of inertia per unit width of the slab, respectively. Besides the flexural capacities of shear-reinforced connections reported in the literature, the equivalent yield-line analysis introduced by Gar et al. (2014) is used in this study to estimate the flexural capacity of shear-reinforced FRP-RC connections subjected to reversed-cyclic lateral load according to the pattern shown in Figure 7.2, where X is a parameter defining the pattern.

$$M_p = 0.5M_n + 0.5\left(1 - \frac{I_{cr}}{2I_g}\right)\left(\frac{M_{cr}}{M_n}\right)M_{cr} \qquad \text{Equation 7.26}$$

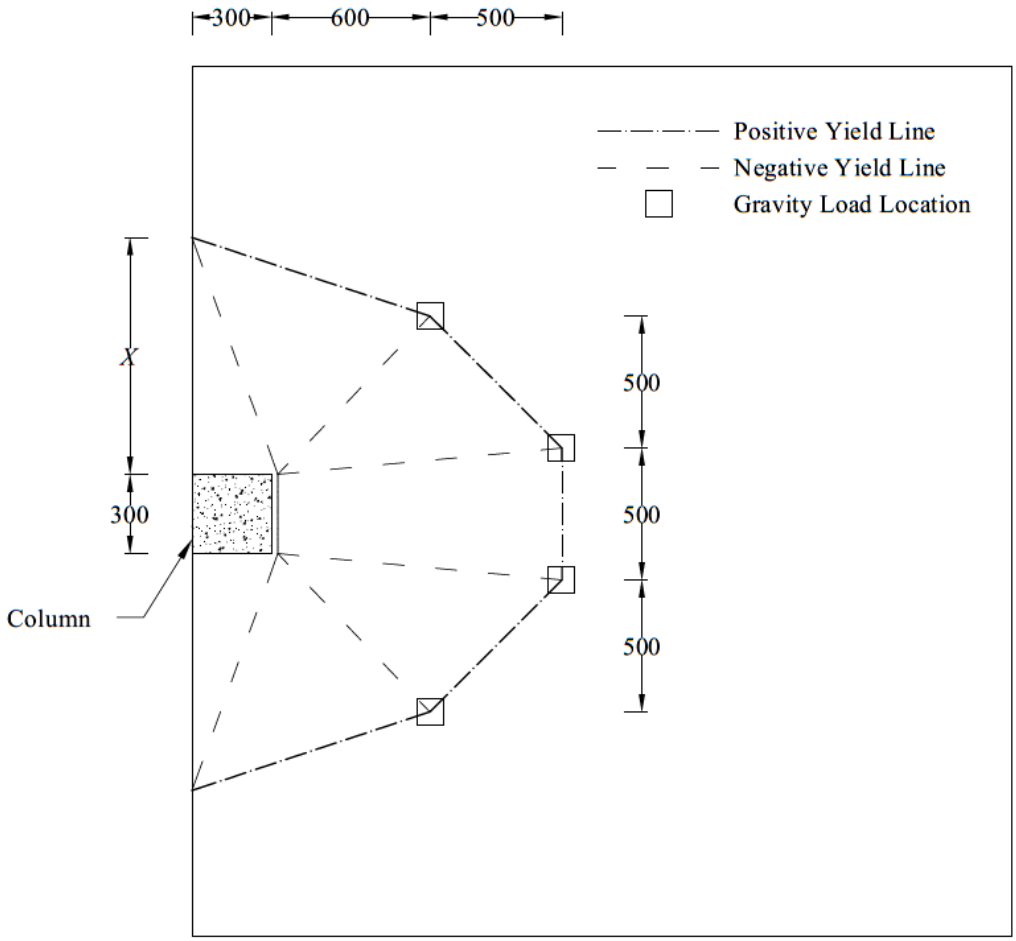

Figure 7.2: Equivalent yield-line pattern

7.4. Database of Experimental Research on FRP-RC Two-Way Slabs and Slab-Column Connections

Recently, the punching shear behavior of FRP-RC slab-column connections subjected to simultaneous concentric shear force and unbalanced moment transfer has gained considerable attraction (El-Gendy and El-Salakawy 2016, 2018a, 2019, 2020a, 2020b; Gouda and El-Salakawy

2016a, 2016b; Hussein and El-Salakawy 2018; Mostafa and El-Salakawy 2018; Salama et al. 2019). In the majority of these tests, the slabs were simply supported at the assumed locations of contra-flexure lines, while the shear force and unbalanced moment were applied at the column. The only exception was the research recently conducted by the authors on edge connections subjected to cyclic lateral load (El-Gendy and El-Salakawy 2019, 2020a, 2020b), where the connections were pinned at the contra-flexure lines in the slab and the column base. In that case, the vertical gravity load was applied to the slab, while the reversed cyclic lateral load was applied to the column.

However, the punching shear behavior of FRP-RC slabs subjected to concentric shear forces through a steel plate or a column stub has been studied starting late 1990s. Two different test setups were used in these tests. In the first one, the slabs were supported at their perimeter, while the concentric shear force was applied by pushing a steel plate or a short column stub through the slab (Matthys and Taerwe 2000; Ospina et al. 2003; Nguyen-Minh and Rovňák 2013; Dulude et al. 2013; Hassan et al. 2013a, 2013b, 2014). In the second one, the slab was supported on a column stub, while the load was applied at the slab perimeter (El-Ghandour et al. 2003; Lee et al. 2009). For simplicity, these concentric slab specimens will also be referred to as slab-column connections in this paper.

Notwithstanding, all the aforementioned test setups and boundary conditions are similar in the sense that the maximum negative moment and maximum shear force in the slab are located in the vicinity of the column or plate, while the negative moment is reduced closer to the slab perimeter, where it diminishes. Table 7.1 and Table 7.2 list data for a total of 70 FRP-RC connections without shear reinforcement reported in the literature including 56 interior and 14 edge connections,

respectively. Similarly, Table 7.3 and Table 7.4 list data for a total of 23 shear-reinforced FRP-RC connections from literature including 12 interior and 11 edge connections, respectively.

These 93 connections cover a large spectrum of material and geometrical properties with a wide range of slab dimensions (1,000 to 2,800 mm), column widths (71 to 450 mm), slab thicknesses (120 to 350 mm), effective depths of slabs (89 to 284 mm), concrete strengths (28.9 to 118.0 MPa), average flexural reinforcement ratios (0.19 to 3.76%), average modulus of elasticity of flexural reinforcement (28.4 to 147.6 GPa), moment-to-shear ratios (0 to 0.4 m), types of FRP flexural reinforcement (GFRP bars; CFRP bars and grids; hybrid grids), types of FRP shear reinforcement (GFRP studs, corrugated bars, stirrups and spirals; CFRP stirrups and spirals), and modulus of elasticity of shear reinforcement (44.8 to 130.4 GPa). All connections were subjected to monotonic gravity load only except those tested previously by the authors (ElGendy and El-Salakawy 2019, 2020a, 2020b), which were subjected to a combination of gravity load and uniaxial reversed-cyclic lateral load.

Table 7.1: Test data for interior connections without shear reinforcement

Specimen	L_1 [a] (mm)	L_2 [a] (mm)	C (mm)	h [b] (mm)	f_c' (MPa)	a (mm)	Flexural reinforcement			M/V (m)	V_{exp} (kN)
							Type [c]	ρ_F [d] (%)	E_F [d] (GPa)		
Hussein and El-Salakawy (2018)											
H-1.0-XX	2800 (2600)	2800 (2600)	300	200 (160)	80.0	19	G Bars	0.98	65.0	0.15	461
H-1.5-XX	2800 (2600)	2800 (2600)	300	200 (160)	84.0	19	G Bars	1.46	65.0	0.15	541
H-2.0-XX	2800 (2600)	2800 (2600)	300	200 (160)	87.0	19	G Bars	1.93	65.0	0.15	604
Gouda and El-Salakawy (2016a)											
GN-0.65	2800 (2600)	2800 (2600)	300	200 (160)	42.0	-	G Bars	0.65	68.0	0.15	363
GN-0.98	2800 (2600)	2800 (2600)	300	200 (160)	38.0	-	G Bars	0.98	68.0	0.15	378
GN-1.30	2800 (2600)	2800 (2600)	300	200 (160)	39.0	-	G Bars	1.13	68.0	0.15	425
GH-0.65	2800 (2600)	2800 (2600)	300	200 (160)	70.0	-	G Bars	0.65	68.0	0.15	380
Gouda and El-Salakawy (2016b)											
G-00-XX	2800 (2600)	2800 (2600)	300	200 (160)	38.0	19	G Bars	0.65	68.0	0	421
G-30-XX	2800 (2600)	2800 (2600)	300	200 (160)	42.0	19	G Bars	0.65	68.0	0.30	296
R-15-XX	2800 (2600)	2800 (2600)	300	200 (160)	40.0	19	G Bars	0.65	63.1	0.15	320
Dulude et al. (2013)											
$G_{(0.7)}30/20$	2500 (2000)	2500 (2000)	300	200 (134)	34.3	-	G Bars	0.71	48.2	0	329
$G_{(1.6)}30/20$	2500 (2000)	2500 (2000)	300	200 (131)	38.6	-	G Bars	1.56	48.1	0	431
$G_{(0.7)}45/20$	2500 (2000)	2500 (2000)	450	200 (134)	44.9	-	G Bars	0.71	48.2	0	400
$G_{(1.6)}45/20$	2500 (2000)	2500 (2000)	450	200 (131)	32.4	-	G Bars	1.56	48.1	0	504
$G_{(0.3)}30/35$	2500 (2000)	2500 (2000)	300	350 (284)	34.3	-	G Bars	0.34	48.2	0	825
$G_{(0.7)}30/35$	2500 (2000)	2500 (2000)	300	350 (281)	39.4	-	G Bars	0.73	48.1	0	1071
$G_{(0.3)}45/35$	2500 (2000)	2500 (2000)	450	350 (284)	48.6	-	G Bars	0.34	48.2	0	911
$G_{(0.7)}45/35$	2500 (2000)	2500 (2000)	450	350 (281)	29.6	-	G Bars	0.73	48.1	0	1248

Table 7.1: Test data for interior connections without shear reinforcement (continued)

Specimen	L_1 [a] (mm)	L_2 [a] (mm)	C (mm)	h [b] (mm)	f_c' (MPa)	a (mm)	Flexural reinforcement			M/V (m)	V_{exp} (kN)
							Type [c]	ρ_F [d] (%)	E_F [d] (GPa)		
Hassan et al. (2013a)											
$G_{(1.6)}30/20$-H	2500 (2000)	2500 (2000)	300	200 (131)	75.8	-	G Bars	1.56	57.4	0	547
$G_{(1.2)}30/20$	2500 (2000)	2500 (2000)	300	200 (131)	37.5	-	G Bars	1.21	64.9	0	438
$G_{(1.6)}30/35$	2500 (2000)	2500 (2000)	300	350 (275)	38.2	-	G Bars	1.61	57.4	0	1492
$G_{(1.6)}30/35$-H	2500 (2000)	2500 (2000)	300	350 (275)	75.8	-	G Bars	1.61	57.4	0	1600
Hassan et al. (2013b)											
$G_{(0.7)}30/20$-B	2500 (2000)	2500 (2000)	300	200 (134)	39.0	-	G Bars	0.71	48.2	0	386
$G_{(1.6)}30/20$-B	2500 (2000)	2500 (2000)	300	200 (131)	32.0	-	G Bars	1.56	48.1	0	451
$G_{(1.6)}45/20$-B	2500 (2000)	2500 (2000)	450	200 (131)	39.0	-	G Bars	1.56	48.1	0	511
$G_{(0.3)}30/35$-B	2500 (2000)	2500 (2000)	300	350 (284)	39.0	-	G Bars	0.34	48.2	0	782
$G_{(0.7)}30/35$-B-1	2500 (2000)	2500 (2000)	300	350 (281)	30.0	-	G Bars	0.73	48.1	0	1027
$G_{(0.7)}30/35$-B-2	2500 (2000)	2500 (2000)	300	350 (281)	47.0	-	G Bars	0.73	48.1	0	1195
$G_{(0.3)}45/35$-B	2500 (2000)	2500 (2000)	450	350 (284)	32.0	-	G Bars	0.34	48.2	0	1020
Nguyen-Minh and Rovnak (2013)											
GSL-PUNC-0.4	2200 (2000)	2200 (2000)	200	150 (129)	39.0	20-25	G Bars	0.48	48.0	0	180
GSL-PUNC-0.6	2200 (2000)	2200 (2000)	200	150 (129)	39.0	20-25	G Bars	0.68	48.0	0	212
GSL-PUNC-0.8	2200 (2000)	2200 (2000)	200	150 (129)	39.0	20-25	G Bars	0.92	48.0	0	244

Table 7.1: Test data for interior connections without shear reinforcement (continued)

Specimen	L_1 [a] (mm)	L_2 [a] (mm)	C (mm)	h [b] (mm)	f_c' (MPa)	a (mm)	Flexural reinforcement			M/V (m)	V_{exp} (kN)
							Type [c]	ρ_F [d] (%)	E_F [d] (GPa)		
Lee et al. (2009)											
GFU1	2300 (2000)	2300 (2000)	225	150 (110)	36.3	-	G Bars	1.18	48.2	0	222
GFB2	2300 (2000)	2300 (2000)	225	150 (110)	36.3	-	G Bars	2.15	48.2	0	246
GFB3	2300 (2000)	2300 (2000)	225	150 (110)	36.3	-	G Bars	3.00	48.2	0	248
El-Ghandour et al. (2003)											
SG1	2000 (1700)	2000 (1700)	200	175 (142)	32.0 [e]	-	G Bars	0.18	45.0	0	170
SC1	2000 (1700)	2000 (1700)	200	175 (142)	32.8 [e]	-	C Bars	0.15	110.0	0	229
SG2	2000 (1700)	2000 (1700)	200	175 (142)	46.4 [e]	-	G Bars	0.38	45.0	0	271
SG3	2000 (1700)	2000 (1700)	200	175 (142)	30.4 [e]	-	G Bars	0.38	45.0	0	237
SC2	2000 (1700)	2000 (1700)	200	175 (142)	29.6 [d]	-	C Bars	0.35	110.0	0	317
Ospina et al. (2003)											
GFR-1	2150 (1670)	2150 (1670)	250	155 (120)	29.5	-	G Bars	0.73	34.0	0	199
GFR-2	2150 (1670)	2150 (1670)	250	155 (120)	28.9	-	G Bars	1.46	34.0	0	249
NEF-1	2150 (1670)	2150 (1670)	250	155 (120)	37.5	-	G Grid	0.87	28.4	0	203

Table 7.1: Test data for interior connections without shear reinforcement (continued)

Specimen	L_1 [a] (mm)	L_2 [a] (mm)	C (mm)	h [b] (mm)	f_c' (MPa)	a (mm)	Flexural reinforcement			M/V (m)	V_{exp} (kN)
							Type [c]	ρ_F [d] (%)	E_F [d] (GPa)		
Matthys and Taerwe (2000)											
C1	1000 (900)	1000 (900)	134 [f]	120 (96)	36.7	-	C Grid	0.27	91.8	0	181
C1'	1000 (900)	1000 (900)	205 [f]	120 (96)	37.3	-	C Grid	0.27	91.8	0	189
C2	1000 (900)	1000 (900)	136 [f]	120 (95)	35.7	-	C Grid	1.05	95.0	0	255
C2'	1000 (900)	1000 (900)	205 [f]	120 (95)	36.3	-	C Grid	1.05	95.0	0	273
C3	1000 (900)	1000 (900)	134 [f]	150 (126)	33.8	-	C Grid	0.52	92.0	0	347
C3'	1000 (900)	1000 (900)	205 [f]	150 (126)	34.3	-	C Grid	0.52	92.0	0	343
CS	1000 (900)	1000 (900)	134 [f]	120 (95)	32.6	-	C Bars	0.19	147.6	0	142
CS'	1000 (900)	1000 (900)	205 [f]	120 (95)	33.2	-	C Bars	0.19	147.6	0	150
H1	1000 (900)	1000 (900)	134 [f]	120 (95)	118.0	-	H Grid	0.62	37.3	0	207
H2	1000 (900)	1000 (900)	134 [f]	120 (89)	35.8	-	H Grid	3.76	40.7	0	231
H2'	1000 (900)	1000 (900)	71 [f]	120 (89)	35.9	-	H Grid	3.76	40.7	0	171
H3	1000 (900)	1000 (900)	134 [f]	150 (122)	32.1	-	H Grid	1.22	44.8	0	237
H3'	1000 (900)	1000 (900)	71 [f]	150 (122)	32.1	-	H Grid	1.22	44.8	0	217

Note: L_1 = slab dimension perpendicular to unbalanced moment, if any; L_2 = slab dimension parallel to unbalanced moment, if any; C = column width; h = slab thickness; f_c' = concrete compressive strength; a = maximum aggregate size; ρ_F = average flexural reinforcement ratio; E_F = average flexural reinforcement modulus; M/V = moment-to-shear ratio; V_{exp} = ultimate capacity of connection.

[a] Value between parentheses represents supported dimension
[b] Value between parentheses represents slab effective depth
[c] C stands for carbon; G stands for glass; and H stands for hybrid (carbon and glass)
[d] Calculated using nominal dimensions of the FRP reinforcement
[e] Width of a square column with the same area as the used circular column
[f] Estimated as 80% of the reported cube strength

Table 7.2: Test data for edge connections without shear reinforcement

Specimen	L_1 [a] (mm)	L_2 [a] (mm)	C (mm)	h [b] (mm)	f_c' (MPa)	a (mm)	Flexural reinforcement			M/V (m)	V_{exp} (kN)
							Type [c]	ρ_F [d] (%)	E_F [d] (GPa)		
El-Gendy and El-Salakawy (2020b) [e]											
E50	3300 (3300)	3100 (2900)	300	200 (160)	47.0	-	G Bars	1.35	60.7	-	189
E60	3300 (3300)	3100 (2900)	300	200 (160)	48.0	-	G Bars	1.35	60.7	-	228
El-Gendy and El-Salakawy (2019) [e]											
EG-0.7	3300 (3300)	3100 (2900)	300	200 (160)	46.0	-	G Bars	0.68	60.7	-	119
EG-1.4	3300 (3300)	3100 (2900)	300	200 (160)	49.0	-	G Bars	1.35	60.7	-	153
Salama et al. (2019)											
G	2500 (2000)	1350 (1150)	300	200 (160)	41.4	-	G Bars	1.55	53.0	0.31	314
El-Gendy and El-Salakawy (2018a)											
GSC-1.35	2800 (2600)	1550 (1450)	300	200 (160)	42.0	19	G Bars	1.28	60.9	0.40	264
GSC-1.8	2800 (2600)	1550 (1450)	300	200 (160)	42.0	19	G Bars	1.70	60.9	0.40	278

Table 7.2: Test data for edge connections without shear reinforcement (continued)

Specimen	L_1 [a] (mm)	L_2 [a] (mm)	C (mm)	h [b] (mm)	f_c' (MPa)	a (mm)	Flexural reinforcement			M/V (m)	V_{exp} (kN)
							Type [c]	ρ_F [d] (%)	E_F [d] (GPa)		
Mostafa and El-Salakawy (2018)											
H-0.9-XX	2800 (2600)	1550 (1450)	300	200 (160)	81.0	-	G Bars	0.85	60.9	0.40	251
H-1.35-XX	2800 (2600)	1550 (1450)	300	200 (160)	85.0	-	G Bars	1.28	60.9	0.40	272
H-1.8-XX	2800 (2600)	1550 (1450)	300	200 (160)	80.0	-	G Bars	1.70	60.9	0.40	288
El-Gendy and El-Salakawy (2016)											
RD-XX-M	2800 (2600)	1550 (1450)	300	200 (160)	45.8	-	G Bars	0.85	60.2	0.40	191
SC-XX-L	2800 (2600)	1550 (1450)	300	200 (160)	49.4	-	G Bars	0.85	60.9	0.20	239
SC-XX-M	2800 (2600)	1550 (1450)	300	200 (160)	47.3	-	G Bars	0.85	60.9	0.40	227
SC-XX-H	2800 (2600)	1550 (1450)	300	200 (160)	48.4	-	G Bars	0.85	60.9	0.60	159

Note: L_1 = slab dimension perpendicular to unbalanced moment, if any; L_2 = slab dimension parallel to unbalanced moment, if any; C = column width; h = slab thickness; f_c' = concrete compressive strength; a = maximum aggregate size; ρ_F = average flexural reinforcement ratio; E_F = average flexural reinforcement modulus; M/V = moment-to-shear ratio; V_{exp} = ultimate capacity of the connection.

[a] Value between parentheses represents supported dimension
[b] Value between parentheses represents slab effective depth
[c] G stands for glass
[d] Calculated using nominal dimensions of the FRP reinforcement
[e] Specimens subjected to reversed-cyclic lateral load

Table 7.3: Test data for shear-reinforced interior connections

Specimen	L_1 [a] (mm)	L_2 [a] (mm)	h [b] (mm)	f_c' (MPa)	Flexural reinforcement [c]		Shear reinforcement					M/V (mm)	V_{exp} (kN)
					ρ_F [d] (%)	E_F [d] (GPa)	Type [e]	A_s [d] (mm^2)	n	s (mm)	E_{Fv} [d] (GPa)		
Hussein and El-Salakawy (2018)													
N-1.0-S5	2800 (2600)	2800 (2600)	200 (160)	43.0	0.98	65.0	G-SS	127	12	120	68.0	0.15	595
N-1.0-S6	2800 (2600)	2800 (2600)	200 (160)	43.0	0.98	65.0	G-SS	127	12	120	68.0	0.15	583
N-1.0-C5	2800 (2600)	2800 (2600)	200 (160)	43.0	0.98	65.0	G-CB	71	12	120	52.0	0.15	527
Gouda and El-Salakawy (2016b)													
R-15-75	2800 (2600)	2800 (2600)	200 (160)	42.0	0.65	63.1	G-SS	113	8	120	60.0	0.15	385
R-15-50	2800 (2600)	2800 (2600)	200 (160)	42.0	0.65	63.1	G-SS	113	8	80	60.0	0.15	401
Hassan et al. (2014)													
$G_{(1.2)}$200-GCS(d/2)	2500 (2000)	2500 (2000)	200 (131)	37.5	1.21	64.9	G-ST	71	16	70	44.8	0	614
$G_{(1.2)}$200-CCS(d/2)	2500 (2000)	2500 (2000)	200 (131)	37.5	1.21	64.9	C-ST	71	8	70	130.4	0	514
$G_{(0.3)}$350-GSS(d/4)	2500 (2000)	2500 (2000)	350 (284)	29.5	0.34	48.2	G-SP	129	8	70	44.6	0	885
$G_{(1.6)}$350-GSS(d/4)	2500 (2000)	2500 (2000)	350 (280)	40.2	1.61	56.7	G-SP	129	8	70	44.6	0	1761

Table 7.3: Test data for shear-reinforced interior connections (continued)

Specimen	L_1 [a] (mm)	L_2 [a] (mm)	h [b] (mm)	f_c' (MPa)	Flexural reinforcement [c]		Shear reinforcement					M/V (mm)	V_{exp} (kN)
					ρ_F [d] (%)	E_F [d] (GPa)	Type [e]	A_s [d] (mm^2)	n	s (mm)	E_{Fv} [d] (GPa)		
Hassan et al. (2014) - continued													
$G_{(1.6)}$350-GBSS(d/4)	2500 (2000)	2500 (2000)	350 (280)	37.5	1.61	56.7	G-BSP	129	16	70	44.6	0	1869
$G_{(1.6)}$350-CSS(d/4)	2500 (2000)	2500 (2000)	350 (280)	38.2	1.61	56.7	C-SP	129	8	70	124.4	0	2024
$G_{(1.6)}$350-CSS(d/3)	2500 (2000)	2500 (2000)	350 (280)	40.2	1.61	56.7	C-SP	129	8	100	124.4	0	1886

Note: L_1 = slab dimension perpendicular to unbalanced moment, if any; L_2 = slab dimension parallel to unbalanced moment, if any; h = slab thickness; f_c' = concrete compressive strength; ρ_F = average flexural reinforcement ratio; E_F = average flexural reinforcement modulus; A_s = area of a single shear stud or vertical stem of corrugate bars, stirrups and spirals; n = number of vertical stems of shear reinforcement in a peripheral row around the column; s = radial spacing of vertical stems of shear reinforcement; E_{Fv} = shear reinforcement modulus; M/V = moment-to-shear ratio; V_{exp} = ultimate capacity of the connection. All columns are 300-mm square columns.

[a] Value between parentheses represents supported dimension
[b] Value between parentheses represents slab effective depth
[c] All flexural reinforcement are GFRP bars
[d] Calculated using nominal dimensions of the FRP reinforcement
[e] C stands for carbon; G stands for glass; SS stand for shear studs; CB stands for corrugated bars; ST stands for stirrups; SP stands for spirals; and BSP stands for bundled spirals

Table 7.4: Test data for shear-reinforced edge connections

Specimen	L_1 [a] (mm)	L_2 [a] (mm)	h [b] (mm)	f_c' (MPa)	Flexural reinforcement [c]		Shear reinforcement					M/V (m)	V_{exp} (kN)
					ρ_F [d] (%)	E_F [d] (GPa)	Type [e]	A_s [d] (mm^2)	n	s (m)	E_{Fv} [d] (GPa)		
El-Gendy and El-Salakawy (2020) [f]													
ESS	3300 (3300)	3100 (2900)	200 (160)	49.0	1.35	60.7	G-SS	129	6	80	68.0	-	229
ECB	3300 (3300)	3100 (2900)	200 (160)	41.0	1.35	60.7	G-CB	129	6	80	52.0	-	217
Salama et al. (2019)													
G-CS-1.75d	2500 (2000)	1350 (1150)	200 (160)	47.6	1.55	53.0	G-ST	71	12	80	45.7	0.31	370
G-CS-4.25d	2500 (2000)	1350 (1150)	200 (160)	51.3	1.55	53.0	G-ST	71	12	80	45.7	0.30	444
G-SS-4.25d	2500 (2000)	1350 (1150)	200 (160)	52.5	1.55	53.0	G-SP	71	12	80	45.7	0.30	486
Mostafa and El-Salakawy (2018)													
N-0.9-S8	2800 (2600)	1550 (1450)	200 (160)	43.0	0.85	60.9	G-SS	127	8	120	68.0	0.40	294
N-0.9-C8	2800 (2600)	1550 (1450)	200 (160)	43.0	0.85	60.9	G-CB	71	8	120	52.0	0.40	286
N-0.9-S6	2800 (2600)	1550 (1450)	200 (160)	44.0	0.85	60.9	G-SS	127	6	120	68.0	0.40	298
N-0.9-C6	2800 (2600)	1550 (1450)	200 (160)	45.0	0.85	60.9	G-CB	71	6	120	52.0	0.40	253

Table 7.4: Test data for shear-reinforced edge connections (continued)

Specimen	L_1 [a] (mm)	L_2 [a] (mm)	h [b] (mm)	f_c' (MPa)	Flexural reinforcement [c]		Shear reinforcement					M/V (m)	V_{exp} (kN)
					ρ_F [d] (%)	E_F [d] (GPa)	Type [e]	A_s [d] (mm^2)	n	s (m)	E_{Fv} [d] (GPa)		
El-Gendy and El-Salakawy (2016)													
RD-75-M	2800 (2600)	1550 (1450)	200 (160)	41.0	0.85	60.2	G-SS	113	6	120	60.0	0.40	256
RD-50-M	2800 (2600)	1550 (1450)	200 (160)	38.0	0.85	60.2	G-SS	113	6	80	60.0	0.40	273

Note: L_1 = slab dimension perpendicular to unbalanced moment, if any; L_2 = slab dimension parallel to unbalanced moment, if any; h = slab thickness; f_c' = concrete compressive strength; ρ_F = average flexural reinforcement ratio; E_F = average flexural reinforcement modulus; A_s = area of a single shear stud or vertical stem of corrugate bars, stirrups and spirals; n = number of vertical stems of shear reinforcement in a peripheral row around the column; s = radial spacing of vertical stems of shear reinforcement; E_{Fv} = shear reinforcement modulus; M/V = moment-to-shear ratio; V_{exp} = ultimate capacity of the connection. All columns are 300-mm square columns.

[a] Value between parentheses represents supported dimension
[b] Value between parentheses represents slab effective depth
[c] All flexural reinforcement are GFRP bars
[d] Calculated using nominal dimensions of the FRP reinforcement
[e] G stands for glass
[f] Specimens subjected to reversed-cyclic lateral load

7.5. Punching Shear Capacity

7.5.1. Assessment of design models for connections without shear reinforcement

Table 7.5 and Table 7.6 list comparisons between the experimental and predicted shear strength of interior and edge connections without shear reinforcement, respectively. It is worth mentioning that all strength and material factors were set to 1.0 in all calculations. As can be noticed in Figure 7.3, both the CSA S806-12 (CSA 2017) and JSCE (JSCE 1997) models give slightly conservative estimates for interior connections. The CSA S806-12 model predicted the capacity with a mean v_{exp}/v_{pred}, coefficient of variation (COV) and coefficient of determination (R^2) of 1.20 ± 0.22, 18.3% and 0.62, respectively. Similarly, the JSCE model had a mean v_{exp}/v_{pred}, COV and R^2 of 1.19 ± 0.20, 16.6% and 0.68, respectively. The ACI 440.1R-15 model (ACI 2015), however, highly underestimates the strength with a mean v_{exp}/v_{pred}, COV and R^2 of 2.18 ± 0.43, 19.7% and 0.64, respectively, since it assumes that shear stresses are resisted solely by the uncracked concrete, ignoring the aggregate interlock and dowel action contributions.

On the other hand, the early model proposed by Matthys and Taerwe (2000), *Model I*, provided similar conservative estimates to the CSA S806-12 (CSA 2017) and JSCE (JSCE 1997) ones with a mean v_{exp}/v_{pred} of 1.19 ± 0.18 and improved COV and R^2 of 14.9% and 0.74, respectively. The three other models proposed in the literature (*Models II* to *IV*), give much better estimates with a mean v_{exp}/v_{pred} close to unity. Out of all models, *Model IV* (Hassan et al. 2017) produced the best estimates. With a mean v_{exp}/v_{pred}, COV and R^2 of 1.01 ± 0.14, 13.6% and 0.78, respectively, it provides the least scattered results and best fit for interior connections.

Table 7.5: Model comparisons for interior connections without shear reinforcement

Connection	$v_{exp,\ 0.5d}$ (MPa)	$v_{exp,\ 1.5d}$ (MPa)	Test-to-predicted strength								
			CSA S806-12	ACI 440.1R-15	JSCE 1997	*Models*					
						I	*II*	*III*	*IV*	*P-I*	*P-II*
Hussein and El-Salakawy (2018)											
H-1.0-XX	2.16	1.13	1.14	1.89	1.30	1.01	0.78	0.81	0.93	0.81	0.93
H-1.5-XX	2.54	1.33	1.18	1.84	1.34	1.02	0.79	0.81	0.95	0.81	0.95
H-2.0-XX	2.83	1.49	1.20	1.79	1.36	1.02	0.79	0.81	0.95	0.81	0.95
Gouda and El-Salakawy (2016a)											
GN-0.65	1.70	0.89	1.15	2.10	1.16	1.11	0.85	0.99	1.03	0.99	1.03
GN-0.98	1.77	0.93	1.08	1.87	1.05	1.04	0.80	0.94	0.97	0.94	0.97
GN-1.30	1.99	1.05	1.09	1.84	1.08	1.06	0.81	0.96	0.98	0.96	0.98
GH-0.65	1.78	0.94	1.07	1.92	1.21	0.98	0.75	0.81	0.91	0.81	0.91
Gouda and El-Salakawy (2016b)											
G-00-XX	1.43	0.84	1.00	1.82	0.97	1.09	0.83	0.88	0.90	0.88	0.90
G-30-XX	1.77	0.86	1.19	2.19	1.21	1.07	0.82	1.03	1.07	1.03	1.07
R-15-XX	1.50	0.79	1.05	1.94	1.05	1.02	0.79	0.92	0.95	0.92	0.95
Dulude et al. (2013)											
$G_{(0.7)}30/20$	1.41	0.87	1.11	2.08	1.11	1.21	1.03	1.04	1.01	1.04	1.01
$G_{(1.6)}30/20$	1.91	1.19	1.11	1.90	1.13	1.21	1.03	1.03	1.01	1.03	1.01
$G_{(0.7)}45/20$	1.28	0.88	0.92	1.75	1.04	1.11	0.94	0.91	0.91	0.91	0.91
$G_{(1.6)}45/20$	1.66	1.14	1.02	1.73	1.10	1.23	1.05	1.09	1..01	1.09	1..01
$G_{(0.3)}30/35$	1.24	0.63	1.25	2.58	1.20	1.35	0.95	0.96	1.09	0.96	1.09
$G_{(0.7)}30/35$	1.64	0.83	1.22	2.29	1.20	1.32	0.93	0.92	1.06	0.92	1.06
$G_{(0.3)}45/35$	1.09	0.62	0.98	2.07	1.10	1.17	0.83	0.79	0.93	0.79	0.93
$G_{(0.7)}45/35$	1.52	0.86	1.24	2.29	1.31	1.49	1.05	1.09	1.18	1.09	1.18

Table 7.5: Model comparisons for interior connections without shear reinforcement (continued)

Connection	$v_{exp,\ 0.5d}$ (MPa)	$v_{exp,\ 1.5d}$ (MPa)	Test-to-predicted strength								
			CSA S806-12	ACI 440.1R-15	JSCE 1997	*Models*					
						I	*II*	*III*	*IV*	*P-I*	*P-II*
Hassan et al. (2013a)											
$G_{(1.6)}$30/20-H	2.42	1.51	1.15	1.85	1.35	1.16	0.96	0.88	0.97	0.88	0.97
$G_{(1.2)}$30/20	1.94	1.21	1.12	1.91	1.13	1.22	0.99	1.04	1.02	1.04	1.02
$G_{(1.6)}$30/35	2.36	1.21	1.28	2.15	1.25	1.39	0.96	0.98	1.12	0.98	1.12
$G_{(1.6)}$30/35-H	2.53	1.29	1.18	1.91	1.34	1.18	0.82	0.75	0.95	0.75	0.95
Hassan et al. (2013b)											
$G_{(0.7)}$30/20-B	1.66	1.03	1.25	2.35	1.27	1.36	1.16	1.15	1.14	1.15	1.14
$G_{(1.6)}$30/20-B	2.00	1.24	1.24	2.10	1.25	1.35	1.15	1.18	1.13	1.18	1.13
$G_{(1.6)}$45/20-B	1.68	1.16	0.97	1.67	1.06	1.18	1.00	1.00	0.96	1.00	0.96
$G_{(0.3)}$30/35-B	1.18	0.60	1.13	2.36	1.11	1.22	0.86	0.85	0.98	0.85	0.98
$G_{(0.7)}$30/35-B-1	1.57	0.80	1.28	2.37	1.26	1.38	0.98	1.01	1.11	1.01	1.11
$G_{(0.7)}$30/35-B-2	1.83	0.93	1.28	2.44	1.34	1.39	0.98	0.94	1.12	0.94	1.12
$G_{(0.3)}$45/35-B	1.22	0.69	1.26	2.58	1.31	1.51	1.06	1.09	1.20	1.09	1.20
Nguyen-Minh and Rovnak (2013)											
GSL-PUNC-0.4	1.06	0.59	0.91	1.81	0.87	0.89	0.77	0.76	0.76	0.76	0.76
GSL-PUNC-0.6	1.25	0.70	0.96	1.81	0.92	0.94	0.80	0.80	0.79	0.80	0.79
GSL-PUNC-0.8	1.44	0.81	0.99	1.81	0.95	0.97	0.84	0.83	0.83	0.83	0.83

Table 7.5: Model comparisons for interior connections without shear reinforcement (continued)

Connection	$v_{exp,\ 0.5d}$ (MPa)	$v_{exp,\ 1.5d}$ (MPa)	Test-to-predicted strength								
			CSA S806-12	ACI 440.1R-15	JSCE 1997	*Models*					
						I	*II*	*III*	*IV*	*P-I*	*P-II*
Lee et al. (2009)											
GFU1	1.51	0.91	0.98	1.73	0.96	0.99	0.89	0.89	0.85	0.89	0.85
GFB2	1.67	1.01	0.89	1.47	0.87	0.90	0.80	0.81	0.77	0.81	0.77
GFB3	1.68	1.02	0.80	1.28	0.78	0.81	0.73	0.73	0.69	0.73	0.69
El-Ghandour et al. (2003)											
SG1	0.88	0.48	1.14	2.58	1.06	1.11	0.94	0.95	0.94	0.95	0.94
SC1	1.18	0.64	1.20	2.46	1.11	1.17	0.86	1.00	0.99	1.00	0.99
SG2	1.40	0.76	1.25	2.62	1.24	1.22	1.03	0.99	1.03	0.99	1.03
SG3	1.22	0.67	1.26	2.56	1.18	1.23	1.04	1.06	1.04	1.06	1.04
SC2	1.63	0.89	1.29	2.36	1.22	1.27	0.92	1.10	1.07	1.10	1.07
Ospina et al. (2003)											
GFR-1	1.12	0.68	1.03	1.99	1.04	1.07	0.99	0.97	0.90	0.97	0.90
GFR-2	1.40	0.85	1.03	1.82	1.04	1.07	0.99	0.98	0.90	0.98	0.90
NEF-1	1.14	0.69	0.97	1.91	0.96	1.01	0.96	0.88	0.85	0.88	0.85

Table 7.5: Model comparisons for interior connections without shear reinforcement (continued)

Connection	$v_{exp,\ 0.5d}$ (MPa)	$v_{exp,\ 1.5d}$ (MPa)	Test-to-predicted strength								
			CSA S806-12	ACI 440.1R-15	JSCE 1997	*Models*					
						I	*II*	*III*	*IV*	*P-I*	*P-II*
Matthys and Taerwe (2000)											
C1	2.05	1.12	1.76	3.44	1.61	1.55	1.29	1.44	1.36	1.44	1.36
C1'	1.64	1.00	1.39	2.73	1.38	1.38	1.14	1.27	1.18	1.27	1.18
C2	2.94	1.60	1.59	2.64	1.46	1.41	1.16	1.31	1.23	1.31	1.23
C2'	2.40	1.47	1.29	2.15	1.28	1.28	1.06	1.19	1.10	1.19	1.10
C3	2.65	1.35	1.87	3.36	1.65	1.65	1.28	1.45	1.42	1.45	1.42
C3'	2.06	1.17	1.45	2.59	1.37	1.43	1.10	1.25	1.21	1.25	1.21
CS	1.64	0.88	1.40	2.67	1.30	1.21	0.93	1.19	1.09	1.19	1.09
CS'	1.32	0.79	1.12	2.14	1.11	1.08	0.83	1.06	0.96	1.06	0.96
H1	2.38	1.30	1.77	3.03	1.92	1.25	1.21	0.95	1.09	0.95	1.09
H2	2.92	1.62	1.37	2.18	1.27	1.21	1.17	1.15	1.06	1.15	1.06
H2'	3.00	1.42	1.41	2.24	1.17	1.06	1.03	1.01	0.95	1.01	0.95
H3	1.90	0.97	1.31	2.30	1.17	1.15	1.01	1.03	0.99	1.03	0.99
H3'	2.30	1.02	1.58	2.78	1.28	1.21	1.06	1.07	1.06	1.07	1.06
Mean			1.20	2.18	1.19	1.19	0.96	1.00	1.01	1.00	1.01
SD			0.22	0.43	0.20	0.18	0.14	0.16	0.14	0.16	0.14
COV (%)			18.3	19.7	16.6	14.9	14.6	16.2	13.6	16.2	13.6
R^2			0.62	0.64	0.68	0.74	0.70	0.70	0.78	0.70	0.78

Note: $v_{exp,\ 0.5d}$ = shear stress resistance provided by concrete at a critical section located at a distance of 0.5*d* from column face; $v_{exp,\ 1.5d}$ = shear stress resistance provided by concrete at a critical section located at a distance of 1.5*d* from column face.

Table 7.6: Model comparisons for edge connections without shear reinforcement

Connection	$v_{exp,\ 0.5d}$ (MPa)	$v_{exp,\ 1.5d}$ (MPa)	Test-to-predicted strength								
			CSA S806-12	ACI 440.1R-15	JSCE 1997	*Models*					
						I	*II*	*III*	*IV*	*P-I*	*P-II*
El-Gendy and El-Salakawy (2020b) [a]											
E50	2.28	1.07	1.20	2.06	1.20	1.04	0.81	0.84	0.92	0.97	1.03
E60	2.28	1.09	1.19	2.05	1.20	1.05	0.82	0.83	0.91	0.96	1.03
El-Gendy and El-Salakawy (2019) [a]											
EG-0.7	1.87	0.86	1.25	2.33	1.24	1.06	0.83	0.88	0.96	1.01	1.08
EG-1.4	2.23	1.03	1.16	2.00	1.18	0.99	0.78	0.81	0.89	0.93	1.00
Salama et al. (2019)											
G	2.43	1.19	1.26	2.16	1.23	1.16	0.91	0.92	0.98	1.07	1.10
El-Gendy and El-Salakawy (2018a)											
GSC-1.35	2.36	1.14	1.32	2.26	1.27	1.17	0.92	0.94	1.01	1.08	1.13
GSC-1.8	2.48	1.20	1.26	2.10	1.21	1.12	0.88	0.90	0.96	1.04	1.09
Mostafa and El-Salakawy (2018)											
H-0.9-XX	2.24	1.08	1.27	2.16	1.38	1.03	0.80	0.74	0.88	0.85	0.99
H-1.35-XX	2.43	1.17	1.21	1.92	1.31	0.96	0.75	0.68	0.82	0.78	0.92
H-1.8-XX	2.57	1.24	1.16	1.82	1.26	0.94	0.73	0.68	0.81	0.78	0.91

Table 7.6: Model comparisons for edge connections without shear reinforcement (continued)

Connection	$v_{exp,\ 0.5d}$ (MPa)	$v_{exp,\ 1.5d}$ (MPa)	Test-to-predicted strength								
			CSA S806-12	ACI 440.1R-15	JSCE 1997	*Models*					
						I	*II*	*III*	*IV*	*P-I*	*P-II*
El-Gendy and El-Salakawy (2016)											
RD-XX-M	1.71	0.82	1.10	1.99	1.05	0.98	0.77	0.79	0.84	0.91	0.95
SC-XX-L	1.50	0.76	1.00	1.79	0.93	0.93	0.73	0.73	0.77	0.84	0.86
SC-XX-M	2.03	0.98	1.32	2.37	1.25	1.17	0.92	0.95	1.01	1.09	1.14
SC-XX-H	1.84	0.87	1.23	2.19	1.13	1.07	0.83	0.90	0.94	1.03	1.06
Mean			1.21	2.09	1.20	1.05	0.82	0.83	0.91	0.95	1.02
SD			0.09	0.18	0.11	0.08	0.07	0.09	0.08	0.11	0.09
COV (%)			7.1	8.4	9.2	8.1	8.1	11.2	8.4	11.2	8.4
R^2			0.81	0.78	0.70	0.74	0.74	0.63	0.73	0.63	0.73

Note: $v_{exp,\ 0.5d}$ = shear stress resistance provided by concrete at a critical section located at a distance of 0.5*d* from column face; $v_{exp,\ 1.5d}$ = shear stress resistance provided by concrete at a critical section located at a distance of 1.5*d* from column face.

[a] Specimens subjected to reversed cyclic lateral load.

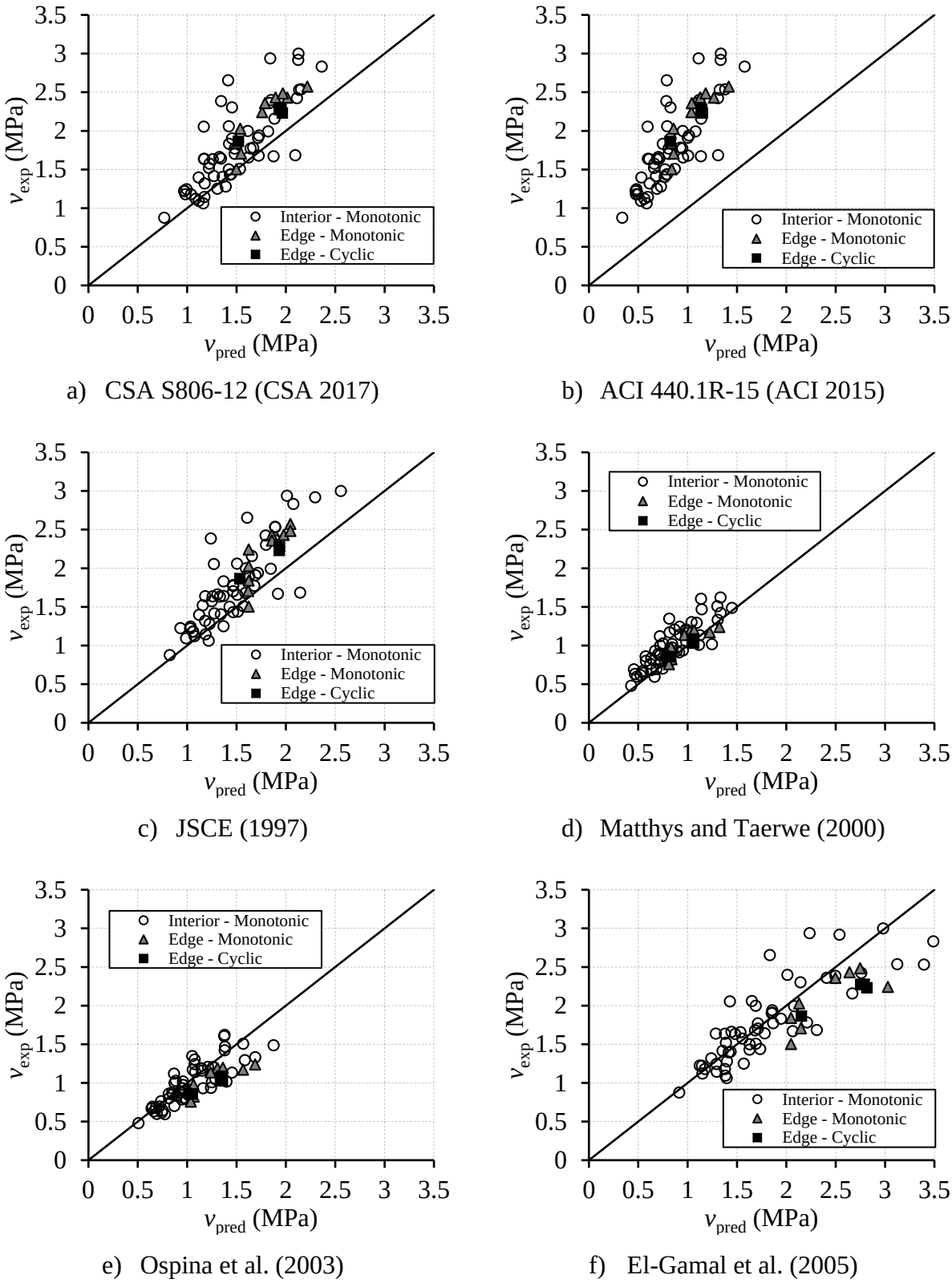

a) CSA S806-12 (CSA 2017)

b) ACI 440.1R-15 (ACI 2015)

c) JSCE (1997)

d) Matthys and Taerwe (2000)

e) Ospina et al. (2003)

f) El-Gamal et al. (2005)

Figure 7.3: Predictions of available models for connections without shear reinforcement

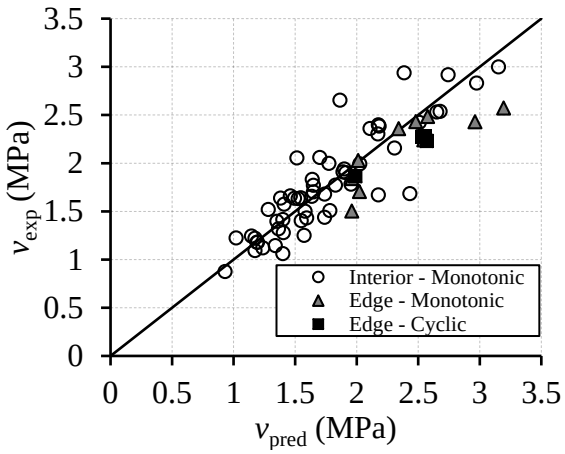

g) Hassan et al. (2017)

Figure 7.3: Predictions of available models for connections without shear reinforcement

(continued)

For edge connections, the models of the three codes give consistent estimates as in the case of interior connections. Both the CSA S806-12 (CSA 2017) and JSCE (JSCE 1997) models consistently give reasonable predictions with a mean v_{exp}/v_{pred} of 1.21 ± 0.09, and 1.20 ± 0.11, respectively. However, the CSA S806-12 model produces less scattered results and better fits the data for edge connections with COV and R^2 of 7.1% and 0.81, respectively, compared to 9.2% and 0.70 for the JSCE model, respectively. Again, the ACI 440.1R-15 model (ACI 2015) was too conservative with a mean v_{exp}/v_{pred} of 2.09 ± 0.18.

Model I, proposed by Matthys and Taerwe (2000), provides accurate estimates for edge connections with a mean v_{exp}/v_{pred}, COV and R^2 of 1.05 ± 0.08, 8.1% and 0.74, respectively. This is a better mean than that of the CSA S806-12 model with a comparable R^2 value. The main difference between *Model I* and the CSA S806-12 model is that the former considers the size effect for all slab thicknesses, unlike the latter, which includes a size effect only for slabs with effective depth more than 300 mm. On the other hand, despite giving good predictions for interior

connections, *Models II* to *IV* overestimate the capacity of edge connections and provide unconservative predictions with a mean v_{exp}/v_{pred} of 0.82 ± 0.07, 0.83 ± 0.09 and 0.91 ± 0.08, respectively. In *Model II* (Equation 7.16), the coefficient 2.77 was selected so that the average test-to-predicted value for the tested interior connections is close to unity. On the other hand, *Models III* and *IV* (Equation 7.17 and Equation 7.18) consider the effect of shear perimeter-to-depth ratio (b_o/d) without considering the effect of connection location, i.e., interior, edge, or corner.

7.5.2. Proposed design model for connections without shear reinforcement

Although the CSA S806-12 (CSA 2017) and JSCE (JSCE 1997) models provide consistent reasonable estimates for both interior and edge connections, several models proposed in the literature have a potential to produce better predictions with few modifications. As mentioned earlier, *Model I* (Matthys and Taerwe 2000) gives consistently accurate predictions for both interior and edge connections; however, it considers the critical section at 1.5*d* from the column face. This is different from the approach followed by the CSA S806-12 and ACI 440.1R-15 models, which considers the critical section at 0.5*d* from the column face. On the other hand, *Models III* and *IV* (El-Gamal et al. 2005; Hassan et al. 2017) accurately estimate the capacity of interior connections but considerably overestimate that of the edge ones. This deems them deficient in designing flat plate systems, which consist of both interior and edge connections. Thus, a location factor is introduced to both models to make them suitable for all types of connections.

The CSA S806-12 model (CSA 2017) considers the location of the connection and the confinement provided by the slab surrounding the critical section through a dimensionless coefficient, α_s. In case of interior connections, where the critical section is confined from all four directions, this factor is taken as 4. When the confinement is reduced to only three and two sides in the case of

edge and corner connections, this factor is taken as 3 and 2, respectively. Thus, when the perimeter of the critical section is reduced due to the discontinuity of the slab in case of exterior connections, the estimated punching strength is reduced accordingly.

By implementing this modification in *Models III* and *IV*, *Models P-I* and *P-II* (Equation 7.27 and Equation 7.28) are proposed to evaluate the punching capacity of FRP-RC two-way slabs regardless of the connection location. The test-to-predicted ratios using the proposed models are listed in Table 7.5 and Table 7.6 and shown in Figure 7.4. *Model P-I* slightly overestimates the capacity of edge connections with a mean v_{exp}/v_{pred}, COV and R^2 of 0.95 ± 0.11, 11.2% and 0.63, respectively. *Model P-II*, however, produced reliable predictions with a precise mean v_{exp}/v_{pred} of 1.02 ± 0.09, a COV of 8.4% and a coefficient of determination of 0.73 for edge connections, which is consistent with its predictions for interior ones.

$$v_c = 0.33\sqrt{f_c'}\left[0.62\left(\rho_F E_F\right)^{1/3}\left(1+\frac{2\alpha_s d}{b_{o,0.5d}}\right)\right](1.2)^N \qquad \text{Equation 7.27}$$

$$v_c = 0.065\lambda\phi_c\left(\alpha_s\frac{d}{b_{o,0.5d}}+0.65\right)\left(E_F\rho_F f_c'\right)^{1/3}\left(125/d\right)^{1/6} \qquad \text{Equation 7.28}$$

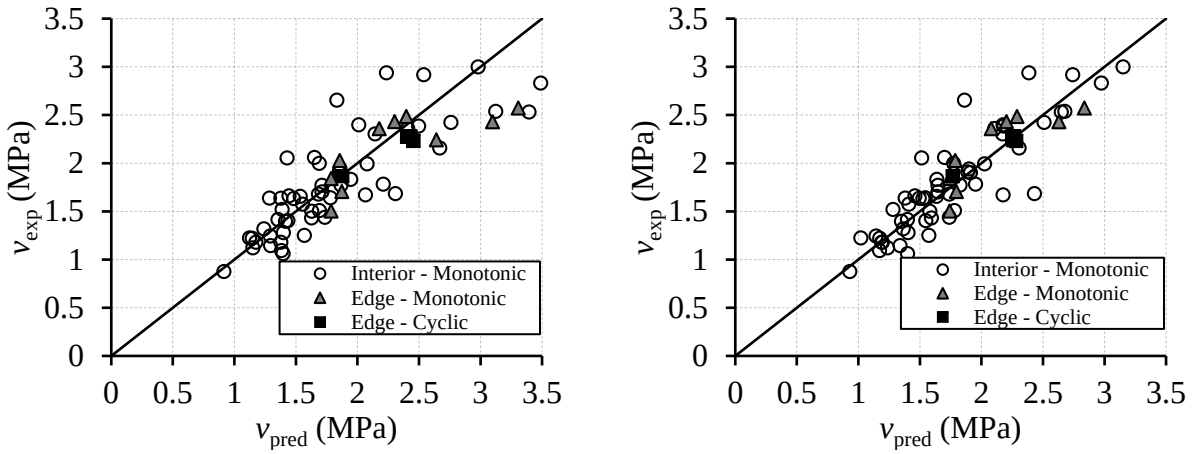

a) Model P-I b) Model P-II

Figure 7.4: Predictions of the proposed models for connections without shear reinforcement

7.5.3. Assessment of design models for shear-reinforced connections

Table 7.7 and Table 7.8 list comparisons between the experimental and predicted shear strengths of shear-reinforced interior and edge connections, respectively. As can be noticed in Figure 7.5, *Model V* (Hassan et al. 2014) underestimates the capacity of shear-reinforced interior connections with a mean v_{exp}/v_{pred} of 1.30 ± 0.30. With COV and R^2 of 22.8% and 0.60, respectively, the model provides scattered and poorly fitted results. This could be attributed to the relatively low concrete and shear reinforcement contributions that the model considers (Equation 7.19 to Equation 7.21), which are 50% of that recommended by CSA S806-12 (CSA 2017) for connections without shear reinforcement (Equation 7.6) and 2,800 με, respectively. *Model VI* (El-Gendy and El-Salakawy 2016), on the contrary, provided accurate, low-scattered predictions with a mean v_{exp}/v_{pred} and COV of 1.05 ± 0.13 and 12.6%, respectively. Furthermore, it had a close to unity R^2 of 0.96, which indicates that the model explains all the considered variability factors of the capacity of shear-reinforced interior connections with a reasonable degree of accuracy. Similarly, *Model VII* (Salama

et al. 2019) provided reasonable estimations with a slightly conservative v_{exp}/v_{pred} of 1.14 ± 0.20 and a high R^2 of 0.94.

For shear-reinforced edge connections, the inaccuracy of *Model V* is further intensified with a mean v_{exp}/v_{pred} of 1.52 ± 0.25 and a considerably low R^2 of 0.43. On the contrary, as for interior connections, *Model VI* consistently provided precise predictions with a mean v_{exp}/v_{pred} value of 0.97 ± 0.17. However, its R^2 was only 0.79 in case of edge connections due to the inefficiency in predicting the capacity of edge connections subjected to cyclic loads. For the two shear-reinforced connections subjected to cyclic loads, the mean v_{exp}/v_{pred} was 0.78 ± 0.08. This considerable overestimation is attributed to the inability of GFRP shear reinforcement to attain the relatively high strain limit of 5,000 με in connections subjected to reversed-cyclic lateral loads. Similarly, *Model VII* provided reasonable conservative predictions with a mean v_{exp}/v_{pred}, COV and R^2 of 1.11 ± 0.22, 19.9% and 0.74, respectively, while overestimating the capacity of connections subjected to cyclic loads with a mean v_{exp}/v_{pred} of 0.89 ± 0.11.

Table 7.7: Model comparisons for shear-reinforced interior connections

Connection	Experimental results			Test-to-predicted strength				
	$v_{exp,\ 0.5d}$ (MPa)		Failure type [a]	Flexural capacity	*Model V*	*Model VI*	*Model VII*	*Model P-III*
	Inner	Outer						
Hussein and El-Salakawy (2018)								
N-1.0-S5	2.79	0.85	F-P	0.96	1.29	1.01	1.01	1.01
N-1.0-S6	2.73	0.72	F-P	0.94	1.27	0.85	0.86	0.85
N-1.0-C5	2.47	0.78	P	0.85	1.76	1.10	1.34	1.10
Gouda and El-Salakawy (2016b)								
R-15-75	1.80	0.60	P	0.74	1.64	1.13	1.44	1.13
R-15-50	1.88	0.62	P	0.77	1.46	1.01	1.23	1.01

Table 7.7: Model comparisons for shear-reinforced interior connections (continued)

Connection	Experimental results			Test-to-predicted strength				
	$v_{exp,\ 0.5d}$ (MPa)		Failure type [a]	Flexural capacity	*Model V*	*Model VI*	*Model VII*	*Model P-III*
	Inner	Outer						
Hassan et al. (2014)								
G(1.2)200-GCS(d/2)	2.72	0.79	P	-	1.33	0.92	0.92	0.92
G(1.2)200-CCS(d/2)	2.28	0.66	P	-	0.88	0.77	0.77	0.77
G(0.3)350-GSS(d/4)	1.33	0.49	P	-	1.06	1.03	1.03	1.03
G(1.6)350-GSS(d/4)	2.71	0.98	P	-	1.57	1.05	1.15	1.05
G(1.6)350-GBSS(d/4)	2.88	1.04	P	-	1.15	1.15	1.15	1.15
G(1.6)350-CSS(d/4)	3.12	1.13	P	-	1.00	1.23	1.23	1.23
G(1.6)350-CSS(d/3)	2.90	1.05	P	-	1.17	1.13	1.13	1.13
Mean [b]					1.30	1.05	1.14	1.05
SD [b]					0.30	0.13	0.20	0.13
COV (%) [b]					22.8	12.6	17.2	12.6
R^2 [b]					0.60	0.96	0.94	0.96

Note: $v_{exp,\ 0.5d}$ = shear stress resistance provided by concrete at a critical section located at a distance of 0.5*d* from column face or outermost shear reinforcement row.

[a] Reported in the literature (F = flexural failure; P = punching failure; and F-P = mixed flexural/punching failure).
[b] For connections failing in punching only

Table 7.8: Model comparisons for shear-reinforced edge connections

Connection	Experimental results			Test-to-predicted strength				
	$v_{exp,\ 0.5d}$ (MPa)		Failure type [a]	Flexural capacity	*Model V*	*Model VI*	*Model VII*	*Model P-III*
	Inner	Outer						
El-Gendy and El-Salakawy (2020) [b]								
ESS	2.96	0.64	P	0.52	1.20	0.72	0.81	0.98
ECB	2.91	0.63	P	0.56	1.38	0.84	0.97	1.10
Salama et al. (2019)								
G-CS-1.75d	2.87	1.07	P	-	1.36	1.08	1.08	1.08
G-CS-4.25d	3.38	0.65	P	-	1.58	0.97	1.12	0.97
G-SS-4.25d	3.70	0.71	P	-	1.73	1.06	1.23	1.06
Mostafa and El-Salakawy (2018)								
N-0.9-S8	2.63	0.72	F	0.98	1.25	0.91	0.91	0.91
N-0.9-C8	2.56	0.70	F	0.95	1.89	1.18	1.42	1.18
N-0.9-S6	2.66	0.70	F	0.98	1.49	0.91	1.04	0.91
N-0.9-C6	2.26	0.60	P	0.82	1.85	1.17	1.45	1.17

Table 7.8: Model comparisons for shear-reinforced edge connections (continued)

Connection	Experimental results			Test-to-predicted strength				
	$v_{exp,\ 0.5d}$ (MPa)		Failure type [a]	Flexural capacity	*Model V*	*Model VI*	*Model VII*	*Model P-III*
	Inner	Outer						
El-Gendy and El-Salakawy (2016)								
RD-75-M	2.29	0.61	F-P	0.88	1.91	1.32	1.66	1.32
RD-50-M	2.44	0.65	F	0.97	1.77	1.22	1.48	1.22
Mean [c]					1.52	0.97	1.11	1.06
SD [c]					0.25	0.17	0.22	0.08
COV (%) [c]					16.3	17.2	19.9	7.3
R^2 [c]					0.43	0.79	0.74	0.97

Note: $v_{exp,\ 0.5d}$ = shear stress resistance provided by concrete at a critical section located at a distance of 0.5*d* from column face or outermost shear reinforcement row.

[a] Reported in the literature (F = flexural failure; P = punching failure; and F-P = mixed flexural/punching failure)
[b] Specimens subjected to reversed cyclic lateral load
[c] For connections failing in punching only

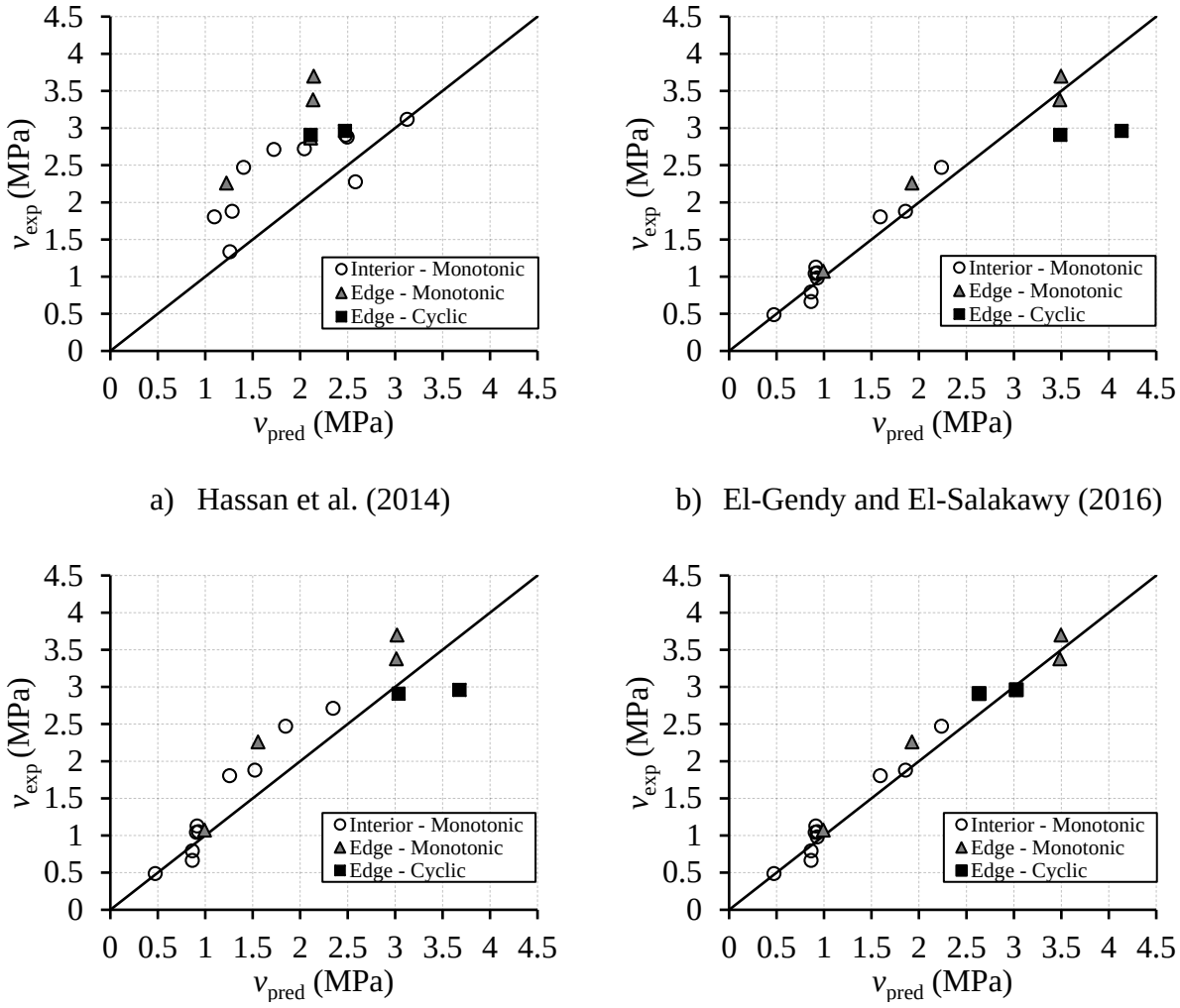

a) Hassan et al. (2014)

b) El-Gendy and El-Salakawy (2016)

c) Salama et al. (2019)

d) Proposed model (*Model P-III*)

Figure 7.5: Predictions for shear-reinforced connections

Thus, *Model VI* provides the most accurate predictions (i.e., closest mean v_{exp}/v_{pred} to unity and highest R^2) for both interior and edge connections; however, it overestimates the capacity of connections subjected to cyclic loads. The authors (El-Gendy and El-Salakawy 2020a) demonstrated that GFRP shear reinforcement in slab-column edge connections subjected to reversed-cyclic lateral load can only achieve a tensile strain of 3,000 με, as opposed to the 5,000 με strain limit suggested by CSA S806-12 (CSA 2017). As such, the GFRP shear reinforcement strain limit for connections subjected to cyclic load is limited to 3,000 με in the proposed *Model*

P-III. This resulted in a reasonable mean v_{exp}/v_{pred} of 1.04 ± 0.09 for the two connections subjected to cyclic loads. In addition, it significantly enhanced the R^2 value to 0.97 in case of edge connections.

7.6. Gravity Shear Limits for Connections Subjected to Cyclic Load

It has been demonstrated that the maximum lateral drift at which steel-RC connections may fail when subjected to cyclic loads depends on the gravity shear ratio (Pan and Moehle 1989). According to CSA A23.3-19 (CSA 2019b), the gravity shear ratio applied to connections without shear reinforcement should not exceed the value calculated by Equation 7.29; otherwise, shear reinforcement must be used. Similarly, according to ACI 318-19 (ACI 2019a), the maximum drift ratio a slab-column connection without shear reinforcement can withstand is a function of the gravity shear ratio as calculated by Equation 7.30.

$$\frac{V_g}{V_c} \le \left(\frac{0.005}{\delta}\right)^{0.85} \quad \text{, where } \delta \ge 0.005 \qquad \text{Equation 7.29}$$

$$\delta \le 0.035 - 0.05\left(\frac{V_g}{\phi V_c}\right) \quad \text{, where } \delta \ge 0.005 \qquad \text{Equation 7.30}$$

A graphical representation of the requirements of both codes in addition to plots of the lateral drift ratio before failure for the edge connections subjected to cyclic loads as a function of the applied gravity shear ratio are shown in Figure 7.6. In both cases, the theoretical punching shear strength provided by concrete, V_c, was calculated using the CSA S806-12 model (CSA 2017). It is clear that all GFRP-RC edge connections without shear reinforcement can exceed the minimum drift ratio suggested by both models. When adequate shear reinforcement is used, higher drift ratios can be attained before failure.

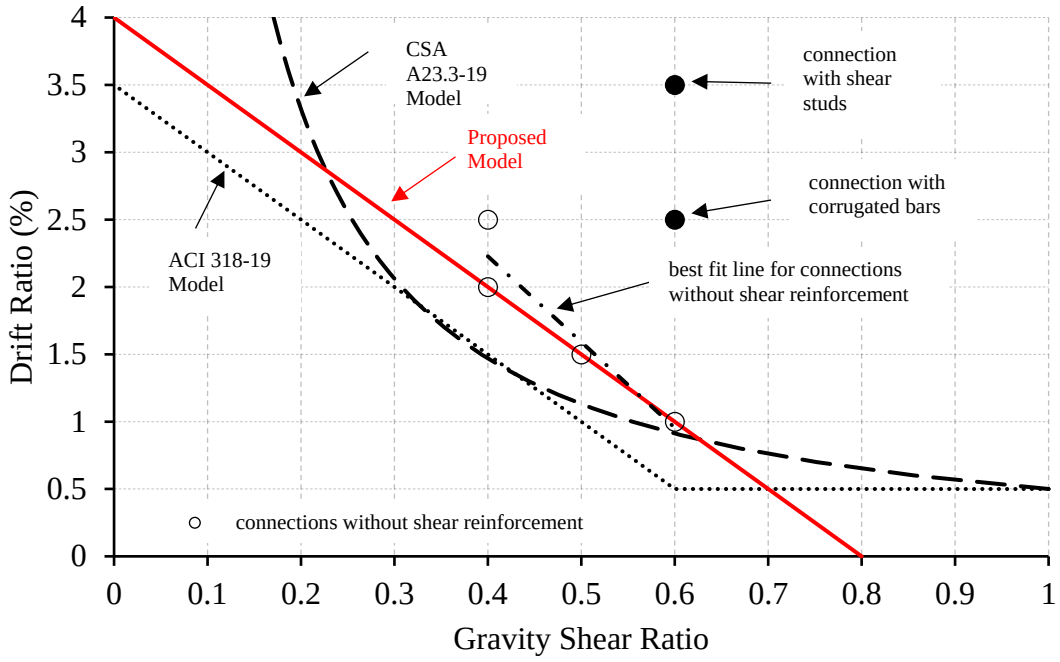

Figure 7.6: Relationship between gravity shear ratio and drift ratio

Both models provide a conservative lower bound to the actual drift ratios; Figure 7.6 suggests that FRP-RC edge connections without shear reinforcement can sustain higher drift ratios before failure than that sustained by steel-RC connections. The higher drift capacities are attributed to the low modulus of elasticity of the FRP reinforcement, which makes FRP-RC connections more flexible under lateral deformations. Consequently, a relaxed model is proposed to estimate the maximum interstory drift ratio permitted for FRP-RC edge connections in the absence of shear reinforcement as listed in Equation 7.31. Based on this model, for an FRP-RC edge connection without shear reinforcement to withstand at least 1.50% drift ratio, the applied gravity shear ratio should not exceed 0.5. This represents a 25% increase in the current gravity shear ratio limit set at 0.4. Further research is needed to verify the applicability of this model on different types of connections with different types and configurations of shear reinforcement.

$$\delta \leq 0.04 - 0.05\left(\frac{V_g}{V_c}\right) \qquad \text{Equation 7.31}$$

7.7. Conclusions

Based on the experimental and analytical investigations, the following conclusions can be drawn:

1. The punching shear design model implemented in CSA S806-12 (CSA 2017) provided consistent, yet slightly conservative, predictions for both interior and edge FRP-RC connections with a mean v_{exp}/v_{pred} of 1.20 ± 0.22 and 1.21 ± 0.09, respectively. Similar trend is exhibited by the JSCE model (JSCE 1997). The ACI 440.1R-15 model (ACI 2015), on the other hand, highly underestimated the capacity of both interior and edge connections with a mean v_{exp}/v_{pred} of 2.18 ± 0.43 and 2.09 ± 0.18, respectively.
2. The early model proposed by Matthys and Taerwe (2000), which considers the critical section at 1.5*d* from the column face, provided better predictions than that of the CSA S806-12 model (CSA 2017) producing a mean v_{exp}/v_{pred} of 1.19 ± 0.18 and 1.05 ± 0.08 for interior and edge connections, respectively, with comparable R^2 values. The other three empirical models (Ospina et al. 2003; El-Gamal et al. 2005; Hassan et al. 2017), despite reasonably predicting the capacity of interior connections, failed to safely estimate that of edge ones.
3. Two new models (*Models P-I* and *P-II*) were proposed by modifying the ones by El-Gamal et al. (2005) and Hassan et al. (2017) to account for the connection location and the confinement provided by the slab surrounding the critical section. *Model P-I* slightly overestimated the capacity of edge connections with a mean v_{exp}/v_{pred} and R^2 of 0.95 ± 0.11 and 0.63, respectively. *Model P-II*, however, produced reliable predictions for edge connections with a precise mean v_{exp}/v_{pred} of 1.02 ± 0.09 and R^2 of 0.73.

4. For shear-reinforced FRP-RC slabs, the model proposed by El-Gendy and El-Salakawy (2016) provided the most accurate estimates for both interior and edge connections with a mean v_{exp}/v_{pred} of 1.05 ± 0.13 and 0.97 ± 0.17, respectively, and R^2 of 0.96 and 0.79, respectively. This model, however, overestimated the capacity of connections subjected to cyclic loads with a mean v_{exp}/v_{pred} of 0.78 ± 0.08. Limiting the allowable strain in GFRP shear reinforcement to 3,000 με enhanced this mean v_{exp}/v_{pred} to 1.04 ± 0.09 and improved the overall R^2 for GFRP-RC edge connections to 0.97.

The proposed models, *Model P-II* and *P-III*, are universal models capable of accurately estimating the capacity of all connection types without and with shear reinforcement, respectively, regardless of the type of load. Further research is needed to verify the applicability of both models on GFRP-RC corner connections and on FRP-RC connections with restrained slab edges.

CHAPTER 8. FINITE ELEMENT ANALYSIS OF FRP-REINFORCED CONCRETE SLAB-COLUMN EDGE CONNECTIONS SUBJECTED TO REVERSED-CYCLIC LATERAL LOADS

Authors and affiliation:

- Mohammed G. El-Gendy, PhD Candidate, Department of Civil Engineering, University of Manitoba
- Ehab F. El-Salakawy, Professor, Department of Civil Engineering, University of Manitoba

Journal and Status:

American Society of Civil Engineers (ASCE) Journal of Composites for Construction, revisions requested, on July 08, 2020.

Reference:

El-Gendy, M., and El-Salakawy, E. forthcoming. “Finite element analysis of FRP-reinforced concrete slab-column edge connections subjected to reversed-cyclic lateral loads." *J. Compos. Constr.*, ASCE, under review.

Note:

The manuscript had been slightly altered from the original paper by renumbering the tables and figures to include the chapter number. In addition, the reference list and list of notations have been moved to the appropriate sections in the thesis as indicated in the table of contents.

Abstract

A series of finite element analyses for slab-column edge connections reinforced with fiber-reinforced polymer (FRP) reinforcement and subjected to reversed-cyclic lateral load is conducted and discussed. A three-dimensional non-linear finite element model (FEM) is constructed using a commercially available software. The FEM is validated against the results of experimental studies conducted previously by the authors. Subsequently, the validated FEM is used to carry out an extensive parametric study investigating the influence of key parameters including the gravity shear ratio (0.2 to 0.8), flexural reinforcement type (glass and carbon FRP), column aspect ratio (0.25 to 4.00), flexural reinforcement ratio (0.7 to 1.4%), and slab thickness (150 to 400 mm). The results showed that the drift capacity of edge connections reinforced with either glass FRP (GFRP) or carbon FRP (CFRP) reinforcement is reduced when the applied gravity shear ratio is increased. However, GFRP-RC connections were able to undergo larger drift ratios than their CFRP-RC counterparts. In addition, increasing the slab thickness reduced the punching shear strength of GFRP-RC connections, even for slabs with an effective depth less than 300 mm.

Keywords: CFRP; column rectangularity; cyclic load; drift capacity; finite element analysis; GFRP; gravity shear ratio; punching shear capacity; size effect; slab-column connection.

8.1. Introduction

Reinforced concrete (RC) flat plate systems are susceptible to brittle punching shear failure at the locations of slab-column connections, where significant shear forces and unbalanced moments are transferred. When fiber-reinforced polymer (FRP) composite bars are used to take advantage of their non-corrodible nature, the punching shear capacity of two-way slabs and slab-column connections is further reduced due to the lower stiffness of FRP reinforcement compared to that of their steel counterpart (Matthys and Taerwe 2000; Dulude et al. 2013; Gouda and El-Salakawy 2016a; El-Gendy and El-Salakawy 2018a). Nonetheless, several studies conducted during the last two decades demonstrated that the punching shear capacity of FRP-RC two-way slabs and slab-column connections subjected to monotonically increased gravity loads could be enhanced by several measures. These measures include using well-anchored shear reinforcement, increasing the flexural reinforcement ratio, or increasing the concrete strength (Ospina et al. 2003; Dulude et al. 2013; Gouda and El-Salakawy 2016a; El-Gendy and El-Salakawy 2016; Salama et al. 2019).

Based on this promising behavior of FRP-RC slab-column connections subjected to gravity loads, the authors conducted a pioneer experimental study to investigate the effect of different parameters on the seismic response of glass FRP (GFRP)-RC slab-column edge connections (El-Gendy and El-Salakawy 2019, 2020a, 2020b). These studies demonstrated the feasibility of using GFRP reinforcement in edge connections subjected to simulated seismic loads. The combination of high tensile strength and low stiffness of GFRP reinforcement allowed the edge connections to undergo and exceed the 1.5% minimum drift ratio suggested by Sozen (1980) before punching failure. Nonetheless, in a recent effort to investigate the response of GFRP-RC slab-column interior connections subjected to lateral cyclic loads, Eladawy et al. (2019; 2020) demonstrated that such

connections can only sustain the 1.5% minimum drift ratio when significantly low gravity loads are applied.

Despite the recent surge in the number of experimental studies investigating the behavior of FRP-RC slab-column connections, the influence of several parameters on the behavior of such connections, particularly those subjected to simulated seismic load, still needs to be studied. In this sense, non-linear finite element analysis (FEA) can provide reliable rapid insight regarding the behavior of FRP-RC connections. Few recent studies have utilized FEA to investigate the behavior of FRP-RC slab-column connections subjected to monotonically increased gravity loads (Gouda and El-Salakawy 2015; Salama et al. 2020). In the present study, a three-dimensional (3D) non-linear finite element model (FEM) is constructed using ATENA-3D, version 5.3.4 (Červenka et al. 2018). Recently, this software package has been extensively used in numerical studies simulating the behavior of different RC elements internally reinforced with FRP reinforcement (Mahmoud and El-Salakawy 2016; Ghomi and El-Salakawy 2018; Attia et al. 2020) and externally strengthened with FRP laminates (El-Maaddawy and Sherif 2014; Kalfat and Al-Mahaidi 2014; Saleh et al. 2018).

The FEM is validated against the experimental results of GFRP-RC edge connections previously tested by the authors (El-Gendy and El-Salakawy 2019, 2020b). Subsequently, the validated FEM is used to carry out an extensive parametric study investigating the influence of key parameters known to affect the seismic response of slab-column connections. These parameters are the gravity shear ratio, flexural reinforcement type, column aspect ratio, flexural reinforcement ratio, and slab thickness.

8.2. Punching Shear Capacity of FRP-RC Slab-Column Edge Connections

In a previous study by the authors (El-Gendy and El-Salakawy 2020c), it was demonstrated that the punching shear model implemented in CSA S806-12 (CSA 2017) is the most reliable design model incorporated in current design standards and guidelines. It provided consistent mean test-to-predicted shear capacity of 1.20 ± 0.22 and 1.21 ± 0.09 for interior and edge connections, respectively, for a wide spectrum of experimentally tested connections from the literature. According to this model, the punching shear strength provided by concrete shall not exceed the smallest of Equation 8.1 to Equation 8.3:

$$v_c = \left(1 + \frac{2}{\beta_c}\right) 0.028 \lambda \phi_c \left(E_F \rho_F f_c^{'}\right)^{1/3} \qquad \text{Equation 8.1}$$

$$v_c = \left[\left(\frac{\alpha_s d}{b_{o,0.5d}}\right) + 0.19\right] 0.147 \lambda \phi_c \left(E_F \rho_F f_c^{'}\right)^{1/3} \qquad \text{Equation 8.2}$$

$$v_c = 0.056 \lambda \phi_c \left(E_F \rho_F f_c^{'}\right)^{1/3} \qquad \text{Equation 8.3}$$

where v_c is the shear stress resistance provided by concrete (MPa), β_c is the ratio of the long to short sides of the column, λ is a factor to account for concrete density, ϕ_c is the concrete resistance factor, E_F is the modulus of elasticity of FRP reinforcement (MPa), ρ_F is the longitudinal FRP reinforcement ratio, $f_c^{'}$ is the concrete compressive strength (MPa) and shall not be taken greater than 60 MPa, α_s is a coefficient equal to 4, 3 or 2 for interior, edge and corner connections, respectively, $b_{o,0.5d}$ is the perimeter of the critical section located at a distance of 0.5d from the column face, and d is the average slab depth. This model considers the effect of column rectangularity and shear perimeter-to-slab depth ratio in Equation 8.1 and Equation 8.2,

respectively. However, Equation 8.1 and Equation 8.2 do not govern the design unless the rectangularity factor (β_c) exceeds 2.0 or the perimeter-to-depth ratio exceeds 15.7. The slab size effect is considered if the effective slab depth exceeds 300 mm by multiplying v_c by $\left(300/d\right)^{0.25}$.

A new universal model was proposed to accurately estimate the punching shear capacity of interior and edge connections subjected to gravity and cyclic lateral loads (El-Gendy and El-Salakawy 2020c) as given in Equation 8.4. This model produced close to unity predictions for a wide range of FRP-RC interior and edge connections from the literature with a mean test-to-predicted punching shear capacity of 1.01 ± 0.14 and 1.02 ± 0.09, respectively.

$$v_c = 0.065\lambda\phi_c\left(\alpha_s\frac{d}{b_{o,0.5d}}+0.65\right)\left(E_F\rho_F f_c^{'}\right)^{1/3}\left(125/d\right)^{1/6} \qquad \text{Equation 8.4}$$

8.3. Drift Capacity of FRP-RC Connections

The drift capacity of RC slab-column connections depends on the applied gravity shear ratio, V_g/V_c (Pan and Moehle 1989), where V_g is the gravity shear force transferred between the slab and the column and V_c is the punching shear capacity provided by concrete calculated as shown in Equation 8.5. According to CSA A23.3-19 (CSA 2019b), the gravity shear ratio applied to connections without shear reinforcement should not exceed the value calculated by Equation 8.6; otherwise, shear reinforcement must be used. Similarly, according to ACI 318-19 (ACI 2019a), the drift ratio, δ, a connection without shear reinforcement can withstand is a function of the gravity shear ratio (Equation 8.7**)**. In a recent study, the authors proposed relaxing these requirements for GFRP-RC edge connections as calculated by Equation 8.8 (El-Gendy and El-Salakawy 2020c).

$$V_c = v_c \times (b_o \times d) \quad \text{Equation 8.5}$$

$$\frac{V_g}{V_c} \le \left(\frac{0.005}{\delta}\right)^{0.85} \text{, where } \delta \ge 0.005 \quad \text{Equation 8.6}$$

$$\delta \le 0.035 - 0.05\left(\frac{V_g}{\phi V_c}\right) \text{, where } \delta \ge 0.005 \quad \text{Equation 8.7}$$

$$\delta \le 0.04 - 0.05\left(\frac{V_g}{V_c}\right) \quad \text{Equation 8.8}$$

8.4. Summary of Cyclic Tests on FRP-RC Edge Connections

In previous studies conducted by the authors, four isolated, full-scale, GFRP-RC slab-column edge connections without shear reinforcement were constructed and tested to failure under a combination of gravity and uniaxial reversed-cyclic lateral loads (El-Gendy and El-Salakawy 2019, 2020b). This section summarizes the main test parameters, procedure and results.

8.4.1. Test specimens

As shown in Figure 8.1, the isolated edge connections had slab dimensions of 3,300×3,100×200 mm with 300-mm square edge columns extending 1,900 and 970 mm above and below the slab surfaces, respectively. All slabs had top and bottom flexural reinforcement assemblies (Figure 8.1c). The studied parameters were the flexural reinforcement ratio (0.7, and 1.4%) and the gravity shear ratio (0.4, 0.5, and 0.6). For clarity, the designation of the test specimens in this study consists of three parts. The first part indicates the connection location (E for edge), the second part indicates the top reinforcement ratio in the column strip, ρ (0.7 for ρ = 0.7%, 1.4 for ρ = 1.4%), and the third part indicates the gravity shear ratio, V_g/V_c (40 for V_g/V_c = 0.4, 50 for V_g/V_c = 0.5, 60 for V_g/V_c =

0.6). The connections were constructed using ready-mix concrete with a target 28-day compressive strength of 40 MPa. Size No. 15 sand-coated GFRP bars were used as flexural reinforcement; the properties of the reinforcement are listed in Table 8.1. Further information regarding the design of the experimental specimens can be found elsewhere (El-Gendy and El-Salakawy 2019, 2020b).

8.4.2. Test setup and procedure

The test setup, shown in Figure 8.2, was designed so that a test specimen is pinned at the top of the column to a horizontal hydraulic actuator and at the bottom of the column to a steel hinge support. The slab was supported along the edge parallel to the free edge by a set of link assemblies to simulate a roller support. Therefore, the slab was free to translate and rotate at this supported edge; thus, no membrane action was introduced. The gravity load was applied to the slab at four discrete locations by an assembly of hydraulic jacks. The test started by locking the actuator in place to restrain the lateral displacement of the column, while applying the gravity load on the slab. This resulted in both vertical and lateral reactions at the column hinged support (bottom of the column) and a lateral reaction at the actuator (top of the column), with no lateral displacement of the column. Once the specified gravity load was reached, it was kept constant and the actuator started to apply the lateral load.

The lateral load was simulated by a displacement-controlled quasi-static reversed-cyclic load following the sequence shown in Figure 8.3 (ACI 2019b). Each loading step consisted of three identical loading cycles to ensure stable crack propagation. In this loading scheme, the drift ratio was calculated as the ratio between the applied drifts to the distance between the horizontal axis of the actuator applying the drifts and the axis of rotation of the hinged support at the bottom of the column, which is 2,920 mm as shown in Figure 8.1. The drift was considered positive when

the actuator was pushing the column towards the slab and negative when it was pulling it away. Further details on the experimental test setup and procedure can be found elsewhere (El-Gendy and El-Salakawy 2019, 2020b).

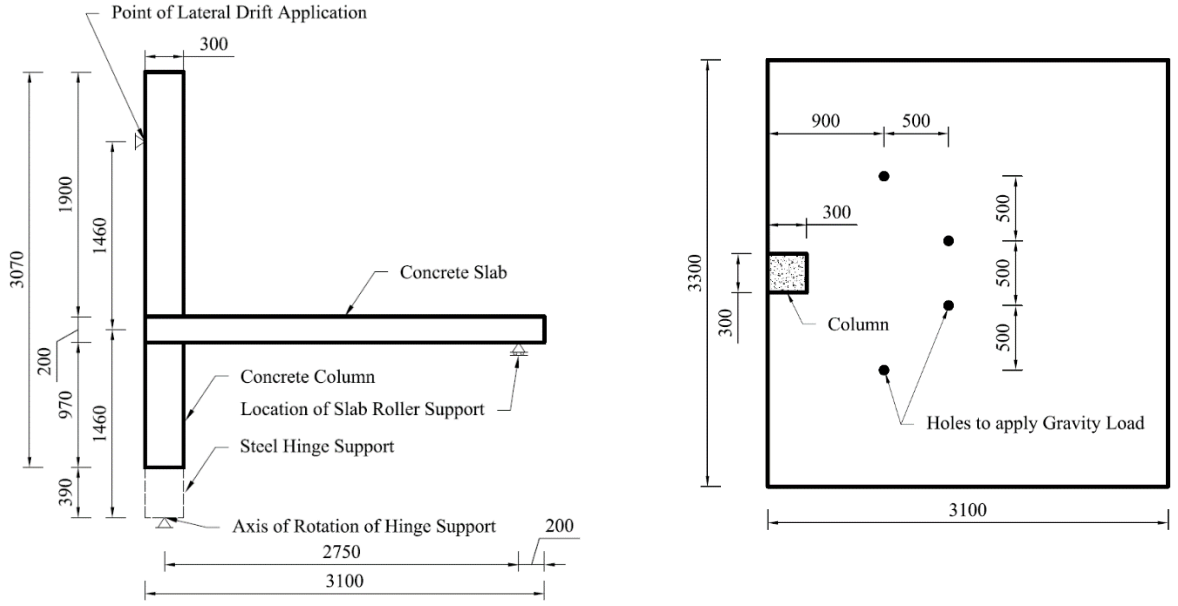

a) Elevation view b) Plan view

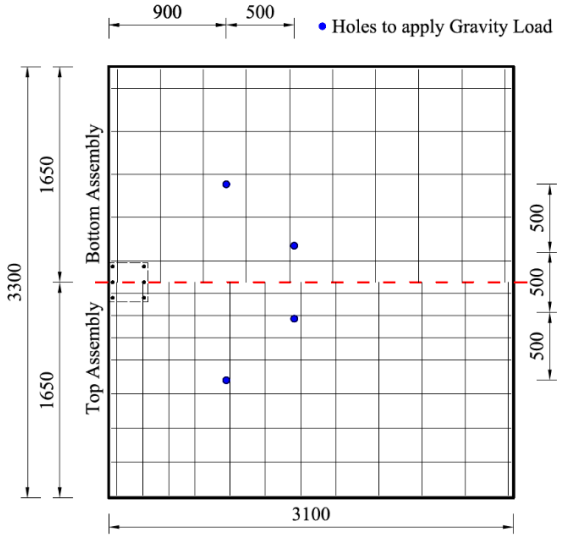

c) Typical reinforcement layout

Figure 8.1: Details of experimental specimens (dimensions in mm)

Table 8.1: Mechanical properties of the reinforcement used in cyclic tests and FEA

Type	Shape	Size (No.)	Tensile strength (MPa)	Modulus of elasticity (GPa)	Ultimate strain (%)
GFRP [a]	Straight	15	1,712	66	2.60
GFRP [a]	Hooked	15	1,405	52	2.70
CFRP [b]	Straight	15	1,899	144	1.32
CFRP [b]	Hooked	15	1,596	120	1.33

[a] Reported by El-Gendy and El-Salakawy (2019, 2020b)
[b] Reported by Afifi et al. (2015)

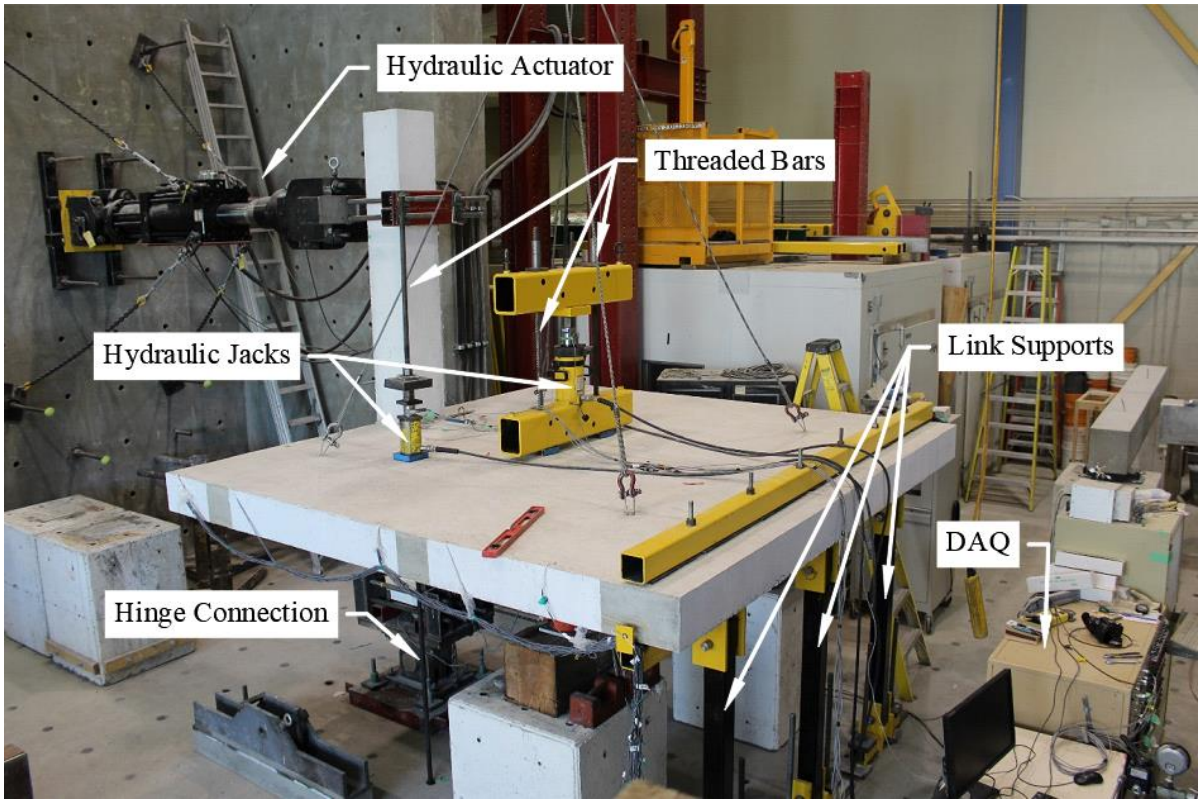

Figure 8.2: Experimental test setup

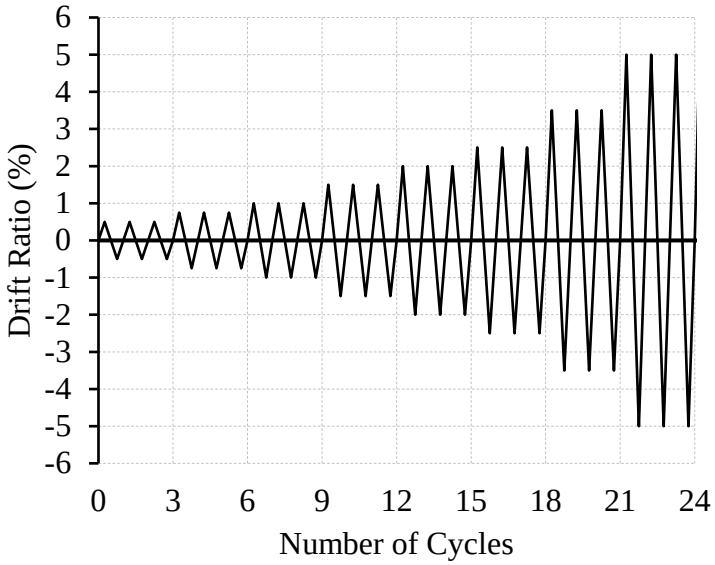

Figure 8.3: Lateral drift sequence

8.4.3. Main test results

All test specimens failed by punching of the slab in the column vicinity with different deformability levels. Deformability is used to quantify the ability of the connections to undergo inelastic deformations before failure. It is calculated as the ratio between the ultimate drift ratio at failure to an equivalent drift ratio to the yield drift ratio in steel-RC connections. Further information regarding how deformability and the equivalent yield drift ratio are calculated for FRP-RC connections can be found elsewhere (El-Gendy and El-Salakawy 2018b). Increasing the gravity shear ratio from 0.4 to 0.5 and further to 0.6 decreased the deformability of the connections by 33 and 38% and the lateral load capacity by 5 and 14%, respectively. On the other hand, doubling the GFRP reinforcement ratio from 0.7 to 1.4% enhanced the deformability and lateral load capacity by 45 and 17%, respectively. Envelopes of the hysteresis diagrams for the test specimens are shown in Figure 8.4. Before punching failure, all connections were able to achieve or exceed the 1.5% minimum drift ratio except connection E-1.4-60, which was subjected to a high

gravity shear ratio of 0.6. At this high gravity shear ratio, the use of shear reinforcement is essential to prevent punching failure and improve the drift capacity of slab-column edge connections.

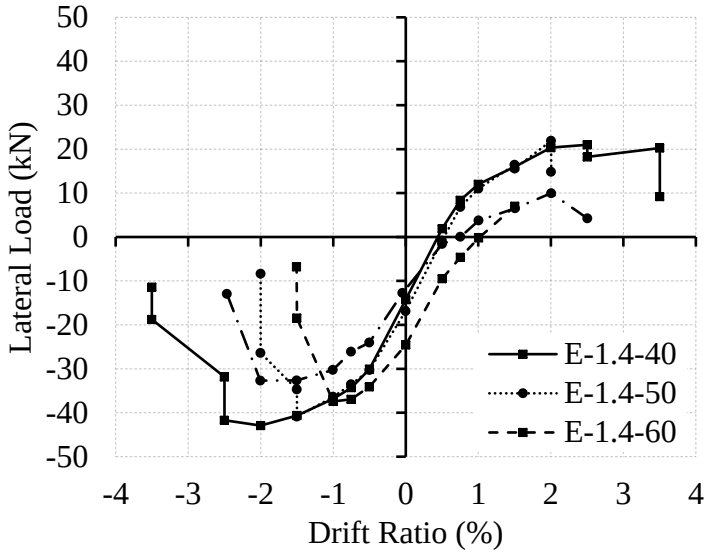

Figure 8.4: Envelopes of hysteresis diagrams

8.5. Characteristics of Finite Element Model

The software package ATENA-3D was used to construct a FEM of the test specimens, which was validated against the above experimental results (El-Gendy and El-Salakawy 2019, 2020b). The following sections describe the basic characteristics of the constructed FEMs. Further details can be found in the software documentation package (Červenka et al. 2018).

8.5.1. Geometry and boundary conditions

The details of the constructed FEM are shown in Error! Reference source not found.. The concrete and steel elements were modelled by four-node tetrahedral elements with a maximum mesh size of 100 mm. Initially, brick elements were selected to model the connections and a mesh sensitivity analysis was conducted on a half FEM (taking advantage of the connection symmetry). Reducing the brick element size from 100 to 40 mm, in 10 mm increments, changed the drift capacity of the

connections. However, a further reduction to 30 mm did not result in any appreciable difference. Nonetheless, despite employing symmetry, the running time of the model with 40-mm brick elements was impractical. Therefore, the applicability of using tetrahedral elements with a larger maximum mesh size was examined. In this context, the advantage of tetrahedral elements is the non-uniform distribution of the elements, which results in having several elements with different sizes across the slab thickness. Using tetrahedral elements with a maximum size of 100 mm in a full FEM resulted in comparable results to the case when brick elements with 40 mm maximum size were used in a half FEM. In addition, due to the orientation and shape of the tetrahedral elements, a sophisticated mesh with different element sizes was generated inside the slab, where up to six elements were generated through the slab thickness in the column vicinity as shown in Error! Reference source not found.b.

The hinge support at the column base was simulated by a 100-mm thick steel plate. The translation of the plate was restrained in all directions; thus, allowing only rotation in the direction of the lateral displacement. Three steel blocks were used to simulate the link assemblies of the slab support. These blocks were free to translate and rotate in the direction of the lateral displacement to simulate a roller support. A rigid steel collar was used at the top of the column to simulate the actuator grip on the column shown in Figure 8.2. This collar prevents stress concentrations at the location of displacement application. Four 25×100×100 mm steel plates were used at the locations of gravity load application. Area loads were used to apply the gravity load at these locations. The dimensions of the connections used in the parametric study (Error! Reference source not found.) match those of the experimental connection shown in Figure 8.1. The dimensions were only changed to investigate the effect of the column aspect ratio and slab thickness as will be discussed later.

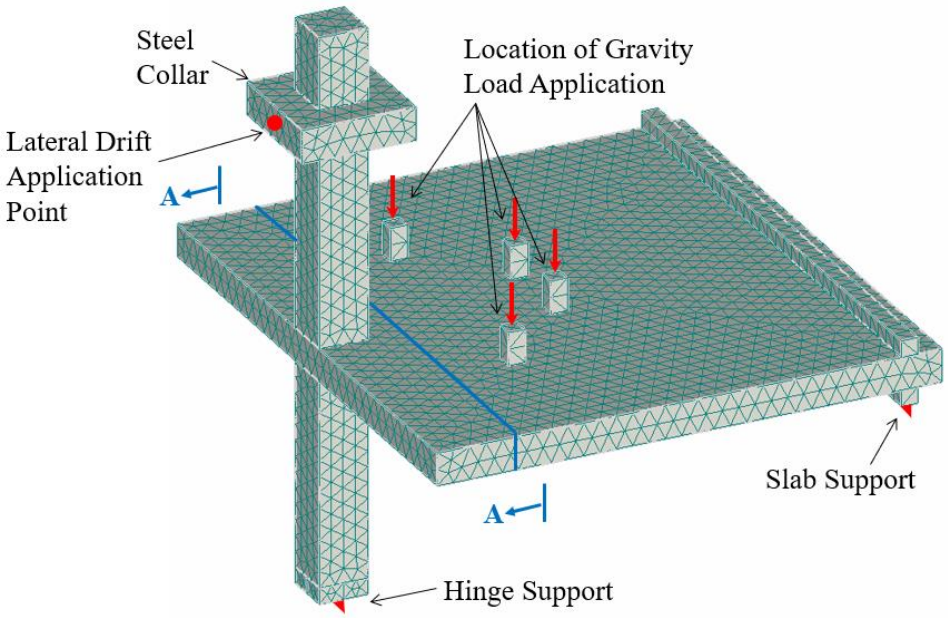

a) Macroelements and boundary conditions

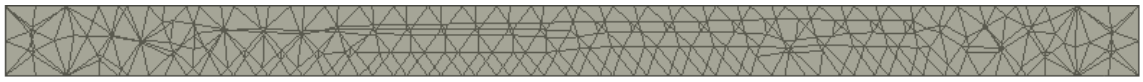

b) Mesh discretization at section A-A

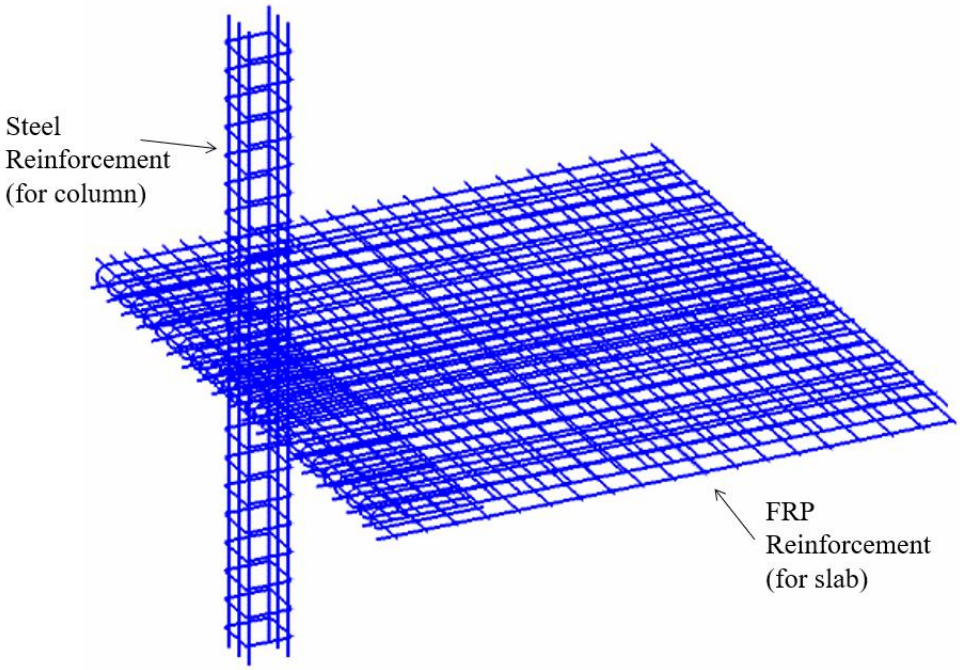

c) Discrete reinforcement

Figure 8.5: Typical details of FEM

8.5.2. Concrete material

The fracture-plastic constitutive model implemented in ATENA-3D was adopted for the modeling of concrete. This model combines constitutive models for the tensile (fracture) and compressive (plastic) behavior of concrete. The fracture model employs Rankine failure criterion with exponential softening. This model implements the smeared crack approach for modelling concrete cracks with options for both fixed and rotated crack models. The fixed crack option was adopted in this study, where the crack direction is set by the direction of the principle stress when the crack is initiated. Similar approach was followed by other researchers (El-Maaddawy and Sherif 2014; Kalfat and Al-Mahaidi 2014). In addition, the effect of tension stiffening, i.e., the contribution of cracked concrete to the tensile stiffness of reinforcing bars when cracks do not fully develop along the section, is accounted for by a factor that represents the relative limiting value of tensile strength in the tension-softening diagram. This factor was set to 0.3 in this study based on a sensitivity analysis as shown in Figure 8.6.

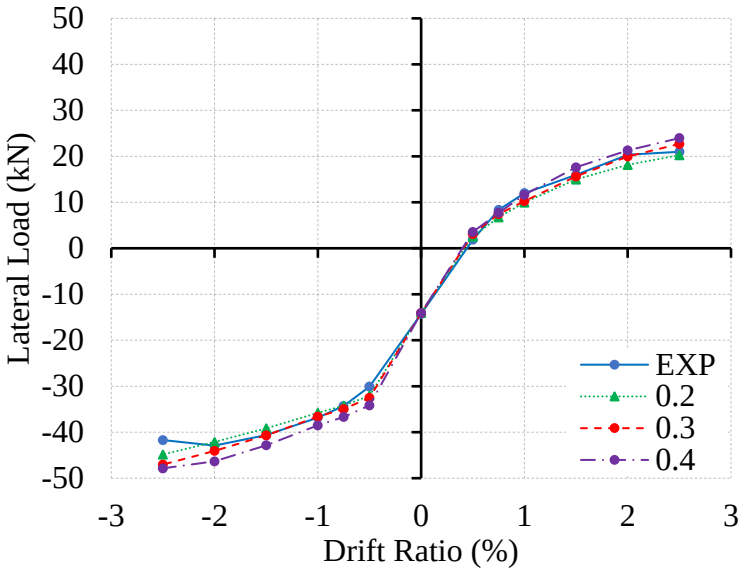

Figure 8.6: Effect of tension stiffening

To simulate crack closure when the load is reversed, an unloading factor was set to zero, which indicates unloading to the origin (Červenka et al. 2018). The shear strength of cracked concrete is calculated in ATENA-3D according to the modified compression field theory (Vecchio and Collins 1986). In this model, the shear strength, σ_{sh}, is a function of the compressive strength of concrete, f_c', crack width, w_{cr}, and aggregate size, a_g, as described in Equation 8.9. In addition, the shear stiffness tangential to cracks, K_t, is taken as a function of the stiffness normal to cracks, K_n, as shown in Equation 8.10. The latter stiffness is a function of the tensile stress at the crack location, $f_{t\text{-}cr}$, and the crack width, w_{cr}, as explained in Equation 8.11 (Červenka et al. 2018). This makes the shear stiffness dependent on the crack width as well. Therefore, the change in the crack width due to the reversed nature of the load significantly affects both the shear strength and stiffness. The default value of 20 for the crack shear stiffness factor, S_F, in Equation 8.10 and an aggregate size of 20 mm were employed in this study.

$$\sigma_{sh} \le \frac{0.18\sqrt{f_c'}}{0.31+\frac{24w_{cr}}{a_g+16}} \qquad \text{Equation 8.9}$$

$$K_t = S_F K_n \qquad \text{Equation 8.10}$$

$$K_n = \frac{f_{t-cr}}{w_{cr}} \qquad \text{Equation 8.11}$$

On the other hand, the compressive behavior of concrete is simulated according to Van Mier (1986), where the elliptical hardening and linear softening laws shown in Figure 8.7 are used. While the elliptical hardening law is strain-based, the linear softening law considers the plastic displacement w_c. The critical compressive displacement at the end point of the softening law, w_d,

was assumed to be equal to 0.5 mm according to Van Mier (1986). Similar approach was followed by other researchers (Awani et al. 2016; Attia et al. 2020). When RC slab-column connections are subjected to reversed cyclic loads, the reversed nature of the load produces significant tensile stresses in regions that are otherwise only compressed. Vecchio and Collins (1986) showed that cracked concrete has a lower compressive strength and a softer response in the direction parallel to the cracks than uncracked concrete.

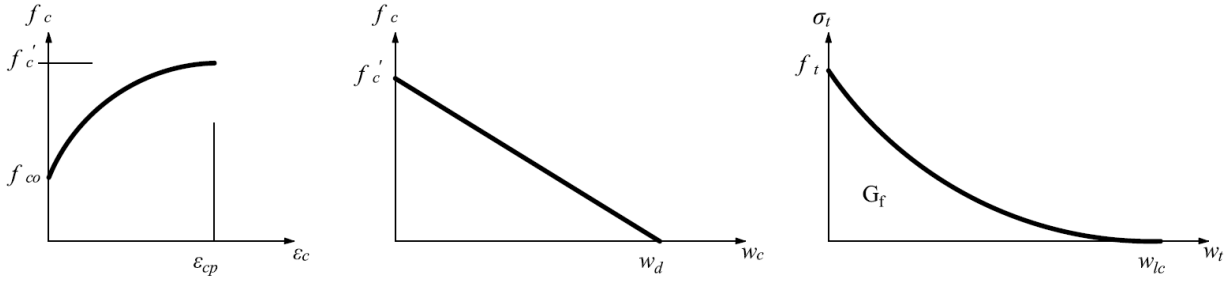

a) Compressive hardening b) Compressive softening c) Tension softening

Figure 8.7: Constitutive laws of concrete (Červenka et al. 2018)

In ATENA-3D, reduction of concrete compressive strength after cracking is accounted for by a factor representing the relative limiting value of compressive strength in the direction of cracks. In this study, this factor was set to 0.7, which means that the compressive strength in the direction of cracks may be reduced to a minimum of 70% of its maximum value. The default concrete parameters, i.e., tensile strength, modulus of elasticity and fracture energy, are a function of the concrete compressive strength (Červenka et al. 2018) as shown in Equation 8.12 to Equation 8.14:

$$f_t^{'} = 0.27\, f_c^{'\frac{2}{3}} \qquad \text{Equation 8.12}$$

$$E_c = \left(6500 - 19.8 f_c^{'}\right)\sqrt{f_c^{'}} \qquad \text{Equation 8.13}$$

$$G_F = 0.000025 f_t^{'} \qquad \text{Equation 8.14}$$

where $f_t^{'}$ is the concrete tensile strength (MPa), $f_c^{'}$ is the concrete compressive strength (MPa), E_c is the modulus of elasticity of concrete (MPa), and G_F is the fracture energy (MN/m). Values of the main parameters used in the concrete constitutive model are listed in Table 8.2.

Table 8.2: Input parameters for the concrete model used in the parametric study

Property	**Value**
Compressive strength, $f_c^{'}$	48.4 MPa
Modulus of elasticity, E_c	38,620 MPa
Poisson's ratio, μ	0.2
Fracture energy, G_f	88.8 N/m
Critical compressive displacement, w_d	0.5 mm
Shear stiffness factor	20
Crack orientation	fixed
Tension stiffening factor, c_{ts}	0.3
Unloading factor	0
Reduction of compressive strength factor, $r_{c,lim}$	0.7
Solution method	Newton-Raphson

8.5.3. Steel material

All steel plates used for supports and load application were modelled using an elastic isotropic material. The parameters of this material were defined with a modulus of elasticity of 200 GPa and a Poisson's ratio of 0.3 without defining a yielding point to avoid any premature failure in the steel plates.

8.5.4. Reinforcement material

All reinforcement was modelled by truss discrete elements. ATENA-3D provides three constitutive laws to model the behavior of reinforcement materials, i.e., bi-linear, user-defined multi-line law, and cyclic reinforcement law. For FRP reinforcement, the linear law with the material properties listed in Table 8.1 was used. On the other hand, the built-in cyclic reinforcement law originally proposed by Menegotto and Pinto (1973) was used to model the steel reinforcement used in the columns. Yield stress and strain of 400 MPa and 0.002, respectively, were employed. It is to be noted that column steel reinforcement did not reach yielding in any of the FEMs. Further details about the built-in cyclic reinforcement law can be found elsewhere (Červenka et al. 2018).

8.5.5. Bond model

Besides assuming a perfect bond between the reinforcement and the surrounding concrete, ATENA-3D provides two built-in bond-slip models and a user-defined one. The former approach is often unrealistic since significant drifts and cracks result in slippage of reinforcement. Therefore, one of the built-in models described in the CEB-FIB model code 1990 (CEB 1990) was used to model steel reinforcement bond to surrounding concrete. On the other hand, a user-defined model was used to model FRP reinforcement bond to the surrounding concrete as shown in Figure 8.8. This model was based on experimental testing conducted previously (Alves et al. 2011). It has been successfully used in several numerical studies to model the bond behavior of sand-coated FRP reinforcement to the surrounding concrete (El-Mogy et al. 2013; Gouda and El-Salakawy 2015; Mahmoud and El-Salakawy 2016).

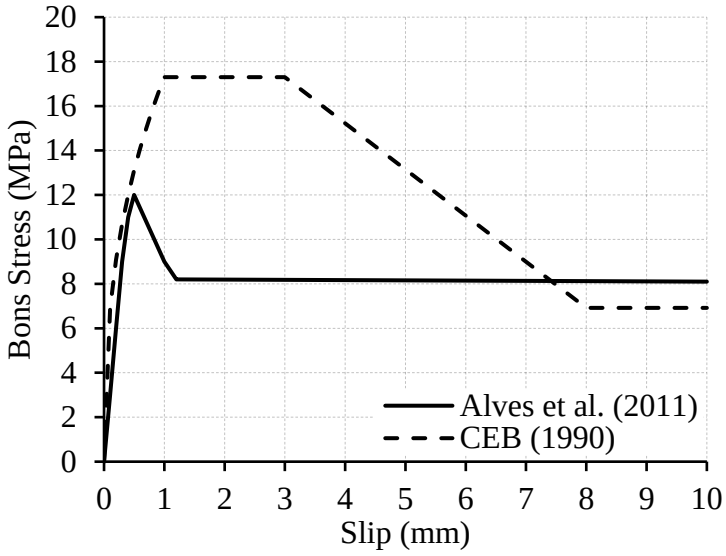

Figure 8.8: Bond-slip models

8.5.6. Load application and solution method

The gravity load was first applied in ten load-controlled increments. Each increment represents 10% of the specified gravity load. This was done before applying the lateral drifts to simulate the loading procedure followed during the experimental testing as mentioned earlier. The applied gravity load was then maintained, while the lateral drifts were applied to the upper column. The drift scheme shown in Figure 8.3 was followed in a displacement-controlled mode with increments of 7.3 mm (corresponding to 0.25% drift ratio). For example, to apply 1.0% drift ratio (a drift of 29.2 mm), the top of the column was programmed to move four steps in the positive direction (pushing the column towards the slab), eight in the negative direction (pulling the column back and away from the slab), and other four in the positive direction to reach zero-displacement. This represents a full cycle of 16 steps, which is repeated three times for each drift ratio.

The standard Newton-Raphson iterative solution method implemented in ATENA-3D was employed in the analysis. In this method, iterations are performed at each loading step, where the

stiffness matrix is recalculated until four convergence criteria are satisfied, i.e., relative deformations, relative forces, absolute forces and relative energy. The default convergence error for the first three criteria in ATENA-3D is set to 1%. This default value was used in this study. At failure, the FEM fails to reach convergence and the analysis is stopped when the convergence error at the end of a given step exceeds 10%. A similar approach was followed by Attia et al. (2020).

8.6. Model Validation

8.6.1. Hysteretic response

In general, the hysteretic response predicted by the FEM was in good agreement with the experiments for all four connections. For example, Figure 8.9a shows the lateral load-drift ratio relationship for E-1.4-40 (only the third cycle of each step was plotted for clarity). The envelopes of the hysteresis loops for experimental and FEM results were similar, if not identical as shown in Figure 8.9b for E-1.4-40. The FEM captures the gravity lateral load (which is the lateral load reaction after the application of gravity loads on the slab) and the peak lateral load (which is the maximum lateral load that a connection was able to reach) with a reasonable degree of accuracy as listed in Table 8.3. Most of the predictions were within 10% of the experimental values. The mean ratio between the FEM prediction and the experimental value for the gravity lateral load ($P_{g\text{-}FEM}/P_{g\text{-}EXP}$) was 1.00 ± 0.16 with a coefficient of variation (COV) and coefficient of determination (R^2) values of 16.44% and 0.79, respectively. It is to be noted that higher R^2 values (closer to unity) indicate that the FEM explains the considered variability factors of the predicted behavior. For the peak lateral load, the mean ($P_{p\text{-}FEM}/P_{p\text{-}EXP}$) was 0.97 ± 0.06 with COV and R^2 values of 6.66% and 0.75, respectively.

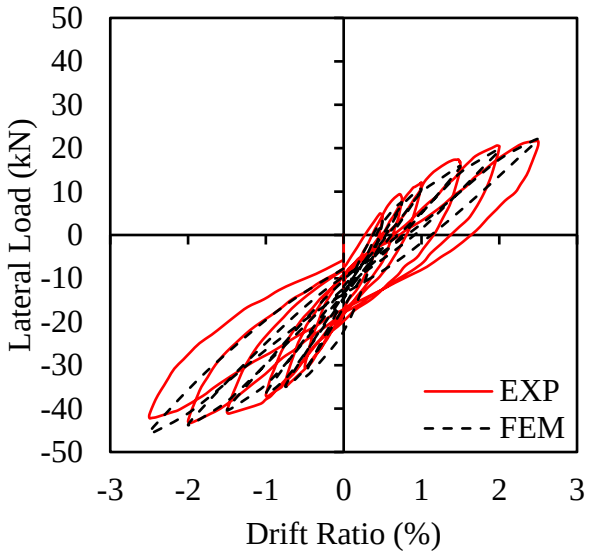

a) Hysteretic response

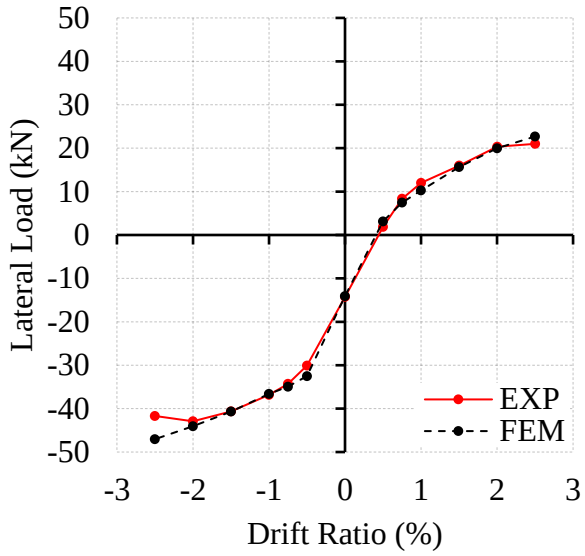

b) Drift envelope

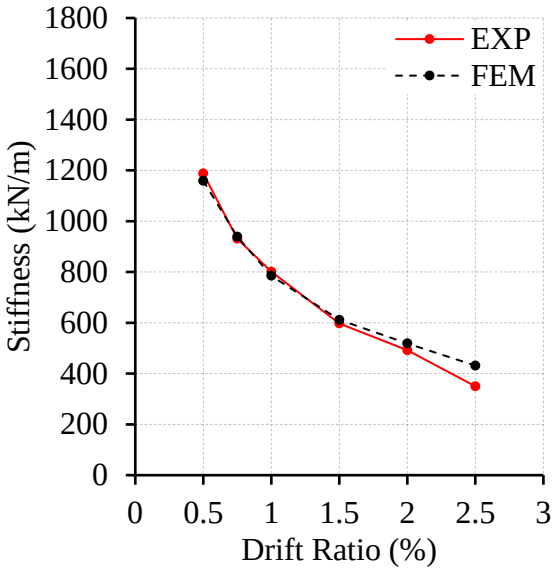

c) Stiffness degradation

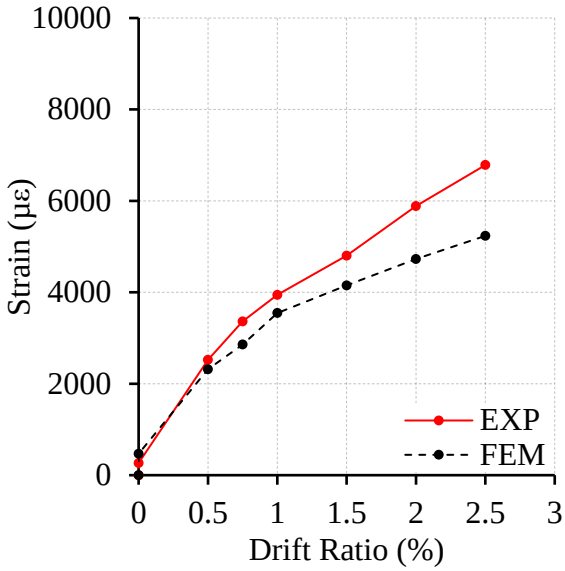

d) Flexural reinforcement strain

Figure 8.9: Validation of FEM – connection E-1.4-40

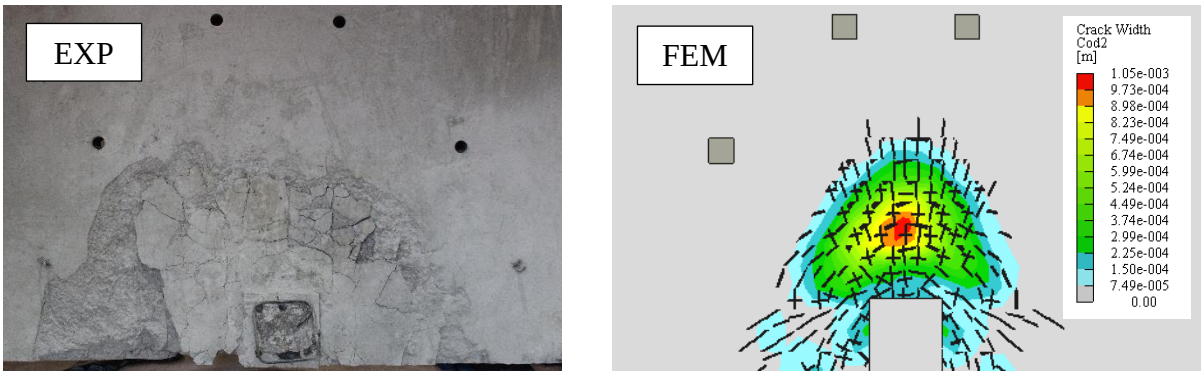

e) Cracking pattern at failure

Figure 8.9: Validation of FEM – connection E-1.4-40 (continued)

8.6.2. Stiffness

Figure 8.9c shows the relationship between the stiffness factor and the drift ratio for E-1.4-40. The stiffness factors were calculated as the slope of the straight line connecting the two peaks of the third hysteresis loop at each loading cycle. The FEMs were able to closely model the stiffness degradation of the test specimens. Values of the initial stiffness of the connections (the stiffness at 0.5% drift ratio) are listed in Table 8.3. The mean (k_{FEM}/k_{EXP}) for the initial stiffness was 0.94 ± 0.04 with COV and R^2 values of 4.15% and 0.97, respectively.

8.6.3. Reinforcement strain and cracking pattern

The relationship between the reinforcement strain at the column face of E-1.4-40 and the drift ratio is shown in Figure 8.9d. The predicted strains by the FEM were in good agreement with the experimental results; however, with less accuracy than that demonstrated in the case of hysteretic response and stiffness degradation. The ratio between the FEM and experimental reinforcement strain at ultimate in connections E-0.7-40 and E-1.4-40 was 0.84 and 0.77, respectively. This value was increased in connections E-1.4-50 and E-1.4-60 to 0.95 and 0.98, respectively. Experimental strain values were captured at specific locations along the reinforcing bar, which were sensitive to

several factors, including locations of cracks and distribution of aggregate in concrete. When the location of a reinforcement strain gauge coincides with the location of a crack, higher strains will be recorded by those strain gauges. Therefore, slight deviations in the FEM results are typically expected and accepted. The mean value of the ratio between the FEM and experimental reinforcement strains in the four connections was 0.89 ± 0.10 with COV and R^2 values of 10.97% and 0.86, respectively. Figure 8.9e shows the cracking pattern on the top (tension) surface of the slab in the column vicinity at failure, obtained experimentally and using FEM. It is clear that the cracking pattern obtained by FEM closely resembles that of the experimental specimen, with the location of highest crack width in the FEM coinciding with the location of main punching shear crack in the experimental connection.

8.7. Parametric Study

The validated FEM was used to conduct an extensive parametric study investigating the effect of key parameters on the seismic response of edge connections. These parameters are: 1) gravity shear ratio on GFRP-RC and carbon FRP (CFRP)-RC connections, 2) flexural reinforcement type, 3) column aspect ratio, 4) flexural reinforcement ratio, and 5) slab thickness. Therefore, the designations of the FEMs consist of five parts representing the five parameters. The first part indicates the reinforcement type (G for GFRP, C for CFRP), the second part indicates the flexural reinforcement ratio (e.g., 0.9 for ρ = 0.875%), the third part indicates the applied gravity shear ratio, V_g/V_c (e.g., 20 for V_g/V_c = 0.2), the fourth part indicates the column width perpendicular to the free edge of the slab, C_1 (e.g., 36 for C_1 = 360 mm), and the fifth part indicates the slab thickness (e.g., 20 for thickness of 200 mm).

Table 8.3: Validation of FEM

Specimen	Gravity lateral load			Peak lateral load			Ultimate drift ratio			Initial stiffness		
	$P_{g\text{-}EXP}$ (kN)	$P_{g\text{-}FEM}$ (kN)	$P_{g\text{-}EXP}$ / $P_{g\text{-}FEM}$	$P_{p\text{-}EXP}$ (kN)	$P_{p\text{-}FEM}$ (kN)	$P_{p\text{-}FEM}$ / $P_{p\text{-}EXP}$	$\delta_{u\text{-}EXP}$ (%)	$\delta_{u\text{-}FEM}$ (%)	$\delta_{u\text{-}FEM}$ / $\delta_{u\text{-}EXP}$	k_{EXP} (kN/m)	k_{FEM} (kN/m)	k_{FEM} / k_{EXP}
E-0.7-40	13.1	16.1	1.23	37.1	35.1	0.95	2.00	2.00	1.00	828	738	0.89
E-1.4-40	14.2	14.1	0.99	43.3	45.6	1.05	2.50	2.50	1.00	1,188	1,159	0.98
E-1.4-50	16.9	14.7	0.87	40.9	36.8	0.90	1.50	1.50	1.00	1,075	985	0.92
E-1.4-60	24.6	22.0	0.89	37.4	36.6	0.98	1.00	1.00	1.00	918	881	0.96
Mean			1.00			0.97			1.00			0.94
SD			0.16			0.06			0.00			0.04
COV (%)			16.44			6.66			0.00			4.15
R^2			0.79			0.75			1.00			0.97

Note: $P_{g\text{-}EXP}$ = experimental gravity lateral load (kN); $P_{g\text{-}FEM}$ = gravity lateral load estimated by FEM (kN); $P_{p\text{-}EXP}$ = experimental peak lateral load (kN); $P_{p\text{-}FEM}$ = peak lateral load estimated by FEM (kN); $\delta_{u\text{-}EXP}$ = experimental ultimate drift ratio (%); $\delta_{u\text{-}FEM}$ = ultimate drift ratio estimated by FEM (%); k_{EXP} = experimental initial stiffness (kN/m); k_{FEM} = initial stiffness estimated by FEM (kN/m).

8.7.1. Effect of gravity shear ratio

The experimental results (El-Gendy and El-Salakawy 2020b) revealed that the applied gravity shear ratio must be limited to 0.5 in order for GFRP-RC edge connections, without shear reinforcement, to sustain a minimum drift of 1.5% without punching failure. In this study, the investigation was expanded to include a wide spectrum of gravity shear ratios between 20 and 80% (with an increment of 10%) applied to connections reinforced with either GFRP or CFRP reinforcement as listed in Table 8.4.

Figure 8.10a shows envelopes of the hysteretic response of the GFRP-RC connections. It is clear that increasing the applied gravity shear ratio reduced the lateral drift capacity of the GFRP-RC connections. Connection G-1.4-20-30-20 (subjected to a low gravity shear ratio of 0.2) was able to sustain 3.5% drift ratio before failure. Connections G-1.4-30-30-20 and G-1.4-40-30-20 failed at a lower drift ratio of 2.5%. On the other hand, G-1.4-60-30-20, G-1.4-70-30-20, and G-1.4-80-30-20 were not able to withstand the 1.5% minimum recommended drift ratio (Sozen 1980). Nonetheless, the drift capacities of all GFRP-RC connections were in good agreement with the model by El-Gendy and El-Salakawy (2020c) and satisfied the CSA A23.3-19 (CSA 2019) and ACI 318-19 (ACI 2019a) drift requirements as shown in Figure 8.11.

Table 8.4: Details of FEMs investigating the effect of gravity shear ratio

FEM	Reinforcement type	Gravity shear ratio	$P_{g\text{-}FEM}$	$P_{p\text{-}FEM}$	$\delta_{p\text{-}FEM}$	$\delta_{u\text{-}FEM}$	k_{FEM} (kN/m)	Punching strength		
								v_{FEM} (MPa)	v_{FEM} / v_{CSA}	v_{FEM} / $v_{E\text{-}E}$
G-1.4-20-30-20	GFRP	0.2	7.7	53.7	3.50	3.50	1,252	2.35	1.23	1.06
G-1.4-30-30-20	GFRP	0.3	9.3	46.4	2.50	2.50	1,195	2.21	1.16	1.00
G-1.4-40-30-20 [a]	GFRP	0.4	14.1	45.6	2.50	2.50	1,159	2.32	1.21	1.05
G-1.4-50-30-20 [a]	GFRP	0.5	14.7	36.8	1.50	1.50	985	2.12	1.11	0.95
G-1.4-60-30-20 [a]	GFRP	0.6	22.0	36.6	1.00	1.00	881	2.25	1.18	1.01
G-1.4-70-30-20	GFRP	0.7	28.0	37.5	1.00	1.00	814	2.43	1.27	1.09
G-1.4-80-30-20	GFRP	0.8	31.9	41.7	0.75	0.75	790	2.73	1.43	1.23
C-1.4-20-30-20	CFRP	0.2	20.9	58.4	2.00	2.50	1,567	2.62	1.05	0.90
C-1.4-30-30-20	CFRP	0.3	24.2	61.4	1.50	2.00	1,494	2.91	1.17	1.00
C-1.4-40-30-20	CFRP	0.4	24.3	59.7	2.00	2.00	1,369	3.02	1.21	1.04
C-1.4-50-30-20	CFRP	0.5	31.8	58.1	1.50	1.50	1,283	3.14	1.26	1.09
C-1.4-60-30-20	CFRP	0.6	35.1	56.0	1.00	1.00	1,267	3.24	1.30	1.12
C-1.4-70-30-20	CFRP	0.7	37.8	56.1	1.00	1.00	1,183	3.42	1.37	1.18
C-1.4-80-30-20	CFRP	0.8	41.9	57.3	0.75	0.75	1,144	3.65	1.46	1.26
Mean									1.24	1.07
SD									0.12	0.10
COV (%)									9.43	9.43
R^2									0.71	0.71

Note: P_g = gravity lateral load (kN); P_p = peak lateral load (kN); δ_p = peak drift ratio (%); δ_u = ultimate drift ratio (%); k = initial stiffness (kN/m); v_{FEM} = punching strength of FEM; v_{CSA} = punching strength predicted by CSA S806-12 (CSA 2017); $v_{E\text{-}E}$ = punching strength predicted by El-Gendy and El-Salakawy (2020c).

[a] Models validated by experimental testing

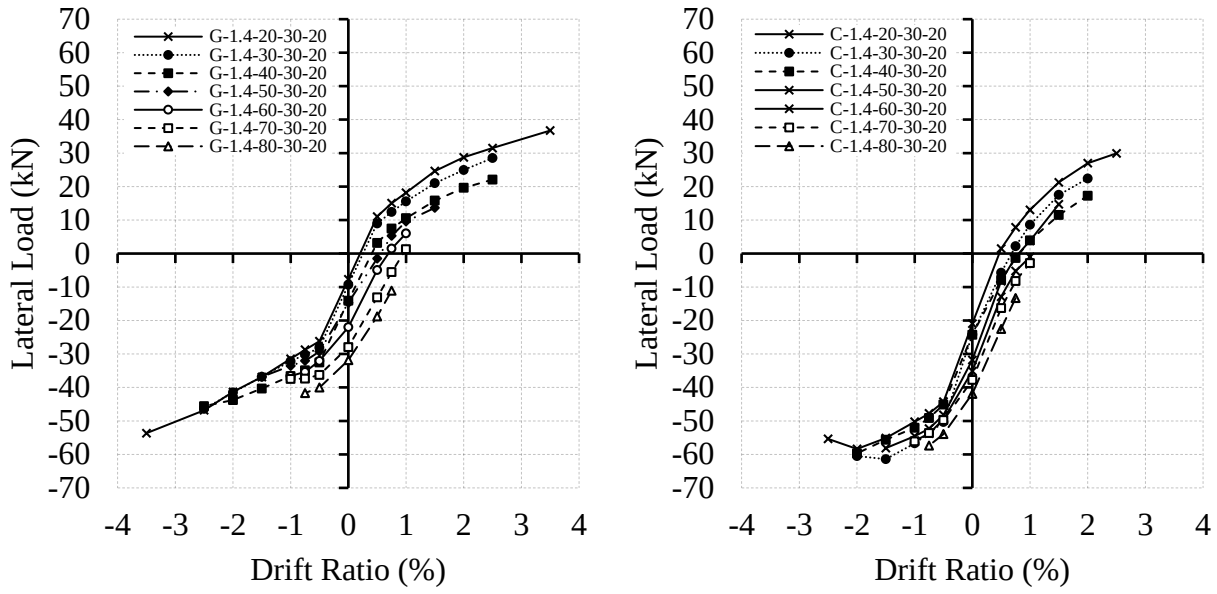

a) GFRP-RC connections b) CFRP-RC connections

Figure 8.10: Drift envelopes of connections under different gravity shear ratios

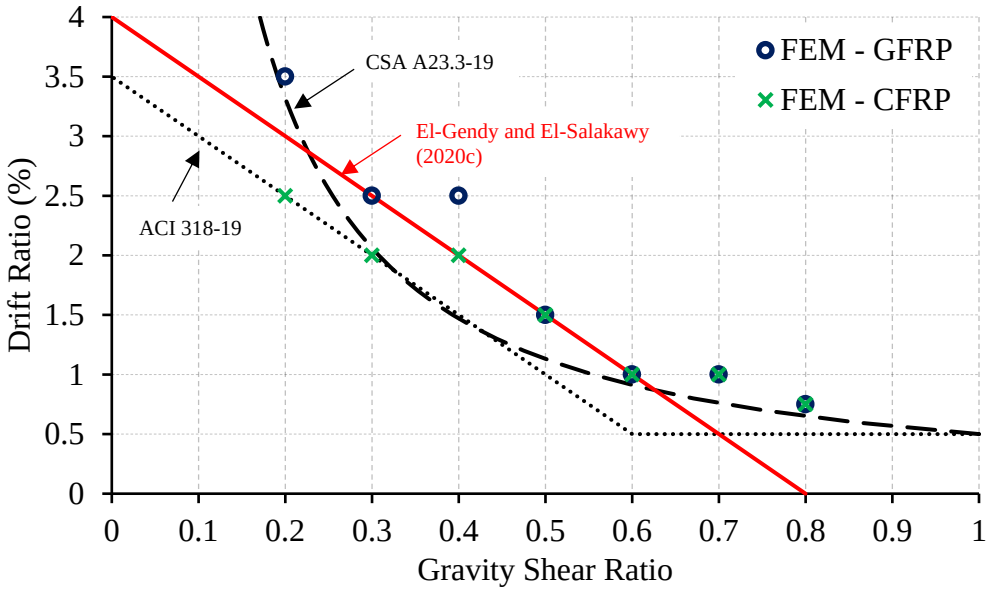

Figure 8.11: Drift capacity of GFRP-RC connections under different gravity shear ratios

Similar trend was observed for the CFRP-RC connections as shown in Figure 8.10b. Connections C-1.4-20-30-20 and C-1.4-30-30-20 were able to sustain drift ratios of 2.5 and 2.0%, respectively.

Despite satisfying the requirements of ACI 318-19, these values fail to satisfy the requirements of CSA A23.3-19. In addition, according to El-Gendy and El-Salakawy (2020c), these two connections should have been able to withstand at least 3.0 and 2.5% drift ratios, respectively. Applying a gravity shear ratio of 0.4 in C-1.4-40-30-20 decreased the ultimate drift ratio (which is the maximum drift ratio that a connection can withstand before failure) to 2.0%. Similar to the case of GFRP-RC connections, applying a gravity shear ratio higher than 0.5 resulted in punching shear failure at drift ratios less than 1.5%.

Figure 8.12 demonstrates the stiffness degradation of the GFRP-RC and CFRP-RC connections. Increasing the gravity shear ratio resulted in considerable cracks under gravity loads. This resulted in a significant reduction in the initial stiffness of the connections (which is defined as the stiffness after 0.5% drift ratio) as listed in Table 8.4. For the GFRP-RC connections, increasing the gravity shear ratio from 0.2 to 0.4, then further to 0.6 and 0.8 resulted in 7.4, 29.6, and 36.9% reduction in the initial stiffness, respectively. Similarly, these reduction percentages were 13, 20 and 27%, respectively, for the CFRP-RC connections.

The results of the FEMs models were used to further assess the two punching strength models discussed earlier. Table 8.4 lists the comparisons between the punching strength estimated by the FEMs (v_{FEM}) and that predicted by both models (v_{CSA} and $v_{E\text{-}E}$). The punching strength, estimated by the FEMs, was calculated according to Equation 8.15 and Equation 8.16:

$$v_{FEM} = \frac{V_0}{b_o d} + \frac{\gamma_v M_{unb}}{J} e \qquad \text{Equation 8.15}$$

$$\gamma_v = 1 - \frac{1}{1 + (2/3)\sqrt{b_1/b_2}} \qquad \text{Equation 8.16}$$

where M_{unb} is the maximum unbalanced moment transferred between the slab and the column (calculated as the product of the peak lateral load, $P_{p\text{-}FEM}$, and the distance between the horizontal axis of the actuator applying the drifts and the axis of rotation of the hinge support at the bottom of the column, which is 2,920 mm), e is the distance from the centroid of the critical section to the point where maximum shear stress is being calculated, J is a property of the critical section analogous to the polar moment of inertia, and γ_v is a factor accounting for the portion of the unbalanced moment transferred by eccentricity of shear as given by Equation 8.16, where b_1 is the width of the critical section in the direction of the unbalanced moment, and b_2 is the width of the critical section perpendicular to b_1.

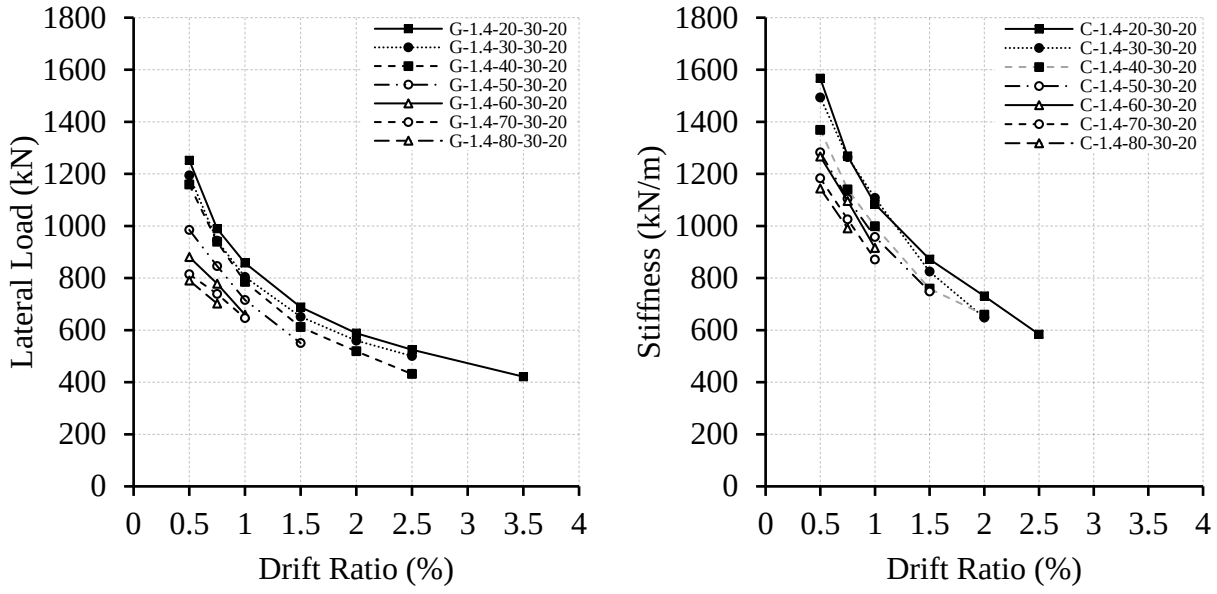

a) GFRP-RC connections b) CFRP-RC connections

Figure 8.12: Stiffness degradation for connections under different gravity shear ratios

The CSA S806-12 model (CSA 2017) gave slightly conservative predictions with an average v_{FEM}/v_{CSA} of 1.23 ± 0.10 and 1.26 ± 0.14 for the GFRP-RC and CFRP-RC connections, respectively. On the other hand, the model by El-Gendy and El-Salakawy (2020c) provided closer to unity ratios of 1.06 ± 0.09 and 1.09 ± 0.12 for GFRP-RC and CFRP-RC connections, respectively.

8.7.2. Effect of flexural reinforcement type

Compared to GFRP bars, CFRP bars have considerably higher tensile strength and stiffness. This, however, comes at the expense of their ultimate strain, which is considerably lower than that of GFRP bars as listed in Table 8.1. The high tensile strength and stiffness of CFRP reinforcement could be utilized in several applications, such as prestressed concrete and near surface mounted (NSM) strengthening. Nonetheless, the relatively low ultimate strain of CFRP bars may hinder their utilization in flat plates susceptible to punching failure, especially when subjected to cyclic loads. In an early effort, Zaghloul (2007) investigated the punching shear behavior of CFRP-RC half-scale edge connections subjected to monotonically increased axial load and unbalanced moment. The unbalanced moment was applied via changing the eccentricity of the vertical load applied on the upper column stub, while no loads (neither vertical nor lateral) were applied at the lower column stub. Surprisingly, replacing steel flexural reinforcement with the same amount of CFRP reinforcement did not affect the punching shear capacity of the connections. Furthermore, although increasing the CFRP flexural reinforcement ratio by 46% increased the ultimate capacity by 21%, it had no effect on the post-cracking stiffness of the connections.

To date, no experimental studies have been conducted to study the behavior of full-scale CFRP-RC slab-column edge connections. As mentioned earlier, a series of FEMs is constructed to

simulate such connections subjected to different gravity shear ratios (Table 8.4). Figure 8.13 shows the hysteretic response of G-1.4-40-30-20 and C-1.4-40-30-20 subjected to a gravity shear ratio of 0.4. Connection C-1.4-40-30-20 failed at a 31% higher lateral load than that of G-1.4-40-30-20. However, it only sustained a drift ratio of 2.0%, which is 20% lower than that sustained by G-1.4-40-30-20. Both connections reached the lateral load capacity predicted by CSA S806-12 (CSA 2017) and the model by El-Gendy and El-Salakawy (2020c).

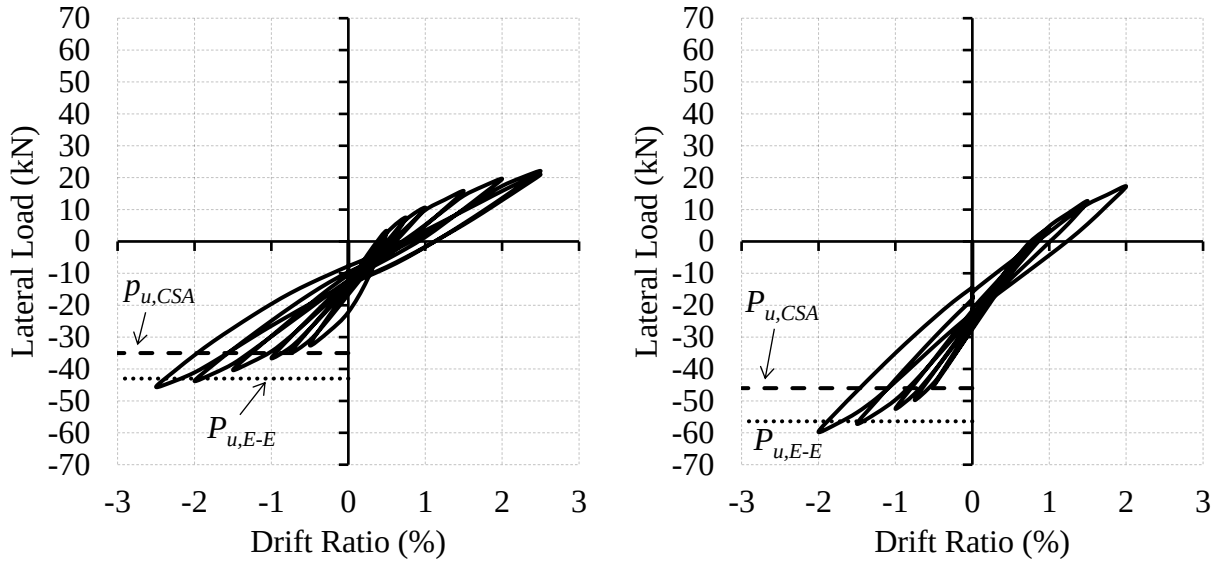

a) G-1.4-40-30-20 b) C-1.4-40-30-20

Figure 8.13: Hysteretic response of edge connections with different flexural reinforcement types

On the other hand, despite being subjected to a higher gravity load, C-1.4-40-30-20 had consistently higher stiffness at all drift ratios than that of G-1.4-40-30-20 as shown in Figure 8.14 (a). Connection C-1.4-40-30-20 had 18% higher initial stiffness than that of G-1.4-40-30-20 due to the higher modulus of elasticity of the reinforcement. Consistently, the reinforcement strains in G-1.4-40-30-20 were higher than those captured in C-1.4-40-30-20 at the same drift ratio, as shown

in Figure 8.14b. At failure, the reinforcement strain in G-1.4-40-30-20 was 34% higher than that in C-1.4-40-30-20.

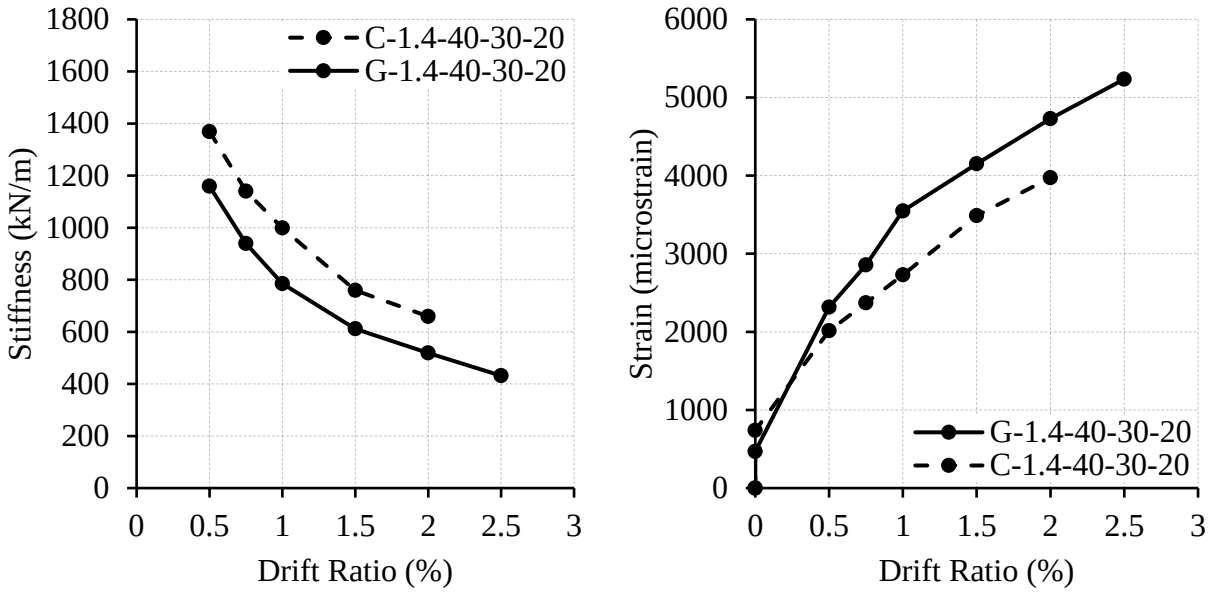

a) Stiffness degradation b) Flexural reinforcement strain

Figure 8.14: Comparisons between edge connections with different flexural reinforcement types

8.7.3. Effect of column aspect ratio

Rectangular columns are frequently required in RC flat plate systems to satisfy architectural demands. To date, no experimental studies have been conducted to investigate the punching behavior of FRP-RC slabs supported on rectangular columns. Furthermore, scarce experimental data on steel-RC slabs supported on rectangular columns are available (Teng et al. 2004; Anggadjaja and Teng 2008). Therefore, a series of FEMs is constructed to investigate the punching behavior of GFRP-RC edge connections with rectangular columns having different aspect ratios ranging between 1:4 to 4:1.

Figure 8.15 shows typical column orientations of the constructed FEMs. All dimensions of the connections were kept constant (Figure 8.1) while changing the column dimensions. The side dimension of the column perpendicular to the free edge, C_1, was progressively reduced from 300 mm in the control FEM to 150 mm in 50 mm increments, while maintaining the column area of the control FEM of G-1.4-40-30-20 (90,000 mm^2) as listed in Table 8.5. Therefore, G-1.4-40-25-20, G-1.4-40-20-20, and G-1.4-40-15-20 had column dimensions of 250×360, 200×450, and 150×600 mm, respectively. This was carried out to study the behavior of the connections when the lateral load is applied to the weak axis of the column. In addition, three FEMs were constructed with the same column dimensions, while the columns were 90 degree rotated about their longitudinal axis. This way, the lateral load is applied to the strong axis of the column. The latter three FEMs, G-1.4-40-36-20, G-1.4-40-45-20, and G-1.4-40-60-20 had column dimensions of 360×250, 450×200, and 600×150 mm, respectively.

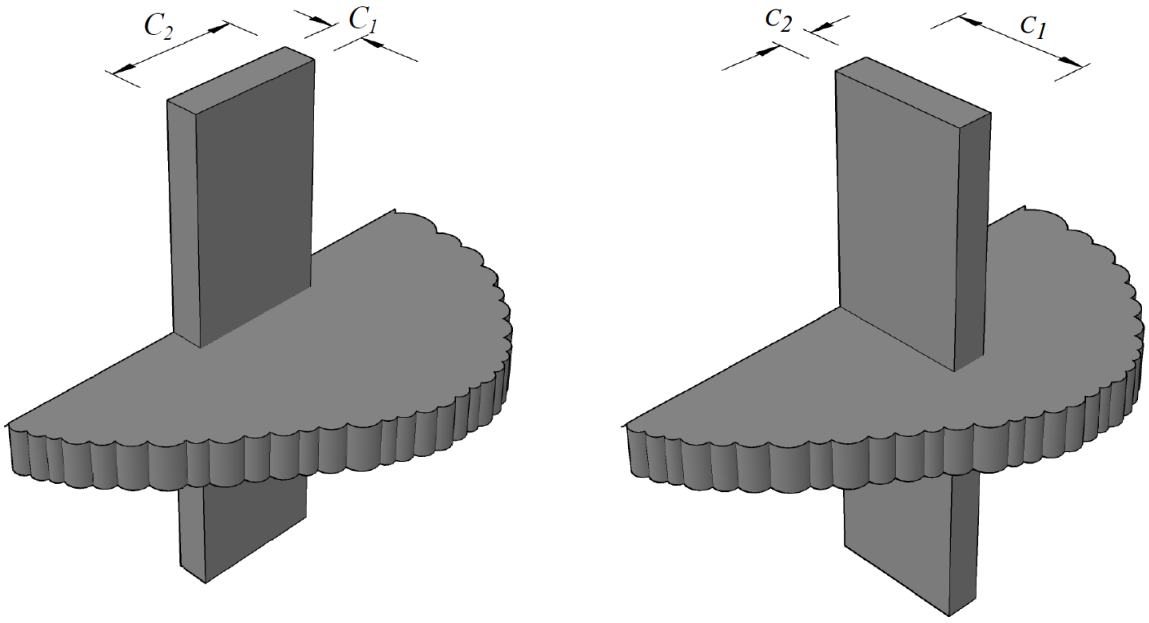

a) Loading on weak axis b) Loading on strong axis

Figure 8.15: Layout of FEMs investigating the effect of column aspect ratios

Table 8.5: Details of FEMs investigating the effect of column rectangularity

FEM	C_1 (mm)	C_2 (mm)	Aspect ratio	$P_{g\text{-}FEM}$	$P_{p\text{-}FEM}$	$\delta_{p\text{-}FEM}$	$\delta_{u\text{-}FEM}$	k_{FEM} (kN/m)
G-1.4-40-15-20	150	600	1:4.00	10.8	30.2	2.00	2.50	791
G-1.4-40-20-20	200	450	1:2.25	15.4	41.8	2.50	2.50	894
G-1.4-40-25-20	250	360	1:1.44	18.1	43.3	2.50	2.50	993
G-1.4-40-30-20 [a]	300	300	1:1	14.1	45.6	2.50	2.50	1,159
G-1.4-40-36-20	360	250	1.44:1	21.8	48.7	2.00	2.50	1,250
G-1.4-40-45-20	450	200	2.25:1	24.0	54.7	2.00	2.00	1,364
G-1.4-40-60-20	600	150	4.00:1	22.1	60.1	2.00	2.00	1,659

Note: C_1 = column width perpendicular to free edge; C_2 = column width parallel to free edge; P_g = gravity lateral load (kN); P_p = peak lateral load (kN); δ_p = peak drift ratio (%); δ_u = ultimate drift ratio (%); k = initial stiffness (kN/m).

[a] Model validated by experimental testing

Connection G-1.4-40-15-20 (C_1 = 150 mm) experienced the most deformable behavior with the least lateral load transferred between the slab and the column as shown in Figure 8.16. It reached a lateral load of 28.1 kN at 1.5% drift ratio. This load hardly increased to 30.2 kN at 2.00% (7.5% increase) and remained approximately constant until failure at 2.5% drift ratio. On the other hand, G-1.4-40-60-20 (C_1 = 600 mm) experienced the least deformable behavior and the highest lateral load transferred between the slab and the column. The lateral load capacity kept increasing gradually with increasing the drift until a peak value of 60.1 kN was reached. This was approximately double that experienced by G-1.4-40-15-20. Similar trend was reported in the literature for steel-RC edge connections (Anggadjaja and Teng 2008).

Reducing the column side dimension perpendicular to the free edge, C_1, did not affect the drift capacity of the connections; however, it reduced their lateral load capacity. Similar to the control connection with a 300-mm square column, all connections with C_1 less than 300 mm were able to sustain a drift ratio of 2.5% as shown in Figure 8.17a. Reducing C_1 from 300 to 250 and further to 200 mm marginally reduced the lateral load capacity by 5 and 8%, respectively. However, a 50%

reduction in C_1 to 150 mm resulted in a significant reduction in the lateral load capacity of 30%. On the other hand, increasing C_1 affected both the drift and lateral load capacities of the connections as shown in Figure 8.17b. Increasing C_1 from 300 to 360, then further to 450 and 600 mm increased the lateral load capacity by 7, 20, and 32%, respectively. Moreover, connections G-1.4-40-45-20 and G-1.4-40-60-20 was only able to undergo a drift ratio of 2.0%.

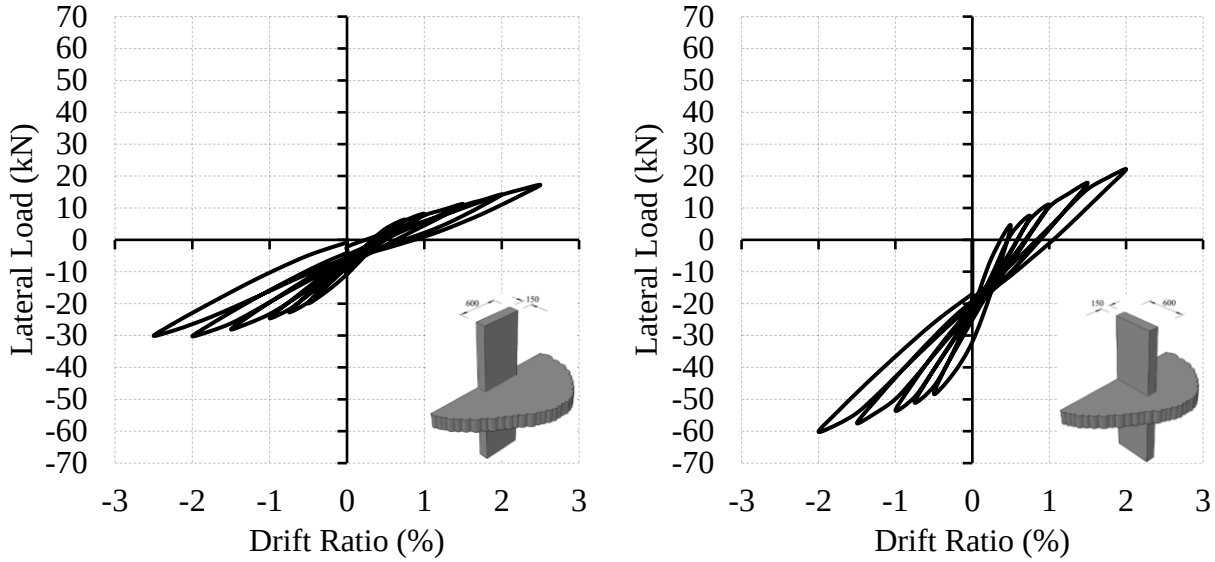

a) G-1.4-40-15-20 b) G-1.4-40-60-20

Figure 8.16: Hysteretic response of edge connections with rectangular columns

Anggadjaja and Teng (2008) suggested reducing the gravity shear ratio limit on steel-RC connections with column aspect ratio of 5.0 from 0.4 to 0.3. Although such reduction may not be required for GFRP-RC connections, further investigation is needed for connections with rectangular columns subjected to biaxial lateral load. As shown in Figure 8.18, increasing C_1 significantly increased the stiffness of the connections, and vice versa. Connection G-1.4-40-60-20 (C_1 = 600 mm) had 43% higher initial stiffness than that of G-1.4-40-30-20 (C_1 = 300 mm). On the contrary, G-1.4-40-15-20 (C_1 = 150 mm) had 32% lower initial stiffness than that of G-1.4-40-

30-20 (C_1 = 300 mm). Furthermore, G-1.4-40-60-20 (C_1 = 600 mm) had 110% higher initial stiffness than that of G-1.4-40-15-20 (C_1 = 150 mm).

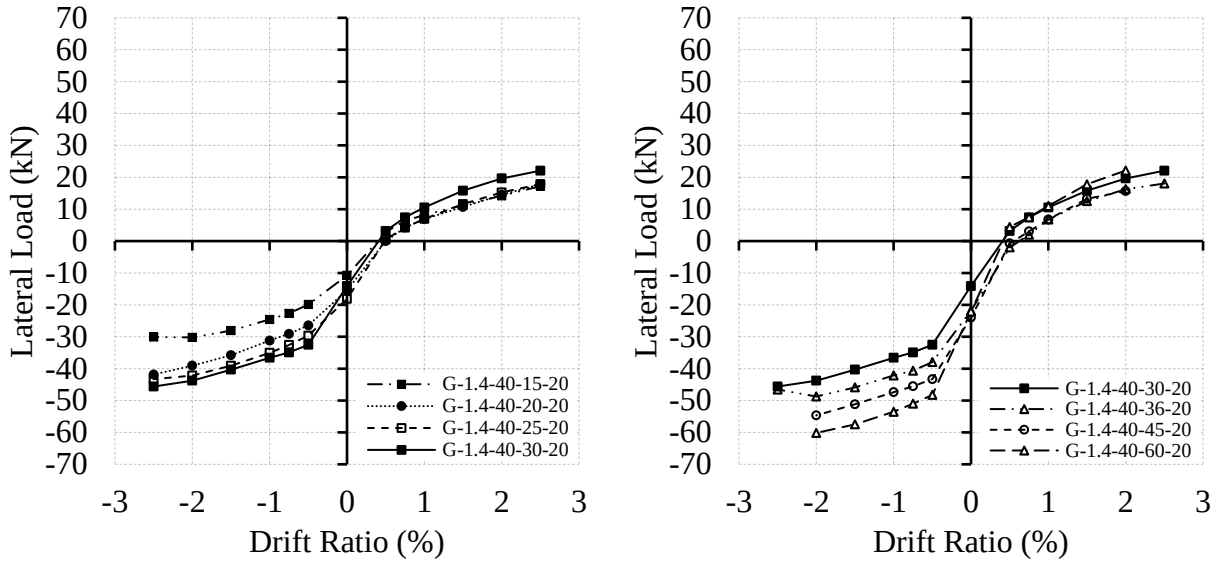

a) Loading on weak axis b) Loading on strong axis

Figure 8.17: Drift envelopes of GFRP-RC connections with rectangular columns

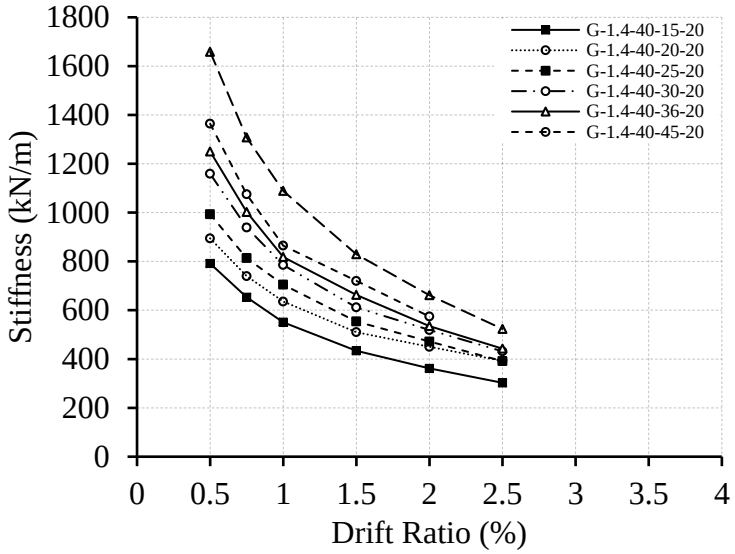

Figure 8.18: Stiffness degradation for connections with rectangular columns

8.7.4. Effect of slab thickness

It is well established that the shear strength of steel-RC members without shear reinforcement decreases as the member depth increases (Kani 1967; Bazant and Cao 1987; Rizk et al. 2011). Wider diagonal cracks are formed as the depth increases, which jeopardizes the aggregate interlock contribution to the shear strength. Recent studies on GFRP-RC beams concluded that similar size effect exists in simply supported beams (Bentz et al. 2010). Surprisingly, Dulude et al. (2013) concluded that increasing the slab thickness from 200 to 350 mm resulted in a 63% average increase in the punching strength of GFRP-RC two-way slabs. This conclusion is against the general consensus amongst researchers regarding the size effect on the shear strength of steel-RC or GFRP-RC members.

To date, all experimental studies on FRP-RC slab-column connections were conducted on connections with a slab thickness of 200 mm (Gouda and El-Salakawy 2016; El-Gendy and El-Salakawy 2016; Salama et al. 2019). As mentioned earlier, CSA S806-12 (CSA 2017) considers the size effect for slabs with a depth larger than 300 mm. Therefore, a series of FEMs is constructed to investigate whether a size effect exists for connections with slab thickness ranging between 150 and 400 mm as listed in Table 8.6. This was done while keeping the maximum mesh size constant. Therefore, the number of elements through the slab thickness was increased with increasing the slab thickness. All dimensions of the connections were kept constant (Figure 8.1) while changing the slab thickness, which resulted in a varied shear span-to-depth ratio. A similar approach was followed when Rizk et al. (2011) experimentally investigated the size effect of steel-RC interior connections subjected to concentric loading. The slab thickness was changed between 300 and 400 mm, while keeping all other dimensions constant. This resulted in shear span-to-depth ratios ranging between 3.33 and 4.80.

Table 8.6: Details of FEMs investigating the size effect

FEM	Slab thickness (mm)	Effective slab depth (mm)	$P_{g\text{-}FEM}$	$P_{p\text{-}FEM}$	$\delta_{p\text{-}FEM}$	$\delta_{u\text{-}FEM}$	k_{FEM} (kN/m)	Punching strength		
								v_{FEM} (MPa)	v_{FEM} / v_{CSA}	v_{FEM} / $v_{E\text{-}E}$
G-1.4-40-30-15	150	110	10.5	27.7	2.50	3.50	698	2.49	1.30	1.12
G-1.4-40-30-20 [a]	200	160	14.1	45.6	2.50	2.50	1,159	2.32	1.21	1.05
G-1.4-40-30-25	250	210	30.2	72.0	2.00	2.00	1,414	2.26	1.18	0.99
G-1.4-40-30-30	300	260	37.0	77.1	1.00	1.00	1,866	1.76	0.92	0.75
G-1.4-40-30-35	350	310	44.4	81.7	1.00	1.00	2,066	1.42	0.75 [b]	0.59
G-1.4-40-30-40	400	360	48.3	83.1	0.75	0.75	2,452	1.18	0.65 [b]	0.48

Note: P_g = gravity lateral load (kN); P_p = peak lateral load (kN); δ_p = peak drift ratio (%); δ_u = ultimate drift ratio (%); k = initial stiffness (kN/m); v_{FEM} = punching strength of FEM; v_{CSA} = punching strength predicted by CSA S806-12 (CSA 2017); $v_{E\text{-}E}$ = punching strength predicted by El-Gendy and El-Salakawy (2020c).

[a] Model validated by experimental testing
[b] Considering size effect factor in CSA S806-12 (2017)

Increasing the slab thickness considerably decreased the drift capacity of the connections as shown in Figure 8.19a. Doubling the slab thickness from 150 to 300 mm reduced the ultimate drift capacity from 3.5 to 1.0%. A further increase in the thickness to 400 mm decreased the drift capacity to 0.75%. A deformation-based mechanical model proposed by Darakatos et al. (2018), based on the critical shear crack theory, demonstrated a similar trend for steel-RC interior connections. It showed that increasing the effective slab depth (while maintaining the shear span-to-depth ratio) resulted in a significant reduction in the rotation capacity of the connections. On the other hand, increasing the slab thickness resulted in a substantial increase in the initial stiffness and lateral load capacity of the connections. As shown in Figure 8.19b, connections with 200, 250, 300, 350 and 400-mm thick slabs had 66, 103, 167, 196, and 251% higher initial stiffness and 65, 160, 178, 195, and 200% higher lateral load capacity than that of G-1.4-40-30-15 (with a 150-mm thick slab), respectively.

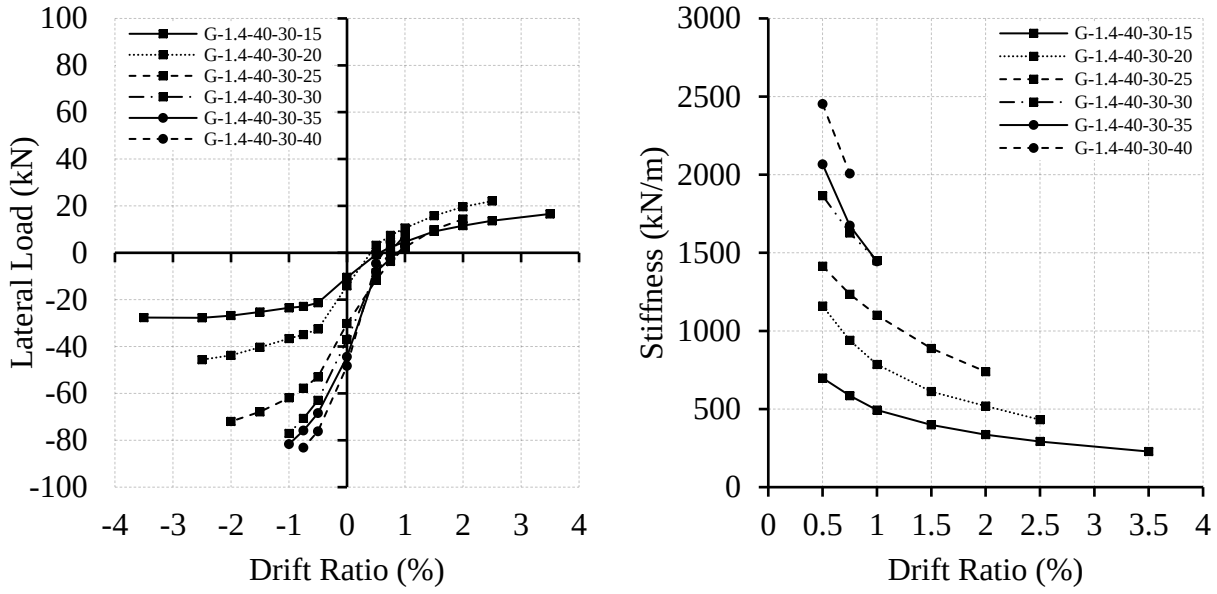

a) Drift envelope b) Stiffness degradation

Figure 8.19: Size effect on GFRP-RC connections

Despite their higher lateral load capacity, slabs thicker than 250 mm failed at a lower punching strength as shown in Figure 8.20. Connections G-1.4-40-30-30, G-1.4-40-30-35, and G-1.4-40-30-40 had a punching strength of 1.76, 1.42, and 1.18 MPa. These values are 8, 25, and 35% lower than that predicted by CSA S806-12 (CSA 2017) and 25, 41, and 52% lower than that predicted by the model by El-Gendy and El-Salakawy (2020c), respectively. The former model does not consider the size effect for slabs with effective depths less than 300 mm. On the other hand, despite having a size effect factor for all slab depths, the former model overestimated the capacity of thick slabs due the depth-to-shear perimeter factor incorporated in the model. Further research is needed to calibrate both models.

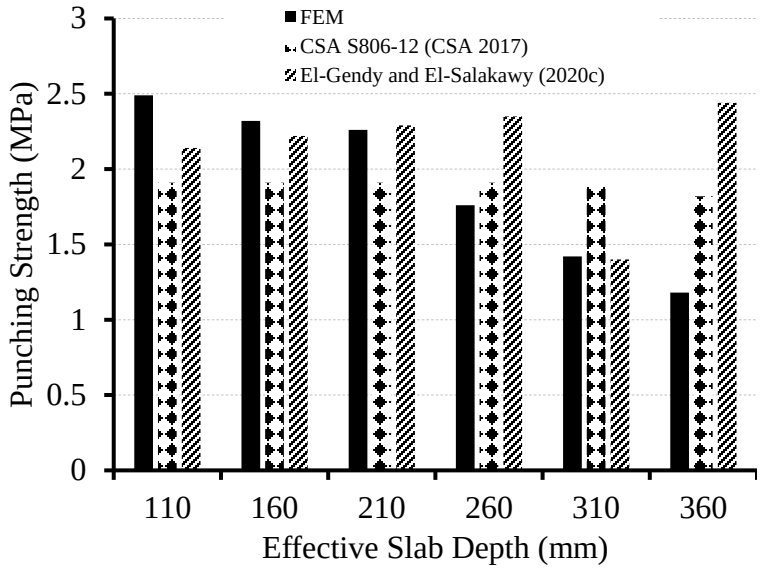

Figure 8.20: Size effect on punching strength of GFRP-RC connections

8.7.5. Effect of flexural reinforcement ratio

Contradicting conclusions were reported in the literature regarding the effect of reinforcement ratio, ρ, on the drift capacity of steel-RC connections. Ghali et al. (1976) reported that increasing the reinforcement ratio from 0.5 to 1.0 and further to 1.5% reduced the rotation capacity of interior

connections subjected to dynamic loads by 58 and 62%, respectively. However, Marzouk et al. (2001) and Emam et al. (2007) showed that doubling the reinforcement ratio from 0.5 to 1.0% in interior connections made of normal strength concrete did not affect their drift capacity. Furthermore, Robertson and Johnson (2006) showed that increasing the reinforcement in interior connections from 0.3 to 0.5% increased the drift capacity at failure from 5.0 to 8.0%. Nonetheless, a further increase in the reinforcement ratio to 0.8% reduced the drift capacity at failure to 5.0%. A recent experimental study by the authors (El-Gendy and El-Salakawy 2019) on GFRP-RC edge connections reported that doubling the reinforcement ratio from 0.7 to 1.4% increased the drift capacity by 25%. In this study, the investigation is expanded and a series of FEMs is constructed to investigate the effect of different reinforcement ratios ranging between 0.7 (3.2 times the balanced ratio) and 1.4% (6.4 times the balanced ratio), in increments of 0.175%.

Figure 8.21 shows the drift envelopes of the FEMs investigating the effect of reinforcement ratio. Connection G-0.9-40-30-20 (ρ = 0.875%) had a 12% higher lateral load capacity than that of G-0.7-40-30-20 (ρ = 0.7%). However, both connections sustained the same 2.0% drift ratio. Increasing the reinforcement ratio by 50% (from 0.70 to 1.05%) enhanced the lateral load and drift capacities by 23 and 25%, respectively. Further increase in the reinforcement ratio marginally enhanced the lateral load capacity and did not affect the drift capacity. On the other hand, increasing the reinforcement ratio improved the initial stiffness of the connections. As listed in Table 8.7, a 50% increase in the reinforcement ratio (from 0.70 to 1.05%) resulted in a 39% improvement in the initial stiffness. When the GFRP reinforcement ratio increases, the punching shear capacity increases due to the enhanced control of diagonal cracks, increased uncracked concrete depth, and improved dowel action of longitudinal reinforcement. Besides increasing the stiffness of the connections, this allows the connections to undergo higher drifts before failure.

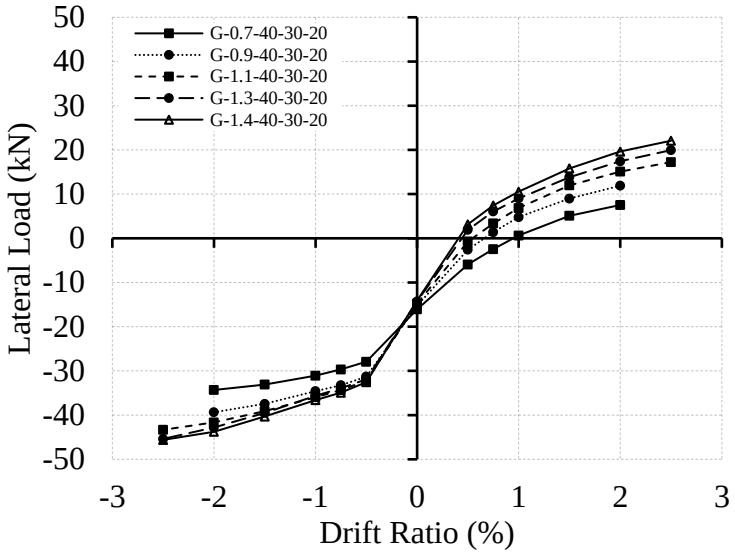

Figure 8.21: Drift envelope of GFRP-RC connections with varying reinforcement ratios

Table 8.7: Details of FEMs investigating the effect of reinforcement ratio

FEM	Flexural reinforcement ratio (%)	$P_{g\text{-}FEM}$	$P_{p\text{-}FEM}$	$\delta_{p\text{-}FEM}$	$\delta_{u\text{-}FEM}$	k_{FEM} (kN/m)
G-0.7-40-30-20 [a]	0.700	16.1	35.1	2.0	2.0	738
G-0.9-40-30-20	0.875	15.2	39.4	2.0	2.0	942
G-1.1-40-30-20	1.050	14.8	43.3	2.5	2.5	1,029
G-1.2-40-30-20	1.275	14.3	45.4	2.5	2.5	1,102
G-1.4-40-30-20 [a]	1.400	14.1	45.6	2.5	2.5	1,159

Note: P_g = gravity lateral load (kN); P_p = peak lateral load (kN); δ_p = peak drift ratio (%); δ_u = ultimate drift ratio (%); k = initial stiffness (kN/m).

[a] Model validated by experimental testing

8.8. Conclusions

Based on the finite element analysis presented in this paper, the following conclusions can be drawn:

1. The lateral drift capacity of GFRP-RC edge connections subjected to gravity shear ratios between 0.2 and 0.8 satisfied the requirements of both CSA A23.3-19 (CSA 2019b) and ACI 318-19 (ACI 2019a) and were in good agreement with the model by El-Gendy and

El-Salakawy (2020c). On the other hand, CFRP-RC edge connections subjected to gravity shear ratios lower than 0.4 were only able to satisfy the requirements of ACI 318-19. Therefore, despite providing higher stiffness and lateral load capacity to the connections, CFRP reinforcement are not preferred for the construction of flat plates subjected to seismic loads.

2. The punching design model in CSA S806-12 (CSA 2017) provided conservative estimates for GFRP-RC and CFRP-RC connections subjected to different gravity shear ratios with a mean v_{FEM} / v_{CSA} of 1.23 ± 0.10 and 1.26 ± 0.14, respectively. On the other hand, the model by El-Gendy and El-Salakawy (2020c) produced a closer to unity mean v_{FEM} / $v_{E\text{-}E}$ of 1.06 ± 0.09 and 1.09 ± 0.12 for GFRP-RC and CFRP-RC connections, respectively.
3. Reducing the column side length perpendicular to the free edge by 50% (the lateral load applied to the weak axis), while maintaining the column area, did not affect the drift capacity of edge connections; however, it reduced their lateral load capacity by 30%. On the other hand, doubling this dimension (100% increase) reduced the drift capacity by 20%, while increasing the lateral load capacity by 32%.
4. Despite the enhancement of the stiffness and lateral load capacity, increasing the slab thickness of GFRP-RC connections without shear reinforcement substantially decreased their drift capacity. Connections with a slab thicker than 250 mm could not sustain the 1.5% drift ratio.
5. The GFRP-RC connections exhibited a size effect for slabs with an effective depth less than 300 mm. The connection with a 300-mm thick slab (effective depth of 260 mm) had an 8 and 25% lower punching strength than that predicted by CSA S806-12 (CSA 2017)

and the model by El-Gendy and El-Salakawy (2020c), respectively. This reduction was magnified for connections with 350 and 400-mm thick slabs.

6. Increasing the flexural reinforcement ratio improved the behavior of the connections. Increasing this ratio by 50% (from 0.70 to 1.05%) enhanced the lateral load capacity, drift capacity, and stiffness of the connection by 23, 25, and 39%, respectively.

CHAPTER 9. CONCLUSIONS AND FUTURE WORK

9.1. Summary

This pioneer research study investigated the seismic response of GFRP-RC slab-column edge connections. The study consisted of three phases: experimental, analytical and numerical. The experimental phase comprised the construction and testing of seven full-scale slab-column edge connections to study the effects of the gravity shear ratio (0.4, 0.5, and 0.6), the flexural reinforcement type (steel and GFRP) and ratio (0.7 and 1.4%), and the presence of different types of GFRP shear reinforcement (shear studs and corrugated bars) on the behaviour of such connections. Each specimen had slab dimensions of 3,300 × 3,100 × 200 mm with 300-mm wide square columns extending above and below the slab.

On the other hand, the analytical phase involved the assessment of current punching shear design models for FRP-RC slabs with and without shear reinforcement and the introduction of new universal models. Finally, the numerical phase included the construction and validation of a FEM to simulate the seismic behaviour of the FRP-RC edge connections using a commercial finite element software, ATENA-3D. This validated FEM was then used to conduct a parametric study to investigate the effect of several key parameters on the cyclic response of the connections. These parameters included a wide spectrum of gravity shear ratios, flexural reinforcement type, column aspect ratio, flexural reinforcement ratio, and slab thickness.

9.2. Conclusions

Based on the results of the results of the three phases, the following conclusions can be drawn:

9.2.1. Conclusions from the experimental phase

1. Glass fibre-reinforced polymer (GFRP) composite bars can be used as slab reinforcement in reinforced concrete slab-column edge connections subjected to simulated seismic loads. The large elastic deformations of GFRP bars resulting from the combination of their low modulus of elasticity and high ultimate strength can compensate for the absence of the yielding plateau of steel.
2. All connections without shear reinforcement failed in a brittle punching shear mode, regardless of the type of reinforcement and the gravity shear ratio. Nonetheless, increasing the applied gravity shear ratio resulted in a more brittle punching shear failure without sufficient amble warning.
3. Both steel-RC and GFRP-RC edge connections with the same flexural reinforcement ratio of 0.7% and subjected to the same gravity shear ratio of 0.4 experienced punching failure at drift ratios higher than the minimum 1.50%. However, while the steel-RC connection lost its lateral load capacity gradually before punching, the failure of the GFRP-RC connection was more brittle with a rapid drop in the lateral load capacity during the 2.5% drift ratio step.
4. The gravity shear ratio is a primary factor affecting the seismic response of GFRP-RC slab-column edge connections. Increasing the gravity shear ratio reduced the drift capacity, deformability, stiffness, energy dissipation, and lateral load capacity of the connections. The properly designed GFRP-RC edge connections with a flexural reinforcement ratio of 1.4% and without shear reinforcement were able to undergo or exceed the 1.50% drift ratio

suggested by Sozen (1980) before punching failure if the gravity shear ratio does not exceed 0.5. This value is higher than the 0.4 limit in ACI 318-19 (2019a) for steel-RC connections.

5. Doubling the GFRP reinforcement ratio from 0.7 to 1.4% allowed the connection to undergo slightly larger drifts and reduced the brittleness of the failure. In addition, it resulted in an enhancement of 45 and 42% in the deformability and initial stiffness of the connections. However, it did not significantly affect the stiffness degradation.
6. The residual reinforcement strain in the steel-RC connection after 1.00% drift ratio was 2.6 times higher than that in its GFRP-RC counterpart due to the permanent yielding of steel reinforcement. This demonstrates the considerable self-centering capabilities of the GFRP-RC connections. Therefore, such connections will sustain significantly less residual damage after surviving the seismic excitation.
7. Despite their relatively low transverse stiffness, the bottom GFRP slab reinforcement running through the column (integrity bars) held the slab after punching and prevented the entire collapse of the specimens.
8. When subjected to high gravity shear ratio of 0.6, GFRP-RC slab-column edge connections without shear reinforcement could not sustain 1.50% drift ratio before experiencing brittle punching failure.
9. The use of well-anchored GFRP shear reinforcement resulted in a substantial increase in the drift capacity and deformability of connections subjected to a high gravity shear ratio, which allowed them to sustain large seismically-induced deformations without jeopardizing their gravity load capacity.

10. The use of GFRP shear studs and corrugated bars in connections subjected to a high gravity shear ratio of 0.6 increased the lateral load capacity of the connections by 47 and 44%, respectively, and allowed the connections to undergo large inelastic deformations associated with 3.50 and 2.50% lateral inter-story drift ratio, respectively, without punching failure.
11. The higher stiffness and the superior anchorage of the shear studs compared to those of the corrugated bars allowed the connection with shear studs to exhibit 40 and 15% higher drift capacity and deformability, respectively, than the connection with corrugated bars.
12. The equivalent yield drift ratio concept can be used to assess the deformability of GFRP-RC slab-column connections. Both types of GFRP shear reinforcement substantially enhanced the deformability of the connections and allowed them to exceed the required level of deformability (Marzouk et al. 2001).
13. Both types of GFRP shear reinforcement enhanced the initial stiffness of the connections and resulted in a significantly lower rate of stiffness degradation and, in turn, higher stiffness at the same drift ratio.
14. For the connection with GFRP shear studs, extracted GFRP studs showed no signs of severe damage despite the significant concrete damage in the column vicinity. This suggests that the punching failure was triggered by the loss of confinement around the heads of the studs rather than the malfunction of the shear studs.
15. The design strain of GFRP shear stud reinforcement in slab-column connections should be limited to 3,000 με.

9.2.2. Conclusions from the analytical phase

1. The punching shear design model implemented in CSA S806-12 (CSA 2017) provided consistent, yet slightly conservative, predictions for both interior and edge FRP-RC connections with a mean v_{exp}/v_{pred} of 1.20 ± 0.22 and 1.21 ± 0.09, respectively. Similar trend was exhibited by the JSCE model (JSCE 1997). The ACI 440.1R-15 model (ACI 2015), on the other hand, highly underestimated the capacity of both interior and edge connections with a mean v_{exp}/v_{pred} of 2.18 ± 0.43 and 2.09 ± 0.18, respectively.
2. The early model proposed by Matthys and Taerwe (2000), which considers the critical section at 1.5*d* from the column face, provided better predictions than that of the CSA S806-12 model (CSA 2017) producing a mean v_{exp}/v_{pred} of 1.19 ± 0.18 and 1.05 ± 0.08 for interior and edge connections, respectively, with comparable R^2 values. Three empirical models from the literature (Ospina et al. 2003; El-Gamal et al. 2005; Hassan et al. 2017) failed to safely estimate the capacity of edge connections, despite reasonably predicting that of interior ones.
3. Two new models (Models P-I and P-II) were proposed by modifying the ones by El-Gamal et al. (2005) and Hassan et al. (2017) to account for the connection location and the confinement provided by the slab surrounding the critical section. These two models are universal models capable of accurately estimating the capacity of all connection types without and with shear reinforcement, respectively, regardless of the type of load. Nonetheless, they do not consider the effect of column rectangularity.
4. Model P-I slightly overestimated the capacity of edge connections with a mean v_{exp}/v_{pred} and R^2 of 0.95 ± 0.11 and 0.63, respectively. Model P-II, on the other hand, produced

reliable predictions for edge connections with a precise mean v_{exp}/v_{pred} of 1.02 ± 0.09 and R^2 of 0.73.

5. For shear-reinforced FRP-RC slabs, the model proposed by El-Gendy and El-Salakawy (2016) provided the most accurate estimates for both interior and edge connections with a mean v_{exp}/v_{pred} of 1.05 ± 0.13 and 0.97 ± 0.17, respectively, and R^2 of 0.96 and 0.79, respectively. This model, however, overestimated the capacity of connections subjected to cyclic loads with a mean v_{exp}/v_{pred} of 0.78 ± 0.08. Limiting the allowable strain in GFRP shear reinforcement to 3,000 με as recommended earlier enhanced this mean v_{exp}/v_{pred} to 1.04 ± 0.09 and improved the overall R^2 for GFRP-RC edge connections to 0.97.
6. Since GFRP-RC edge connections was able to safely satisfy and exceed the drift requirements of CSA A23.3-19 (CSA 2019b) and ACI 318-19 (2019a), a relaxed model was proposed to estimate the maximum inter-story drift ratio a GFRP-RC edge connection without shear reinforcement can withstand without punching failure.

9.2.3. Conclusions from the numerical phase

1. All GFRP-RC edge connections subjected to gravity shear ratio ranging between 0.2 and 0.8 satisfied the drift demands of both CSA A23.3-19 (CSA 2019b) and ACI 318-19 (ACI 2019a) and were in good agreement with the model proposed in the analytical phase. On the other hand, CFRP-RC edge connections subjected to gravity shear ratios lower than 0.4 were only able to satisfy the requirements of ACI 318-19. Therefore, despite providing higher stiffness and lateral load capacity to the connections, CFRP reinforcement are not preferred for the construction of flat plates subjected to seismic loads.

2. The punching shear design model proposed in the analytical phase (Model P-II) produced a close to unity mean v_{FEM} / $v_{E\text{-}E}$ of 1.06 ± 0.09 and 1.09 ± 0.12 for GFRP-RC and CFRP-RC connections subjected to different gravity shear ratios, respectively.
3. Reducing the column side length perpendicular to the free edge by 50% (the lateral load applied to the weak axis), while maintaining the column area, did not affect the drift capacity of edge connections; however, it reduced their lateral load capacity by 30%. On the other hand, doubling this dimension (100% increase) reduced the drift capacity by 20%, while increasing the lateral load capacity by 32%.
4. Despite the enhancement of the stiffness and lateral load capacity, increasing the slab thickness of GFRP-RC connections without shear reinforcement substantially decreased their drift capacity. Connections with a slab thicker than 250 mm could not sustain the 1.5% drift ratio.
5. The GFRP-RC connections exhibited a size effect for slabs with an effective depth less than 300 mm. The connection with a 300-mm thick slab (effective depth of 260 mm) had an 8 and 25% lower punching strength than that predicted by CSA S806-12 (CSA 2017) and the model proposed in the analytical phase (Model P-II), respectively. This reduction was magnified for connections with 350 and 400-mm thick slabs.
6. Increasing the flexural reinforcement ratio improved the behaviour of the connections. Increasing this ratio by 50% (from 0.70 to 1.05%) enhanced the lateral load capacity, drift capacity, and stiffness of the connection by 23, 25, and 39%, respectively.

9.3. Recommendations for Future Work

The findings of this research study present the cornerstone of future research investigating the seismic response of FRP-RC slab-column connections. Future studies are recommended to cover the following:

1. The connections in this study were subjected to uniaxial reversed-cyclic lateral load. During an earthquake, however, lateral loads are likely applied at multiple directions. Therefore, testing of GFRP-RC connections subjected to bi-axial reversed-cyclic lateral load is necessary to understand the behaviour of such connections when the cyclic lateral load is applied at multiple directions.
2. The connections in the experimental phase of this study had square columns. The conducted finite element analysis showed that column rectangularity significantly affects the behaviour of the connections. Experimental studies may be conducted to confirm these findings.
3. The connections in this study employed hooked flexural reinforcement to provide the required anchorage for the negative moment reinforcement perpendicular to the free edge. This may result in congested slabs in the column vicinity, especially when high flexural reinforcement ratios and shear reinforcement are implemented. Accordingly, experimental studies on FRP-RC edge connections employing headed-end bars as negative moment reinforcement perpendicular to the free edge is recommended.
4. Experimental studies on FRP-RC connections with different shear reinforcement types and configurations are recommended to demonstrate layout and extension of different shear reinforcement types in the column vicinity.

5. Since the slab area in the column vicinity is extremely congested in edge connections, the use of fibre-reinforced concrete in this area of the slab may be effective to enhance the behaviour of the connections and eliminate the need for shear reinforcement. Experimental studies are recommended to investigate this issue.
6. Experimental studies investigating the slab size effect on the punching behaviour of slab-column connections is recommended.
7. Experimental studies are needed to confirm the applicability of the proposed punching shear design models on slab-column connections with rectangular columns and thick slabs.

REFERENCES

ACI (American Concrete Institute). 2005a. *Building code requirements for structural concrete and commentary*. ACI 318, Farmington Hills, MI, ACI.

ACI (American Concrete Institute). 2005b. *Acceptance criteria for moment frames based on structural testing and commentary*. ACI 374.1, Farmington Hills, MI, ACI.

ACI (American Concrete Institute). 2010. *Guide to seismic design of punching shear reinforcement in flat plates*. ACI 421.2R, Farmington Hills, MI, ACI.

ACI (American Concrete Institute). 2011. *Guide for design of slab-column connections in monolithic concrete structures*. ACI 352.1R, Farmington Hills, MI, ACI.

ACI (American Concrete Institute). 2014a. *Building code requirements for structural concrete and commentary*. ACI 318, Farmington Hills, MI, ACI.

ACI (American Concrete Institute). 2014b. *Acceptance criteria for moment frames based on structural testing and commentary*. ACI 374.1 (R2014), Farmington Hills, MI, ACI.

ACI (American Concrete Institute). 2015. *Guide for the design and construction of structural concrete reinforced with fiber-reinforced polymer (FRP) bars*. ACI 440.1R, Farmington Hills, MI, ACI.

ACI (American Concrete Institute). 2019a. *Building code requirements for structural concrete and commentary*. ACI 318, Farmington Hills, MI, ACI.

ACI (American Concrete Institute). 2019b. *Acceptance criteria for moment frames based on structural testing and commentary*. ACI 374.1 (R2019), Farmington Hills, MI, ACI.

Afifi, M., Mohamed, H., Chaallal, O., and Benmokrane, B. 2015. "Confinement model for concrete columns internally confined with carbon FRP spirals and hoops." *J. Struct. Eng.*, ASCE, 141(9), 04014219.

AlAjarmeh, O., Manalo, A., Benmokrane, B., Karunasena, W., and Mendis, P. 2019. "Axial performance of hollow concrete columns reinforced with GFRP composite bars with different reinforcement ratios." *Compos. Struct.*, 213, 153–164.

Ali, M., and El-Salakawy, E. 2016. "Seismic performance of GFRP-reinforced concrete rectangular columns." *J. Compos. Constr.*, ASCE, 20(3), 04015074.

Alves, J., El-Ragaby, A., and El-Salakawy, E. 2011. "Durability of GFRP bars' bond to concrete under different loading and environmental conditions." *J. Compos. Constr.*, ASCE, 15(3), 249–262.

Anggadjaja, E., and Teng, S. 2008. "Edge-column slab connections under gravity and lateral loading." *ACI Struct. J.*, 105(5), 541–551.

Arafa, A., Farghaly, A., and Benmokrane, B. 2018. "Experimental behavior of GFRP-reinforced concrete squat walls subjected to simulated earthquake load." *J. Compos. Constr.*, ASCE, 22(2), 04018003.

ASCE-ACI Committee 426. 1974. "The shear strength of reinforced concrete members - slabs." *J. Struct. Div.*, ASCE, 100(8), 1543–1590.

ASTM. 2014. Standard test method for strength of fiber reinforced polymer (FRP) bent bars in bend locations. ASTM D7914/D7914M. West Conshohocken, PA, ASTM.

ASTM. 2016. Standard test method for tensile properties of fiber reinforced polymer matrix composite bars. ASTM D7205/D7205M. West Conshohocken, PA, ASTM.

ASTM. 2017. Standard test methods and definitions for mechanical testing of steel products. ASTM A370. West Conshohocken, PA, ASTM.

ASTM. 2019. Standard test methods and definitions for mechanical testing of steel products. ASTM A370. West Conshohocken, PA, ASTM.

Attia, K., El Refai, A., and Alnahhal, W. 2020. "Flexural behavior of basalt fiber–reinforced concrete slab strips with BFRP bars: experimental testing and numerical simulation." *J. Compos. Constr.*, 24(2), 04020007.

Awani, O., El-Maaddawy, T., and El Refai, A. 2016. "Numerical simulation and experimental testing of concrete beams strengthened in shear with fabric-reinforced cementitious matrix." *J. Compos. Constr.*, ASCE, 20(6), 04016056.

Banthia, N., Al-Asaly, M., and Ma, S. 1995. "Behavior of concrete slabs reinforced with fiber-reinforced plastic grid." *J. Mater. Civ. Eng.*, 7(4), 252–257.

Bazant, Z., and Cao, Z. 1987. "Size effect in punching shear failure of slabs." *ACI Struct. J.*, 84(1), 44–53.

Benmokrane, B., Tighiouart, B., and Chaallal, O. 1996. "Bond strength and load distribution of composite GFRP reinforcing bars in concrete." *ACI Mater. J.*, 93(3), 246–252.

Bentz, E., Massam, L., and Collins, M. 2010. "Shear strength of large concrete members with FRP reinforcement." *J. Compos. Constr.*, ASCE, 14(6), 637–646.

Berg, A., Bank, L., Oliva, M., and Russell, J. 2006. "Construction and cost analysis of an FRP reinforced concrete bridge deck." *Constr. Build. Mater.*, 20(8), 515-526.

Bigaj, A. 1999. *Structural dependence of rotation capacity of plastic hinges in RC beams and slabs*." PhD Thesis, Faculty of Civil Engineering, Delft University of Technology, Delft, Netherlands, 230 pp.

Broms, C. 2007. "Flat plates in seismic areas: comparison of shear reinforcement systems." *ACI Struct. J.*, 104(6), 712–721.

BSI (British Standards Institution). 1997. Structural use of concrete: part 1—code of practice for design and construction. BS8110, London, UK, BSI.

Canadian Consulting Engineer. 2008. "*Fatal parking garage roof collapse in Montreal*." Accessed on August 19, 2020. https://www.canadianconsultingengineer.com/engineering/fatal-parking-garage-roof-collapse-in-montreal/1000087799/.

Carpenter, J., Kaar, P., and Corley, W. 1973. "Design of ductile flat plate structures to resist earthquakes." *The 5th World Conf. on Earthquake Engineering,* Rome, Italy, International Association for Earthquake Engineering.

CEB (Comité Euro-International du Béton). 1993. *CEB-FIB Model Code 90*. London, UK, CEB.

Červenka, V., L. Jendele, and J. Červenka. 2018. *ATENA program documentation. 1: Theory*. Prague, Czech Republic, Cervenka Consulting.

Cheng, M., and Giduquio, M. 2014. "Experimental study of corner slab-column connection." *ACI Struct. J.,* 111(5), 1123–1134.

Cheng, M., Parra-Montesinos, G., and Shield, C. 2010. "Shear strength and drift capacity of fiber-reinforced concrete slab-column connections subjected to biaxial displacements." *J. Struct. Eng.*, ASCE, 136(9), 1078–1088.

Corley, G., and Hawkins, N. (1968). "Shearhead reinforcement for slabs." *ACI J. Proc.,* 65(10), 811-824.

Cosenza, E., Manfredi, G., and Realfonzo, R. 1997. "Behavior and modeling of bond of FRP rebars to concrete." *J. Compos. Constr.*, ASCE, 1(5), 40–51.

CSA (Canadian Standards Association). 2014a. *Design of concrete structures*. CSA/A23.3, Toronto, ON, CSA.

CSA (Canadian Standards Association). 2014b. Concrete materials and methods of concrete construction / Test methods and standard practices for concrete. CSA A23.1-14/A23.2, Toronto, ON, CSA.

CSA (Canadian Standards Association). 2015. *Specification for fibre-reinforced polymers*. CAN/CSA S807 (R2015), Toronto, ON, CSA.

CSA (Canadian Standards Association). 2017. *Design and construction of building structures with fibre-reinforced polymer*. CAN/CSA S806 (R2017), Toronto, ON, CSA.

CSA (Canadian Standards Association). 2019a. *Canadian highway bridge design code*. CAN/CSA S6-19, Toronto, ON, CSA.

CSA (Canadian Standards Association). 2019b. *Design of concrete structures*. CAN/CSA A23.3, Toronto, ON, CSA.

CSA (Canadian Standards Association). 2019c. Concrete materials and methods of concrete construction / Test methods and standard practices for concrete. CAN/CSA A23.1-14/A23.2, Toronto, ON, CSA.

CSA (Canadian Standards Association). 2019d. *Specification for fibre-reinforced polymers*. CAN/CSA S807, Toronto, ON, CSA.

CSA (Canadian Standards Association). 2019e. *Parking structures*. CAN/CSA 413 (R2019), Toronto, ON, CSA.

Drakatos, I., Muttoni, A., and Beyer, K. 2016. "Internal slab-column connections under monotonic and cyclic imposed rotations." *Eng. Struct.*, 123, 501–516.

Dilger, W., and Ghali, A. 1981. "Shear reinforcement for concrete slabs." *J. Struct. Div.*, ASCE, 107(12), 2403–2420.

Dilger, W., Dechka, D., and Brown, S. 2005. "Slab-column connections under seismic actions." *ACI Spec. Publ.*, 232, 127–146.

Dulude, C., Hassan, M., Ahmed, E, and Benmokrane, B. 2013. "Punching shear behavior of two-way flat concrete slabs reinforced with glass fiber-reinforced polymer bars," *ACI Struct. J.*, 110(5), 723-734.

Durrani, A., Du, Y., and Luo, Y. 1995. "Seismic resistance of nonductile slab-column connections in existing flat-slab buildings." *ACI Struct. J.*, 92(4), 479–487.

Eladawy, M., Hassan, M. and Benmokrane, B., 2019. "Experimental study of interior glass fiber-reinforced polymer-reinforced concrete slab-column connections under lateral cyclic load." *ACI Struct. J.*, 116(6), 165-180.

Eladawy, M., Hassan, M., Benmokrane, B. and Ferrier, E., 2020. "Lateral cyclic behavior of interior two-way concrete slab–column connections reinforced with GFRP bars." *Eng. Struct.*, 209, 109978.

El-Gamal, S., El-Salakawy, E., and Benmokrane, B. 2005. "Behavior of concrete bridge deck slabs reinforced with fiber-reinforced polymer bars under concentrated loads." *ACI Struct. J.*, 102(5), 727-735.

El-Gendy, M., and El-Salakawy, E. 2016. "Effect of shear studs and high moments on punching behavior of GFRP-RC slab–column edge connections." *J. Compos. Constr.*, ASCE, 20(4), 04016007.

El-Gendy, M., and El-Salakawy, E. 2018a. "Punching shear behavior of GFRP-RC slab-column edge connections." *ACI Spec. Publ.*, 322, 5.1-5.20.

El-Gendy, M., and El-Salakawy, E. 2018b. "Lateral displacement deformability of GFRP-RC slab-column edge connections." *ACI Spec. Publ.*, 327, 52.1–52.20.

El-Gendy, M., and El-Salakawy, E. 2019. “Effect of flexural reinforcement type and ratio on the punching behavior of RC slab-column edge connections subjected to reversed-cyclic lateral loads.” *Eng. Struct.*, 200, 109703.

El-Gendy, M., and El-Salakawy, E. 2020a. “GFRP shear reinforcement for slab-column edge connections subjected to reversed-cyclic lateral load.” *J. Compos. Constr.,* ASCE, 24(2), 04020003.

El-Gendy, M., and El-Salakawy, E. 2020b. “Gravity load effect on seismic response of glass fiber-reinforced polymer-reinforced concrete slab-column edge connections.” *ACI Struct. J.*, 117(5), https://doi.org/10.14359/51724665.

El-Gendy, M., and El-Salakawy, E. 2020c. “Assessment of punching shear design models for GFRP-RC slab-column connections." *J. Compos. Constr.*, ASCE, 24(5), 04020047.

El-Gendy, M., and El-Salakawy, E. Forthcoming. “Finite element analysis of GFRP-RC slab-column edge connections subjected to reversed-cyclic lateral load." *J. Compos. Constr.*, under review.

El-Ghandour, A., Pilakoutas, K., and Waldron, P. 2003. “Punching shear behavior of fiber reinforced polymers reinforced concrete flat slabs: Experimental study.” *J. Compos. Constr.*, ASCE, 7(3), 258–265.

El-Maaddawy, T., and Sherif, E. 2014. “Response of concrete corbels reinforced with internal steel rebars and external composite sheets: experimental testing and finite element modeling.” *J. Compos. Constr.*, ASCE, 18(1), 04013020.

El-Mogy, M., El-Ragaby, A., and El-Salakawy, E. 2013. “Experimental testing and finite element modeling on continuous concrete beams reinforced with fibre reinforced polymer bars and stirrups.” *Can. J. Civ. Eng.*, 40(11), 1091–1102.

Emam, M., Marzouk, H., and Hilal, M. 1997. “Seismic response of slab-column connections constructed with high-strength concrete.” *ACI Struct. J.*, 94(2), 197–205.

Gar, S., Mander, J., Head, M., and Hurlebaus, S. 2014. “FRP slab capacity using yield line theory.” *J. Compos. Constr.*, ASCE, 18(6), 04014021.

Ghali, A., Elmarsri, M., and Dilger, W. 1976. “Punching of flat plates under static and dynamic horizontal forces.” *ACI J. Proc.*, 73(10), 566–572.

Ghomi, S., and El-Salakawy, E. 2016. “Seismic performance of GFRP-RC exterior beam-column joints with lateral beams.” *J. Compos. Constr.*, ASCE, 20(1), 04015019.

Ghomi, S. and El-Salakawy, E. 2018. “Seismic behavior of exterior GFRP-RC beam–column connections: analytical study.” *J. Compos. Constr.*, ASCE, 22(4), 04018022.

Ghomi, S. and El-Salakawy, E. 2019. “Seismic behavior of GFRP-reinforced concrete interior beam–column–slab subassemblies.” *J. Compos. Constr.*, ASCE, 23(6), 04019047.

Giduquio, M., Cheng, M., and Dlamini, L. 2019. “Reexamination of strength and deformation of corner slab-column connection with varied slab reinforcement ratio.” *ACI Struct. J.*, 116(2), 53–63.

Gouda, A., and El-Salakawy, E. 2015. “Finite element modeling of GFRP-reinforced concrete interior slab-column connections subjected to moment transfer.” *Fibers*, 3(4), 411-431.

Gouda, A., and El-Salakawy, E. 2016a. “Punching shear strength of GFRP-RC interior slab-column connections subjected to moment transfer.” *J. Compos. Constr.*, ASCE, 20(1), 04015037.

Gouda, A., and El-Salakawy, E. 2016b. “Behavior of GFRP-RC interior slab-column connections with shear studs and high-moment transfer.” *J. Compos. Constr.*, ASCE, 20(4), 04016005.

Hao, Q., Wang, Y., He, Z., and Ou, J. 2009. "Bond strength of glass fiber reinforced polymer ribbed rebars in normal strength concrete." *Constr. Build. Mater.*, 23(2), 865–871.

Hasaballa, M., El-Ragaby, A., and El-Salakawy, E. 2011. "Seismic performance of exterior beam-column joints reinforced with glass fibre reinforced polymer bars and stirrups." *Can. J. Civ. Eng.*, 38(10), 1092–1102.

Hassanein, A., Mohamed, N., Farghaly, A., and Benmokrane, B. 2019. "Experimental investigation: New ductility-based force modification factor recommended for concrete shear walls reinforced with glass fiber-reinforced polymer bars." *ACI Struct. J.*, 116(1), 213–224.

Hassan, M., Ahmed, E., and Benmokrane, B. 2013a. "Punching-shear strength of normal- and high-strength two-way concrete slabs reinforced with GFRP bars," *J. Compos. Constr.*, ASCE, 17(6), 04013003.

Hassan, M., Ahmed, E., and Benmokrane, B. 2013b. "Punching-shear strength of GFRP-reinforced concrete flat slabs," *Can. J. Civ. Eng.*, 40(10), 951-960.

Hassan, M., Ahmed, E., and Benmokrane, B. 2014. "Punching-shear design equation for two-way concrete slabs reinforced with FRP bars and stirrups." *Constr. Build. Mater.*, 66, 522-532.

Hassan, M., Ahmed, E., and Benmokrane, B. 2015. "Punching shear behavior of two-way slabs reinforced with FRP shear reinforcement." *J. Compos. Constr.*, ASCE, 19(1), 04014030.

Hassan, M., Fam, A., Benmokrane, B., and Ferrier, E. 2017. "Effect of column size and reinforcement ratio on shear strength of glass fiber-reinforced polymer reinforced concrete two-way slabs." *ACI Struct. J.*, 114(4), 937-950.

Hawkins, N., Mitchell, D., and Sheu, M. 1974. Cyclic behavior of six reinforced concrete slab-column specimens transferring moment and shear. Progress Report on NSF Project GI-38717.

Hawkins, N., Mitchell, D., and Hanna, S. 1975. "The effects of shear reinforcement on the reversed cyclic loading behavior of flat plate structures." *Can. J. Civ. Eng.*, 2(4), 572–582.

Hossain, K., Ametrano, D., and Lachemi, M. 2014. "Bond strength of standard and high-modulus GFRP bars in high-strength concrete." *J. Mater. Civ. Eng.*, ASCE, 26(3), 449–456.

Hueste, M., and Wight, J. 1999. "Nonlinear punching shear failure model for interior slab-column connections." *J. Struct. Eng.*, ASCE, 125(9), 997–1008.

Hussein, A., and El-Salakawy, E. 2018. "Punching shear behavior of glass fiber-reinforced polymer–reinforced concrete slab-column interior connections." *ACI Struct. J.*, 115(4), 1075-1088.

Hwang, S., and Moehle, J. 2000. "Vertical and lateral load tests of nine-panel flat-plate frame." *ACI Struct. J.*, 97(1), 193–203.

Islam, S., and Park, R. 1976. "Tests on slab-column connections with shear and unbalanced flexure." *J. Struct. Div.*, ASCE, 102(3), 549–568.

JSCE (Japan Society of Civil Engineering). 1997. *Recommendation for design and construction of concrete structures using continuous fibre reinforcing materials*. Concrete Engineering Series 23, Tokyo, Japan, JSCE.

Kalfat, R., and Al-Mahaidi, R. 2014. "Numerical and experimental validation of FRP patch anchors used to improve the performance of FRP laminates bonded to concrete." *J. Compos. Constr.*, ASCE, 18(3), 04013008.

Kang, T., and Wallace, J. 2005. "Dynamic responses of flat plate systems with shear reinforcement." *ACI Struct. J.*, 102(5), 763–773.

Kani, G. 1967. "How safe are our large reinforced concrete beams?" *ACI J. Proc.*, 64(3), 128–141.

Lee, J., Yoon, Y., and Mitchell, D. 2009. "Improving punching shear behavior of glass fiber-reinforced polymer reinforced slabs," *ACI Struct. J.*, 106 (4), 427-434.

Lenschow, R., and Sozen, M. 1967. "A yield criterion for reinforced concrete slabs." *ACI J. Proc.*, 64(5), 266–273.

Li, R., Cho, Y., and Zhang, S. 2007. "Punching shear behavior of concrete flat plate slab reinforced with carbon fiber reinforced polymer rods." *Composites Part B*, 38(5), 712–719.

Mady, M., El-Ragaby, A., and El-Salakawy, E. (2011). "Seismic behavior of beam-column joints reinforced with GFRP bars and stirrups." *J. Compos. Constr.*, ASCE, 15(6), 875–886.

Mahmoud, K., and El-Salakawy, E. 2016. "Effect of transverse reinforcement ratio on the shear strength of GFRP-RC continuous beams." *J. Compos. Constr.*, ASCE, 20(1), 04015023.

Marzouk, H., Osman, M., and Hussein, A. 2001. "Cyclic loading of high-strength lightweight concrete slabs." *ACI Struct. J.*, 98(2), 207–214.

Masmoudi, R., Masmoudi, A., Ouezdou, M., and Daoud, A. (2011). "Long-term bond performance of GFRP bars in concrete under temperature ranging from 20°C to 80°C." *Constr. Build. Mater.*, 25(2), 486–493.

Matzke, E., Lequesne, R., Parra-Montesinos, G., and Shield, C. 2015. "Behavior of biaxially loaded slab-column connections with shear studs." *ACI Struct. J.*, 112(3), 335–346.

Matthys, S., and Taerwe, L. 2000. "Concrete slabs reinforced with FRP grids. II: punching resistance." *J. Compos. Constr.,* ASCE, 4(3), 154-161.

Megally, S. 1998. *Punching shear resistance of concrete slabs to gravity and earthquake forces*. PhD Thesis, Department of Civil Engineering, University of Calgary, Calgary, AB, 501 pp.

Megally, S., and Ghali, A. 1994. "Design considerations for slab-column connections in seismic zones." *ACI Struct. J.*, 91(3), 303–314.

Megally, S., and Ghali, A. 2000a. "Seismic behavior of edge column-slab connections with stud shear reinforcement." *ACI Struct. J.*, 97(1), 53–60.

Megally, S., and Ghali, A. 2000b. "Punching shear design of earthquake-resistant slab-column connections." *ACI Struct. J.*, 97(5), 720–730.

Megally, S., and Ghali, A. 2000c. "Seismic behavior of slab-column connections." *Can. J. Civ. Eng.*, 27(1), 84–100.

Menegotto, M., and Pinto, P. 1973. "Method of analysis for cyclically loaded reinforced concrete plane frames including changes in geometry and non-elastic behavior of elements under combined normal force and bending," *IABSE Symposium*, Lisbon, Spain, 15–22.

Menétrey, P., and Willam, K. 1995. "Triaxial failure criterion for concrete and its generalization." *ACI Struct. J.*, 92(3), 311-318.

Mitchell, D., Tinawi, R., and Redwood, R. 1990. "Damage to buildings due to the 1989 Loma Prieta earthquake – a Canadian code perspective." *Can. J. Civ. Eng.*, 17(5), 813–834.

Moehle, J. 1996. "Seismic design considerations for flat-plate construction." *ACI Spec. Publ.*, 162(1), 1–34.

Mohamed, N., Farghaly, A., Benmokrane, B., and Neale, K. 2014. "Experimental investigation of concrete shear walls reinforced with glass fiber–reinforced bars under lateral cyclic loading." *J. Compos. Constr.*, ASCE, 18(3), A4014001.

Mokhtar, A., Ghali, A., and Dilger, W. 1985. "Stud shear reinforcement for flat concrete plates." *ACI J. Proc.*, 82(5), 676–683.

Mortin, J., and Ghali, A. 1991. "Connection of flat plates to edge columns." *ACI Struct. J.*, 88(2), 191–198.

Mostafa, A., and El-Salakawy, E. 2018. "Behavior of GFRP-RC slab-column edge connections with high-strength concrete and shear reinforcement." *J. Compos. Constr.*, ASCE, 22(2), 04018001.

Naqvi, S., and El-Salakawy, E. 2017. "Lap splice in GFRP-RC rectangular columns subjected to cyclic-reversed loads." *J. Compos. Constr.*, ASCE, 21(4), 04016117.

Neville, A. 1995. "Chloride attack of reinforced concrete: an overview." *Mater. Struct.*, 28(63).

Nguyen-Minh, L., and Rovňák, M. 2013. "Punching-shear resistance of interior GFRP reinforced slab-column connection," *J. Compos. Constr.*, ASCE, 17(1), 2–13.

NRCC (National Research Council of Canada). 1995. *National building code of Canada*. NBCC 1995, Ottawa, ON.

NRCC (National Research Council of Canada). 2015. *National building code of Canada*. NBCC 2015, Ottawa, ON.

Ospina, C., Alexander, S., and Cheng, J. 2003. "Punching of two-way concrete slabs with fiber-reinforced polymer reinforcing bars or grids." *ACI Struct. J.*, 100 (5), 589-598.

Pan, A., and Moehle, J. 1989. "Lateral displacement ductility of reinforced concrete flat plates." *ACI Struct. J.*, 86(3), 250–258.

Pan, A., and Moehle, J. 1992. "An experimental study of slab-column connections." *ACI Struct. J.*, 89, 626–638.

Polak, M., El-Salakawy, E., and Hammill, N. 2005. "Shear reinforcement for concrete flat slabs." *ACI Spec. Publ.*, 232, 75–96.

Rha, C., Kang, T., Shin, M., and Yoon, J. 2014. "Gravity and lateral load-carrying capacities of reinforced concrete flat plate systems." *ACI Struct. J.*, 111(4), 753–764.

Rizk, E., Marzouk, H. and Hussein, A. 2011. "Punching shear of thick plates with and without shear reinforcement." *ACI Struct. J.*, 108(5), 581–591.

Robertson, I., and Durrani, A. 1991. "Gravity load effect on seismic behavior of exterior slab-column connections." *ACI Struct. J.*, 88(3), 255–267.

Robertson, I., and Durrani, A. 1992. "Gravity load effect on seismic behavior of interior slab-column connections." *ACI Struct. J.*, 89(1), 37–45.

Robertson, I., and Johnson, G. 2006. "Cyclic lateral loading of nonductile slab-column connections." *ACI Struct. J.*, 103(3), 356–364.

Robertson, I., Kawai, T., Lee, J., and Enomoto, B. 2002. "Cyclic testing of slab-column connections with shear reinforcement." *ACI Struct. J.*, 99(5), 605–613.

Salama, A., Hassan, M., and Benmokrane, B. 2019. "Effectiveness of glass fiber-reinforced polymer stirrups as shear reinforcement in glass fiber-reinforced polymer-reinforced concrete edge slab-column connections." *ACI Struct. J.*, 116(5), 97-112.

Salama, A., Hassan, M., and Benmokrane, B. 2020. "Effect of GFRP shear stirrups on strength of two-way GFRP RC edge slabs: experimental and finite-element investigations." *J. Struct. Eng.*, ASCE, 146(5), 04020056.

Saleh, H., Kalfat, R., Abdouka, K., and Al-Mahaidi, R. 2018. "Experimental and numerical study into the punching shear strengthening of RC flat slabs using post-installed steel bolts." *Constr. Build. Mater.*, 188, 28-39.

Sharbatdar, M., and Saatcioglu, M. 2009. "Seismic design of FRP reinforced concrete structures." *Asian Journal of Applied Sciences*, 2(3), 211–222.

Sozen, M. 1980. “Review of earthquake response of R.C. buildings with a view to drift control.” *7th World Conf. on Earthquake Engineering*, Rome, Italy, International Association for Earthquake Engineering.

Stark, A., Binici, B., and Bayrak, O. 2005. “Seismic upgrade of reinforced concrete slab-column connections using carbon fiber-reinforced polymers.” *ACI Struct. J.*, 102(2), 324–333.

Stein, T., Ghali, A., and Dilger, W. 2007. “Distinction between punching and flexural failure modes of flat plates.” *ACI Struct. J.*, 104(3), 357–365.

Swamy, R., and Ali, S. 1982. “Punching shear behavior of reinforced slab-column connections made with steel fiber concrete.” *ACI J. Proc.*, 79(5), 392–406.

Tavassoli, A., Liu, J., and Sheikh, S. 2015. “Glass fiber-reinforced polymer-reinforced circular columns under simulated seismic loads.” *ACI Struct. J.*, 112(1), 103–114.

Teng, S., Cheong, H., Kuang, K., and Geng, J. 2004. “Punching shear strength of slabs with openings and supported on rectangular columns.” *ACI Strut. J.*, 101(5), 678–687.

Van Mier, J. 1986. “Multiaxial strain-softening of concrete.” *Mater. Strut.*, 19, 179–190.

Vecchio, F., and Collins, M. 1986. “Modified compression-field theory for reinforced concrete beams subjected to shear.” *ACI J. Proc.*, 83(2), 219–231.

Wey, E., and Durrani, A. 1992. “Seismic response of interior slab-column connections with shear capitals.” *ACI Struct. J.*, 89(6), 682–691.

Wight, J., and MacGregor, J. 2011. *Reinforced concrete: Mechanics and design*. Prentice Hall, 1177 pp.

Younis, A., Ebead, U., and Judd, S. 2018. “Life cycle cost analysis of structural concrete using seawater, recycled concrete aggregate, and GFRP reinforcement.” *Constr. Build. Mater.*, 175(4), 152-160.

Zaghloul, A. 2007. “Punching shear strength of interior and edge column-slab connections in CFRP reinforced flat plate structures transferring shear and moment.” Ph.D. thesis, Dept. of Civil and Environmental Engineering, Carleton Univ., Ottawa, ON, Canada, 400 p.

Zee, H., and Moehle, J. 1984. Behavior of interior and exterior flat plate connections subjected to inelastic load reversals. Report No. UCB/EERC-84/07, Berkeley, USA.

APPENDIX A

Flexural Design of a Steel-RC Flat Plate System (Parking Garage)

A.1. Layout of the Flat Plate System

The dimensions and reinforcement ratios of the connections were defined by performing an elastic analysis of a typical parking garage system consisting of three 5.5 m-long square bays in both directions. The analysis was carried out according to the Direct Design Method as described in the CSA A23.3-19 (CSA 2019b) and CSA S806-12 (CSA 2017) standards, when applicable. Two orthogonal strips were designed: a strip in the direction perpendicular to the free edge and another one in the direction parallel to the free edge as shown in Figure A.1 and A.2.

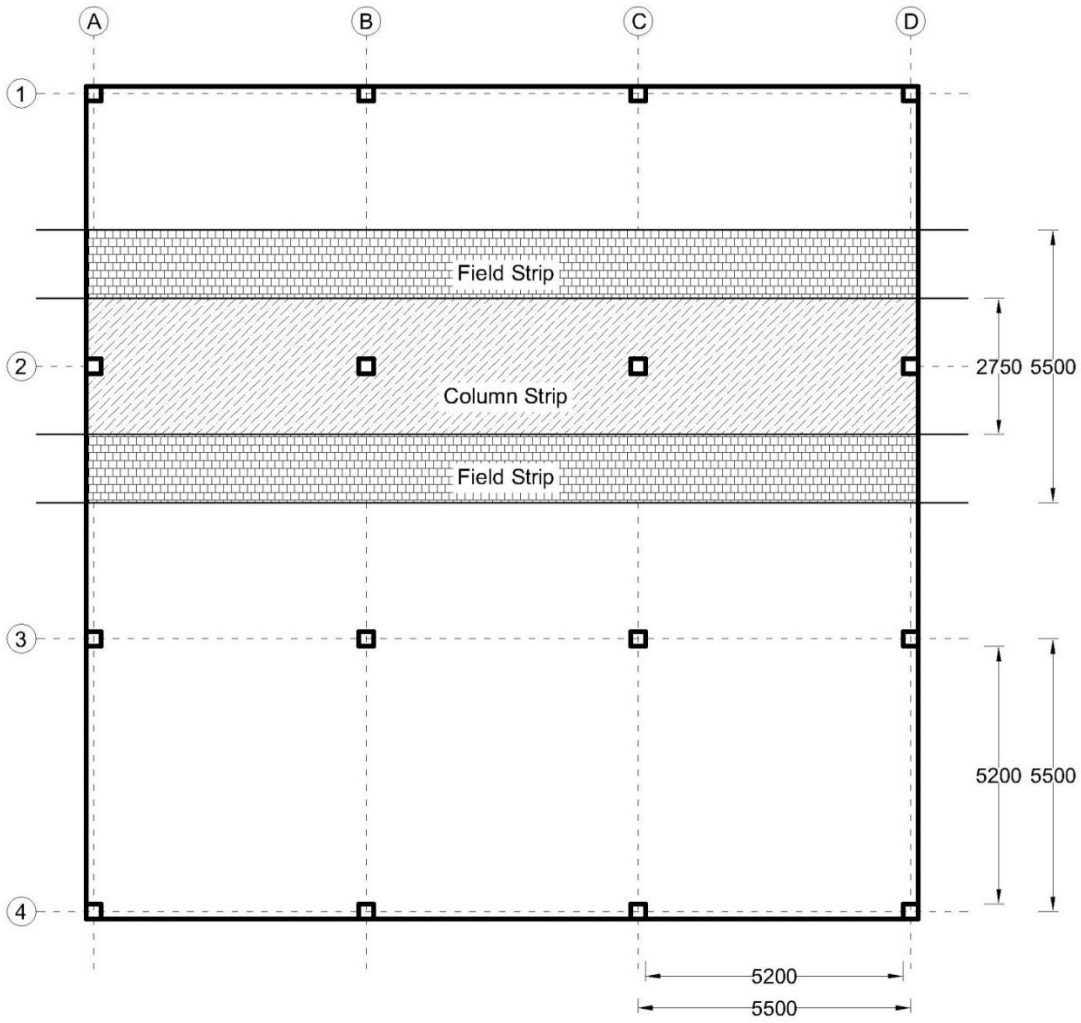

Figure A.1: Design strip perpendicular to free edge

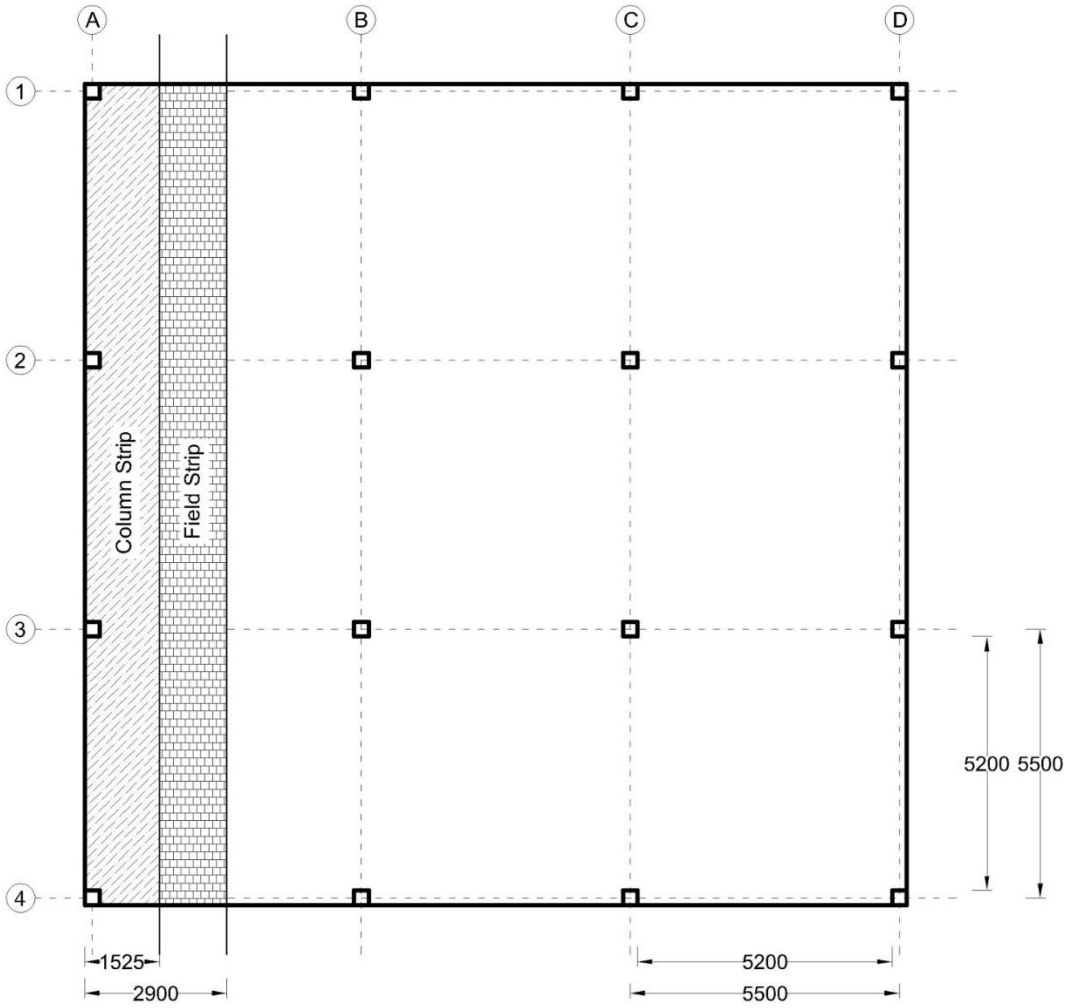

Figure A.2: Design strip parallel to free edge

A.2. Properties of Concrete

Compressive strength of concrete $f_c^{'} = 40$ MPa

Material resistance factor $\phi_c = 1.0$

Modulus of elasticity $E_c = 4500\sqrt{f_c^{'}} = 4,500\sqrt{40} = 28,460$ MPa

8.6.2.3 (A23.3-19)

Ultimate compressive strain for concrete ε_{cu} = 0.0035 **10.1.3 (A23.3-19)**

$\alpha_1 = 0.85 - 0.0015 f_c^{'} = 0.85 - 0.0015 \times 40 = 0.79$ **10.1.7 (A23.3-19)**

$\beta_1 = 0.97 - 0.0025 f_c^{'} = 0.97 - 0.0025 \times 40 = 0.87$ **10.1.7 (A23.3-19)**

A.3. Properties of Reinforcement

Use No. 15M bars d_b = 16 mm A_b = 200 mm^2

Yield strength of steel f_y = 400 MPa

Material resistance factor $\phi_s = 1.0$

Yield strain for steel ε_y = 0.002

A.4. Loads

$w_{ll} = 2.4$ kN/m^2 **4.1.5.3 (NRCC 2015)**

$w_{dl} = \text{self-weight} + \text{partition allowance} = 24 \times 0.2 + 1.0 = 5.8$ kN/m^2 **4.1.4.1 (NRCC 2015)**

$w_f = 1.4 w_{dl} = 1.4 \times 5.8 = 8.12$ kN/m^2

$= 1.25 w_{dl} + 1.5 w_{ll} = 1.25 \times 5.8 + 1.5 \times 2.4 = 7.25 + 3.6 = 10.85$ kN/m^2

4.1.3.2 (NRCC 2015)

Specified load $w_s = w_{dl} + w_{ll} = 5.8 + 2.4 = 8.2$ kN/m^2 **4.1.3.4 (NRCC 2015)**

A.5. Design Moments in the Perpendicular Strip

A.5.1. Factored moments

$$M_o = \frac{w_f \times l_{2a} \times l_n^2}{8} = \frac{10.85 \times 5.5 \times 5.2^2}{8} = 201.7 \text{ kN.m}$$ **13.9.2 (A23.3-19)**

This moment should be distributed as listed in Table A.1.

Table A.1: Factored moment distribution in a perpendicular design strip

Axis	A			B		C	Units	Code Article (A23.3-19)
l_n	5200			5200				
M_{Design}	26	52	70	65	35	65	%	13.9.3
	52	105	141	131	71	131	kN.m	
$M_{Col.Strp.}$	100	55-65	70-90	70-90	55-65	70-90	%	13.11.2
	52	58-68	99-127	92-118	39-46	92-118	kN.m	
$M_{Fld.Strp.}$	0	45-35	30-10	30-10	45-35	30-10	%	13.11.2
	0	**47**-37	42-14	39-13	32-25	39-13	kN.m	

A.5.2. Unfactored moments

$$M_s = \frac{w_s \times l_{2a} \times l_n^2}{8} = \frac{8.2 \times 5.5 \times 5.2^2}{8} = 152.4 \text{ kN.m}$$ **13.9.2 (A23.3-19)**

This moment should be distributed as listed in Table A.2.

Table A.2: Unfactored moment distribution in a perpendicular design strip

Axis	A			B		C	Units	Code Article (A23.3-19)
l_n	5200			5200				
M_{Design}	26	52	70	65	35	65	%	13.9.3
	40	79	107	99	53	99	kN.m	
$M_{Col.Strp.}$	100	55-65	70-90	70-90	55-65	70-90	%	13.11.2
	40	43-51	75-96	69-89	29-34	69-89	kN.m	
$M_{Fld.Strp.}$	0	45-35	30-10	30-10	45-35	30-10	%	13.11.2
	0	**36**-28	32-11	30-10	14-19	30-10	kN.m	

A.6. Design Moments in the Parallel Strip

A.6.1. Factored moments

$$M_o = \frac{w_f \times l_{2a} \times l_n^2}{8} = \frac{10.85 \times 2.9 \times 5.2^2}{8} = 106.4 \text{ kN.m}$$ **13.9.2 (A23.3-19)**

This moment should be distributed as listed in Table A.3.

Table A.3: Factored moment distribution in a parallel design strip

Axis	A			B		C	Units	Code Article (A23.3-19)
l_n	5200			5200				
M_{Design}	26	52	70	65	35	65	%	13.9.3
	28	55	74	69	37	69	kN.m	
$M_{Col.Strp.}$	100	55-65	70-90	70-90	55-65	70-90	%	13.11.2
	28	30-36	**52**-67	48-62	20-24	48-62	kN.m	
$M_{Fld.Strp.}$	0	45-35	30-10	30-10	45-35	30-10	%	13.11.2
	0	**25**-19	**22**-7	21-7	17-13	21-7	kN.m	

A.6.2. Unfactored moments

$$M_s = \frac{w_s \times l_{2a} \times l_n^2}{8} = \frac{8.2 \times 2.9 \times 5.2^2}{8} = 80.4 \text{ kN.m}$$ **13.9.2 (A23.3-19)**

This moment should be distributed as listed in Table A.4.

Table A.4: Unfactored moment distribution in a parallel design strip

Axis	A			B		C	Units	Code Article (A23.3-19)
l_n	5200			5200				
M_{Design}	26	52	70	65	35	65	%	13.9.3
	21	42	56	52	28	52	kN.m	
$M_{Col.Strp.}$	100	55-65	70-90	70-90	55-65	70-90	%	13.11.2
	21	23-27	39-50	36-47	15-18	36-47	kN.m	
$M_{Fld.Strp.}$	0	45-35	30-10	30-10	45-35	30-10	%	13.11.2
	0	**19**-15	17-6	16-5	13-10	16-5	kN.m	

A.7. Slab Thickness, h_s

Minimum slab thickness, $h_s = 1.1 \times \frac{l_n(0.6 + f_y/1000)}{30}$ **13.2.3 (A23.3-19)**

$$\rightarrow h_s = 1.1 \times \frac{5200 \times (0.6 + 400/1000)}{30} = 191 \text{mm}$$

Take h_s = 200 mm

A.8. Design of Negative Moment Section (Perpendicular Strip)

$d = h - \text{clear cover} - d_b/2 = 200 - 24 - 16/2 = 168 \text{ mm}$

A.8.1. For the band width, b_b:

A.8.1.1. Flexural design

$M_{Design} = 52 \text{ kN.m}$

Reinforcement for the total factored negative moment transferred to the exterior columns shall be placed within a band width $b_b = \text{column width} + 3h_s$. **13.10.3 (A23.3-19)**

$b_b = \text{column width} + 3h_s = 300 + 3 \times 200 = 900 \text{ mm}$

$$a = \frac{\phi_s A_s f_y}{\alpha_1 \phi_c f_c' b} = \frac{1.0 \times A_s \times 400}{0.79 \times 1.0 \times 40 \times 900} = 14.06 \times 10^{-3} A_s$$

$$M_r = \phi_s A_s f_y \times (d - a/2)$$

$$\rightarrow 52 \times 10^6 = 1.0 \times A_s \times 400 \times \left(168 - \left(14.06 \times 10^{-3} A_s\right)/2\right)$$

$$\rightarrow 2.81 A_s^2 - 67,200 A_s + 52 \times 10^6 = 0$$

$$\rightarrow A_s = 801 \text{ mm}^2$$

$$A_s = \frac{b_b}{s} A_b$$

$$\rightarrow s = \frac{b_b}{A_s} A_b = \frac{900}{801} \times 200 = 224 \text{ mm}$$ Use 15M @ 190 mm c/c

$$\rightarrow A_{s,act} = \frac{b_b}{s} A_b = \frac{900}{190} \times 200 = 947 \text{ mm}^2$$

Check for the Balanced Reinforcement Ratio, ρ_b :

$$\rho = \frac{A_{s,act}}{b_b d} = \frac{947}{900 \times 168} = 0.63\%$$

$$\rho_b = \alpha_1 \beta_1 \frac{\phi_c f_c^{'}}{\phi_s f_y} \times \frac{\varepsilon_{cu}}{\varepsilon_{cu} + \varepsilon_y} = 0.79 \times 0.87 \times \frac{1.0 \times 40}{1.0 \times 400} \times \frac{0.0035}{0.0035 \times 0.002} = 4.37\%$$

$\rho < \rho_b$ Under-reinforced, Ok

A.8.1.2. Serviceability check

Service moment at the edge connection = 40 kN.m

$$n = \frac{E_s}{E_c} = \frac{200,000}{28,460} = 7.03$$

$$k = \sqrt{2\rho n + (\rho n)^2} - \rho n$$

$$k = \sqrt{2 \times 0.0063 \times 7.03 + (0.0063 \times 7.03)^2} - 0.0063 \times 7.03 = 0.256$$

$$j = 1 - k/3 = 1 - 0.256/3 = 0.915$$

Service stress $f_s = \frac{M_s}{A_s jd} = \frac{40 \times 10^6}{947 \times 0.915 \times 168} = 275$ MPa

Crack control parameter, *z*: **10.6.1 (A23.3-19)**

$$d_c = h_s - d = 200 - 168 = 32 \text{ mm}$$

$$A = 2 \times s \times d_c = 2 \times 190 \times 32 = 12,160 \text{ mm}$$

$$z = f_s \sqrt[3]{d_c A} = 275 \times \sqrt[3]{32 \times 12,160} = 20,077 \text{ N/mm} < 25000 \text{ N/mm}$$

A.8.1.3. Development length, l_d **12.2 (A23.3-19)**

$$l_d = 0.45 k_1 k_2 k_3 k_4 \frac{f_y}{\sqrt{f_c'}} d_b$$ **12.2.3 (A23.3-19)**

$k_1 = 1.0$ for horizontal reinforcement placed in such a way that less than 300 mm of fresh concrete is cast in the member below the development length

$k_2 = 1.0$ for uncoated reinforcement

$k_3 = 1.0$ for normal density concrete

$k_4 = 0.8$ for 20M and smaller bars

$$\rightarrow l_d = 0.45 \times 1.0 \times 1.0 \times 1.0 \times 0.8 \times \frac{400}{\sqrt{40}} \times 16 = 364 \text{ mm} > 280 \text{ mm}$$

Use hooked bars:

$$l_{dh} = 0.7 \times \left(100 \frac{d_b}{\sqrt{f_c'}} \right) = 0.7 \times \left(100 \times \frac{16}{\sqrt{40}} \right) = 177 \text{ mm} < 280 \text{ mm}$$ **12.5 (A23.3-19)**

A.8.2. For the rest of the column strip:

Use minimum reinforcement, $A_{s,min}$ **13.10.9 (A23.3-19)**

$$A_{s,\min} = 0.002 A_g = 0.002 \times (200 \times 1000) = 400 \text{ mm}^2/\text{m}$$ **7.8.1 (A23.3-19)**

$$s = \frac{b}{A_{s,\min}} A_b = \frac{1000}{400} \times 200 = 500 \text{ mm}$$ Use 15M @ 500 mm

Maximum spacing $s_{max} = 3h_s = 3 \times 200 = 600$ mm

or $= 500$ mm **13.10.4 (A23.3-19)**

Summary:

- Use **15M @ 190 mm c/c** in a 900-mm wide wand centred on the column.
- Use **15M @ 500 mm c/c** for the rest of the strip.

A.9. Design of Negative Moment Section (Parallel Strip)

$$d = h - \text{clear cover} - d_b - d_b/2 = 200 - 24 - 16 - 16/2 = 152 \text{ mm}$$

A.9.1. For the band width, b_b:

A.9.1.1. Flexural design

Design moment for the entire design strip, $M_{Design} = 74$ kN.m

At interior columns, the band width, b_b, shall be designed to resist at least one-third of the total factored negative moment in the entire design strip. **13.11.2.7 (A23.3-19)**

$$b_b = \text{column width} + 1.5h_s = 300 + 1.5 \times 200 = 600 \text{ mm}$$

$$a = \frac{\phi_s A_s f_y}{\alpha_1 \phi_c f_c' b} = \frac{1.0 \times A_s \times 400}{0.79 \times 1.0 \times 40 \times 600} = 21.1 \times 10^{-3} A_s$$

$$M_r = \phi_s A_s f_y \times (d - a/2)$$

$$\rightarrow \frac{74 \times 10^6}{3} = 1.0 \times A_s \times 400 \times \left(152 - \left(21.1 \times 10^{-3} A_s\right)/2\right)$$

$$\rightarrow 4.22 A_s^2 - 60,800 A_s + 24.7 \times 10^6 = 0$$

$$\rightarrow A_s = 418 \text{ mm}^2$$

$$A_s = \frac{b_b}{s} A_b$$

$$\rightarrow s = \frac{b_b}{A_s} A_b = \frac{600}{418} \times 200 = 287 \text{ mm}$$ Use 15M @ 285 mm c/c

$$\rightarrow A_{s,act} = \frac{b_b}{s} A_b = \frac{600}{285} \times 200 = 421 \text{ mm}^2$$

Check for the balanced reinforcement ratio, ρ_b :

$$\rho = \frac{A_{s,act}}{b_b d} = \frac{421}{600 \times 152} = 0.46\%$$

$$\rho_b = 4.37\%$$

$\rho < \rho_b$ Under-reinforced, Ok

Check for the Unbalanced Moment, M_{unb}:

$$M_{unb} = 0.07\left[\left(w_{df} + 0.5w_{lf}\right) l_{2a} l_n^2 - w_{df}^{'} l_{2a}^{'} \left(l_n^{'}\right)^2\right]$$

$$M_{unb} = 0.07\left[\left(7.25 + 0.5 \times 3.6\right) \times 2.9 \times 5.2^2 - 7.25 \times 2.9 \times 5.2^2\right] = 9.9 \text{ kN.m}$$ **13.9.4 (A23.3-19)**

The fraction to be carried by flexure within width b_b is γ_f **13.10.2 (A23.3-19)**

$$\gamma_f = \frac{1}{1 + \frac{2}{3}\sqrt{\frac{b_1}{b_2}}} = \frac{1}{1 + \frac{2}{3}\sqrt{\frac{376}{452}}} = 0.62$$ **13.3.5.3 (A23.3-19)**

$\gamma_f M_{unb} = 0.62 \times 9.9 = 6.1 \text{ kN.m} < M_r = 24.7 \text{ kN.m}$ OK

A.9.1.2. Serviceability check

Service moment at the interior connection $= \frac{0.7M_s}{3} = \frac{0.7 \times 80.4}{3} = 18.8 \text{ kN.m}$

13.10.3 (A23.3-19)

$n = 7.03$

$\rho = 0.46\%$

$k = \sqrt{2\rho n + (\rho n)^2} - \rho n$

$k = \sqrt{2 \times 0.0046 \times 7.03 + (0.0046 \times 7.03)^2} - 0.0046 \times 7.03 = 0.224$

$j = 1 - k/3 = 1 - 0.224/3 = 0.925$

Service stress $f_s = \dfrac{M_s}{A_s jd} = \dfrac{18.8 \times 10^6}{421 \times 0.925 \times 152} = 315$ MPa

Crack control parameter, *z*: **10.6.1 (A23.3-19)**

$d_c = h_s - d = 200 - 152 = 48$ mm

$A = 2 \times s \times d_c = 2 \times 285 \times 48 = 27,360$ mm

$z = f_s \sqrt[3]{d_c A} = 315 \times \sqrt[3]{48 \times 27,360} = 34,496$ N/mm > 25000 N/mm

Try 15M@195 mm

$A_{s,act} = \dfrac{b_b}{s} A_b = \dfrac{600}{195} \times 200 = 615$ mm^2

$\rho = \dfrac{A_{s,act}}{b_b d} = \dfrac{615}{600 \times 152} = 0.67\%$

$k = \sqrt{2 \times 0.0067 \times 7.03 + (0.0067 \times 7.03)^2} - 0.0067 \times 7.03 = 0.264$

$j = 1 - k/3 = 1 - 0.264/3 = 0.912$

$$f_s = \frac{M_s}{A_s jd} = \frac{18.8\times10^6}{615\times0.912\times152} = 219 \text{ MPa}$$

$$A = 2\times s\times d_c = 2\times195\times46 = 18,720 \text{ mm}$$

$$z = f_s\sqrt[3]{d_c A} = 219\times\sqrt[3]{48\times18,720} = 21,133 \text{ N/mm} < 25000 \text{ N/mm}$$

A.9.1.3. Development length, l_d **12.2 (A23.3-19)**

$$l_d = 0.45k_1k_2k_3k_4\frac{f_y}{\sqrt{f_c'}}d_b$$ **12.2.3 (A23.3-19)**

$k_1 = 1.0$ for horizontal reinforcement placed in such a way that less than 300 mm of fresh concrete is cast in the member below the development length

$k_2 = 1.0$ for uncoated reinforcement

$k_3 = 1.0$ for normal density concrete

$k_4 = 0.8$ for 20M and smaller bars

$$\rightarrow l_d = 0.45\times1.0\times1.0\times1.0\times0.8\times\frac{400}{\sqrt{40}}\times16 = 364 \text{ mm}$$

A.9.2. For the rest of the column strip:

A.9.2.1. Flexural design

$$b = 1525 - 600 = 925 \text{ mm}$$

$$M = 0.7\times74 - \frac{74}{3} = 27 \text{ kN.m}$$

$$a = \frac{\phi_s A_s f_y}{\alpha_1\phi_c f_c' b} = \frac{1.0\times A_s\times400}{0.79\times1.0\times40\times925} = 13.68\times10^{-3}A_s$$

$$M_r = \phi_s A_s f_y \times (d - a/2)$$

$$\rightarrow 27\times10^6 = 1.0\times A_s \times 400\times\left(152-\left(13.68\times10^{-3}A_s\right)/2\right)$$

$$\rightarrow 2.74A_s^2 - 60{,}800A_s + 27\times10^6 = 0$$

$$\rightarrow A_s = 459 \text{ mm}^2$$

$$A_s = \frac{b}{s}A_b$$

$$\rightarrow s = \frac{b}{A_s}A_b = \frac{925}{459}\times200 = 403 \text{ mm}$$ Use 15M @ 400 mm c/c

$$\rightarrow A_{s,act} = \frac{b}{s}A_b = \frac{925}{400}\times200 = 463 \text{ mm}^2$$

$$\rho = \frac{A_{s,act}}{bd} = \frac{463}{925\times152} = 0.33\%$$

A.9.2.2. Serviceability check

Service moment at the interior connection: **13.10.3 (A23.3-19)**

$$= 0.7\times(0.7M_s) - \frac{0.7M_s}{3} = 0.7\times(0.7\times80.4) - \frac{0.7\times80.4}{3} = 20.6 \text{ kN.m}$$

$$n = 7.03$$

$$k = \sqrt{2\rho n + (\rho n)^2} - \rho n$$

$$k = \sqrt{2\times0.0033\times7.03 + (0.0033\times7.03)^2} - 0.0033\times7.03 = 0.193$$

$$j = 1 - k/3 = 1 - 0.193/3 = 0.936$$

Service stress $f_s = \dfrac{M_s}{A_s jd} = \dfrac{20.6\times10^6}{463\times0.936\times152} = 309$ MPa

Crack control parameter, *z*: **10.6.1 (A23.3-19)**

$d_c = 48$ mm

$A = 2\times s\times d_c = 2\times400\times48 = 38,400$ mm

$z = f_s\sqrt[3]{d_c A} = 309\times\sqrt[3]{48\times38,400} = 37,886$ N/mm > 25000 N/mm

Try 15M@255 mm

$A_{s,act} = \dfrac{b}{s}A_b = \dfrac{925}{255}\times200 = 725$ mm^2

$\rho = \dfrac{A_{s,act}}{b_b d} = \dfrac{725}{925\times152} = 0.52\%$

$k = \sqrt{2\times0.0052\times7.03+(0.0052\times7.03)^2} - 0.0052\times7.03 = 0.235$

$j = 1-k/3 = 1-0.235/3 = 0.922$

$f_s = \dfrac{M_s}{A_s jd} = \dfrac{20.6\times10^6}{725\times0.922\times152} = 200$ MPa

$A = 2\times s\times d_c = 2\times255\times48 = 24,480$ mm^2

$z = f_s\sqrt[3]{d_c A} = 200\times\sqrt[3]{48\times24,480} = 21,105$ N/mm < 25000 N/mm

A.9.3. For the field strip:

A.9.3.1. Flexural design

$b = 1,375$ mm

$M = 0.3 \times 74 = 22.2$ kN.m

$$a = \frac{\phi_s A_s f_y}{\alpha_1 \phi_c f_c' b} = \frac{1.0 \times A_s \times 400}{0.79 \times 1.0 \times 40 \times 1,375} = 9.2 \times 10^{-3} A_s$$

$$M_r = \phi_s A_s f_y \times (d - a/2)$$

$$\rightarrow 22.2 \times 10^6 = 1.0 \times A_s \times 400 \times \left(152 - \left(9.2 \times 10^{-3} A_s\right)/2\right)$$

$$\rightarrow 1.84 A_s^2 - 60,800 A_s + 22.2 \times 10^6 = 0$$

$$\rightarrow A_s = 366 \text{ mm}^2$$

$$A_s = \frac{b}{s} A_b$$

$$\rightarrow s = \frac{b}{A_s} A_b = \frac{1,375}{366} \times 200 = 750 \text{ mm}$$

Use minimum reinforcement, $A_{s,min}$ **13.10.9 (A23.3-19)**

$A_{s,\min} = 0.002 A_g = 0.002 \times (200 \times 1000) = 400 \text{ mm}^2/\text{m}$ **7.8.1 (A23.3-19)**

$s = \frac{b}{A_{s,\min}} A_b = \frac{1000}{400} \times 200 = 500$ mm Use 15M @ 400 mm c/c

Maximum spacing $s_{max} = 3h_s = 3 \times 200 = 600$ mm

Or $= 500$ mm **13.10.4 (A23.3-19)**

$$\rightarrow A_{s,act} = \frac{b}{s} A_b = \frac{1,375}{400} \times 200 = 688 \text{ mm}^2$$

$$\rho = \frac{A_{s,act}}{bd} = \frac{688}{1,375 \times 152} = 0.33\%$$

A.9.3.2. Serviceability check

Service moment at the interior connection = 17 kN.m **13.10.3 (A23.3-19)**

$n = 7.03$

$k = \sqrt{2\rho n + (\rho n)^2} - \rho n$

$k = \sqrt{2 \times 0.0033 \times 7.03 + (0.0033 \times 7.03)^2} - 0.0033 \times 7.03 = 0.193$

$j = 1 - k/3 = 1 - 0.193/3 = 0.936$

Service stress $f_s = \dfrac{M_s}{A_s jd} = \dfrac{17 \times 10^6}{688 \times 0.936 \times 152} = 174$ MPa

Crack control parameter, *z*: **10.6.1 (A23.3-19)**

$d_c = 48$ mm

$A = 2 \times s \times d_c = 2 \times 400 \times 48 = 38,400$ mm

$z = f_s \sqrt[3]{d_c A} = 174 \times \sqrt[3]{48 \times 38,400} = 21,334$ N/mm < 25000 N/mm

Summary:

- Use **15M @ 195 mm** c/c in a 600-mm edge band.
- Use **15M @ 255 mm** c/c for the rest of the 1,525-mm wide column strip.
- Use **15M @ 400 mm** c/c for the 1,375-mm wide field strip.

A.10. Design of Positive Moment Section (Perpendicular Strip)

$d = h - \text{clear cover} - d_b/2 = 200 - 24 - 16/2 = 168$ mm

A.10.1.Column strip

A.10.1.1. Flexural design

$M = 105$ kN.m

The column strip should be designed to resist 55-65% of the total design moment of the design strip. **13.11.2.2 (A23.3-19)**

$M_{Design} = 0.55 \times 105 = 58$ kN.m

$$a = \frac{\phi_s A_s f_y}{\alpha_1 \phi_c f_c' b} = \frac{1.0 \times A_s \times 400}{0.79 \times 1.0 \times 40 \times 2,750} = 4.6 \times 10^{-3} A_s$$

$$M_r = \phi_s A_s f_y \times (d - a/2)$$

$$\rightarrow 58 \times 10^6 = 1.0 \times A_s \times 400 \times \left(168 - \left(4.6 \times 10^{-3} A_s\right)/2\right)$$

$$\rightarrow 0.92 A_s^2 - 67,200 A_s + 58 \times 10^6 = 0$$

$$\rightarrow A_s = 874 \text{ mm}^2$$

$$A_s = \frac{b_b}{s} A_b$$

$$\rightarrow s = \frac{b_b}{A_s} A_b = \frac{2,750}{874} \times 200 = 625 \text{ mm}$$

Use minimum reinforcement, $A_{s,min}$ **13.10.9 (A23.3-19)**

$A_{s,\min} = 0.002 A_g = 0.002 \times (200 \times 1000) = 400$ mm^2/m **7.8.1 (A23.3-19)**

$$s = \frac{b}{A_{s,\min}} A_b = \frac{1000}{400} \times 200 = 500 \text{ mm}$$ Use 15M @ 430 mm c/c

$$\rightarrow A_{s,act} = \frac{b}{s} A_b = \frac{2,750}{430} \times 200 = 1,279 \text{ mm}^2$$

$$\rho = \frac{A_{s,act}}{bd} = \frac{1,279}{2,750 \times 168} = 0.28\%$$

A.10.1.2. Serviceability check

Positive service moment at the edge connection: **13.10.3 (A23.3-19)**

$$= 0.55 \times (0.52 \times M_s) = 0.55 \times (0.52 \times 152.4) = 43.6 \text{ kN.m}$$

$$n = 7.03$$

$$k = \sqrt{2 \times 0.0028 \times 7.03 + (0.0028 \times 7.03)^2} - 0.0028 \times 7.03 = 0.179$$

$$j = 1 - k/3 = 1 - 0.179/3 = 0.94$$

Service stress $f_s = \frac{M_s}{A_s jd} = \frac{43.6 \times 10^6}{1,279 \times 0.94 \times 168} = 178 \text{ MPa}$

Crack control parameter, *z*: **10.6.1 (A23.3-19)**

$$d_c = h_s - d = 200 - 168 = 32 \text{ mm}$$

$$A = 2 \times s \times d_c = 2 \times 430 \times 32 = 27,520 \text{ mm}$$

$$z = f_s \sqrt[3]{d_c A} = 178 \times \sqrt[3]{32 \times 27,520} = 17,062 \text{ N/mm} < 25000 \text{ N/mm}$$

A.10.1.3. Development Length, l_d **12.2 (A23.3-19)**

$$l_d = 0.45 k_1 k_2 k_3 k_4 \frac{f_y}{\sqrt{f_c'}} d_b$$ **12.2.3 (A23.3-19)**

$k_1 = 1.0$ for horizontal reinforcement placed in such a way that less than 300 mm of fresh concrete is cast in the member below the development length

$k_2 = 1.0$ for uncoated reinforcement

$k_3 = 1.0$ for normal density concrete

$k_4 = 0.8$ for 20M and smaller bars

$$\rightarrow l_d = 0.45 \times 1.0 \times 1.0 \times 1.0 \times 0.8 \times \frac{400}{\sqrt{40}} \times 16 = 364 \text{ mm}$$

Summary:

- Use **15M @ 430 mm** c/c for the entire column strip.

A.11. Design of Positive Moment Section (Parallel Strip)

$$d = h - \text{clear cover} - d_b - d_b/2 = 200 - 24 - 16 - 16/2 = 152 \text{ mm}$$

A.11.1. For the column strip:

A.11.1.1. Flexural design

$M = 55$ kN.m

The column strip should be designed to resist 55-65% of the total design moment of the design strip. **13.11.2.2 (A23.3-19)**

$M_{Design} = 0.55 \times 71 = 30$ kN.m

Use minimum reinforcement, $A_{s,min}$ **13.10.9 (A23.3-19)**

$A_{s,\min} = 0.002 A_g = 0.002 \times (200 \times 1000) = 400 \text{ mm}^2/\text{m}$ **7.8.1 (A23.3-19)**

$$s = \frac{b}{A_{s,\min}} A_b = \frac{1000}{400} \times 200 = 500 \text{ mm}$$ Use 15M @ 500 mm c/c

$$\rightarrow A_{s,act} = \frac{b}{s} A_b = \frac{1,525}{500} \times 200 = 610 \text{ mm}^2$$

$$\rho = \frac{A_{s,act}}{bd} = \frac{610}{1,525 \times 168} = 0.26\%$$

A.11.1.2. Serviceability check

Positive service moment = 23 kN.m

$n = 7.03$

$\rho = 0.26\%$

$$k = \sqrt{2 \times 0.0026 \times 7.03 + (0.0026 \times 7.03)^2} - 0.0026 \times 7.03 = 0.175$$

$$j = 1 - k/3 = 1 - 0.175/3 = 0.942$$

Service stress $f_s = \frac{M_s}{A_s jd} = \frac{23 \times 10^6}{610 \times 0.942 \times 152} = 263$ MPa

Crack control parameter, *z*: **10.6.1 (A23.3-19)**

$$d_c = h_s - d = 200 - 152 = 48 \text{ mm}$$

$$A = 2 \times s \times d_c = 2 \times 500 \times 48 = 48,000 \text{ mm}$$

$$z = f_s \sqrt[3]{d_c A} = 263 \times \sqrt[3]{48 \times 48,000} = 34,736 \text{ N/mm} > 25000 \text{ N/mm}$$

Use 15M@340 mm

$$A_{s,act} = \frac{b}{s} A_b = \frac{1,525}{340} \times 200 = 897 \text{ mm}^2$$

$$\rho = \frac{A_{s,act}}{bd} = \frac{897}{1{,}525 \times 152} = 0.39\%$$

$$k = \sqrt{2 \times 0.0039 \times 7.03 + (0.0039 \times 7.03)^2} - 0.0039 \times 7.03 = 0.208$$

$$j = 1 - k/3 = 1 - 0.208/3 = 0.931$$

$$f_s = \frac{M_s}{A_s jd} = \frac{23 \times 10^6}{897 \times 0.931 \times 152} = 181 \text{ MPa}$$

$$A = 2 \times s \times d_c = 2 \times 340 \times 48 = 32{,}640 \text{ mm}^2$$

$$z = f_s \sqrt[3]{d_c A} = 181 \times \sqrt[3]{48 \times 32{,}640} = 21{,}022 \text{ N/mm} < 25000 \text{ N/mm}$$

A.11.1.3. Development Length, l_d **12.2 (A23.3-19)**

$$l_d = 0.45 k_1 k_2 k_3 k_4 \frac{f_y}{\sqrt{f_c'}} d_b$$ **12.2.3 (A23.3-19)**

$k_1 = 1.0$ for horizontal reinforcement placed in such a way that less than 300 mm of fresh concrete is cast in the member below the development length

$k_2 = 1.0$ for uncoated reinforcement

$k_3 = 1.0$ for normal density concrete

$k_4 = 0.8$ for 20M and smaller bars

$$\rightarrow l_d = 0.45 \times 1.0 \times 1.0 \times 1.0 \times 0.8 \times \frac{400}{\sqrt{40}} \times 16 = 364 \text{ mm}$$

A.11.2.For the field strip:

A.11.2.1. Flexural design

$M_{Design} = 0.45 \times 55 = 25 \text{ kN.m}$

Use minimum reinforcement, $A_{s,min}$ **13.10.9 (A23.3-19)**

$A_{s,\min} = 0.002 A_g = 0.002 \times (200 \times 1000) = 400 \text{ mm}^2/\text{m}$ **7.8.1 (A23.3-19)**

$s = \frac{b}{A_{s,\min}} A_b = \frac{1000}{400} \times 200 = 500 \text{ mm}$ Use 15M @ 500 mm c/c

$\rightarrow A_{s,act} = \frac{b}{s} A_b = \frac{1,375}{500} \times 200 = 550 \text{ mm}^2$

$\rho = \frac{A_{s,act}}{bd} = \frac{550}{1,375 \times 152} = 0.26\%$

A.11.2.2. Serviceability check

Positive service moment = 19 kN.m

$n = 7.03$

$\rho = 0.26\%$

$k = \sqrt{2 \times 0.0026 \times 7.03 + (0.0026 \times 7.03)^2} - 0.0026 \times 7.03 = 0.175$

$j = 1 - k/3 = 1 - 0.175/3 = 0.942$

Service stress $f_s = \frac{M_s}{A_s jd} = \frac{19 \times 10^6}{550 \times 0.942 \times 152} = 241 \text{ MPa}$

Crack control parameter, *z*: **10.6.1 (A23.3-19)**

$$d_c = h_s - d = 200 - 152 = 48 \text{ mm}$$

$$A = 2 \times s \times d_c = 2 \times 500 \times 48 = 48{,}000 \text{ mm}$$

$$z = f_s \sqrt[3]{d_c A} = 241 \times \sqrt[3]{48 \times 48{,}000} = 31{,}831 \text{ N/mm} > 25{,}000 \text{ N/mm}$$

Try 15M@365 mm

$$A_{s,act} = \frac{b}{s} A_b = \frac{1{,}575}{365} \times 200 = 753 \text{ mm}^2$$

$$\rho = \frac{A_{s,act}}{bd} = \frac{753}{1{,}575 \times 152} = 0.36\%$$

$$k = \sqrt{2 \times 0.0036 \times 7.03 + (0.0036 \times 7.03)^2} - 0.0036 \times 7.03 = 0.201$$

$$j = 1 - k/3 = 1 - 0.201/3 = 0.933$$

$$f_s = \frac{M_s}{A_s jd} = \frac{19 \times 10^6}{753 \times 0.933 \times 152} = 178 \text{ MPa}$$

$$A = 2 \times s \times d_c = 2 \times 365 \times 48 = 35{,}040 \text{ mm}^2$$

$$z = f_s \sqrt[3]{d_c A} = 178 \times \sqrt[3]{48 \times 35{,}040} = 21{,}168 \text{ N/mm} < 25{,}000 \text{ N/mm}$$

Summary:

- Use **15M @ 340 mm** c/c for the column strip.
- Use **15M @ 365 mm** c/c for the 1,375-mm wide field strip.

APPENDIX B

Flexural Design of a GFRP-RC Flat Plate System (Parking Garage)

B.1. Layout of the Flat Plate System

The dimensions and reinforcement ratios of the connections were defined by performing an elastic analysis of a typical parking garage system consisting of three 5.5 m-long square bays in both directions. The analysis was carried out according to the Direct Design Method as described in the CSA A23.3-19 (CSA 2019b) and CSA S806-12 (CSA 2017) standards, when applicable. Two orthogonal strips were designed: a strip in the direction perpendicular to the free edge and another one in the direction parallel to the free edge as shown in Figure B.1 and B.2.

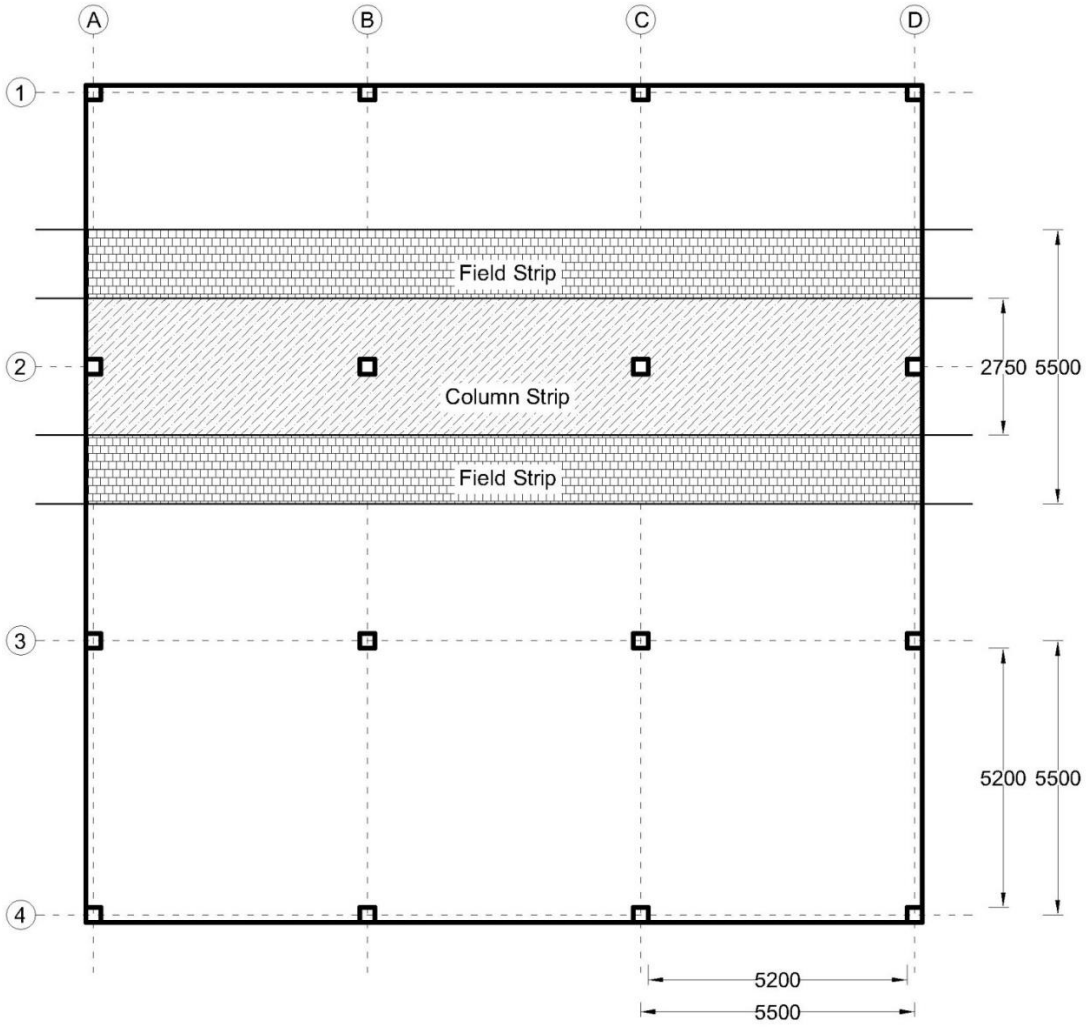

Figure B.1: Design strip perpendicular to free edge

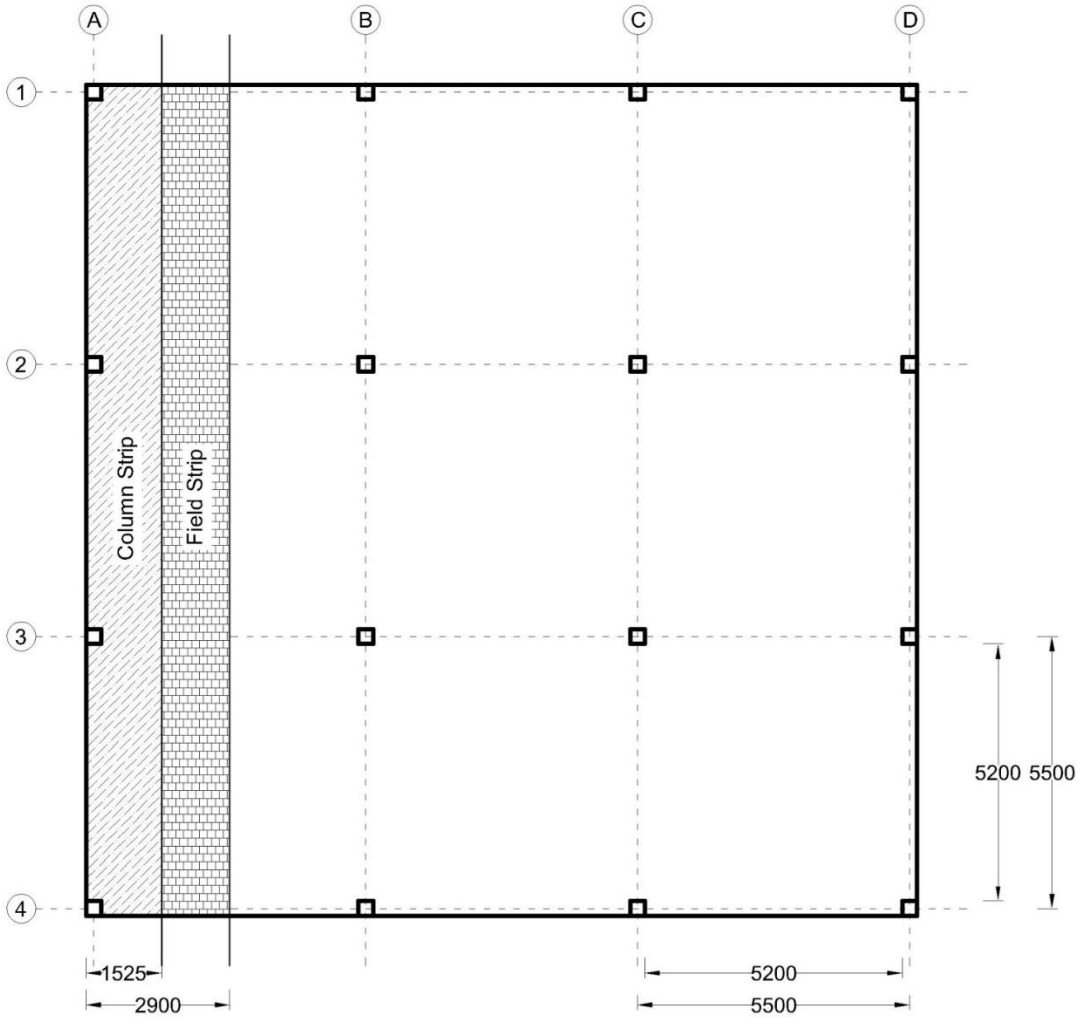

Figure B.2: Design strip parallel to free edge

B.2. Properties of Concrete

Compressive strength of concrete $f_c^{'} = 40$ MPa

Material resistance factor $\phi_c = 1.0$

Modulus of elasticity $E_c = 4,500\sqrt{f_c^{'}} = 4,500\sqrt{40} = 28,460$ MPa **8.6.2.3 (A23.3-19)**

Ultimate compressive strain for concrete ε_{cu} = 0.0035 **10.1.3 (A23.3-19) and 8.4.1.2 (S806-12)**

$\alpha_1 = 0.85 - 0.0015 f_c^{'} = 0.85 - 0.0015 \times 40 = 0.79$ **10.1.7 (A23.3-19) and 8.4.1.5 (S806-12)**

$\beta_1 = 0.97 - 0.0025 f_c^{'} = 0.97 - 0.0025 \times 40 = 0.87$ **10.1.7 (A23.3-19) and 8.4.1.5 (S806-12)**

B.3. Properties of Reinforcement

Use No. 15 bars d_b = 15.9 mm A_b = 199 mm^2

Material resistance factor $\phi_f = 1.0$

B.3.1. Bent bars

Ultimate tensile strength of GFRP $f_{fu} = 1,405$ MPa

Ultimate tensile strain for GFRP $\varepsilon_{fu} = 0.027$

Modulus of elasticity for GFRP $E_f = 52$ GPa

B.3.2. Straight bars

Ultimate tensile strength of GFRP $f_{fu} = 1,712$ MPa

Ultimate tensile strain for GFRP $\varepsilon_{fu} = 0.026$

Modulus of elasticity for GFRP $E_f = 66$ GPa

B.4. Loads

$w_{ll} = 2.4$ kN/m^2 **4.1.5.3 (NRCC 2015)**

$w_{dl} = \text{self-weight} + \text{partition allowance} = 24 \times 0.2 + 1.0 = 5.8$ kN/m^2 **4.1.4.1 (NRCC 2015)**

$w_f = 1.4 w_{dl} = 1.4 \times 5.8 = 8.12$ kN/m^2

or $= 1.25 w_{dl} + 1.5 w_{ll} = 1.25 \times 5.8 + 1.5 \times 2.4 = 7.25 + 3.6 = 10.85$ kN/m^2 Governs

4.1.3.2 (NRCC 2015)

Specified load $w_s = w_{dl} + w_{ll} = 5.8 + 2.4 = 8.2$ kN/m^2 **4.1.3.4 (NRCC 2015)**

B.5. Design Moments in the Perpendicular Strip

B.5.1. Factored moments

$$M_o = \frac{w_f \times l_{2a} \times l_n^2}{8} = \frac{10.85 \times 5.5 \times 5.2^2}{8} = 201.7 \text{ kN.m}$$ **13.9.2 (A23.3-19)**

This moment should be distributed as listed in Table B.1.

Table B.1: Factored moment distribution in a perpendicular design strip

Axis	A			B			C	Units	Code Article (A23.3-19)
l_n	5200			5200					
M_{Design}	26	52	70	65	35	65		%	13.9.3
	52	105	141	131	71	131		kN.m	
$M_{Col.Strp.}$	100	55-65	70-90	70-90	55-65	70-90		%	13.11.2
	52	58-68	99-127	92-118	39-46	92-118		kN.m	
$M_{Fld.Strp.}$	0	45-35	30-10	30-10	45-35	30-10		%	13.11.2
	0	**47**-37	42-14	39-13	32-25	39-13		kN.m	

B.5.2. Unfactored moments

$$M_s = \frac{w_s \times l_{2a} \times l_n^2}{8} = \frac{8.2 \times 5.5 \times 5.2^2}{8} = 152.4 \text{ kN.m}$$ **13.9.2 (A23.3-19)**

This moment should be distributed as listed in Table B.2.

Table B.2: Unfactored moment distribution in a perpendicular design strip

Axis	A			B			C	Units	Code Article (A23.3-19)
l_n	5200			5200					
M_{Design}	26	52	70	65	35	65		%	13.9.3
	40	79	107	99	53	99		kN.m	
$M_{Col.Strp.}$	100	55-65	70-90	70-90	55-65	70-90		%	13.11.2
	40	43-51	75-96	69-89	29-34	69-89		kN.m	
$M_{Fld.Strp.}$	0	45-35	30-10	30-10	45-35	30-10		%	13.11.2
	0	**36**-28	32-11	30-10	14-19	30-10		kN.m	

B.6. Design Moments in the Parallel Strip

B.6.1. Factored moments

$$M_o = \frac{w_f \times l_{2a} \times l_n^2}{8} = \frac{10.85 \times 2.9 \times 5.2^2}{8} = 106.4 \text{ kN.m}$$ **13.9.2 (A23.3-19)**

This moment should be distributed as listed in Table B.3.

Table B.3: Factored moment distribution in a parallel design strip

Axis	A			B		C	Units	Code Article (A23.3-19)
l_n	5200			5200				
M_{Design}	26	52	70	65	35	65	%	13.9.3
	28	55	74	69	37	69	kN.m	
$M_{Col.Strp.}$	100	55-65	70-90	70-90	55-65	70-90	%	13.11.2
	28	30-36	**52**-67	48-62	20-24	48-62	kN.m	
$M_{Fld.Strp.}$	0	45-35	30-10	30-10	45-35	30-10	%	13.11.2
	0	**25**-19	**22**-7	21-7	17-13	21-7	kN.m	

B.6.2. Unfactored moments

$$M_s = \frac{w_s \times l_{2a} \times l_n^2}{8} = \frac{8.2 \times 2.9 \times 5.2^2}{8} = 80.4 \text{ kN.m}$$ **13.9.2 (A23.3-19)**

This moment should be distributed as listed in Table B.4.

Table B.4: Unfactored moment distribution in a parallel design strip

Axis	A			B		C	Units	Code Article (A23.3-19)
l_n	5200			5200				
M_{Design}	26	52	70	65	35	65	%	13.9.3
	21	42	56	52	28	52	kN.m	
$M_{Col.Strp.}$	100	55-65	70-90	70-90	55-65	70-90	%	13.11.2
	21	23-27	39-50	36-47	15-18	36-47	kN.m	
$M_{Fld.Strp.}$	0	45-35	30-10	30-10	45-35	30-10	%	13.11.2
	0	**19**-15	17-6	16-5	13-10	16-5	kN.m	

B.7. Slab Thickness, h_s

Take h_s = 200 mm (to match the steel-RC connection)

B.8. Design of Negative Moment Section (Perpendicular Strip)

Clear concrete clear cover = 24 mm

$$d = h - \text{clear cover} - d_b/2 = 200 - 24 - 15.9/2 = 168 \text{ mm}$$

B.8.1. For the band width, b_b:

B.8.1.1. Flexural design

Design moment for the column strip: $M_{Design} = 52$ kN.m

Reinforcement for the total factored negative moment transferred to the exterior columns shall be placed within a band width $b_b = \text{column width} + 3h_s$. **13.10.3 (A23.3-19)**

$$b_b = \text{column width} + 3h_s = 300 + 3 \times 200 = 900 \text{ mm}$$

$$M_r = \alpha_1 \phi_c f_c' b \beta_1 c \times \left(d - {\beta_1 c}/{2} \right)$$

$$\rightarrow 52 \times 10^6 = 0.79 \times 1.0 \times 40 \times 900 \times 0.87 \times c \times \left(168 - {0.87c}/{2}\right)$$

$$\rightarrow 10,763c^2 - 4,156,790c + 52 \times 10^6 = 0$$

$$\rightarrow c = 12.9 \text{ mm}$$

From strain compatibility:

$$\varepsilon_f = \varepsilon_{cu} \times \left(\frac{d}{c} - 1 \right) = 0.0035 \times \left(\frac{168}{12.9} - 1 \right) = 42.1 \times 10^{-3} > 27 \times 10^{-3}$$

Try minimum area of reinforcement:

$$A_{f,\min} = \frac{400}{E_f} \times A_g = \frac{400}{52,000} \times (900 \times 200) = 1,385 \text{ mm}^2$$ **8.4.2.3 (S806-12)**

From equilibrium:

$$C_r = \alpha_1 \phi_c f_c' b \beta_1 c = 0.79 \times 1.0 \times 40 \times 900 \times 0.87 \times c = 24,742.8c$$

$$Tr = \phi_f f_f A_f = 1.0 \times f_f \times 1,385 = 1,385 f_f$$

$$T_r = C_r \rightarrow f_f = \frac{24,742.8}{1,385} \times c = 17.86c$$ Eq. (I)

From strain compatibility:

$$\varepsilon_f = \varepsilon_{cu} \times \left(\frac{d}{c} - 1 \right) = 0.0035 \times \left(\frac{168}{c} - 1 \right)$$

$$f_f = E_f \times \varepsilon_f = 52,000 \times 0.0035 \times \left(\frac{168}{c} - 1 \right) = 182 \times \left(\frac{168}{c} - 1 \right)$$ Eq. (II)

Solving Eq. (I) and (II):

$$17.86c = 182 \times \left(\frac{168}{c} - 1 \right)$$

$$\rightarrow 17.86c^2 + 182c - 30,576 = 0$$

$$\rightarrow c = 36.6 \text{ mm}$$

$$\rightarrow f_f = 17.86 \times 36.6 = 653.7 \text{ MPa} < f_{fu} = 1,405 \text{ MPa}$$

$$A_f = \frac{b_b}{s} A_b$$

$$\rightarrow s = \frac{b_b}{A_f} A_b = \frac{900}{1,385} \times 199 = 129 \text{ mm}$$ Use No. 15 @ 130 mm c/c

$$\rightarrow A_{f,act} = \frac{b_b}{s} A_b = \frac{900}{130} \times 199 = 1,378 \text{ mm}^2$$

Check for the Balanced Reinforcement Ratio, ρ_b :

$$\rho = \frac{A_{f,act}}{b_b d} = \frac{1,378}{900 \times 168} = 0.91\%$$

$$\rho_b = \alpha_1 \beta_1 \frac{\phi_c f_c^{'}}{\phi_f f_{fu}} \times \frac{\varepsilon_{cu}}{\varepsilon_{cu} + \varepsilon_{fu}} = 0.79 \times 0.87 \times \frac{1.0 \times 40}{1.0 \times 1,405} \times \frac{0.0035}{0.0035 + 0.027} = 0.22\%$$

$\rho > \rho_b$ Over-reinforced, Ok

B.8.1.2. Serviceability check

Service moment at the edge connection = 40 kN.m

$$n = \frac{E_f}{E_c} = \frac{52,000}{28,460} = 1.84$$

$$k = \sqrt{2\rho n + (\rho n)^2} - \rho n$$

$$k = \sqrt{2 \times 0.0091 \times 1.84 + (0.0091 \times 1.84)^2} - 0.0091 \times 1.84 = 0.167$$

$$j = 1 - k/3 = 1 - 0.167/3 = 0.944$$

Service stress $f_s = \frac{M_s}{A_f jd} = \frac{40 \times 10^6}{1,378 \times 0.944 \times 168} = 183 \text{ MPa}$

Service strain $\varepsilon_f = \frac{f_s}{E_f} = \frac{183}{52,000} = 0.0035 > 0.0015$

Crack control parameter, *z*: **8.3.1.1 (S806-12)**

$$d_c = h - d = 200 - 168 = 32 \text{ mm}$$

$$A = 2 \times s \times d_c = 2 \times 130 \times 32 = 8,320 \text{ mm}$$

$$z = f_s k_b \frac{E_s}{E_f} \sqrt[3]{d_c A} = 179.6 \times 1.2 \times \frac{200,000}{52,000} \sqrt[3]{32 \times 8,320} = 53,326 \text{ N/mm} > 38,000 \text{ N/mm}$$

Try No. 15 @ 85 mm

$$A_{f,act} = \frac{b_b}{s} A_b = \frac{900}{85} \times 199 = 2,107 \text{ mm}^2$$

$$\rho = \frac{A_{f,act}}{b_b d} = \frac{2,107}{900 \times 168} = 1.39\%$$

$$k = \sqrt{2 \times 0.0139 \times 1.84 + (0.0139 \times 1.84)^2} - 0.0139 \times 1.84 = 0.202$$

$$j = 1 - k/3 = 1 - 0.202/3 = 0.933$$

$$f_s = \frac{M_s}{A_s j d} = \frac{40 \times 10^6}{2,107 \times 0.933 \times 168} = 121 \text{ MPa}$$

Service strain $\varepsilon_f = \frac{f_s}{E_f} = \frac{121}{52,000} = 0.0023 > 0.0015$

$$A = 2 \times s \times d_c = 2 \times 85 \times 32 = 5,440 \text{ mm}$$

$$z = f_s k_b \frac{E_s}{E_f} \sqrt[3]{d_c A} = 121 \times 1.2 \times \frac{200,000}{52,000} \sqrt[3]{32 \times 5,440} = 31,182 \text{ N/mm} < 38,000 \text{ N/mm}$$

Reinforcement stress limit: **7.1.2.2. (S806-12)**

$$0.25 f_{fu} = 0.25 \times 1,405 = 351 \text{ MPa} > f_s = 121 \text{ MPa}$$

B.8.1.3. Development length, l_d **9.5 (S806-12)**

From equilibrium:

$$C_r = \alpha_1 \phi_c f_c^{'} b \beta_1 c = 0.79 \times 1.0 \times 40 \times 900 \times 0.87 \times c = 24,742.8c$$

$$Tr = \phi_f f_f A_f = 1.0 \times f_f \times 2,107 = 2,107 f_f$$

$$T_r = C_r \rightarrow f_f = \frac{24,742.8}{2,107} \times c = 11.74c \qquad \text{Eq. (I)}$$

From strain compatibility:

$$\varepsilon_f = \varepsilon_{cu} \times \left(\frac{d}{c} - 1 \right) = 0.0035 \times \left(\frac{168}{c} - 1 \right)$$

$$f_f = E_f \times \varepsilon_f = 52,000 \times 0.0035 \times \left(\frac{168}{c} - 1 \right) = 182 \times \left(\frac{168}{c} - 1 \right) \qquad \text{Eq. (II)}$$

Solving Eq. (I) and (II):

$$11.74c = 182 \times \left(\frac{168}{c} - 1 \right)$$

$$\rightarrow 11.74c^2 + 182c - 30,576 = 0$$

$$\rightarrow c = 43.9 \text{ mm}$$

$$\rightarrow f_f = 11.74 \times 43.9 = 515 \text{ MPa} < f_{fu} = 520 \text{ MPa}$$

$k_2 = 1.0$ for normal density concrete

$$\rightarrow l_d = 165 k_2 \frac{d_b}{\sqrt{f_c^{'}}} = 165 \times 1.0 \times \frac{16}{\sqrt{40}} = 417 \text{ mm}$$

B.8.2. For the rest of the column strip:

Design moment = 0

Use minimum reinforcement, $A_{f,min}$ **13.10.9 (A23.3-19)**

Maximum spacing $s_{max} = 3h_s = 3 \times 200 = 600$ mm

Or $= 300$ mm **8.4.2.3 (S806-12)**

Use No. 15 @ 130 mm c/c

Summary:

- Use **No. 15 @ 85 mm** c/c in a 900-mm wide band centred on the column.
- Use **No. 15 @ 130 mm** c/c for the rest of the strip.

B.9. Design of Negative Moment Section (Parallel Strip)

$d = h - \text{clear cover} - d_b - d_b/2 = 200 - 24 - 16 - 16/2 = 152$ mm

B.9.1. For the band width, b_b:

B.9.1.1. Flexural design

Design moment for the column strip: $M_{Design} = 52$ kN.m

At interior columns, the band width, b_b, shall be designed to resist at least one-third of the total factored negative moment in the entire design strip. **13.11.2.7 (A23.3-19)**

$b_b = \text{column width} + 1.5h_s = 300 + 1.5 \times 200 = 600$ mm

$$M_r = \alpha_1 \phi_c f_c' b \beta_1 c \times \left(d - \beta_1 c / 2 \right)$$

$$\rightarrow \frac{74 \times 10^6}{3} = 0.79 \times 1.0 \times 40 \times 600 \times 0.87 \times c \times \left(152 - 0.87c / 2 \right)$$

$$7{,}175c^2 - 2{,}507{,}270c + 24.67\times10^6 = 0$$

$$\rightarrow c = 10.1 \text{ mm}$$

From strain compatibility:

$$\varepsilon_f = \varepsilon_{cu}\times\left(\frac{d}{c}-1\right) = 0.0035\times\left(\frac{152}{10.1}-1\right) = 49\times10^{-3} > 26\times10^{-3}$$

Try minimum area of reinforcement:

$$A_{f,\min} = \frac{400}{E_f}\times A_g = \frac{400}{66{,}000}\times(600\times200) = 727.3 \text{ mm}^2$$ **8.4.2.3 (S806-12)**

From equilibrium:

$$C_r = \alpha_1\phi_c f_c' b\beta_1 c = 0.79\times1.0\times40\times600\times0.87\times c = 16{,}495.2c$$

$$T_r = \phi_f f_f A_f = 1.0\times f_f \times 727.3 = 727.3 f_f$$

$$T_r = C_r \rightarrow f_f = \frac{16{,}495.2}{727.3}\times c = 22.68c$$ Eq. (I)

From strain compatibility:

$$\varepsilon_f = \varepsilon_{cu}\times\left(\frac{d}{c}-1\right) = 0.0035\times\left(\frac{152}{c}-1\right)$$

$$f_f = E_f\times\varepsilon_f = 66{,}000\times0.0035\times\left(\frac{152}{c}-1\right) = 231\times\left(\frac{152}{c}-1\right)$$ Eq. (II)

Solving Eq. (I) and (II):

$$22.68c = 231\times\left(\frac{152}{c}-1\right)$$

$\rightarrow 22.68c^2 + 231c - 35{,}112 = 0$

$\rightarrow c = 34.6$ mm

$\rightarrow f_f = 22.68 \times 34.6 = 785$ MPa $< f_{fu} = 1{,}712$ MPa

$A_f = \frac{b_b}{s} A_b$

$\rightarrow s = \frac{b_b}{A_f} A_b = \frac{600}{727.3} \times 199 = 164$ mm Use No. 15 @ 165 mm c/c

$\rightarrow A_{f,act} = \frac{b_b}{s} A_b = \frac{600}{165} \times 199 = 723.6$ mm^2

Check for the Balanced Reinforcement Ratio, ρ_b :

$\rho = \frac{A_{f,act}}{b_b d} = \frac{723.6}{600 \times 152} = 0.79\%$

$\rho_b = \alpha_1 \beta_1 \frac{\phi_c f_c^{'}}{\phi_f f_{fu}} \times \frac{\varepsilon_{cu}}{\varepsilon_{cu} + \varepsilon_{fu}} = 0.79 \times 0.87 \times \frac{1.0 \times 40}{1.0 \times 1{,}712} \times \frac{0.0035}{0.0035 + 0.026} = 0.19\%$

$\rho > \rho_b$ Over-reinforced, Ok

B.9.1.2. Serviceability check

Service moment at the interior connection $= \frac{0.7 M_s}{3} = \frac{0.7 \times 80.4}{3} = 18.8$ kN.m **13.10.3 (A23.3-19)**

$n = \frac{E_f}{E_c} = \frac{66{,}000}{28{,}460} = 2.32$

$\rho = 0.79\%$

$k = \sqrt{2\rho n + (\rho n)^2} - \rho n$

$$k = \sqrt{2 \times 0.0079 \times 2.32 + (0.0079 \times 2.32)^2} - 0.0079 \times 2.32 = 0.172$$

$$j = 1 - k/3 = 1 - 0.172/3 = 0.943$$

Service stress $f_s = \dfrac{M_s}{A_s jd} = \dfrac{18.8 \times 10^6}{723.6 \times 0.943 \times 152} = 181$ MPa

Service strain $\varepsilon_f = \dfrac{f_s}{E_f} = \dfrac{181}{66,000} = 0.0027 > 0.0015$

Crack control parameter, *z*: **8.3.1.1 (S806-12)**

$$d_c = h_s - d = 200 - 152 = 48 \text{ mm}$$

$$A = 2 \times s \times d_c = 2 \times 165 \times 48 = 15,840 \text{ mm}^2$$

$$z = f_s k_b \frac{E_s}{E_f} \sqrt[3]{d_c A} = 181 \times 1.2 \times \frac{200,000}{66,000} \sqrt[3]{48 \times 15,840} = 60,073 \text{ N/mm} > 38,000 \text{ N/mm}$$

Try No. 15 @ 100 mm

$$A_{f,act} = \frac{b}{s} A_b = \frac{600}{100} \times 199 = 1,194 \text{ mm}^2$$

$$\rho = \frac{A_{f,act}}{b_b d} = \frac{1,194}{600 \times 152} = 1.31\%$$

$$k = \sqrt{2 \times 0.0131 \times 2.32 + (0.0131 \times 2.32)^2} - 0.0131 \times 2.32 = 0.218$$

$$j = 1 - k/3 = 1 - 0.218/3 = 0.927$$

$$f_s = \frac{M_s}{A_s jd} = \frac{18.8 \times 10^6}{1,194 \times 0.927 \times 152} = 112 \text{ MPa}$$

$$A = 2 \times s \times d_c = 2 \times 100 \times 48 = 9,600 \text{ mm}$$

$$z = f_s k_b \frac{E_s}{E_f} \sqrt[3]{d_c A} = 112 \times 1.2 \times \frac{200,000}{66,000} \sqrt[3]{48 \times 9,600} = 31,458 \text{ N/mm} < 38000 \text{ N/mm}$$

B.9.2. For the rest of the column strip:

B.9.2.1. Flexural design

$$b = \frac{2,750}{2} + 150 - 600 = 925 \text{ mm}$$

$$M = 52 - \frac{74}{3} = 27.3 \text{ kN.m}$$

$$M_r = \alpha_1 \phi_c f_c^{'} b \beta_1 c \times \left(d - {\beta_1 c}/{2} \right)$$

$$\rightarrow 27.3 \times 10^6 = 0.79 \times 1.0 \times 40 \times 925 \times 0.87 \times c \times \left(152 - {0.87c}/{2} \right)$$

$$\rightarrow 11,062c^2 - 3,865,375c + 27.3 \times 10^6 = 0$$

$$\rightarrow c = 7.2 \text{ mm}$$

From strain compatibility:

$$\varepsilon_f = \varepsilon_{cu} \times \left(\frac{d}{c} - 1 \right) = 0.0035 \times \left(\frac{152}{7.2} - 1 \right) = 70.4 \times 10^{-3} > 26 \times 10^{-3}$$

Try minimum area of reinforcement:

$$A_{f,\min} = \frac{400}{E_f} \times A_g = \frac{400}{66,000} \times (925 \times 200) = 1,121 \text{ mm}^2$$ **8.4.2.3 (S806-12)**

From equilibrium:

$$C_r = \alpha_1 \phi_c f_c^{'} b \beta_1 c = 0.79 \times 1.0 \times 40 \times 925 \times 0.87 \times c = 25430.1c$$

$$T_r = \phi_f f_f A_f = 1.0 \times f_f \times 1{,}121 = 1{,}121 f_f$$

$$T_r = C_r \rightarrow f_f = \frac{25{,}430.1}{1{,}121} \times c = 22.69c \qquad \text{Eq. (I)}$$

From strain compatibility:

$$\varepsilon_f = \varepsilon_{cu} \times \left(\frac{d}{c} - 1 \right) = 0.0035 \times \left(\frac{152}{c} - 1 \right)$$

$$f_f = E_f \times \varepsilon_f = 66{,}000 \times 0.0035 \times \left(\frac{152}{c} - 1 \right) = 231 \times \left(\frac{152}{c} - 1 \right) \qquad \text{Eq. (II)}$$

Solving Eq. (I) and (II):

$$22.69c = 231 \times \left(\frac{152}{c} - 1 \right)$$

$$\rightarrow 22.69c^2 + 231c - 35{,}112 = 0$$

$$\rightarrow c = 34.6 \text{ mm}$$

$$\rightarrow f_f = 22.69 \times 34.6 = 785 \text{ MPa} < f_{fu} = 1{,}712 \text{ MPa}$$

$$A_f = \frac{b}{s} A_b$$

$$\rightarrow s = \frac{b}{A_f} A_b = \frac{925}{1{,}121} \times 199 = 164 \text{ mm} \qquad \text{Use No. 15 @ 165 mm c/c}$$

$$\rightarrow A_{f,act} = \frac{b}{s} A_b = \frac{925}{165} \times 199 = 1{,}116 \text{ mm}^2$$

$$\rho = \frac{A_{f,act}}{bd} = \frac{1{,}116}{925 \times 152} = 0.79\%$$

B.9.2.2. Serviceability check

Service moment at the interior connection

$$= 0.7 \times \left(0.7 M_s\right) - \frac{0.7 M_s}{3} = 0.7 \times \left(0.7 \times 80.4\right) - \frac{0.7 \times 80.4}{3} = 20.6 \text{ kN.m}$$ **13.10.3 (A23.3-19)**

$n = 2.32$

$\rho = 0.79\%$

$k = 0.172$

$j = 0.943$

Service stress $f_s = \frac{M_s}{A_s\, jd} = \frac{20.6 \times 10^6}{1{,}121 \times 0.943 \times 152} = 128 \text{ MPa}$

Crack control parameter, *z*: **8.3.1.1 (S806-12)**

$d_c = 48 \text{ mm}$

$A = 2 \times s \times d_c = 2 \times 165 \times 48 = 15{,}840 \text{ mm}^2$

$z = f_s k_b \frac{E_s}{E_f} \sqrt[3]{d_c A} = 128 \times 1.2 \times \frac{200{,}000}{66{,}000} \sqrt[3]{48 \times 15{,}840} = 42{,}482 \text{ N/mm} > 38{,}000 \text{ N/mm}$

Try No. 15 @ 135 mm

$A_{f,act} = \frac{b}{s} A_b = \frac{925}{135} \times 199 = 1{,}364 \text{ mm}^2$

$\rho = \frac{A_{f,act}}{bd} = \frac{1{,}364}{925 \times 152} = 0.97\%$

$k = \sqrt{2 \times 0.0097 \times 2.32 + \left(0.0097 \times 2.32\right)^2} - 0.0097 \times 2.32 = 0.191$

$$j = 1 - k/3 = 1 - 0.191/3 = 0.936$$

$$f_s = \frac{M_s}{A_s jd} = \frac{20.6 \times 10^6}{1,364 \times 0.936 \times 152} = 106 \text{ MPa}$$

$$A = 2 \times s \times d_c = 2 \times 135 \times 48 = 12,960 \text{ mm}$$

$$z = f_s k_b \frac{E_s}{E_f} \sqrt[3]{d_c A} = 106 \times 1.2 \times \frac{200,000}{66,000} \sqrt[3]{48 \times 12,960} = 32,905 \text{ N/mm} < 38000 \text{ N/mm}$$

B.9.3. For the field strip:

B.9.3.1. Flexural design

$b = 1,375$ mm

$M = 22$ kN.m

Try minimum area of reinforcement:

$$A_{f,\min} = \frac{400}{E_f} \times A_g = \frac{400}{66,000} \times (1,375 \times 200) = 1,666.7 \text{ mm}^2$$ **8.4.2.3 (S806-12)**

From equilibrium:

$$C_r = \alpha_1 \phi_c f_c' b \beta_1 c = 0.79 \times 1.0 \times 40 \times 1,375 \times 0.87 \times c = 37801.5c$$

$$T_r = \phi_f f_f A_f = 1.0 \times f_f \times 1,666.7 = 1,666.7 f_f$$

$$T_r = C_r \rightarrow f_f = \frac{37,801.5}{1,666.7} \times c = 22.68c$$ Eq. (I)

From strain compatibility:

$$\varepsilon_f = \varepsilon_{cu} \times \left(\frac{d}{c} - 1 \right) = 0.0035 \times \left(\frac{152}{c} - 1 \right)$$

$$f_f = E_f \times \varepsilon_f = 66,00 \times 0.0035 \times \left(\frac{152}{c} - 1\right) = 231 \times \left(\frac{152}{c} - 1\right) \qquad \text{Eq. (II)}$$

Solving Eq. (I) and (II):

$$22.68c = 231 \times \left(\frac{152}{c} - 1\right)$$

$$\rightarrow 22.68c^2 + 231c - 35,112 = 0$$

$$\rightarrow c = 34.6 \text{ mm}$$

$$\rightarrow f_f = 22.68 \times 34.6 = 784.7 \text{ MPa} < f_{fu} = 1,712 \text{ MPa}$$

$$A_f = \frac{b}{s} A_b$$

$$\rightarrow s = \frac{b}{A_f} A_b = \frac{1,375}{1,666.7} \times 199 = 164 \text{ mm} \qquad \text{Use No. 15 @ 165 mm c/c}$$

$$\rightarrow A_{f,act} = \frac{b}{s} A_b = \frac{1,375}{165} \times 199 = 1,658 \text{ mm}^2$$

$$\rho = \frac{A_{f,act}}{bd} = \frac{1,658}{1,375 \times 152} = 0.79\%$$

B.9.3.2. Serviceability check

Service moment at the interior connection = 17 kN.m

$$n = 2.32$$

$$\rho = 0.79\%$$

$$k = 0.172$$

$$j = 0.943$$

Service stress $f_s = \dfrac{M_s}{A_s jd} = \dfrac{16.9\times10^6}{1,658\times0.943\times152} = 71$ MPa

Crack control parameter, *z*: 8.3.1.1 (S806-12)

$d_c = 48$ mm

$A = 2\times s\times d_c = 2\times165\times48 = 15,840$ mm^2

$z = f_s k_b \dfrac{E_s}{E_f}\sqrt[3]{d_c A} = 71\times1.2\times\dfrac{200,000}{66,000}\sqrt[3]{48\times15,840} = 23,364$ N/mm < 38,000 N/mm

Summary:

- Use **No. 15 @ 100 mm** c/c in a 600-mm edge band.
- Use **No. 15 @ 135 mm** c/c for the rest of the 1,525-mm wide column strip.
- Use **No. 15 @ 165 mm** c/c for the 1,375-mm wide field strip.

B.10. Design of Positive Moment Section (Perpendicular Strip)

$d = h - \text{clear cover} - d_b/2 = 200 - 24 - 16/2 = 168$ mm

B.10.1. Column strip

B.10.1.1. Flexural design

$M = 105$ kN.m

The column strip should be designed to resist 55-65% of the total design moment of the design strip. **13.11.2.2 (A23.3-19)**

$M_{Design} = 0.55\times105 = 58$ kN.m

Try minimum area of reinforcement:

$$A_{f,\min} = \frac{400}{E_f} \times A_g = \frac{400}{66,000} \times (2750 \times 200) = 3,333 \text{ mm}^2$$ **8.4.2.3 (S806-12)**

From equilibrium:

$$C_r = \alpha_1 \phi_c f_c' b \beta_1 c = 0.79 \times 1.0 \times 40 \times 2,750 \times 0.87 \times c = 75,603c$$

$$Tr = \phi_f f_f A_f = 1.0 \times f_f \times 3,333 = 3,333 f_f$$

$$T_r = C_r \rightarrow f_f = \frac{75,603}{3,333} \times c = 22.68c$$ Eq. (I)

From strain compatibility:

$$\varepsilon_f = \varepsilon_{cu} \times \left(\frac{d}{c} - 1 \right) = 0.0035 \times \left(\frac{168}{c} - 1 \right)$$

$$f_f = E_f \times \varepsilon_f = 66,000 \times 0.0035 \times \left(\frac{168}{c} - 1 \right) = 231 \times \left(\frac{168}{c} - 1 \right)$$ Eq. (II)

Solving Eq. (I) and (II):

$$22.68c = 231 \times \left(\frac{168}{c} - 1 \right)$$

$$\rightarrow 22.68c^2 + 231c - 38,808 = 0$$

$$\rightarrow c = 36.6 \text{ mm}^2$$

$$\rightarrow f_f = 22.68 \times 36.6 = 830 \text{ MPa} < f_{fu} = 1,712 \text{ MPa}$$

$$A_f = \frac{b}{s} A_b$$

$$\rightarrow s = \frac{b}{A_f} A_b = \frac{2,750}{3,333} \times 199 = 164 \text{ mm}$$ Use No. 15 @ 165 mm c/c

$$\rightarrow A_{f,act} = \frac{b}{s} A_b = \frac{2,750}{165} \times 199 = 3,317 \text{ mm}^2$$

$$\rho = \frac{A_{f,act}}{bd} = \frac{3,317}{2,750 \times 168} = 0.72\%$$

B.10.1.2. Serviceability check

Positive service moment $= 0.55 \times (0.52 \times M_s) = 0.55 \times (0.52 \times 152.4) = 43.6$ kN.m

13.10.3 (A23.3-19)

$n = 2.32$

$$k = \sqrt{2 \times 0.0072 \times 2.32 + (0.0072 \times 2.32)^2} - 0.0072 \times 2.32 = 0.169$$

$$j = 1 - k/3 = 1 - 0.169/3 = 0.944$$

Service stress $f_s = \frac{M_s}{A_s jd} = \frac{43.6 \times 10^6}{3,317 \times 0.944 \times 168} = 82.9$ MPa

Crack control parameter, *z*: **8.3.1.1 (S806-12)**

$d_c = 32$ mm

$A = 2 \times s \times d_c = 2 \times 165 \times 32 = 10,560$ mm

$$z = f_s k_b \frac{E_s}{E_f} \sqrt[3]{d_c A} = 82.9 \times 1.2 \times \frac{200,000}{66,000} \sqrt[3]{32 \times 10,560} = 20,997 \text{ N/mm} < 38,000 \text{ N/mm}$$

Use minimum reinforcement for the direction parallel to the free edge, as well.

Summary:

- Use **No. 15 @ 165 mm** c/c for the entire design strip in both perpendicular and parallel directions.